COMMISSIONING OF A

MAGNETIC SUSPENSION DENSITOMETER

FOR HIGH-ACCURACY DENSITY MEASUREMENTS

OF NATURAL GAS MIXTURES

A Dissertation

by

PRASHANT VITHAL PATIL

Submitted to the Office of Graduate Studies of
Texas A&M University
in partial fulfillment of the requirements for the degree of

DOCTOR OF PHILOSOPHY

May 2005

Major Subject: Chemical Engineering

COMMISSIONING OF A

MAGNETIC SUSPENSION DENSITOMETER

FOR HIGH-ACCURACY DENSITY MEASUREMENTS

OF NATURAL GAS MIXTURES

A Dissertation

by

PRASHANT VITHAL PATIL

Submitted to Texas A&M University
in partial fulfillment of the requirements
for the degree of

DOCTOR OF PHILOSOPHY

Approved as to style and content by:

Kenneth R. Hall (Co-Chair of Committee)	James C. Holste (Co-Chair of Committee)
Maria A. Barrufet (Member)	David M. Ford (Member)
	Kenneth R. Hall (Head of Department)

May 2005

Major Subject: Chemical Engineering

ABSTRACT

Commissioning of a Magnetic Suspension Densitometer for High-accuracy Density Measurements of Natural Gas Mixtures. (May 2005)

Prashant Vithal Patil, B. Chem. Engg., University of Bombay, Bombay, India;

M.S., Chemical Engineering, The University of Tulsa

Co-Chairs of Advisory Committee: Dr. Kenneth R. Hall
Dr. James C. Holste

High-accuracy density measurement data are required to validate equations of state (EOS) for use in custody transfer of natural gas through pipelines. The AGA8-DC92 EOS, which is the current industry standard has already been validated against a databank of natural gas mixtures with compositions containing up to 0.2 mole percent of the heavier C_{6+} fraction and is expected to predict densities of natural gas mixtures containing higher mole percentages of the C_{6+} fraction with the same accuracy. With the advances in exploration, drilling and production, natural gas streams containing higher percentages of the C_{6+} fraction have become available from the deepwater and ultra-deepwater Gulf of Mexico in recent years. High-accuracy, density data for such natural gas mixtures are required to check if the AGA8-DC92 EOS covers the entire range of pressure, temperature and compositions encountered in custody transfer.

A state-of-the-art, high pressure, high temperature, compact single-sinker magnetic suspension densitometer has been used to measure densities of two simulated natural gas mixtures named M91C1 and M94C1 after validating its operation by measuring densities of pure argon, nitrogen and methane in the range (270 to 340) K [(26.33 to152.33) ^{o}F, (-3.15 to 66.85) ^{o}C] and (3.447 to 34.474) MPa [(500 to 5,000) psia]. Measured densities of M91C1, not containing the C_{6+} fraction show larger than expected relative deviations from the AGA8-DC92 EOS predictions in regions 1 and 2 but agree well with predictions from the recently developed REFPROP EOS, implying

that the AGA8-DC92 EOS may be unreliable in its present state even for natural gas mixtures not containing the C_{6+} fraction. Measured densities of M94C1 containing more than 0.2 mole percent of the C_{6+} fraction deviate from the AGA8-DC92 EOS predictions by more than the expected values in region 1 which is not surprising but the agreement with AGA8-DC92 EOS predictions in region 2 is misleading which becomes evident when the measured densities are compared to the REFPROP EOS predictions. The measured data can be used to recalibrate the parameters of the AGA8-DC92 EOS or to validate an entirely new EOS.

ACKNOWLEDGMENTS

I wish to thank Dr. Kenneth R. Hall and Dr. James C. Holste for giving me the opportunity of working on the present research project, for their guidance and support and most importantly for their understanding and patience during difficult periods of this work. I also want to thank Dr. David M. Ford and Dr. Maria A. Barrufet for serving on my research advisory committee.

I wish to express my sincere appreciation of the funding provided by the National Institute of Standards and Technology over the earlier part and by Mardi Gras Transportation Systems, LLC over the latter part of this research work. I owe Dr. Kenneth R. Hall a special sense of gratitude for providing financial support for my graduate studies beyond the anticipated period of completion.

I also thank Mr. Ronald E. Beaty of Premier Measurement Services and Mr. James E. Gallagher of Savant Measurement Corporation for not only making the funding for this research work possible but also for investing their time and effort giving suggestions and feedback on technical matters, for their encouragement and for sharing their invaluable experiences in the oil and gas industry.

Dr. Hans Wilhelm Lösch and Mrs. Cornelia Lösch of Rubotherm Präzisionsmesstechnik GmbH, Bochum, Germany helped troubleshoot the operation of the unique magnetic suspension densitometer used in this research work at several stages. Their long-distance customer support interactions through e-mail and telephonic conversations are greatly appreciated.

I consider myself fortunate to have enjoyed the opportunity of visiting The University of Valladolid over the summer of 2001 for a fortnight. The visit helped me get my first close look at the operation of a magnetic suspension densitometer similar to the one used in the present work and gave me a head start for the present work. I appreciate the sponsorship of this visit by Dr. Miguel Angel Villamanan Olfos and the hospitality and friendship of Dr. Cesar R. Chamorro Camazon.

Although, I did not interact with them directly, I appreciate the provision of the NIST-12 and NIST-23 (REFPROP) software programs by Dr. Eric W. Lemmon and the technical feedback from Dr. Mark O. McLinden. Contributions from both working at the National Institute of Standards and Technology helped make important research related decisions.

Several individuals within the chemical engineering department helped the research work in various ways, which I would like to acknowledge. Mr. Randy Marek helped with several of the ancillary equipment, Dr. Philip T. Eubank graciously allowed the use of the differential pressure indicator from his laboratory, Dr. William Rogers offered advice based on his experience and the undergraduate student workers Mr. Mark Standlee, Mr. Noel Wilcoxon, Ms. Amber Smades and Ms. Aundria Harrell all offered valuable support in trying to meet research goals in a timely manner. Ms. Valerie Green, Ms. Towanna Hubacek and Ms. Ninette Portales helped me stay focused on my research by handling administrative procedures and paperwork. My fellow graduate students Ms. Widya Syamsul, Mr. Jingjun Zhou, Mr. Saquib Ejaz and Mr. Mert Atilhan who also worked on the present research project made work enjoyable by having discussions and offering their friendship, which I shall always cherish.

Finally, I would like to thank my friends Dr. Shyamkumar Surthi, Dr. Srinivas Vuddagiri and Dr. Vijay Mhetar who offered me encouragement and support whenever the going got tough in my career endeavors.

TABLE OF CONTENTS

LIST OF FIGURES

FIGURE Page

FIGURE Page

LIST OF TABLES

CHAPTER I

INTRODUCTION

1.1 Energy Review and Outlook

Fossil fuel in the form of coal, natural gas and petroleum oil has been the major source of energy in the world for the past half century. Natural gas is a mixture of predominantly methane with smaller quantities of nitrogen, carbon dioxide, paraffinic hydrocarbons such as ethane, propane, butane, pentane *etc*. and non-hydrocarbon gases such as helium and hydrogen sulfide and water. Some natural gas inevitably occurs in a petroleum oil reservoir and is referred to as 'associated gas' because of its inseparability during petroleum oil production. A reservoir at higher pressure (P) and higher temperature (T), deep into the earth crust may be a petroleum oil reservoir that underwent a phase change from heavier liquid hydrocarbons to a lighter gaseous form, such as methane, because of its higher T and is capable of producing hydrocarbons as purely 'non-associated gas'.

Annual estimates prior to 1949 and historical energy consumption data since 1949 maintained by the Energy Information Administration of the US Department of Energy (DOE) show that while coal surpassed wood as the primary source of energy in 1885, its use was in turn overtaken by the emergence of petroleum oil around 1950 and natural gas in 1957 as the major sources of energy (Energy Information Administration, 2003). Figure 1.1 shows the historical data since 1949 as well as the outlook through 2025 for domestic fossil fuel energy production and consumption for

---

This dissertation follows the style and format of the *AIChE Journal.*

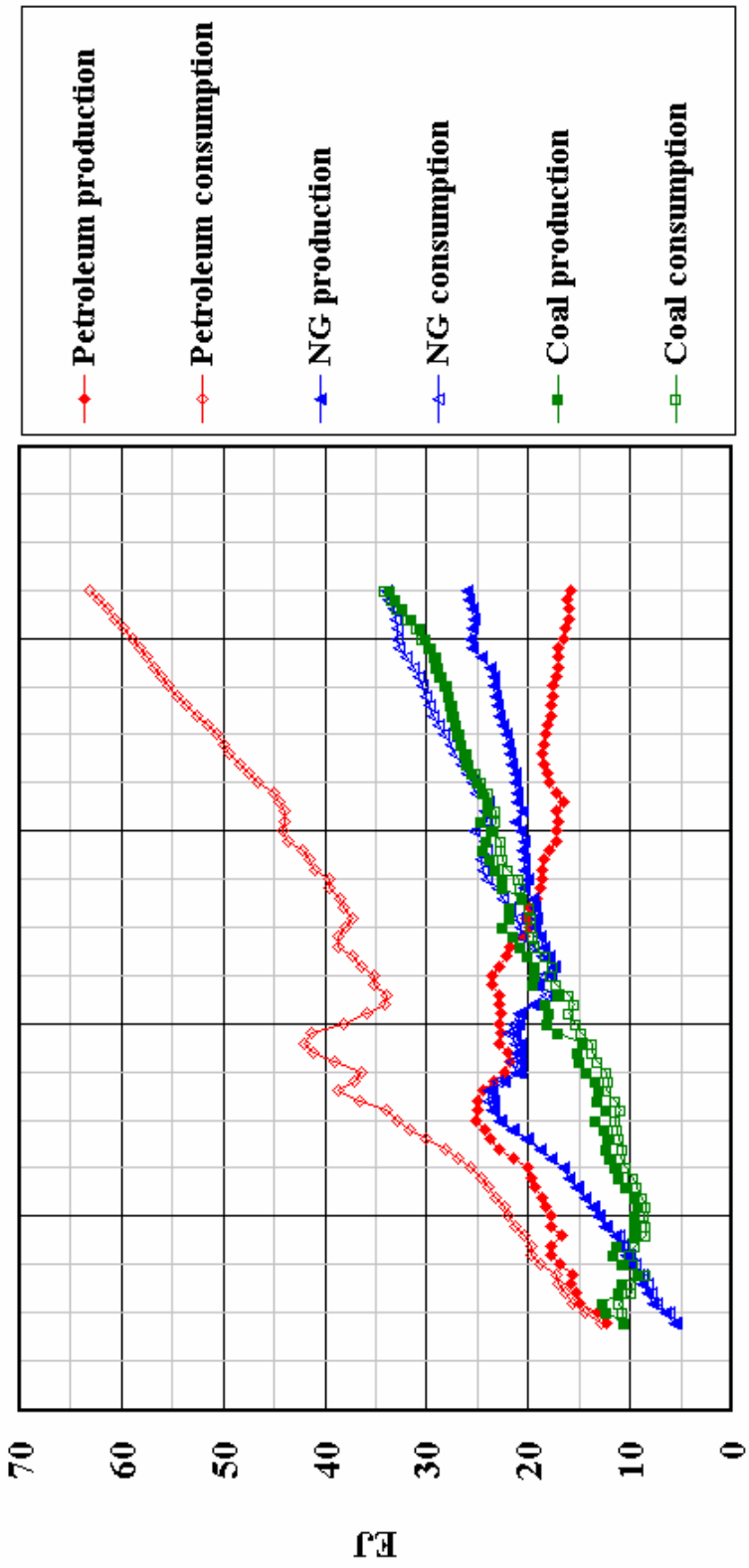

Figure 1.1. History and Outlook for Annual Domestic Fossil Fuel Energy Production and Consumption for the US

the US (Energy Information Administration, 2003; Energy Information Administration, 2004; British Petroleum, 2003). The annual US energy consumption is estimated to increase from approximately 91.5 EJ [86.7 quadrillion Btu] in 2002 to 131.4 EJ [124.5 quadrillion Btu] in 2025. The consumption of petroleum oil far exceeds that of either natural gas or coal. The continuously increasing dependence on preferred fuels such as gasoline and diesel for the transportation sector and on petrochemical feedstock and fuel oil in the industrial sector all obtained by refining of petroleum oil has widened the gap between its domestic production and consumption. This gap has been met by importing petroleum oil from oil-rich countries. However, the vastly energy dependent US economy becomes vulnerable to the unpredictability of prices and supply stability from the oil exporting countries because of geo-political reasons. An alternative is to explore for more reserves of petroleum oil, natural gas and coal and exploit them for increasing production in order to achieve energy self-reliance. The domestic reserves/production ratio at the end of 2002 has been approximately 11 years for petroleum oil, 9.6 years for natural gas and 252 years for coal (British Petroleum 2003).

1.1.1 Coal and Natural Gas as Competitors

Natural gas consumption was spurred through a nationwide network of distribution pipelines for use in the domestic sector for residential space heating and in the industrial sector for electric power generation plants. A conventional electric power plant involves steam generation in either a coal or natural gas fired boiler that is then used to drive a steam turbine or direct combustion of natural gas in a gas turbine. In the turbine, expansion of the working fluid converts heat into mechanical work that drives a generator shaft for electric power (Smith *et al*., 2001). While most domestic coal production continued to be used for electrical power generation, inherently clean burning natural gas started gaining an advantage over coal which generated environmental pollutants such as oxides of sulfur and nitrogen responsible for acid rain, particulate matter, mercury and carbon dioxide which is a greenhouse gas. Until 1978, the federally

regulated price of natural gas encouraged demand but offered little or no incentive to the oil and gas companies to explore or produce more (Oppenheimer, 1982). This led to the generally unfounded perception that the domestic natural gas reserves had dwindled to the point that alternative routes of meeting the energy demand had to be found. This perception of nearly exhausted natural gas reserves, the oil price increases caused by the oil embargo of 1973 and the Iranian crisis of 1979, the environmental responsibility of developing clean coal technology and its abundant, economical domestic sources made coal the focus of attention once again (Ferguson, 2002).

The US DOE in conjunction with the industry initiated a research, development and demonstration (RD&D) program since 1985 aimed at making existing and new coal-based power generation plants cleaner and more efficient at lower capital costs (Eastman, 2003). Major technological advances such as the Integrated Gasification Combined Cycle (IGCC) (Tampa Electric Company, 1996; Tampa Electric Company, 2000) and advanced gas turbines (General Electric Power Systems, 2000) both leading to improved power plant efficiencies and cleaner processes have arisen through this program. A power plant based upon the IGCC technology converts coal into synthesis gas in the presence of steam and oxygen at high pressures, cleans the synthesis gas of pollutants and combusts it in a gas turbine. Synthesis gas is a mixture of carbon monoxide and hydrogen. The heat of the flue gases escaping the gas turbine is used to produce steam which in turn is capable of driving a separate steam turbine. The integration of the steam and gas turbines leads to a better utilization of heat generated per unit mass of coal. The IGCC power plant reduces emission of carbon dioxide by using oxygen instead of air for partial oxidation in the gasification step but does not eliminate it.

The continued RD&D program also aims at proving the technical feasibility and viability of a coal-based zero emissions power plant supplying electricity and hydrogen with carbon dioxide sequestration by 2020 (Der, 2003 and US DOE, 2004). Such a plant would convert coal into synthesis gas just as an IGCC plant does followed by the shift reaction to convert carbon monoxide to carbon dioxide and

hydrogen followed by their separation using membranes. Carbon dioxide would then be injected into either a coal mine to increase coal-bed methane production (Ayers, 2004), into a petroleum reservoir for enhanced oil recovery or into depleted oil and gas reservoirs. Hydrogen would be combusted in a hydrogen turbine to generate electricity, supplied as a clean fuel for fuel cells or sent to a petroleum refinery for hydrogenation processes. Although the IGCC and the zero emissions power plant are being developed with coal for taking advantage of its cheap and abundant domestic supply, both are adaptable to natural gas feed.

A fuel cell is a device capable of supplying electricity by the electrochemical reaction between hydrogen as a fuel and oxygen extracted from the air with only water and heat as the byproducts. Current commercial scale steam reforming of natural gas followed by the shift reaction and separation of hydrogen and carbon dioxide by pressure swing adsorption can be a source of hydrogen for the near future. With the advancements made in coal gasification similar to those in an IGCC power plant, coal may compete with natural gas in the production of hydrogen for fuel cells in the mid-term. An estimated 9.06 quadrillion m^3 [320,000 trillion cubic feet] of natural gas remain trapped as methane hydrates which could potentially supply hydrogen for fuel cells in the long term (US DOE, 2003). Methane hydrates are crystalline solid compounds formed at high P and low T conditions by the entrapment of a small molecule such as methane in a cage of water molecules. The technology to produce natural gas from methane hydrates is however only at a nascent stage (Millheim, 2004).

Until clean coal technologies mature to compete viably with natural gas, production of natural gas must be maintained or increased to avoid dependence upon imported petroleum oil. Although natural gas and coal may appear to rival each other in the mid-term, both are essential during the shift from a carbon to a hydrogen based energy economy.

1.1.2 Synthetic Fuels from Remote Natural Gas Locations and Coal

The high oil prices of the 1970s sparked a renewed interest in exploitation of then available resources of natural gas just as they had for coal. Natural gas from reservoirs connected to the nationwide pipeline distribution network was available for use. However, many natural gas reservoirs remained isolated and unutilized because of lack of an affordable transportation mode for the gas to market areas. Offshore gas reservoirs, the north slope of Alaska (Robertson, 1999) were examples of such remote gas locations where the only options were flaring or re-injecting into reservoirs to increase production or liquefying the associated natural gas. Increasingly stringent environmental regulations ruled out the flaring option. Re-injection and transportation of liquefied natural gas in specially prepared vessels without any value addition to markets were not cost-effective options. Gas to liquids technology (GTL) wherein natural gas is converted to clean synthetic liquid fuels such as gasoline and diesel with higher octane and cetane numbers and transported in standard vessels could make it possible to tap such remote natural gas.

The proven and under-development GTL processes for synthetic fuels and/or petrochemical feedstock may be classified as indirect and direct as follows (Aasberg-Petersen *et al.*, 2001; Macdougall, 1991; Puskas, 1995):

(1) Indirect - natural gas to synthesis gas to synthetic fuel via Fischer-Tropsch synthesis (FTS)
(2) Indirect - natural gas to synthesis gas to methanol to synthetic fuel
(3) Direct - natural gas to methanol or higher hydrocarbons especially ethylene and acetylene

Unlike coal technology that was just evolving in the late 1970s, GTL got a head start not only because of the FTS research since 1923 (Anderson, 1984) but also because Sasol operated proven FTS process plants in South Africa that converted coal to liquid fuels since 1955. FTS involves conversion of synthesis gas obtained either from natural gas or coal to higher aliphatic hydrocarbons in the range C_4 to C_{10} and/or

alcohols by hydrogenation of carbon monoxide over metal catalysts such as iron or cobalt. The need to separate oxygen from air in the synthesis gas production step involves significant costs and makes the FTS process subject to economy of scale. Partial oxidation can become viable only for a large capacity FTS plant. Jager (1998) has summarized developments in the FTS technology at Sasol that includes the latest Sasol Slurry Phase Distillate (SSPD) process using iron catalyst. A 397 m^3/day [2,500 barrel/day] onshore SSPD plant using offshore natural gas transported via a pipeline has been successfully operated by Mossgas at Mossel Bay in South Africa since 1993. A new 5,247 m^3/day [33,000 barrel/day] GTL plant scheduled for completion in 2005 based upon the SSPD process is being commissioned in Nigeria (ChevronTexaco, 2000). Shell has operated a 1,987 m^3/day [12,500 barrel/day] plant for synthetic fuels from offshore natural gas since 1993 at Bintulu, Malaysia based upon its Shell Middle Distillate Synthesis (SMDS) process that uses a multi-tubular trickle bed reactor and a proprietary catalyst (Sie, 1998 and Sie *et al.*, 1991). Shell has also announced its intention of commissioning a 22,258 m^3/day [140,000 barrel/day] synthetic fuels plant based on the SMDS process in Qatar by 2010 (Shell, 2003). ExxonMobil's Advanced Gas Conversion Technology for the 21 century (AGC-21) using a slurry bubble column reactor and cobalt catalyst is also ready for implementation at (7,949 to 15,899) m^3/day [(50,000 to 100,000) barrel/day] capacity in Qatar (Eisenberg et al., 1999; ExxonMobil, 2001). ConocoPhillips has expressed interest in commissioning two 12,719 m^3/day [80,000 barrel/day] natural gas to synthetic fuel plants in Qatar by 2010 based upon its GTL research since 1997 and the success of its 64 m^3/day [400 barrel/day] pilot plant at Ponca City, Oklahoma (Anonymous, Apr. 2002; ConocoPhillips, 2003). A demonstration FTS plant with 11 m^3/day [70 barrel/day] capacity has been built by Syntroleum and Marathon Oil Company near Tulsa, Oklahoma recently (Syntroleum Corporation, 2003). The company focuses upon developing small, modular FTS plants for remote natural gas reserves onshore or offshore in which case they would float on barges.

Mobil (present day ExxonMobil) researchers discovered that their new shape-selective zeolite catalyst ZSM-5 could convert methanol to gasoline (Meisel *et al*., 1976). The discovery of this methanol to gasoline (MTG) process using a fixed bed reactor with the then existing processes for production of synthesis gas from natural gas (Rostrup-Nielsen, 1993) and methanol from synthesis gas (Trimm and Wainwright, 1990) completed the link for indirect conversion of natural gas or coal to gasoline. Based upon the New Zealand government evaluation that the MTG process would be more economical than a FTS process for synthetic fuels to reduce the country's dependence on imported oil and best utilize its domestic natural gas resources, a MTG plant was built in 1986 (Maiden, 1988). Eisenberg *et al*. have reported that with the lower oil prices of the 1990s, Mobil divested its interest because of unfavorable economics from this plant that now produces only methanol and not gasoline.

Parkyns *et al*. (1993) have reviewed processes available for direct conversion of natural gas to chemicals such as methanol, ethylene and acetylene that can in turn be converted to fuels and concluded that they could not compete with the indirect synthetic gas based processes. A direct process for methanol is inspired by the need to eliminate the most expensive synthesis gas preparation step from the indirect route. Homogeneous gas-phase partial oxidation of methane with oxygen gives higher yields of methanol than catalytic oxidation. Oxidative coupling of methane in the presence of alkali metal/alkaline earth metal oxide forms ethylene and ethane (Lunsford, 1990). Pyrolysis of methane in the T range (1,770 to 2,270) K [(2,726.33 to 3,626.33) ^{o}F, (1,496.85 to 1,996.85) ^{o}C] leads to complete dehydrogenation followed by coupling to give acetylene. The review by Aasberg-Petersen *et al*. reported no significant progress since that of Parkyns *et al*. for a direct conversion process. This is affirmed by the trend of almost all new GTL plants being based on the proven FTS technology. However, a new process that is more economical than the FTS process has recently been co-developed by Synfuels and Texas A&M University (Anonymous, Nov. 2002; Hall and Goldman, 2003). The process involves methane pyrolysis to acetylene that can finally be transformed to hydrocarbon liquid.

McDougall (1991) and Rostrup-Nielsen (1993) have opined that the coal feed GTL technology process is not feasible in the USA despite abundant domestic coal reserves because the extra steps of gasification and synthesis gas clean-up from coal feed make it two to three times more costly than processes using remote natural gas feed.

1.2 Deepwater Gulf of Mexico as the New Energy Frontier

Presently, energy demand relies heavily upon domestic natural gas production and is expected to continue to do so in the near-term until advances in clean coal technology are realized as discussed in subsection 1.1.1. Steps such as better utilization of available natural gas resources by GTL conversions described in subsection 1.1.2 and exploration for and production from new oil and natural gas reserves are necessary to meet these near-term energy demands. Production of oil and gas from onshore basins and the north slope of Alaska have matured and now produce lower than their peak rates. Unconventional resources such as tight sands, shale and coal-bed methane can provide some of the natural gas production and energy demand. Oil and natural gas have also been produced from offshore production platforms since 1947. The Minerals Management Service (MMS) of the US Department of the Interior that administers the nation's oil and natural gas resources in the Gulf of Mexico (GoM) has classified production platforms depending on water depth between the platform at the ocean surface and the ocean floor. Platforms at water depths up to 304.8 m [1,000 feet] are described as shallow-water, those greater than 304.8 m [1,000 feet] but lower than 1,524 m [5,000 feet] as deepwater and those greater than 1,524 m [5,000 feet] as ultra-deepwater (Baud *et al*. 2002). Most offshore production since 1947 was shallow-water but the oil price increases of 1973 extended production to deepwater (Priest, 2001).

Baud *et al*. have attributed the rapid growth in deepwater and ultra-deepwater GoM, especially since 1992, to changes in the oil and gas block leasing policy, and technological advances in exploration, drilling, development, production and transportation. The benefits of the Federal government's deepwater royalty relief act of

November 1995, passed to encourage both major and independent companies to explore and produce oil and gas from hostile deepwaters of the GoM have been explained by Derman and Johnston (1999), Derman and Johnston (2000) and Derman and Jacobson (2000). Three-dimensional seismic data acquisition coupled with pre-stack depth migration of seismic data has enabled identification of oil and natural gas reserves hidden under salt canopies in deepwater GoM which had not been possible previously with two-dimensional seismic data. New semi-submersible, floating or platform based well drilling rigs capable of drilling either vertically or directionally up to 3,048 m [10,000 feet] of water depth and up to 9,144 m [30,000 feet] true vertical depth are now available. The progression of platform design and construction capabilities from fixed and/or compliant towers, tension leg platforms (TLP), spars, semi-submersible floating production systems (FPS), floating production storage and offloading (FPSO) vessels and sub-sea tie-back development systems have made economic deepwater and ultra-deepwater production a reality.

A sub-sea tieback development system consists of several well-heads connected to a manifold on the ocean floor through pipeline sections. A larger diameter, longer pipeline section transfers the production from the manifold to a TLP, FPS or FPSO. The pre-existing pipeline network for transporting shallow-water platform production onshore had to be extended, replaced because of age or to accommodate increased capacity from deepwater and ultra-deepwater production. Several such pipeline projects have either been completed (Gallaher and Mahoney, 1997; Warren, 1997; Feltus, 1998), are under construction (Marshall, 2003; Black *et al*., 2003) or are under consideration (Anonymous, 2003). Taking into consideration the large investment needed for deepwater pipeline infrastructure development which may deter independents from treading into deepwater production, many of these new pipelines built by majors or exclusive pipeline transportation entities have the flexibility of merging independent's or major's potential production from sub-sea developments. This 'shared' production can then be transported through the main pipeline to a 'hub' processing facility on a TLP, FPS or FPSO of a major or a third party operator. The sub-sea tieback development

system and the hub concepts are becoming very popular not only in deepwater (Moritis, 2003) but also in shallow-water production as pointed out by Baud *et al*.

The deepwater pipeline network connects most remote natural gas production to the onshore network thus making the GTL concept appear redundant for the GoM. However, a GTL plant on a FPSO vessel would allow exploitation of an isolated deepwater or ultra-deepwater reservoir which may be uneconomical to connect to the pipeline network especially for an independent (Clouser, 2002).

Baud *et al*. have assessed that approximately 79% of the estimated reserves of oil and gas remain to be discovered in deepwater whereas a similar figure for shallow-water is 23%. Maturity of the shallow-water with respect to both oil and natural gas and the technological strides accomplished in deepwater thus far clearly make deepwater GoM the next domestic energy frontier.

1.3 Necessity of Thermodynamic (P - ρ - T) and Phase Equilibrium Data

The oil and natural gas industry requires phase equilibrium and pressure – density – temperature (P - ρ - T) data at several stages between exploration and market-end use (Meyer *et al*., 1996; Curole *et al.*, 1997). Hydrocarbon reserves can be estimated knowing the reservoir pressure and temperature. The true vertical depth (TVD) for an offshore reservoir well is the sum of its water depth (WD) and its depth in the earth's crust up to the reservoir. A shallow-water well can have a WD of up to 304.8 m [1,000 feet] and a TVD of up to 6,096 m [20,000 feet] and the reservoir P and T can be in the range (55.158 to 68.948) MPa [(8,000 to 10,000) psia] and (338.71 to 366.48) K [(150 to 200) ^{o}F, (65.55 to 93.33) ^{o}C] respectively. An ultra-deepwater well can have a WD of up to 3,048 m [10,000 feet] and a TVD of up to 9,144 m [30,000 feet] and the reservoir P and T can be in the range (89.632 to 124.106) MPa [(13,000 to 18,000) psia] and (366.48 to 408.15) K [(200 to 275) ^{o}F, (93.33 to 135.00) ^{o}C] respectively. At the wellhead the production P could be in the range (10.342 to 20.684) MPa [(1,500 to 3,000) psia] or higher. After rising from the reservoir to the ocean floor, the natural gas production

stream T can drop rapidly until it reaches the typical (277.59 to 280.37) K [(40 to 45) ^{o}F, (4.44 to 7.22) ^{o}C] surrounding ocean water temperature. This high pressure, low T state along with the presence of moisture in the gas stream makes conditions amenable for natural gas hydrate formation in the pipeline (Wang, 1994) that may completely plug the pipeline and eventually cause a blowout. Hydrate formation can be suppressed by either increasing the T of the gas by insulating the pipeline, lowering the P or by lowering the dew point of water by adding polar solvents such as methanol or glycols. The gas stream is dehydrated on the platform so that hydrates do not form in pipelines. (P - ρ - T) data are necessary to avoid hydrate formation conditions. Another, significant problem encountered in natural gas transportation is that of retrograde condensation close to the critical region (Katz *et al*. 1959). Operationally, vapor-liquid equilibrium data helps avoid condensation of heavier components in the natural gas mixture pipeline during transportation that could lead to increased cost of compression caused by liquid slug formation. (P - ρ - T) data are also necessary for designing pressure vessels and equipment for flow rate dependent separation, dehydration and other operations that determine the operating capacity of the gas processing plant on the platform.

1.3.1 Necessity of High-accuracy Density Measurements in Custody Transfer

In deepwater GoM, because of the higher reservoir temperatures at greater depths, purely natural gas reservoirs can also be expected in addition to the prevalent oil and associated natural gas reservoirs experienced in shallow-water. The purely natural gas production from sub-sea tie-back or other development systems is collected at the platform. In the case of oil and associated gas producing wells, using multiphase flow pumps the two phase production is brought to the processing platform where the natural gas is separated from the liquid phase and dehydrated. When the processed natural gas is transported onshore through pipelines and connected to the nationwide pipeline distribution network, its custody is transferred from the oil and gas producing company to the local distribution company (LDC). A company may also

allow transportation of shared gas or two phase production with other companies through its pipeline to its own processing facility. Such an arrangement is mutually beneficial to both the pipeline and processing platform owning company which gets the opportunity of optimally using its transportation and processing capacity as well as the other companies that only produce but lack the large investment for transportation and processing infrastructure.

The processed, dry gas at the platform and gas sold to the LDC are all quantified at a known *P* and *T* using mass flow meters such as orifice meters, turbine meters and ultrasonic meters. The mass flow rate is converted to energy flow rate by using accurately measured enthalpy of combustion data of constituent components of the natural gas mixture (Thermodynamic Research Center, 2003a) and on-field accurate measurement of its composition using analytical techniques such as gas chromatography (GC) or separation by gas chromatography followed by mass spectroscopy (GC-MS) (McMurry, 1992; Schupp, 1968). The end-use market value as an energy source thus depends upon accurate temperature, pressure, mass flow, enthalpy of combustion and composition measurements. The multivariable, on-field flow meters can measure mass flow rates with a combined standard uncertainty of at best ±0.25% and normally as high as ±(1-5)% of the reading (Gallagher, 2003; Bowles, 2004). The flow meter uncertainty is very important during custody transfer of natural gas especially because of the large volumes that are traded. The sign of the uncertainty is indicative of a profit or loss experienced by the company and the magnitude gives the extent of the profit or loss. It is for this reason that both the buying and selling companies need a mutually acceptable and consistent standard of quantifying flow rate uncertainty during contractual agreements.

The combined standard uncertainty of measurement of a property of interest depends upon the standard uncertainties of measurements of several other parameters that contribute to that property according to the law of propagation of uncertainty (Taylor and Kuyatt, 1994). To achieve the lowest combined standard uncertainty of the property being measured, each one of its parameters in turn must be

measured with as small a standard uncertainty as possible. About 90% of the gas production and transmission metering stations use the orifice flow meter. The orifice flow equation has density as one of the parameters in addition to the pressure differential, the orifice discharge coefficient and other parameters whose measurement can contribute to the overall uncertainty of flow measurement.

Knowing the temperature, pressure and composition, an accurate density can be calculated from an equation of state (EOS) for the natural gas mixture for use in the orifice flow equation. The use of an EOS allows more frequent calculations of density knowing instantaneous temperature, pressure and compositions in-field. However, such an EOS must be validated for accuracy by comparing its density predictions to experimentally measured density data over a wide range of pressure, temperature and composition including the critical region. The American Gas Association (AGA) has developed the detailed characterization method popularly called the AGA8-DC92 EOS that has been validated against a databank of experimentally measured compressibility factors for pure components, binary, ternary, quaternary and pentanary mixtures as well as multi-component natural gas mixtures.

1.3.2 Inspiration for Current Research Project

The AGA8-DC92 EOS is the current industry benchmark for the natural gas custody transfer business. At the custody transfer points, although the T and P conditions would be nearly the same as those experienced during shallow-water or onshore production and transmission, the compositions of natural gas mixtures from deepwater and ultra-deepwater production are expected to be very different. These are expected to have higher amounts of higher boiling, heavier components above hexane (C_{6+}) because of the higher temperatures of reservoirs. Application of the AGA8-DC92 EOS to natural gas streams with temperature, pressure and compositions different from those used for its validation can give erroneous densities for the orifice flow equation. The AGA8-DC92 EOS must be calibrated so that it is applicable over a much broader

range of temperature, pressure and composition that attend the new deepwater and ultra-deepwater endeavors. Another approach would be to develop an entirely new EOS capable of giving more accurate density or compressibility factor predictions than the AGA8-DC92 or any other existing EOS over a much wider range of conditions.

The present research project for accurate density measurements was inspired by the need to calibrate an existing EOS for immediate use. A state-of-the-art, high pressure, high temperature, single-sinker Magnetic Suspension Densitometer (MSD) was used for accurate density measurements. These density data, along with new measurements such as those by Watson (1998), can also be used to validate a new EOS that is being developed for use in the long-term future (Hall, 2000; Atilhan, 2004). Another part of the same research project that can help deepwater production operationally is the measurement of the vapor-liquid two phase envelope (Zhou, 2002).

1.4 Organization of Dissertation Chapters

The present chapter has explained the need for accurate density measurements in the broader perspective of deepwater GoM oil and gas production that holds the promise of meeting part of the nation's growing energy demand. Chapter II explains the choice of the AGA8-DC92 EOS for calibration over others and also the overall philosophy of measurement followed in this research project by combining the isothermal data from the densitometer and the isochoric data from the isochoric apparatus. The MSD, as developed by Rubotherm Präzisionsmesstechnik GmbH, is a unique apparatus because of its wide P and T ranges. Chapter III describes the working principle, tests for operating range and stability and the ancillary equipment needed for density measurement. Chapter IV addresses P and T measurement and calibration for traceability. Before embarking on natural gas measurements, it is essential to evaluate if the density measuring apparatus has a systematic bias error. If the apparatus does have a bias error, its sign as well as its magnitude are necessary to apply a correction to the measured data. The quality of the corrected data can be evaluated by comparison to

measured data from other laboratories using accurate density measurement apparatuses. Chapter V describes the work to find the bias error of the magnetic suspension densitometer by measuring densities of pure components such as argon, methane and nitrogen. Chapter V also presents density measurements for two natural gas mixtures containing approximately 94 mole percent and 91 mole percent methane. A discussion of the results and inferences reached from the pure component and natural gas mixture density measurements along with the effect of the densitometer operation on the quality of measurements appears in Chapter V. Chapter VI summarizes the research findings of this project until February 2004 and recommends steps to improve the quality of density measurements in the future. Numerical data tables and supporting material such as operating procedures are provided as appendices.

CHAPTER II

EQUATIONS OF STATE AND PHILOSOPHY OF MEASUREMENTS

2.1 Equations of State for Fluids and Fluid Mixtures

An EOS can describe the thermodynamic state of a fluid or fluid mixture and also its vapor-liquid phase equilibrium (VLE) behavior as a (P - ρ - T) correlation for engineering applications. A hypothetical, ideal EOS should be able to predict thermodynamic properties accurately over a wide range of temperature, pressure and composition (x) spanning the vapor and liquid phases, the saturation states, the critical and the super-critical dense-phase region for various polar and non-polar fluids and their mixtures. Most multi-parameter, empirical EOS development efforts since the work of van der Waal in 1873 have undergone gradual progression in the P, T and x range of their applicability and the accuracy of their thermodynamic property predictions depending upon the need of the period.

The accuracy of such EOS in turn depended upon the accuracy of the experimental data to which their parameters were fitted. The quality of predictions from EOS has improved greatly with major enhancements in the experimental methods and instrumentation available for measurement of thermodynamic properties. Some of the earlier EOS developed with less accurate data have become obsolete because of this reason. The normal approach taken for EOS development for a pure fluid was to determine substance-specific parameters for a common functional form from pure component experimental data. For a fluid mixture, composition-dependent mixing/combining rules along with the pure component EOS were used. The validity of the mixing rules could be checked by comparing the mixture property predictions from the EOS with experimentally measured data on mixtures. Binary interaction parameters were included in the mixing rules to describe the size, shape, and polarity differences

between unlike molecules more realistically; thus improving the accuracy of property predictions. Another approach for fluid mixtures was to develop a functional form whose parameters were determined by fitting directly to available experimental data on mixtures.

2.1.1 Cubic Equations of State

Inclusion of more parameters in the EOS validated by accurate experimental data normally resulted in more accurate property predictions but increased the complexity of calculations; thus decreasing computational speed for practical purposes. Cubic EOS with far fewer parameters than complex multiparameter EOS offered a compromise between ease of use and accuracies acceptable to the chemical industry. The RK (Redlich and Kwong, 1949), SRK (Soave, 1972), PR (Peng and Robinson, 1976) and PT (Patel and Teja, 1982) are examples of popular cubic EOS still in use.

2.1.2 The Virial Equation of State

In 1901, Kamerlingh Onnes represented the gas phase behavior of fluids in the form of an empirical virial EOS in terms of density as follows:

$$Z = \frac{P}{\rho RT} = 1 + B\rho + C\rho^2 + ... \qquad (1)$$

where, the compressibility factor Z accounts for the departure of a real gas from ideal gas behavior and B and C are the second and third virial coefficients that characterize two and three body interactions respectively and are functions of temperature for pure fluids and of composition and temperature for fluid mixtures. The form of the virial EOS is the best representation for fluid behavior as it has its basis in the statistical-mechanical

theory. In the early 1980s the European Group for Gas Research (GERG) initiated a research project to develop two versions of EOS meant exclusively for pipeline custody transfer of natural gas. The master version: MGERG EOS (Jaeschke *et al.*, 1989) uses complete compositional analysis of the natural gas as input whereas the standard version: SGERG EOS (Schouten *et al.*, 1990) uses any three of gross calorific (or heating) value, specific gravity (or relative density) and mole fractions of nitrogen and carbon dioxide as inputs for calculating the compressibility factor of natural gas. Both MGERG and SGERG are forms of the virial EOS, the second and third virial coefficients of which have been determined by fitting to a huge databank of experimentally measured compressibility factors (Jaeschke and Humphreys, 1990). Iglesias-Silva and Hall (1996) have extended the applicability of the SGERG EOS to pressures higher than those in the custody transfer range by retaining the virial EOS form.

2.1.3 The Modified Benedict-Webb-Rubin Type of Equation of State

Beattie and Bridgeman (1928) developed an EOS for pure gases which could be expressed in a form similar to the virial EOS. The BWR EOS (Benedict *et al.*, 1940) may be considered an extension of the Beattie and Bridgeman EOS and the virial EOS that is applicable for high density conditions such as the liquid phase and the critical region as well, in addition to the gas phase, because of presence of exponential terms with density powers. Use of the BWR EOS for property prediction of light hydrocarbon mixtures (Benedict *et al.* 1942; Benedict *et al.*, 1951a) and for VLE behavior of binary and ternary hydrocarbon mixtures (Benedict *et al.* 1951b) has been demonstrated. Modified versions of the BWR EOS (MBWR) were developed to improve the accuracy and range of applicability of (P - ρ - T) and VLE property predictions. The BWRS EOS (Starling, 1973) was one among the earliest EOS used for computer property predictions. Early efforts at the National Institute of Standards and Technology (NIST) for developing a fluid property prediction computer program named NIST-14 (or

DDMIX) used a 32 parameter MBWR EOS (Younglove and Ely, 1987). Since 1956 the AGA has developed four versions of EOS meant exclusively for natural gas applications including pipeline custody transfer; namely AGA NX-19 (American Gas Association, 1963), AGA8-85 (American Gas Association, 1986), AGA8-DC92: the detailed characterization method and AGA8-GC92: the gross characterization method (American Gas Association, 1992, Savidge *et al.*, 1995). The AGA8-85 and AGA8-DC92 versions may also be considered as MBWR EOS because they involve virial EOS like density power series terms to account for low density conditions as well as exponential terms with density powers to account for high, liquid-like densities in the supercritical fluid region. The AGA8-GC92 on the other hand is exactly the same as SGERG which is a form of the virial EOS.

2.1.4 Equations of State Based on the Corresponding States Principle

Another set of correlations results from the corresponding states principle originally proposed by van der Waals which states that at the same reduced temperature and reduced pressure all fluids have the same compressibility factor. In reality, this is true only for simple fluids with spherical molecules while fluids with non-spherical molecules deviate from the simple fluids. The acentric factor was introduced as an additional parameter by Pitzer to increase the accuracy of compressibility factor prediction by taking into account the effect of size, shape and polarity on the intermolecular forces among non-spherical molecules (Pitzer *et al.*, 1955; Curl and Pitzer, 1958). The corresponding states principle is also theoretically sound just like the virial EOS because the acentric factor is linked to the intermolecular potential in statistical-mechanical theory (Pitzer, 1955). Lee and Kesler (1975) gave an analytical form to Pitzer's tables by expressing the deviation in compressibility factor of a non-spherical fluid from that of a simple fluid in terms of compressibility factors of a simple fluid and a reference fluid (n-octane) calculated from a BWR type of EOS.

2.1.5 Correlations from Empirical Fits

A completely empirical approach for describing the (P - ρ - T) properties of natural gas mixtures is to fit a correlation to experimentally measured data for the compressibility factor in terms of the pseudoreduced temperature and pseudoreduced pressure of the mixture using appropriate mixing rules. The accuracy of predictions from such empirically fitted correlations cannot be expected to be as good as those from the corresponding states principle correlations because of lack of the acentric factor; nonetheless they are in use because they offer ease of use and speed of computer calculations. Hall and Yarborough (1973) and Yarborough and Hall (1974) have converted the Standing and Katz (1942) charts to such a computer usable correlation (HY) using the mixing rules suggested by Kay (1936). Dranchuk *et al.* (1974) and Dranchuk and Abou-Kassem (1975) achieved the same by using fits of the BWR and BWRS type of EOS respectively.

2.1.6 Equations of State Explicit in Helmholtz Energy and Reference Equations of State

All the EOS mentioned in the preceding subsections were explicit in pressure: $P = P(\rho,T)$. This requires cumbersome integrations in the indirect calculation of thermodynamic properties such as internal energy, enthalpy, Helmholtz energy, Gibbs free energy, entropy, the specific heats at constant volume and pressure and speed of sound. If however, an EOS is expressed in Helmholtz energy explicit form: $A = A(\rho,T)$; which is a fundamental equation, taking derivatives of A with respect to its natural variables ρ and T simplifies calculation of thermodynamic properties. Both the older MBWR and the recent Helmholtz energy explicit forms of EOS have polynomial and exponential terms in density. However, the Helmholtz energy representation offers more flexibility because of the optimization process that allows choice of only as many non-interrelated terms (or functional forms) as are necessary for accurate description of the

thermodynamic surface over a wide range of its variables. The MBWR representation of an EOS on the other hand involves rigid terms that are included based upon the experience and skill of the developer. Moreover, any change in one term affects the constants of the other terms because they are interrelated. Most of the new reference EOS for pure fluids are of the Helmholtz energy optimized form since its introduction separately by Schmidt and Wagner (1985) for oxygen and Jacobsen *et al.* (1986) for nitrogen. A reference EOS is one which describes all accurate thermodynamic property data for a particular fluid within their experimental uncertainty and can be used for identification of a systematic bias error of an experimental apparatus without having to resort to experimental data. In the present work, the reference EOS for methane (Setzmann and Wagner, 1991), nitrogen (Span *et al.,* 2000) and argon (Tegeler *et al.*, 1999) have been used to identify any systematic apparatus bias error of the MSD.

2.1.6.1 Single, Pseudo-pure Fluid Model for Mixtures

The Helmholtz energy representation for pure fluids consists of the ideal gas and the residual terms for deviation of the real fluid from ideal gas behavior. If the functional form of reference EOS for all pure fluids constituting a fluid mixture had been the same it would have been possible to use a simple composition dependent mixing rule and the substance specific reference EOS for describing the residual part of the fluid mixture as a single, pseudo-pure fluid. However, substance-specific reference EOS exist only for the major components and are yet to be developed for heavier and not so common components of natural gas. Even if they are developed, their functional forms would be different because of being substance-specific, rendering the use of mixing rules unfeasible. Thus the single, pseudo-pure fluid approach for natural gas mixtures appears unrealistic.

2.1.6.2 Extended Corresponding States Model for Mixtures and Shape Factor

The restriction of having the same functional form for each constituent pure component of a natural gas mixture is completely circumvented by the extended corresponding states (ECS) model which also allows the EOS for a component to be explicit in different properties. The recent interest in ECS model development (Estela-Uribe and Trusler, 2003; Estela-Uribe *et al.*, 2004) is a progression of the work of Pitzer and then Lee and Kesler, based upon the concepts of 'shape factor' and 'equivalent substance reducing parameters'. According to the simple corresponding states principle the residual Helmholtz energy and the compressibility factor of a fluid of interest at a temperature and density would be equal to those of a reference fluid (such as methane) at a temperature and density scaled for eliminating substance dependence with equivalent substance reducing parameters. The equivalent substance reducing parameters for temperature and density are the ratios of critical temperatures and critical densities of the fluid of interest and the reference fluid. However, the corresponding states principle holds only for non-polar, spherical molecules. For application to a wide variety of fluids, the equivalent substance reducing parameters themselves require corrections called shape factors that are functions of reduced temperature, reduced density, acentric factor and critical compression factor of the fluid of interest. Thus the shape factor may be considered a correction to account for different shapes of the intermolecular potential in much the same way as Pitzer introduced his acentric factor. Mixing rules along with binary interaction parameters can be used to describe the shape factors for fluid mixtures. Shape factors are determined from empirical correlations for pure fluids or fluid mixtures rather than from molecular theory.

2.1.6.3 Multi-fluid Model for Mixtures and Departure Functions

NIST personnel used the shape factor concept for developing NIST-14 (or DDMIX) EOS which is a MBWR type of EOS explicit in pressure. However, its

complex form and numerical inconvenience motivated the development of a simple multi-fluid Helmholtz energy model that directly involved x and a reference EOS for each component of the mixture. The feature of being able to use accurate reference EOS for constituent components each having a different form differentiates the simple multi-fluid approach from the single, pseudo-pure fluid approach and makes it practically usable. Span (2000) has described the improvement in the accuracy of property predictions over those of the simple, multi-fluid model, achieved separately by Tillner-Roth and Lemmon by the introduction of the concept of 'departure functions' that more accurately describe non-idealities of mixtures. The functional forms of both the departure functions are determined by fitting to experimental data; however the binary mixture specific departure functions of Tillner-Roth have been reported to produce more accurate predictions than the generalized departure functions of Lemmon. The use of multi-fluid, departure function models in general gave more accurate predictions than the ECS model or the MBWR EOS using the shape factor. For this reason, NIST has switched from the MBWR EOS with shape factors that it used for NIST-14 (or DDMIX) to the present day multi-fluid, generalized departure function based model (Huber *et al.*, 2000; Lemmon and Jacobsen, 1999) named NIST-23 (or REFPROP) as part of its effort to develop a reference EOS for property predictions of fluid mixtures.

2.1.7 Work in Progress for Mixture Models

Apart from the ECS model of Estela-Uribe and Trusler based upon shape factors and the multi-fluid model of Lemmon and Jacobsen based upon departure functions, the work undertaken by Kunz *et al.* (2003) and that of Hall (2000) and Atilhan (2004) hold promise in developing an improved EOS. While the EOS of Kunz *et al.* is in Helmholtz energy explicit form, the work of Hall and Atilhan is directed towards developing a simple, accurate cubic or quintic EOS explicit in pressure with ease of use and computational speed as main features. Sengers *et al.* (2000) have provided a comprehensive review of the state-of-the-art representation of fluid and fluid mixture

thermodynamic property prediction models whereas Span (2000) and Span *et al.* (2001) have focused upon work on multiparameter EOS only.

2.1.8 Equations of State for Custody Transfer of Natural Gas

Many of the earlier EOS could predict the density or compressibility factor of natural gas with an accuracy that was acceptable for applications other than custody transfer only. Elsharkawy (2003) and Botros (2002) have shown that the SRK, PR, PT and BWRS EOS could predict densities of natural gas in the custody transfer region with at best ±1% accuracy which is not of much significance to the custody transfer business. A modified version of the RK EOS (Robinson and Jacoby, 1965) was used for some period but became obsolete as soon as the more accurate HY correlation and those of Dranchuk and Dranchuk *et al.* became available. The problem was not only the absence of an accurate EOS for density predictions but also the lack of an accepted standard of accuracy across the natural gas industry.

The AGA solved this problem for the first time through its AGA NX-19 report by defining the pressure, temperature and composition range of interest to the natural gas custody transfer industry and also by setting an accuracy of ±0.3% for compressibility factor predictions (Miller, 1996). The AGA NX-19 EOS was restricted for application only to natural gas mixtures containing lighter hydrocarbons without hexane or heavier hydrocarbons. To expand the applicability of the EOS to natural gas with heavier components over a wider pressure and temperature range, the AGA launched a new project in 1981 to develop the AGA8-85 EOS capable of predicting densities with an improved accuracy of ±0.1% in the custody transfer region. However, during the time that the AGA8-85 EOS was being developed simultaneous efforts by GERG resulted in a highly accurate compressibility factor databank of Jaeschke and Humphreys for industrial natural gas samples. An even more accurate, reference quality databank of natural gas density measurements resulted from an international round robin (RR) project among the NIST and Texas A&M University (TAMU) laboratories in the US and van der Waals laboratory at the University of Amsterdam and Ruhrgas

laboratories in Europe (Hwang *et al.*, 1997; Magee *et al.*, 1997) for gravimetrically synthesized natural gas mixtures. The AGA modified its AGA8-85 EOS, validated the new form against the GERG and RR databanks and other open literature including speed of sound data and published it as the AGA8-DC92 EOS. Since 1992, its use has become so popular for custody transfer purposes in the natural gas pipeline transportation industry that it was declared an international standard as has been reported by Span (2000).

In the present work the definition of the custody transfer region follows that of region 1 proposed by the AGA8-DC92 EOS report which is approximately (265 to 335) K [(17.33 to 143.33) ^{o}F, (-8.15 to 61.85) ^{o}C] and up to 12.066 MPa [1,750 psia]. In the custody transfer region the accuracy of AGA8-DC92 EOS compressibility factor prediction is ±0.1% or better. Accuracies over region 2 extending from approximately (210 to 395) K [(-81.67 to 251.33) ^{o}F, (-63.15 to 121.85) ^{o}C] and up to 17.237 MPa [2,500 psia], region 3 extending from approximately (144 to 477) K [(-200.47 to 398.93) ^{o}F, (-129.15 to 203.85) ^{o}C] and up to 68.948 MPa [10,000 psia] and region 4 extending from approximately (144 to 477) K [(-200.47 to 398.93) ^{o}F, (-129.15 to 203.85) ^{o}C] and up to 137.895 MPa [20,000 psia] are ±0.3%, ±0.5% and ±1% respectively. The above accuracies are valid for natural gas samples with compositions in the 'normal range' which was in turn defined by the compositions of the pure, binary, ternary, quaternary, pentenary and multi-component sample data that were used to validate the AGA8-DC92 EOS. The 'normal range' is defined by natural gas containing mole percentages of components in the following range: methane (45 to 100), ethane (0 to 10), propane (0 to 4), butanes (0 to 1), pentanes (0 to 0.3), C_{6+} (0 to 0.2), nitrogen (0 to 50) and carbon dioxide (0 to 30). In addition to the 'normal range' the AGA8-DC92 EOS was only expected to give similar accuracies for natural gas with compositions in the 'expanded range' because none of the mixture data used in the validation of the AGA8-DC92 EOS had a composition in the 'expanded range'. The 'expanded range' is defined by natural gas containing mole percentages of components in the following range: methane (0 to 100), ethane (0 to 100), propane (0 to 12), butanes (0 to 6), pentanes (0 to 4), C_{6+} (0 to

dew point), nitrogen (0 to 100) and carbon dioxide (0 to 100). The interpretation of the (0 to dew point) range of C_{6+} is that the natural gas sample could have hexane and heavier components such as heptane, octane, nonane *etc.* to the extent that they barely dropped out of the gas phase as a retrograde condensate at *P* and *T* conditions above the dew point. Thus the 'extended range' allowed any amount of hexane and heavier components sustainable in the gas phase. It is noteworthy that the AGA8DC-92 EOS was expected to give the same accuracies for the 'extended range' as for the 'normal range' despite being validated by data only in the 'normal range' of compositions.

A closer inspection of several industrial samples and synthesized mixture compositions that were used for AGA8-DC92 EOS validation and compiled by Savidge *et al.* shows that except for one mixture, the C_{6+} fraction composition does not exceed 0.12%. The various data subsets and the corresponding maximum C_{6+} fraction compositions are as follows: RR synthesized mixtures (0.07%), GERG samples (0.12%), speed of sound data on mixtures and samples (0.23%), pentenary mixtures (0%), quaternary mixtures (0%), ternary mixtures (0%), binary mixtures (0.09%) and pure components (0%). Among pure components only methane, ethane, nitrogen and carbon dioxide data have been used for AGA8-DC92 EOS validation. Thus, for any natural gas samples or mixtures containing C_{6+} fraction composition higher than the normal range or in the 'expanded range', application of the AGA8-DC92 EOS is like an extrapolation and the soundness of expecting the same accuracy as with the 'normal range' composition is questionable. As the deepwater and ultra-deepwater natural gas streams are expected to have more than the 'normal range' C_{6+} fraction composition, use of the AGA8-DC92 EOS for custody transfer in its present form can prove to be erroneous. Because of its present status as an international standard, it was decided to calibrate the AGA8-DC92 EOS over other EOS. The calibration process would involve refitting the constants of the EOS to newly measured density data on mixtures with C_{6+} fraction compositions higher than the 'normal range'. From a broader perspective, the calibration of the AGA8-DC92 EOS carried out as part of the present project may be expected to set a new standard in much the same way that the AGA8-DC92 EOS displaced the AGA

NX-19 EOS as a benchmark. Other EOS such as the HY correlation, the NIST-14 (or DDMIX) EOS, the NIST-23 (or REFPROP) EOS and the ECS model with shape factors were also considered for calibration.

2.1.9 Equations of State for Vapor-Liquid Phase Envelope Prediction

During density measurements, it is important to ensure that the natural gas mixture is in a homogeneous gas phase in the MSD cell and feed manifold tubing. Measurement of the dew point and bubble point curves constituting the vapor-liquid phase envelope using an isochoric apparatus for natural gas mixtures was part of this project, however, phase envelopes for the mixtures intended to be measured as part of this project were simultaneously being measured along with density measurements using the MSD. Thus, the experimental phase envelope data were not available before density measurements. While the accuracy of measured phase envelopes from the isochoric apparatus was also important, for the purpose of avoiding the vapor-liquid two phase region during density measurement, even a phase envelope with relatively larger uncertainties would have been acceptable.

For this reason, predictions for the phase envelope from EOS covering the homogeneous liquid and vapor phases including the critical region such as BWR, SRK, PR, PT, BWRS and corresponding states models along with appropriate mixing rules as well as NIST-14, NIST-23 and the ECS model with shape factor could ideally be used. The choice of EOS was deliberately restricted to the SRK, PR and PT EOS only, because cubic EOS are known to provide more accurate predictions when compared to experimentally measured VLE data and are also available as ready-to-implement software programs.

2.1.10 Software Programs for Density and Phase Envelope Predictions

For density predictions of natural gas mixtures, ready-to-implement programs were made available by several sources. NIST-14 or DDMIX (National Institute of Standards and Technology, 1993) and NIST-23 or REFPROP (National Institute of Standards and Technology, 2003) were provided by NIST. The AGA8-DC92 EOS was implemented through a program named Sonicware® provided by Lomic, Inc. (Lomic, 2001a). The ECS model with shape factors could be implemented through two executable programs named ECSmixS1 and ECSmixS2 (Estela-Uribe and Trusler, 2004). ECSmixS1 implements a generalized model over a wide range of T and P whereas ECSmixS2 is meant specifically for the custody transfer region. A simple Excel worksheet with an iterative solution of the HY EOS was developed.

For phase envelope predictions, a program named PhasePro® also provided by Lomic, Inc. was used (Lomic, 2001b). This program implements the PR, SRK and PT EOS. Although it is possible to get phase envelope predictions from NIST-14 and NIST-23, they were not resorted to because of reasons discussed in subsection 2.1.9.

2.2 Prelude to Density Measurements

Densities of three synthesized natural gas mixtures resembling expected compositions of deepwater and ultra-deepwater natural gas samples were to be measured as part of this research project. These are referred to as M94C1, M88C1 and M78C1 based on the approximate mole percentage of methane in them. The C_{6+} fraction composition of these mixtures is at least 0.4% which is much higher than the maximum of 0.12% for samples and mixtures used to validate the AGA8-DC92 EOS. Any deviation between the measured and predicted densities from AGA8-DC92 EOS for these samples would have included the effects caused by the apparatus operation and measurement procedure as well as the effect of having a higher percentage of C_{6+}

fraction. To ensure correctness of the apparatus operation and the measurement procedure, it was decided to reproduce measured densities of the NIST2 mixture that was measured by Hwang *et al.* and Magee *et al.* as part of the round robin project. Such a reproduction would eliminate any apparatus operation and/or measurement operation issues and the deviation between the measured data and AGA8-DC92 EOS predictions for the three samples of interest would be indicative of the effect of higher composition of the C_{6+} fraction. For this reason, an additional mixture named M91C1 without the heavier C_{6+} components, resembling the RR-NIST2 mixture was included for measurement. Table 2.1 summarizes the compositions of the natural gas mixtures M94C1, M88C1, M78C1 and M91C1 and mixture RR-NIST2, which is a reference standard. Density measurement results only for two mixtures, namely M94C1 and M91C1 are presented as part of the present work.

2.2.1 Phase Envelope Predictions for Mixtures

For the same composition, the accuracy of the dew point and bubble point predictions for the phase envelope depends not only on the EOS but also on the mixing rules used for a VLE model. To overcome the problem of a wide range of predictions of dew points and bubble points from different VLE models it was decided not to measure densities at pressures within 1.379 MPa [200 psia] of the highest cricondenbar (CB) and at temperatures within 5 K [9 ^{o}F, 5 ^{o}C] of the highest cricondentherm (CT) predicted by the EOS considered. The CB is the highest *P* and the CT is the highest *T* on the phase envelope. Figure 2.1 shows the large uncertainty in the CT and CB values of the phase envelope predictions using PhasePro® for PR, SRK and PT EOS for the RR-NIST2 mixture. Figure 2.2 shows the phase envelopes for RR-NIST2, M91C1, M94C1, M88C1 and M78C1 mixtures using the PR EOS. The most notable difference between the round robin project and the present project is the inflation of the vapor-liquid two phase envelope as a result of increase in the heavier C_{6+} fraction. While the round robin project mixtures had CT and CB in the approximate range (200 to 250) K [(-99.67 to -9.67) ^{o}F, (-73.15 to -23.15) ^{o}C] and (5.998 to 7.515) MPa [(870 to 1,090) psia] respectively, the

Table 2.1. Mole Fraction Compositions of Natural Gas Mixtures

Component	**RR-NIST2**	**M91C1**	**M94C1**	**M88C1**	**M78C1**
methane	0.90644	0.90991	0.94045	0.88023	0.77762
ethane	0.04553	0.02949	0.01867	0.05824	0.10623
propane	0.00833	0.01513	0.01802	0.03292	0.05993
iso butane	0.00100	0.00755	0.00356	0.00936	0.01731
n butane	0.00156	0.00755	0.00706	0.00537	0.01013
iso pentane	0.00030	0.00299	0.00201	0.00249	0.00460
n pentane	0.00045	0.00304	0.00252	0.00236	0.00436
n hexane	0.00040		0.00199	0.00089	0.00219
n heptane			0.00100	0.00189	0.00130
n octane			0.00052	0.00098	0.00053
n nonane			0.00025	0.00036	0.00029
methyl cyclopentane			0.00006		0.00007
2 methyl pentane				0.00045	0.00135
3 methyl pentane				0.00015	0.00132
benzene					0.00028
2, 3 dimethyl pentane					0.00052
3 methyl hexane					0.00051
toluene					0.00033
methyl cyclohexane					0.00020
2, 2, 4 trimethyl pentane					0.00029
nitrogen	0.03134	0.02031	0.00246	0.00262	0.00660
carbon dioxide	0.00466	0.00403	0.00143	0.00169	0.00404
C_{6+} fraction	**0.00040**	**0.00000**	**0.00382**	**0.00472**	**0.00918**

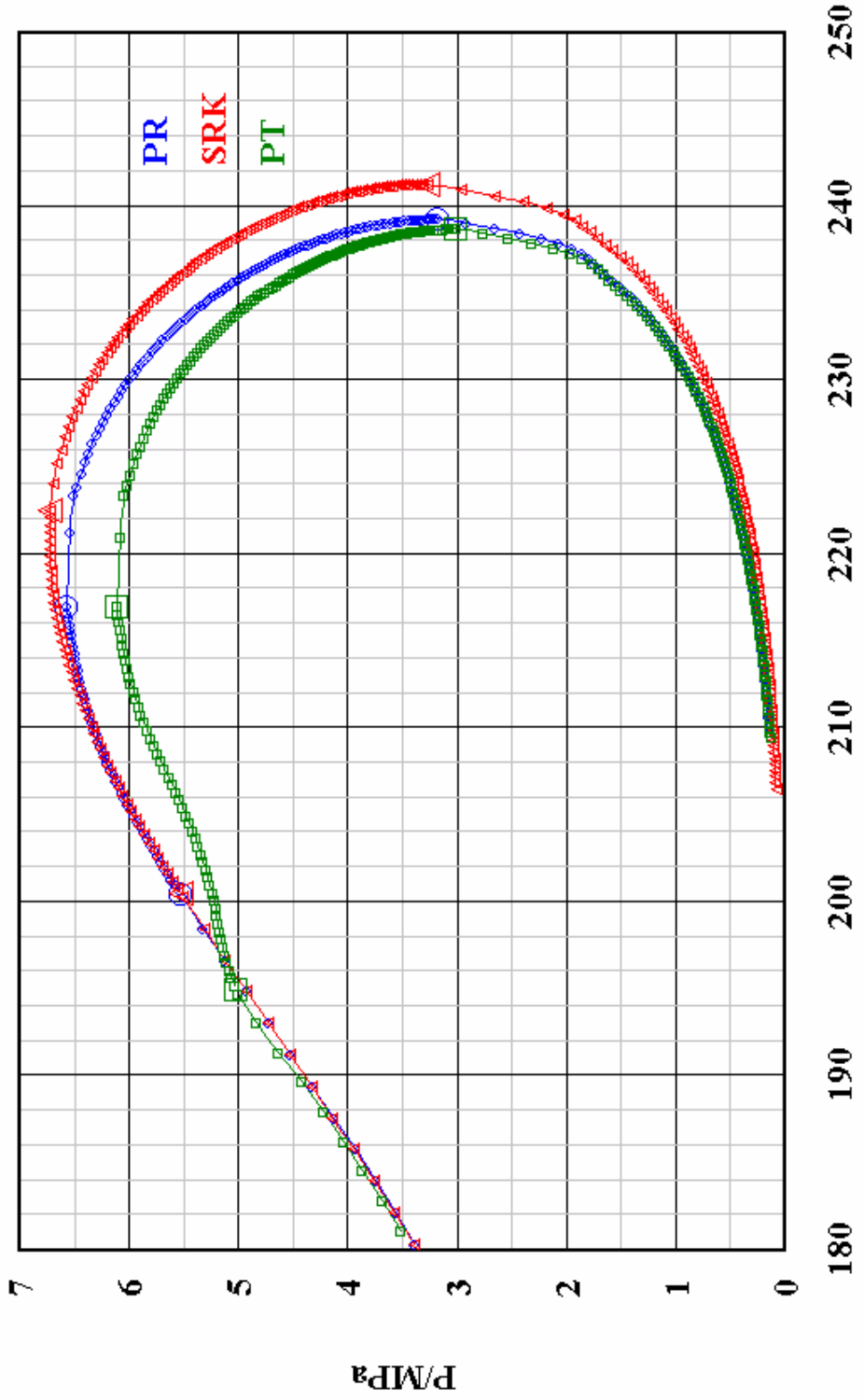

Figure 2.1. Predicted Phase Envelopes for RR-NIST2 Mixture Using PR, SRK and PT EOS

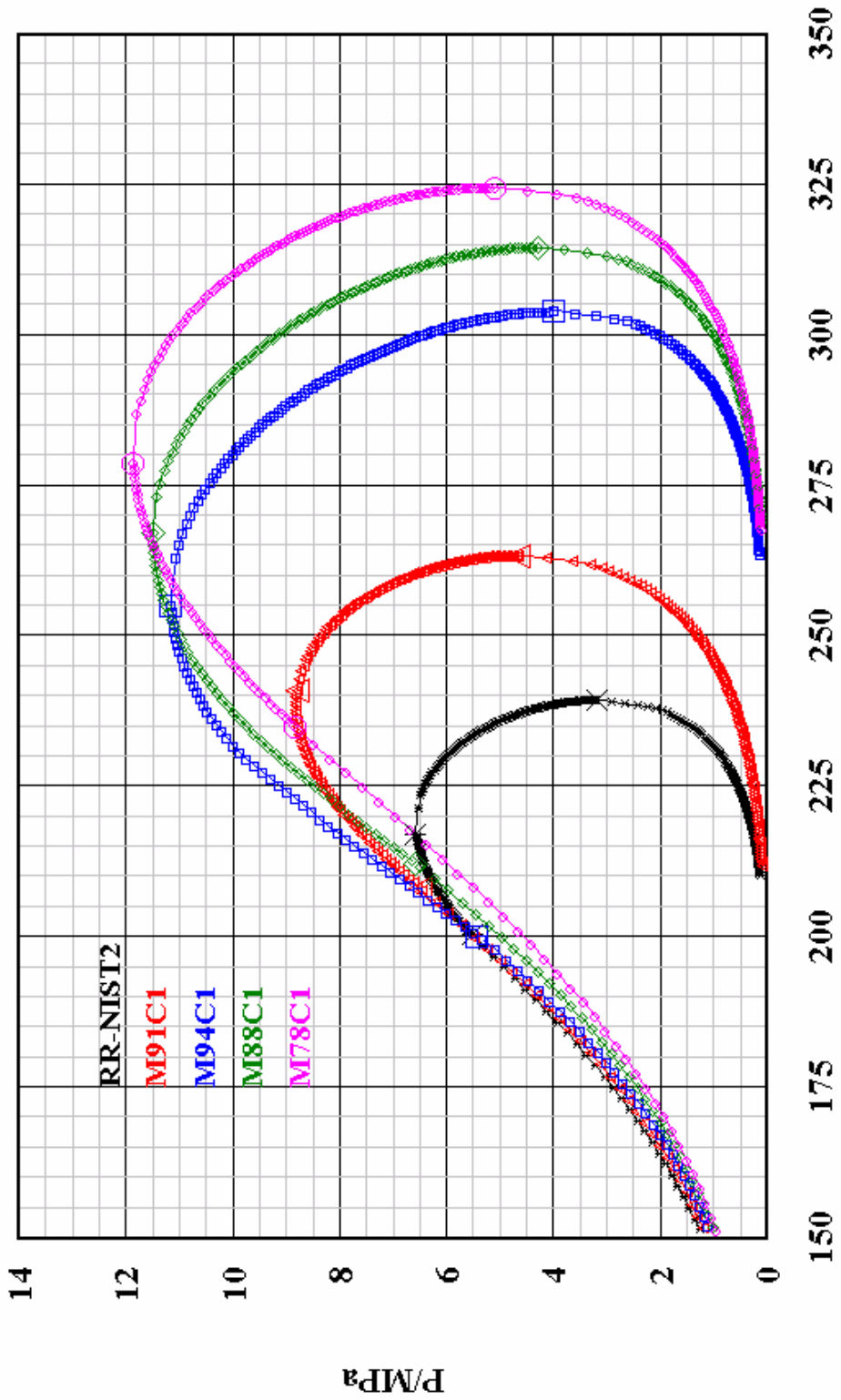

Figure 2.2. Predicted Phase Envelopes for RR-NIST2, M91C1, M94C1, M88C1 and M78C1 Mixtures Using PR EOS

samples measured in the present project had CT and CB in the range (300 to 325) K [(80.33 to 125.33) ^{o}F, (26.85 to 51.85) ^{o}C] and (10.997 to 11.997) MPa [(1,595 to 1,740) psia]. This required additional precautions for density measurements:

(a) If a mixture cylinder at a delivery *P* higher than its CB was stored at ambient *T*, upon withdrawal of the mixture the cylinder *P* could dip into the two phase region causing condensation. The resulting change in composition of the mixture would render density measurements meaningless. However, if the same cylinder were maintained at a *T* higher than the mixture CT, the risk of entering the two phase region upon *P* drop with sample withdrawal would be eliminated. For this reason and to keep the mixtures homogeneously mixed, the mixture cylinders were maintained at approximately 333.15 K [140 ^{o}F, 60 ^{o}C] in a well-insulated, hot box equipped with a temperature controller and heaters. This temperature of the hot box was well above the highest CT of approximately 325 K [125.33 ^{o}F, 51.85 ^{o}C] for M78C1 among mixtures to be measured.

(b) In charging the mixture to the MSD cell from the mixture cylinder through the feed manifold, it would pass through the two phase region if the manifold tubing, valves and fittings were maintained at ambient *T*. To prevent this, the feed manifold boxes including the compressor were maintained at approximately 333.15 K [140 ^{o}F, 60 ^{o}C] by radiative heating from a bank of infra-red bulbs suspended inside the manifold boxes. As many bulbs were used as were required to maintain the insulated manifold boxes at 333.15 K [140 ^{o}F, 60 ^{o}C] in thermal equilibrium with ambient *T*. For extreme drops in ambient *T*, the manifold *T* could still be maintained at 333.15 K [140 ^{o}F, 60 ^{o}C] despite not having a controller, by switching additional bulbs from the bank ‘on’ and allowing an additional period of time for *T* equilibration. Tubing on the feed manifold that were exposed to ambient *T* because of not being part of the feed manifold box were heated, insulated and maintained at approximately 348.15 K [167 ^{o}F, 75 ^{o}C] in thermal equilibrium with ambient *T*. For extreme drops in ambient *T*, the tubing *T* could still be maintained at 348.15 K [167 ^{o}F, 75 ^{o}C] despite not having controllers, by manually adjusting the variac voltage used to power the trace heaters.

(c) For density measurement at a T lower than the CT and at a P above the CB, the MSD could not be charged with the mixture directly because it would pass through the two phase region. Instead, an alternative charging procedure would be required to circumvent the two phase region. Options for such an alternative charging and density measurement procedure are discussed later in section 2.3.

2.2.2 Comparison of Density Predictions from Different Equations of State for Mixtures

The 'true' value of density can be known neither by experimental measurements nor by predictive EOS. The closest value to the true value of density can be predicted by an EOS with very high accuracy, which is in turn validated with high accuracy measured data. Different EOS will predict different densities because of the underlying differences in the model and the accuracy of the experimental data used to develop them. The performance of a new apparatus or method of density measurement is evaluated by comparing the measured data from the new apparatus or method against predictions from an established EOS which may be considered a standard. The question of which EOS should be selected as a standard arises because of the wide variety of predictive EOS available, each one claiming to be more accurate than the others by the respective developer. A good set of measured data may be judged to be bad if compared to the wrong EOS. Thus, the choice of the standard EOS used to judge the quality of measured data deserves great care. This section compares density predictions from the HY, AGA8-DC92 and NIST-23 (or REFPROP) EOS to highlight that predicted densities have high uncertainties among themselves.

A comparison of predicted densities from ECSmixS2 with the RR-NIST2 data in the custody transfer region showed a much larger average absolute deviation than the 0.03% claimed by Estela-Uribe *et al.* (2004). It was inferred that this was the effect of a program anomaly rather than the quality of the ECS model based upon shape factors and ECSmixS2 was excluded from further consideration. NIST-14 (or DDMIX) was

excluded because NIST recommends NIST-23 (or REFPROP) over NIST-14. Reproduction of results for system 1 of Hall and Yarborough (1973) was attempted to check the Excel program that was written, but discrepancies were observed mainly because of two reasons:

(a) The pure component critical property data used by Hall and Yarborough have been updated with more accurate data (Thermodynamic Research Center, 2003b; Smith *et al.*, 2001). Table 2.2 shows the pure component molar mass (M), critical T and critical P data used for density predictions of mixtures given in Table 2.1 using the HY EOS.

(b) Hall and Yarborough have grouped heptane and heavier components as the 'heptanes plus' fraction without mentioning the weights given to each heavy component in their analysis. Although the mole fraction contribution of heavier components is normally very small, their contribution in deciding the mixture pseudocritical *T* and pseudocritical *P* using Kay's mixing rule is significant because of their higher, pure component critical *T* and critical *P* than compared to lighter hydrocarbons. Kay, as well as Lee and Kesler, have pointed out that the mixture pseudocritical *T* and pseudocritical *P* are very important parameters that determine the accuracy of the mixture density. In the present study, the actual mixture compositions have been used for the HY EOS predictions without grouping the heavier components.

Each heavier component of a mixture must be grouped with an allowable component with the closest number of carbon atoms for use with PhasePro®, Sonicware® and REFPROP. Tables 2.3 through 2.7 show the groupings of heavier components that were used for mixtures RR-NIST2, M91C1, M94C1, M88C1 and M78C1 respectively for use with Sonicware® and REFPROP. With PhasePro®, the same compositions were used as with Sonicware®. Figures 2.3 through 2.7 show the pairwise comparisons of predicted densities from the HY, AGA8-DC92 and REFPROP EOS for the RR-NIST2, M91C1, M94C1, M88C1 and M78C1 mixtures respectively. The relative differences for predicted densities are defined as follows:

Table 2.2. Pure Component Data Used for HY EOS

Component	M g/mole	T_c K	P_c MPa
methane	16.043	190.6	4.599
ethane	30.070	305.3	4.872
propane	44.097	369.8	4.248
iso butane	58.123	408.1	3.648
n butane	58.123	425.1	3.796
iso pentane*	72.150	460.4	3.381
n pentane	72.150	469.7	3.370
n hexane	86.177	507.6	3.025
n heptane	100.204	540.2	2.740
n octane	114.231	568.7	2.490
n nonane	128.258	594.6	2.290
methyl cyclopentane	84.161	532.8	3.785
2 methyl pentane*	86.170	497.5	3.010
3 methyl pentane*	86.170	504.4	3.120
benzene	78.114	562.2	4.898
2, 3 dimethyl pentane*	100.204	537.3	2.910
3 methyl hexane*	100.204	535.2	2.810
toluene	92.141	591.8	4.106
methyl cyclohexane	98.188	572.2	3.471
2, 2, 4 trimethyl pentane*	114.231	543.9	2.570
nitrogen	28.014	126.2	3.400
carbon dioxide	44.010	304.2	7.383

* T_c and P_c from Thermodynamic Research Center (2003b)

Table 2.3. RR-NIST2 Mixture Compositions Used for Predictions

Component (i)	**Actual composition**	**Composition for AGA8-DC92 EOS**	**Composition for REFPROP EOS**
	x_i	x_i	x_i
methane	0.90644	0.90644	0.90644
ethane	0.04553	0.04553	0.04553
propane	0.00833	0.00833	0.00833
iso butane	0.00100	0.00100	0.00100
n butane	0.00156	0.00156	0.00156
iso pentane	0.00030	0.00030	0.00030
n pentane	0.00045	0.00045	0.00045
n hexane	0.00040	0.00040	0.00040
n heptane			
n octane			
n nonane			
methyl cyclopentane			
2 methyl pentane			
3 methyl pentane			
benzene			
2, 3 dimethyl pentane			
3 methyl hexane			
toluene			
methyl cyclohexane			
2, 2, 4 trimethyl pentane			
nitrogen	0.03134	0.03134	0.03134
carbon dioxide	0.00466	0.00466	0.00466

Table 2.4. M91C1 Mixture Compositions Used for Predictions

Component (i)	**Actual composition**	**Composition for AGA8-DC92 EOS**	**Composition for REFPROP EOS**
	x_i	x_i	x_i
methane	0.90991	0.90991	0.90991
ethane	0.02949	0.02949	0.02949
propane	0.01513	0.01513	0.01513
iso butane	0.00755	0.00755	0.00755
n butane	0.00755	0.00755	0.00755
iso pentane	0.00299	0.00299	0.00299
n pentane	0.00304	0.00304	0.00304
n hexane			
n heptane			
n octane			
n nonane			
methyl cyclopentane			
2 methyl pentane			
3 methyl pentane			
benzene			
2, 3 dimethyl pentane			
3 methyl hexane			
toluene			
methyl cyclohexane			
2, 2, 4 trimethyl pentane			
nitrogen	0.02031	0.02031	0.02031
carbon dioxide	0.00403	0.00403	0.00403

Table 2.5. M94C1 Mixture Compositions Used for Predictions

Component (i)	**Actual composition**	**Composition for AGA8-DC92 EOS**	**Composition for REFPROP EOS**
	x_i	x_i	x_i
methane	0.94045	0.94045	0.94045
ethane	0.01867	0.01867	0.01867
propane	0.01802	0.01802	0.01802
iso butane	0.00356	0.00356	0.00356
n butane	0.00706	0.00706	0.00706
iso pentane	0.00201	0.00201	0.00201
n pentane	0.00252	0.00252	0.00252
n hexane	0.00199	0.00205	0.00199
n heptane	0.00100	0.00100	0.00100
n octane	0.00052	0.00052	0.00077
n nonane	0.00025	0.00025	0.00000
methyl cyclopentane	0.00006	0.00000	0.00006
2 methyl pentane			
3 methyl pentane			
benzene			
2, 3 dimethyl pentane			
3 methyl hexane			
toluene			
methyl cyclohexane			
2, 2, 4 trimethyl pentane			
nitrogen	0.00246	0.00246	0.00246
carbon dioxide	0.00143	0.00143	0.00143

Table 2.6. M88C1 Mixture Compositions Used for Predictions

Component (i)	**Actual composition**	**Composition for AGA8-DC92 EOS**	**Composition for REFPROP EOS**
	x_i	x_i	x_i
methane	0.88023	0.88023	0.88023
ethane	0.05824	0.05824	0.05824
propane	0.03292	0.03292	0.03292
iso butane	0.00936	0.00936	0.00936
n butane	0.00537	0.00537	0.00537
iso pentane	0.00249	0.00249	0.00249
n pentane	0.00236	0.00236	0.00236
n hexane	0.00089	0.00149	0.00089
n heptane	0.00189	0.00189	0.00189
n octane	0.00098	0.00098	0.00134
n nonane	0.00036	0.00036	0.00000
methyl cyclopentane			0.00060
2 methyl pentane	0.00045	0.00000	0.00000
3 methyl pentane	0.00015	0.00000	0.00000
benzene			
2, 3 dimethyl pentane			
3 methyl hexane			
toluene			
methyl cyclohexane			
2, 2, 4 trimethyl pentane			
nitrogen	0.00262	0.00262	0.00262
carbon dioxide	0.00169	0.00169	0.00169

Table 2.7. M78C1 Mixture Compositions Used for Predictions

Component (i)	**Actual composition**	**Composition for AGA8-DC92 EOS**	**Composition for REFPROP EOS**
	x_i	x_i	x_i
methane	0.77762	0.77762	0.77762
ethane	0.10623	0.10623	0.10623
propane	0.05993	0.05993	0.05993
iso butane	0.01731	0.01731	0.01731
n butane	0.01013	0.01013	0.01013
iso pentane	0.00460	0.00460	0.00460
n pentane	0.00436	0.00436	0.00436
n hexane	0.00219	0.00521	0.00247
n heptane	0.00130	0.00286	0.00286
n octane	0.00053	0.00082	0.00111
n nonane	0.00029	0.00029	0.00000
methyl cyclopentane	0.00007	0.00000	0.00274
2 methyl pentane	0.00135	0.00000	0.00000
3 methyl pentane	0.00132	0.00000	0.00000
benzene	0.00028	0.00000	0.00000
2, 3 dimethyl pentane	0.00052	0.00000	0.00000
3 methyl hexane	0.00051	0.00000	0.00000
toluene	0.00033	0.00000	0.00000
methyl cyclohexane	0.00020	0.00000	0.00000
2, 2, 4 trimethyl pentane	0.00029	0.00000	0.00000
nitrogen	0.00660	0.00660	0.00660
carbon dioxide	0.00404	0.00404	0.00404

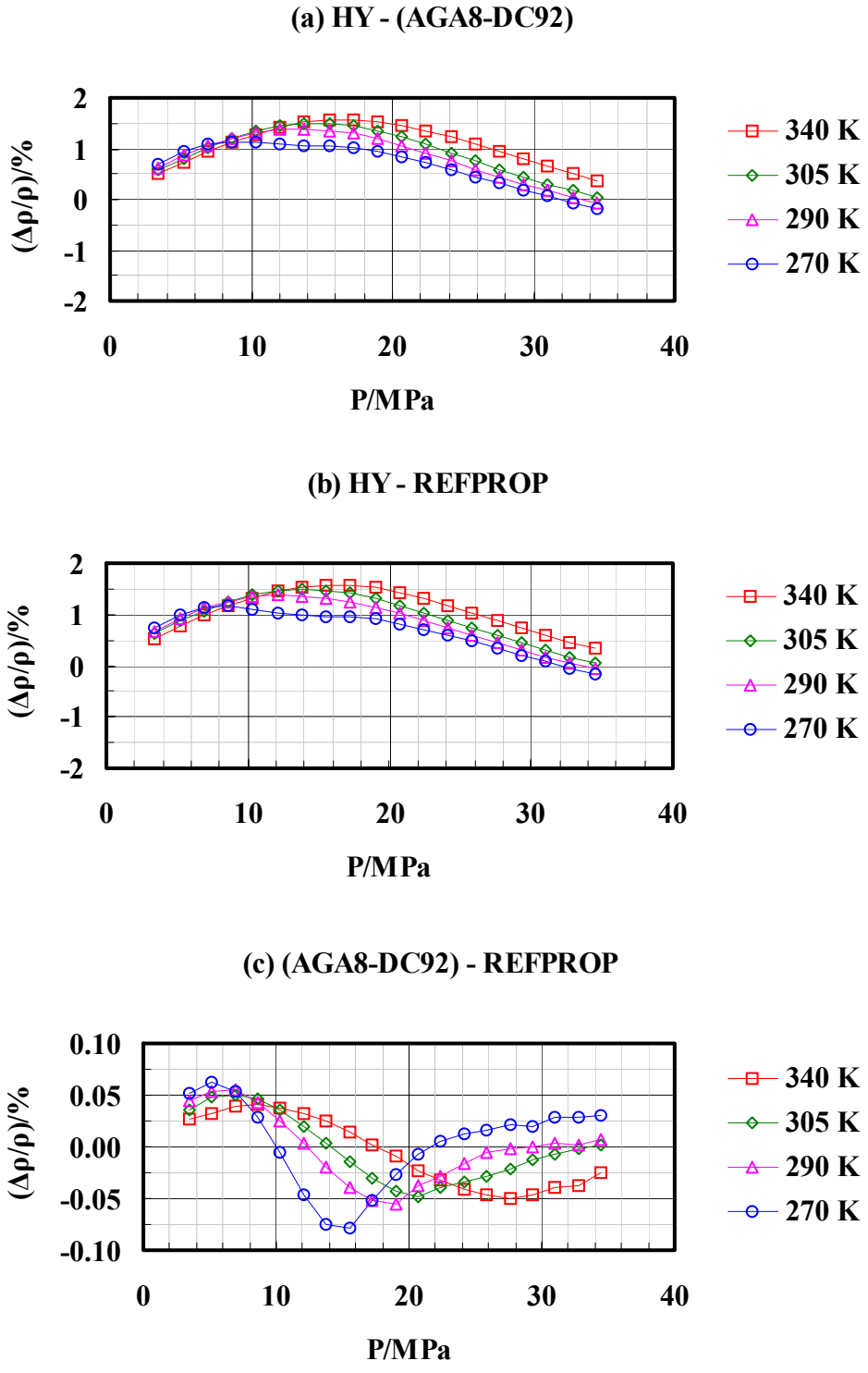

Figure 2.3. Comparison of HY, AGA8-DC92 and REFPROP EOS Density Predictions for RR-NIST2 Mixture

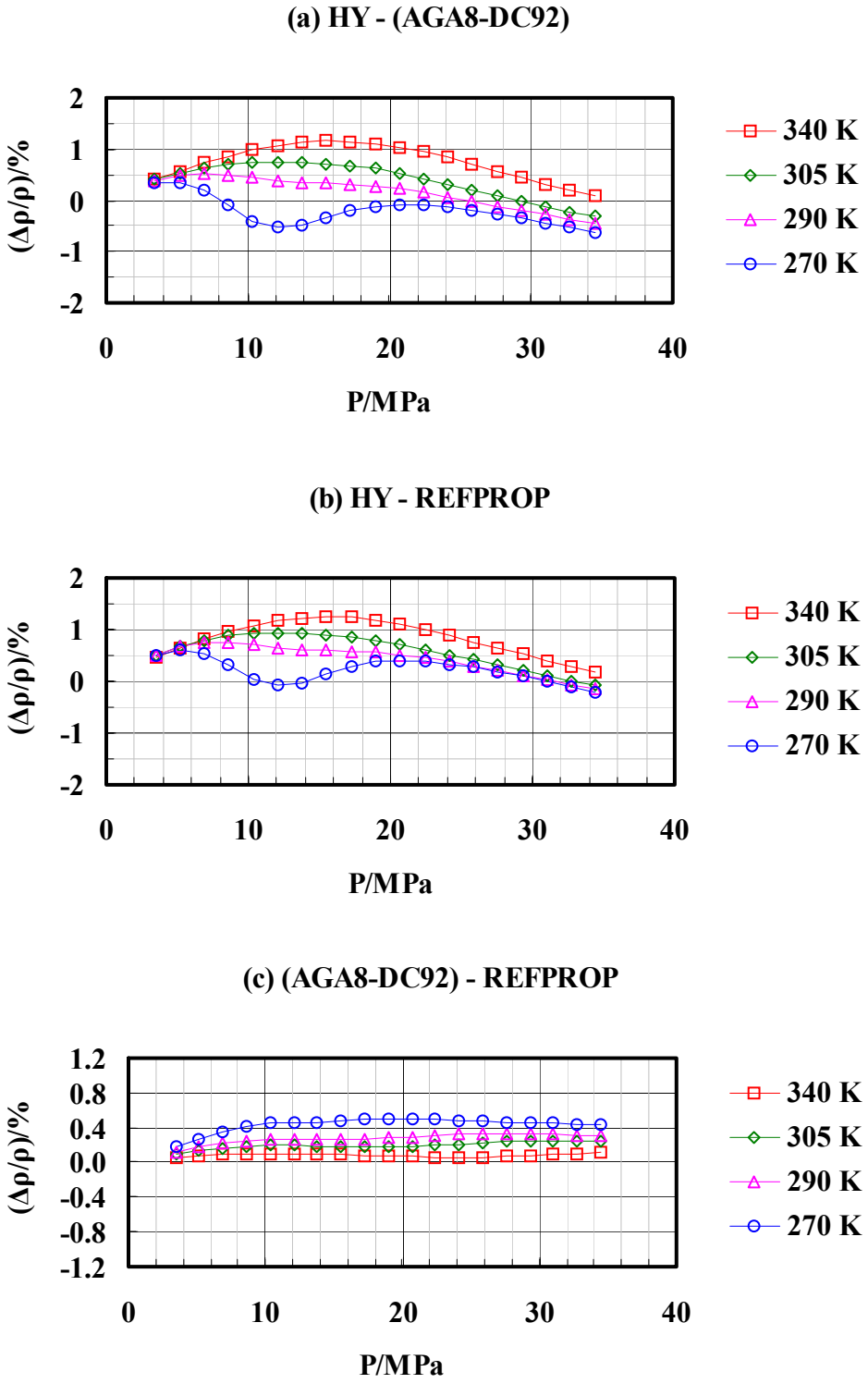

Figure 2.4. Comparison of HY, AGA8-DC92 and REFPROP EOS Density Predictions for M91C1 Mixture

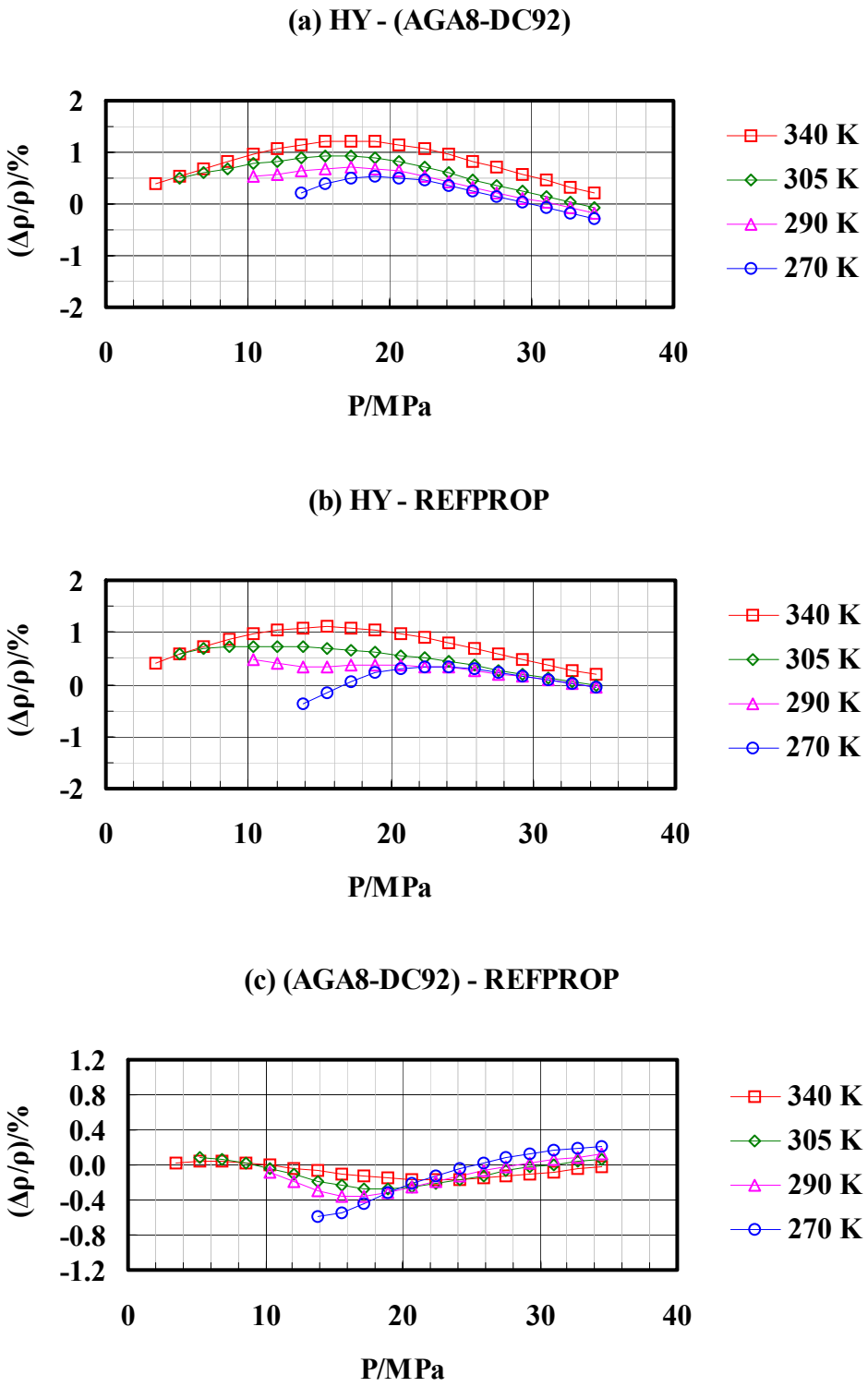

Figure 2.5. Comparison of HY, AGA8-DC92 and REFPROP EOS Density Predictions for M94C1 Mixture

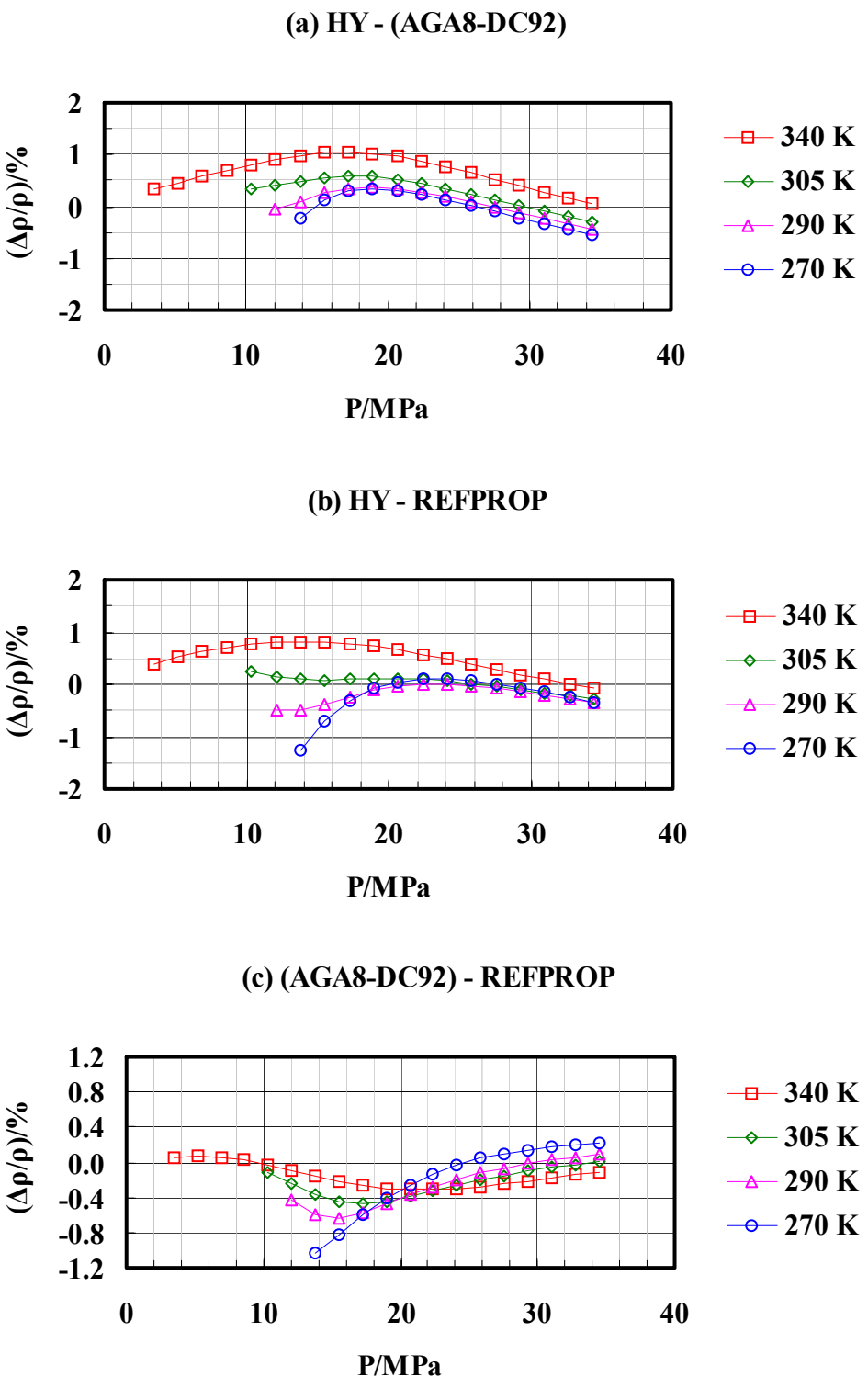

Figure 2.6. Comparison of HY, AGA8-DC92 and REFPROP EOS Density Predictions for M88C1 Mixture

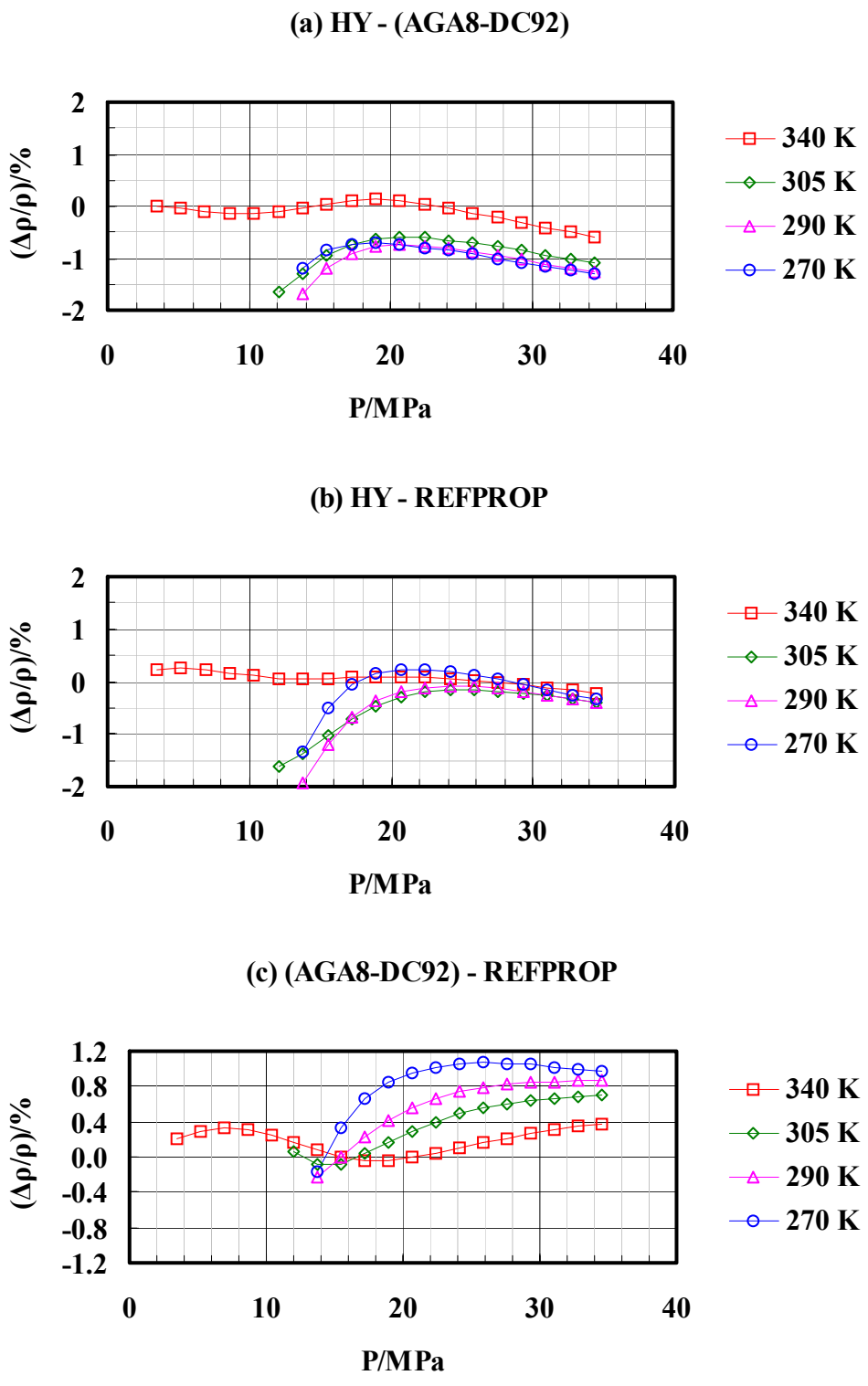

Figure 2.7. Comparison of HY, AGA8-DC92 and REFPROP EOS Density Predictions for M78C1 Mixture

HY- (AGA8-DC92)
$$\frac{\Delta\rho}{\rho} = \left(\frac{\rho_{HY} - \rho_{(AGA8-DC92)}}{\rho_{(AGA8-DC92)}} \right) x100$$

HY- REFPROP
$$\frac{\Delta\rho}{\rho} = \left(\frac{\rho_{HY} - \rho_{REFPROP}}{\rho_{REFPROP}} \right) x100$$

(AGA8-DC92) - REFPROP
$$\frac{\Delta\rho}{\rho} = \left(\frac{\rho_{(AGA8-DC92)} - \rho_{REFPROP}}{\rho_{REFPROP}} \right) x100 \qquad (2)$$

Comparisons have been made over a *T* range of (270 to 340) K [(26.33 to 152.33) ^{o}F, (-3.15 to 66.85) ^{o}C] and a *P* range of approximately (3.447 to 34.474) MPa [(500 to 5,000) psia] that includes the custody transfer region. Experimental densities using the MSD have also been measured over the same range. Points that were predicted to be in the two phase vapor-liquid region according to Figure 2.2 have been excluded from density comparisons. Appendix A includes tables for the density and compressibility factors for the five mixtures from the three EOS along with mixture-specific information such as molar mass, specific gravity, pseudocritical *T* and pseudocritical *P*. Differences in molar mass using different EOS result because of the heavier component groupings. These groupings do not cause differences in the predicted densities from the two methods to be more than ±0.02%.

Table 2.8 summarizes the average, standard deviation (deviation at the 68% confidence interval or 1 σ), the maximum and the minimum values for the relative differences in predicted densities given in Appendix A for the five mixtures. Points lying in the two-phase vapor-liquid region have been excluded from the statistical analyses. In general, the HY EOS predicts densities larger than both the AGA8-DC92 and REFPROP EOS except for the mixture M78C1 and has larger deviations when compared to the deviations for the predicted density differences between the AGA8-DC92 and REFPROP EOS. There is better agreement between the AGA8-DC92 and REFPROP EOS density predictions. The relative difference between density predictions from the AGA8-DC92 and REFPROP EOS clearly shows a dependence on the composition of the C_{6+} fraction in the mixture as indicated by an increase in both the average and deviation

Table 2.8. Statistical Analyses for Relative Differences in Density Predictions

Relative difference in predicted molar density (%)						
	HY - (AGA8-DC92)		HY - REFPROP		(AGA8-DC92) - REFPROP	
Mixture	**μ ± σ**		**μ ± σ**		**μ ± σ**	
RR-NIST2	0.883	0.461	0.881	0.457	-0.001	0.035
M91C1	0.269	0.474	0.515	0.370	0.246	0.140
M94C1	0.533	0.374	0.433	0.337	-0.099	0.166
M88C1	0.274	0.400	0.068	0.399	-0.205	0.250
M78C1	-0.663	0.445	-0.240	0.463	0.465	0.373
Mixture	**max.**	**min.**	**max.**	**min.**	**max.**	**min.**
RR-NIST2	1.566	-0.196	1.574	-0.165	0.062	-0.078
M91C1	1.159	-0.625	1.251	-0.198	0.504	0.046
M94C1	1.222	-0.283	1.108	-0.389	0.220	-0.597
M88C1	1.044	-0.551	0.820	-1.252	0.219	-1.039
M78C1	0.127	-1.695	0.255	-1.914	1.068	-0.223

values for the samples in order of increasing C_{6+} fraction composition. The larger relative difference as well as deviation between the AGA8-DC92 and REFPROP density predictions for M91C1 than RR-NIST2 despite having the same methane content and no C_{6+} fraction is probably because of slightly different compositions. This observation is especially important in Chapter V when comparing measured densities of M91C1 mixture using the MSD against the AGA8-DC92 and REFPROP density predictions. The comparisons also show that the predictions from the HY EOS of 1973 agree within ±1% of predictions from recent, more accurate EOS such as the AGA8-DC92 of 1992 and the REFPROP EOS of 2003 for the five mixtures. The tables in Appendix A for the HY and REFPROP EOS predictions also give the reduced pseudocritical temperature (T_{pr}) and reduced pseudocritical pressure (P_{pr}) to evaluate the validity of the HY EOS for the five mixtures over the range of interest for this project. The ($1.199 < T_{pr} < 1.372$) and ($0.753 < P_{pr} < 7.560$) ranges for the five samples of this project are well within the range of applicability of the HY EOS which explains its relatively good agreement with the more accurate AGA8-DC92 and REFPROP EOS predictions.

2.3 Philosophy of Measurements

The thermodynamic (P - ρ - T) measurements of Hwang *et al.* and Magee *et al.* for the RR-NIST2 mixture have been reproduced in Figure 2.8 to explain the philosophy of measurements. The predicted vapor-liquid two phase envelope obtained from PhasePro® using the PR EOS is also plotted.

Isotherms (IT), which are constant T lines describing change in P due to variation in ρ were measured with a pycnometer (Lau, 1986; Hwang 1988; Lau *et al.*, 1997) and a Burnett apparatus (Burnett, 1936; Stouffer, 1992; Stouffer *et al.*, 2001, Simon, 1991) at TAMU whereas isochores (IC), which are constant ρ lines describing the change in P due to variation in T were measured with an isochoric apparatus by NIST as part of the RR project. The Burnett apparatus was used because of its ability to measure even very low densities with an accuracy of ±0.05% in the T range (250 to 325) K [(-9.67 to 125.33) ^{o}F, (-23.15 to 51.85) ^{o}C] and the P range of approximately (0.179 to

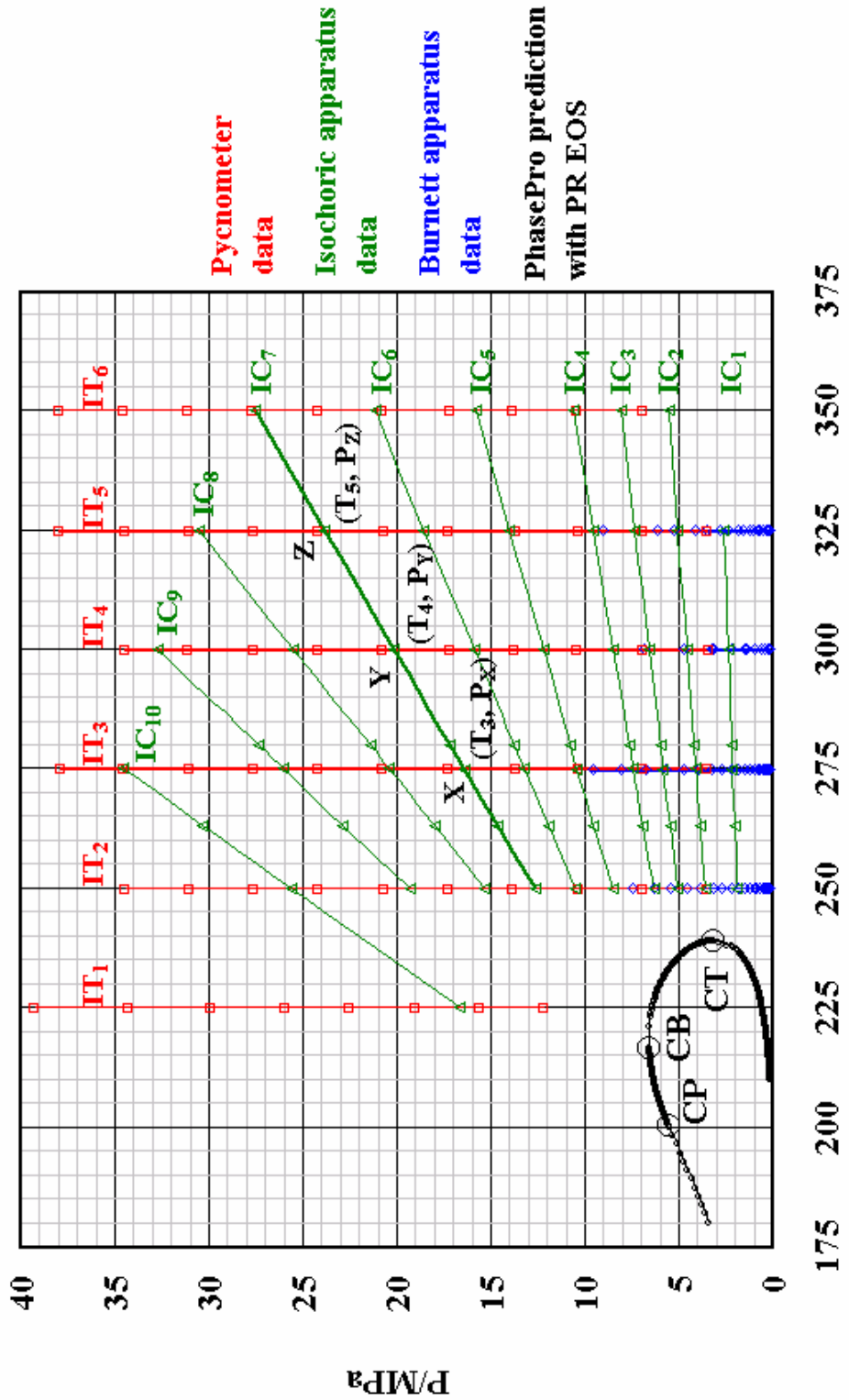

Figure 2.8. Philosophy of (P - ρ - T) Measurements Used in RR Project

11.032) MPa [(26 to 1,600) psia]. The pycnometer was used for measuring higher densities with an accuracy of ±0.1% in the *T* range (225 to 350) K [(-54.67 to 170.33) ^{o}F, (-48.15 to 76.85) ^{o}C] and the *P* range of approximately (2.758 to 68.948) MPa [(400 to 10,000) psia]. The overlapping range of *P* between the Burnett apparatus and the pycnometer was used to check reproducibility of measured densities from the two apparatuses and hence the continuity of an isotherm. NIST used the isochoric apparatus for density measurements by knowing the cell volume accurately and measuring the amount of material in the cell. The isochoric apparatus served an additional purpose by measuring the vapor-liquid two phase envelope based on the sudden change in the slope of an IC at the onset of the two phase region (Eubank and Barrufet, 1987).

Unlike the round robin project where the isochoric apparatus was used for direct measurement of accurate densities, at TAMU, it has been used in conjunction with another apparatus capable of accurate density measurements such as the Burnett apparatus or the pycnometer. In this mode, the isochoric apparatus indeed measures an IC by increasing the *T* of a fixed amount of material and measuring the corresponding *P* but the density is not known because the amount of material is not measured (Yurttaş, 1988; Yurttaş *et al.* 1994; Duarte-Garza, 1988; Duarte-Garza *et al.*, 1995). Instead a base density at the point of intersection of an IC with a measured isotherm from either a Burnett apparatus or a pycnometer is required. Small corrections to the base density caused by pressure and temperature distortion of the isochoric apparatus cell can be applied to calculate accurate densities at other points on the IC. Thus, the accuracy of densities from the isochoric apparatus depends upon the accuracy of the base density. The isochoric apparatus also has been used for measurement of the vapor-liquid two phase envelope by TAMU.

The TAMU strategy has been followed for measurements in the present project, which is similar to the round robin project with the difference that the MSD has been used instead of the Burnett apparatus and the pycnometer for accurate density measurements used as base densities for the IC. The MSD was expected to measure densities with an accuracy of ±0.03% in the *T* range (188.15 to 523.15) K [(-121 to 482)

^{o}F, (-85 to 250) ^{o}C] and the P range of approximately (0 to 206.843) MPa [(0 to 30,000) psia]. Better accuracy of the MSD over T and P ranges wider than those covered by the Burnett apparatus and the pycnometer together and elimination of the need to check continuity of the isotherms from two different apparatuses motivated the replacement.

Figure 2.8 also illustrates the TAMU strategy using IT_3, IT_4 and IT_5 and IC_7. IT_4 can be represented in the form $P = P(T_4, \rho)$ or in a form similar to the virial EOS given by equation (1) containing power terms in ρ as follows:

$$\frac{P}{\rho R T_4} = A_4 + B_4\rho + C_4\rho^2 + \ldots \tag{3}$$

where, A_4, B_4, C_4… are constants obtained from a non-linear regression fit of the measured P-ρ data at constant T_4 from the MSD. A similar representation for IT_5 would be $P = P(T_5, \rho)$ or:

$$\frac{P}{\rho R T_5} = A_5 + B_5\rho + C_5\rho^2 + \ldots \tag{4}$$

IC_7 can be expressed in the form $P = P(T, \rho_7)$ or as an infinite series containing power terms in T as follows:

$$P = a_7 + b_7 T + c_7 T^2 + \ldots \tag{5}$$

where, a_7, b_7, c_7… are constants obtained from a non-linear regression fit of the measured P-T data at constant ρ_7 from the isochoric apparatus. If IT_4 is chosen as the base isotherm then by substituting T_4 in equation (5) we get the point Y (T_4, P_Y) at which the base density value must be known. This base density can be calculated by substituting P_Y known from equation (5) into equation (3) for IT_4. This base density for IC_7 represented by ρ_{7Y} at point Y (T_4, P_Y) would ideally be the same for all points along

IC_7. However, the values of density along an IC need a correction to account for the distortion of the isochoric cell volume with variations in T and P from (T_4, P_Y) at point Y. Because the amount of material in the cell along an IC remains unchanged, the cell volume correction and the corrected density at any other point such as Z (T_5, P_Z) on IC_7 and denoted by ρ_{7Z} is given by:

$$\frac{V_Z}{V_Y} = \frac{\rho_{7Y}}{\rho_{7Z}} = 1 + \alpha\left(T_5 - T_4\right) + \beta\left(P_Z - P_Y\right) \tag{6}$$

where, α is the thermal distortion coefficient and β is the pressure distortion coefficient of the isochoric apparatus cell material. Thus the isochores from the isochoric apparatus and the isotherms from the MSD together give accurate densities at additional points other than at those measured with the MSD only. The density at point Z (T_5, P_Z) can also be calculated by substituting P_Z in equation (4) for IT_5. The corrected density ρ_{7Z} calculated from IC_7 should be within the experimental error of this density from IT_5 for the isochoric apparatus and the MSD data to be ruled consistent. A similar consistency check can be done for density at point X (T_3, P_X). Figures 2.9 and 2.10 show the (P,T) points at which densities of M91C1 and M94C1 mixtures have been measured as part of this work using the MSD, relative to their respective phase envelopes. The isochores were measured separately by Zhou (2002) using an isochoric apparatus.

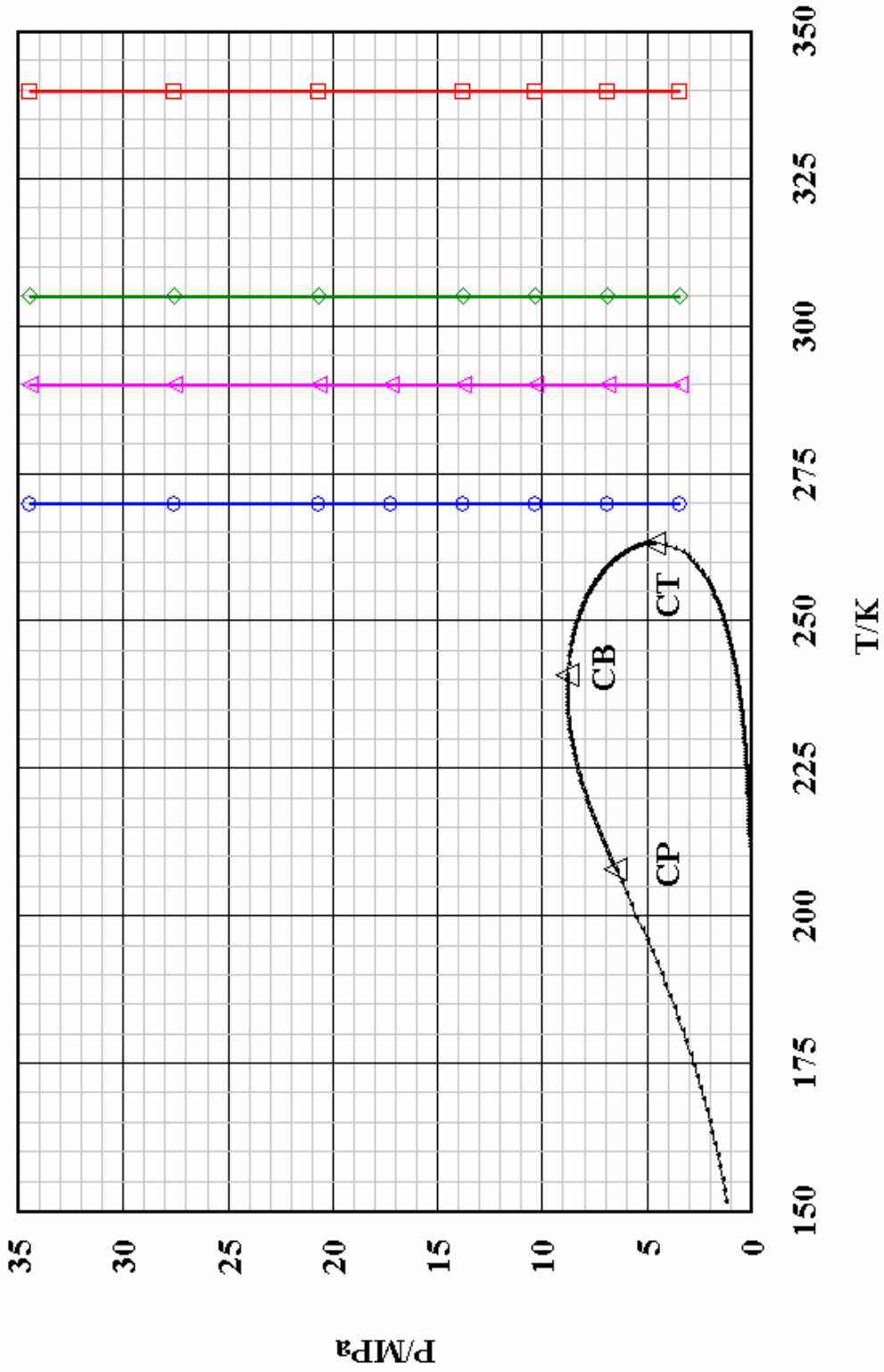

Figure 2.9. Points for Density Measurement of M91C1 Mixture Using MSD, Relative to Its Phase Envelope

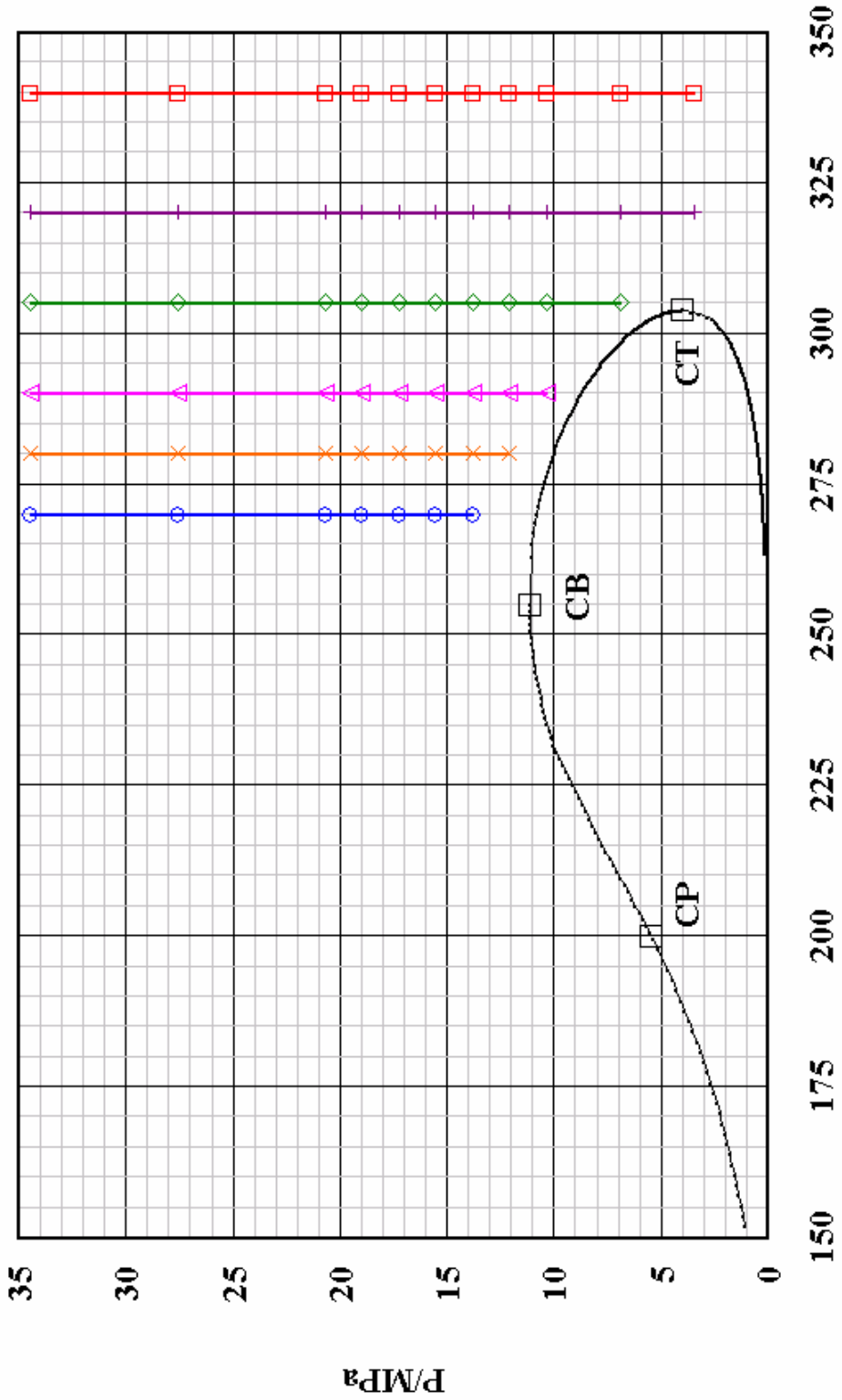

Figure 2.10. Points for Density Measurement of M94C1 Mixture Using MSD, Relative to Its Phase Envelope

CHAPTER III

THE MAGNETIC SUSPENSION DENSITOMETER SETUP

3.1 Density Measurement Methods

The International Union of Pure and Applied Chemistry, (IUPAC) (1975) has reviewed several experimental methods that have evolved for density measurements of fluids. This review has been supplemented with more recent contributions by Holste *et al.* (1986), Lau *et al.* (1997) and the IUPAC (2003). The absolute or relative density measurement methods include:

(1) The hydrostatic buoyancy force technique
(2) The Burnett apparatus (multiple expansion), Z-meter (single expansion), Burnett-isochoric coupled method
(3) The isochoric apparatus or the gasometer
(4) The isochoric substitution method
(5) The continuously weighed pycnometer
(6) The grating interferometer based on refractive index measurement
(7) The vibrating element (wire or tube) method and
(8) The bellows volumometer.

The hydrostatic buoyancy force technique is based upon Archimedes' principle that states when a solid body, hereafter *sinker*, is immersed in a fluid it displaces a volume of fluid the weight of which is equal to the buoyancy force exerted by the fluid on the sinker. The buoyancy force in turn is proportional to the density of the fluid in the measuring cell under pressure. Change from the 'true mass' of the sinker measured with the sinker in vacuum to the 'apparent mass' measured with the sinker surrounded by the pressurized fluid is sensed by suspending it physically from the bottom of the pan of a microbalance with a thin wire. The P and T ranges of earlier versions of hydrostatic

buoyancy force apparatuses were restricted by this physical-contact method between the sinker and the balance for force transmission. Moreover, the accuracies of density measurements were adversely affected because of the surface tension between the sample liquid and the suspension wire, adsorption on the surfaces of the sinker, buoyancy forces acting on parts of the suspension other than the sinker and shift in the zero-point of the balance.

3.1.1 The Two-sinker Magnetic Suspension Densitometer Operating Principle

The restrictions mentioned in the previous subsection were overcome by the pioneering design of Kleinrahm and Wagner (1984, 1986) that combined the hydrostatic buoyancy force method with alternate levitation of two sinkers through a magnetic suspension coupling. The novelty of the magnetic suspension coupling was that it used non-physical-contact force transmission between the sinker in the pressurized cell and the weighing balance at atmospheric pressure, thus allowing a cell design that covered a very wide T and P range (Lösch, 1987). The two sinkers, one a disk or a ring and the other a sphere or a cylinder had the same mass, surface area and surface properties but vastly different volumes. The density of a fluid was calculated by measuring Δm_{v}, the small difference in true masses of the two sinkers under vacuum and Δm_{a}, the difference in apparent masses of the two sinkers with the sample fluid surrounding the sinkers, and v_{d} and v_{sp}, the volumes of the two sinkers in the form of a disk and a sphere:

$$\rho = \frac{\Delta m_{\mathrm{a}} - \Delta m_{\mathrm{v}}}{v_{\mathrm{sp}} - v_{\mathrm{d}}} \tag{7}$$

The use of two sinkers improved the accuracy by compensation of surface tension, buoyancy, adsorption effects and shifts in zero-point of the balance. The two-sinker magnetic suspension densitometer was primarily designed for accurate measurements of

the saturated liquid and vapor densities of pure fluids together with the vapor pressure, but it could be used for homogeneous gas and liquid density measurements as well. The two-sinker densitometer of Kleinrahm and Wagner (1986) had an operating T range of (60 to 340) K [(-351.67 to 152.33) ^{o}F, (-213.15 to 66.85) ^{o}C] and a P range of up to 11.997 MPa [1,740 psia] with an uncertainty in density measurement of ±(0.01 to 0.02)% (IUPAC, 2003). The two-sinker densitometer of Pieperbeck *et al.* (1991) designed especially for density measurement of natural gas mixtures covered the T range (273.15 to 323.15) K [(32 to 122) ^{o}F, (0 to 50) ^{o}C] and P range up to 11.997 MPa [1,740 psia] with an uncertainty in density measurement of ±0.015%. McLinden and Frederick (1993) have developed a two-sinker densitometer at NIST capable of measuring densities over a wider T range of (80 to 520) K [(-315.67 to 476.33) ^{o}F, (-193.15 to 246.85) ^{o}C] and a P range of up to 34.991 MPa [5,075 psia] without compromising the accuracy of density measurements.

3.1.2 The Single-sinker Magnetic Suspension Densitometer Operating Principle

The operation of the two-sinker densitometer was rather complex because of its sinker-changing device that provided the special advantage of high accuracy even at very low densities. This advantage was redundant during medium or high density measurements encountered in many practical applications. Wagner *et al.* (1995) developed the single-sinker densitometer to simplify the operation of density measurement at medium and high densities without loss of accuracy and to broaden the operating P and T ranges over those of the two-sinker densitometers. Klimeck *et al.* (1998) used this single-sinker densitometer in the T range (235 to 520) K [(-36.67 to 476.33) ^{o}F, (-38.15 to 246.85) ^{o}C] and P range up to 30 MPa [4,351.131 psia] to measure densities of nitrogen and argon with an accuracy of ±(0.015 to 0.020)% for densities above 20 kg/m^3. The single-sinker densitometer also operates based upon Archimedes' principle for the buoyancy force acting on a cylindrical sinker in the presence of a fluid. The density is calculated by measuring m_v, the 'true mass' of the sinker in vacuum, m_a,

the ‘apparent mass’ of the sinker in the presence of fluid and v_S, the volume of the sinker:

$$\rho = \frac{m_v - m_a}{v_S} \tag{8}$$

Klimeck *et al.* (1998) have concluded that, even if the accuracy of ±(0.015 to 0.02)% for densities as low as 20 kg/m^3 from their version of the single-sinker densitometer is slightly superior to that from the single-sinker densitometer version of Wagner *et al.* (1995) for densities as low as 50 kg/m^3, the accuracy of density measurement from a single-sinker densitometer is lower than that from a two-sinker densitometer especially for low densities because it lacks compensation for the adsorption effect. They also concluded that the accuracy from a single-sinker densitometer is nonetheless higher than that from a Burnett apparatus because adsorption only on the surface of the sinker and not on the entire cell inner wall contributes to an error in the apparent mass of the sinker. The error caused by adsorption during density measurements using a Burnett apparatus is cumulative and requires correction as analyzed and suggested by Hall and Eubank (1972), Eubank and Kerns (1973) and Eubank *et al.* (1990).

3.1.3 The Compact Single-sinker Magnetic Suspension Densitometer

The single-sinker densitometer versions of Wagner *et al.* (1995) and Klimeck *et al.* (1998) both had a separate thermostated magnetic suspension coupling housing and a pressure cell for the fluid sample and the sinker. To further simplify the operation of the single-sinker densitometer, Wagner *et al.* (1995) designed a compact version that combined the magnetic suspension coupling housing and the sample cell into a single part. This design without the double-wall thermostat has been used for density measurements in the present project. This chapter describes construction details and operation of the compact single-sinker densitometer apparatus manufactured by

Rubotherm Präzisionsmesstechnik GmbH, Germany and its ancillary equipment for density measurements. The apparatus has an accuracy specification from the manufacturer of ±(0.03% + 0.005 kg/m^3) for densities in the range (0 to 2,000) kg/m^3 over a *T* range (193.15 to 523.15) K [(-112 to 482) ^{o}F, (-80 to 250) ^{o}C] and a *P* range up to 200 MPa [29,007.540 psia] with a maximum *P* at 523.15 K [482 ^{o}F, 250 ^{o}C] of 130 MPa [18,854.901 psia]. This operating range is unique among all magnetic suspension densitometers in use presently, worldwide.

3.2 Description of the Compact Single-sinker Magnetic Suspension Densitometer

The main apparatus supplied by the manufacturer consists of a high pressure cell for the sample, an analytical weighing balance, a suspension tube between the cell and the balance, a buoyancy-free basic load compensation device (also called the weight changing device), the magnetic suspension assembly (MSA), a control box for the MSA and a control box for the weight changing device. Figure 3.1 is a schematic diagram for relative positions of the various parts of the MSD.

3.2.1 The High Pressure Cell and the Magnetic Suspension Assembly

The cylindrical, copper beryllium alloy cell was pressure-tested by the manufacturer with water up to 300 MPa [43,511.310 psia]. Copper was used because of its high thermal conductivity to minimize axial and radial thermal gradients across the cell while beryllium was used to increase the mechanical strength of the cell. A groove approximately 0.8 cm x 0.6 cm was cut throughout the length of the cell within which a copper capsule approximately 7 cm long, 0.8 cm wide and 0.6 cm thick could be fit either at the extreme top and/or bottom of the cell. The copper capsule in turn has a cylindrical hole of diameter slightly larger than 0.32 cm drilled along its axis up to half its length for insertion of the platinum resistance thermometer (PRT) for temperature

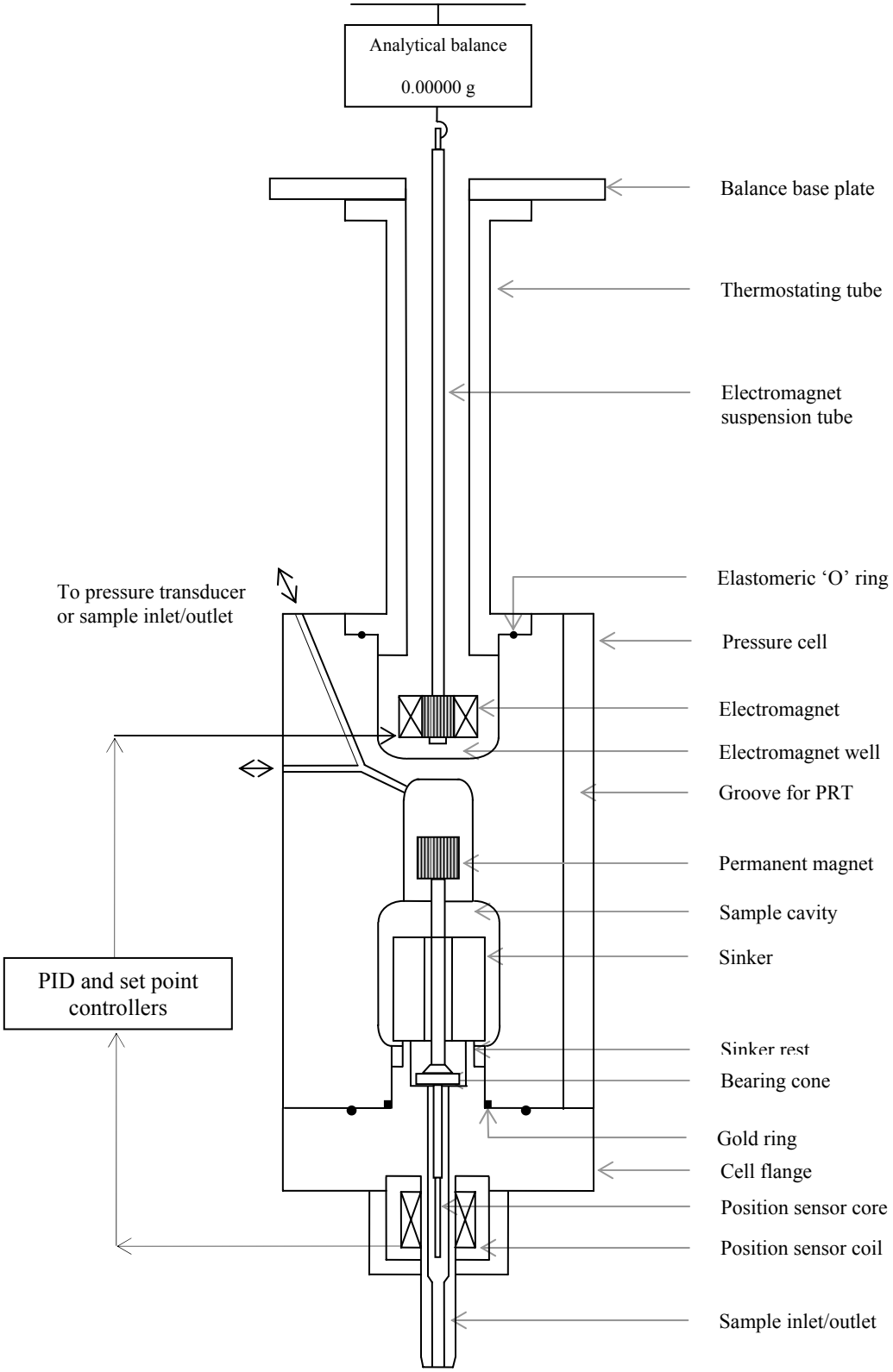

Figure 3.1. Schematic Diagram of the Compact Single-sinker MSD

measurements. The top part of the cell has an axially bored cylindrical depression that extends to about 40 % of its length. The electromagnet is suspended from the bottom hook of the weighing balance pan into this depression (called the 'electromagnet well') with the electromagnet suspension tube. The cell is attached to the bottom of the weighing balance base plate with a stainless steel tube called the thermostating tube having a flange on each end. In the standard version of the single-sinker densitometer with the housing for the magnetic suspension coupling and the cell as separate parts, the thermostating tube is temperature controlled to isolate the balance from the cell temperature. The thermostating tube of the compact version however is not temperature controlled and merely acts as a sleeve for protecting the electromagnet suspension tube from air drafts. The flange of the thermostating tube on the cell side has a groove for an elastomeric 'O' ring to provide a seal between the flange and the cell. The wires carrying current to the electromagnet coil pass through the hollow electromagnet suspension tube.

The lower end of the cell has another bored depression that extends about 50% of the length of the cell, houses the permanent magnet, the bearing cone, the sinker and the position sensor core and holds the sample at high pressures. The remaining 10% of the cell length forms a wall about 1.8 cm thick between the electromagnet at ambient pressure and the permanent magnet at high pressure. The lower depression in the cell is closed with a high pressure stainless steel flange with center tubing for sample feed into or removal from the cell. The inner face of the flange contacting the cell bottom has an elevated cylindrical protrusion that acts as a rest for the sinker when it is not in a state of levitation. A high pressure seal between the flange and the cell bottom is established with a square cross-sectional, gold coated copper ring packing around the protrusion when the bolts of the flange are tightened. The inner face of the flange also has a circular groove approximately midway along the radius where an elastomeric 'O' ring can be used for a face seal with the cell bottom surface. The two elastomeric 'O' rings; one between the thermostating tube flange and the top portion of the cell and the other between the high pressure flange and the bottom surface of the cell prevent any liquid from leaking into the electromagnet well or the cell cavity with the sinker respectively

even if the entire cell is immersed in a liquid bath for thermostatization. The outer face of the flange houses the coil for a position sensor in a sealed enclosure.

The electromagnet, the permanent magnet, the bearing cone and the position sensor coil together form the physical parts of the MSA that lie within the cell. Figure 3.2 shows details of the permanent magnet piece and the bearing cone piece. The permanent magnet piece has a cobalt-samarium permanent magnet connected to one end of a hollow shaft. The inner wall of the other end of this permanent magnet shaft has threading into which the bearing cone can be screwed. The other end of the bearing cone carries the position sensor core. Figure 3.3 shows the distances between the top surface of the permanent magnet and the bottom of the bearing cone plate when the permanent magnet and the bearing cone are completely disengaged, partially engaged and completely engaged. The bearing cone must be screwed completely into the permanent magnet shaft to provide rigidity to the entire assembly as shown in Figure 3.3 (c). The distance between the top of the permanent magnet and the bottom of the bearing cone when the permanent magnet and the bearing cone are completely engaged is 86.6 mm and not 93.3 mm as mentioned in the apparatus user manual (Rubotherm, 1999). The sinker is lifted from its rest by the conical part of the bearing cone while the permanent magnet is in a state of levitation. The bearing cone plate provides a broad support for the permanent magnet and the bearing cone together when the permanent magnet is not in a state of levitation.

Figures 3.4 and 3.5 show a scaled, cross sectional diagram of the cell and the MSA parts adapted from Rubotherm (1999), Lösch and Wagner (1998) and Lösch (2005). These figures accentuate the horizontal clearances along the radius and the vertical clearances along the axis among the MSA parts, the sinker and the cell inner walls. Appendix B presents a table of dimensions of the MSA parts, the sinker and the cell that were measured to estimate these horizontal and vertical clearances.

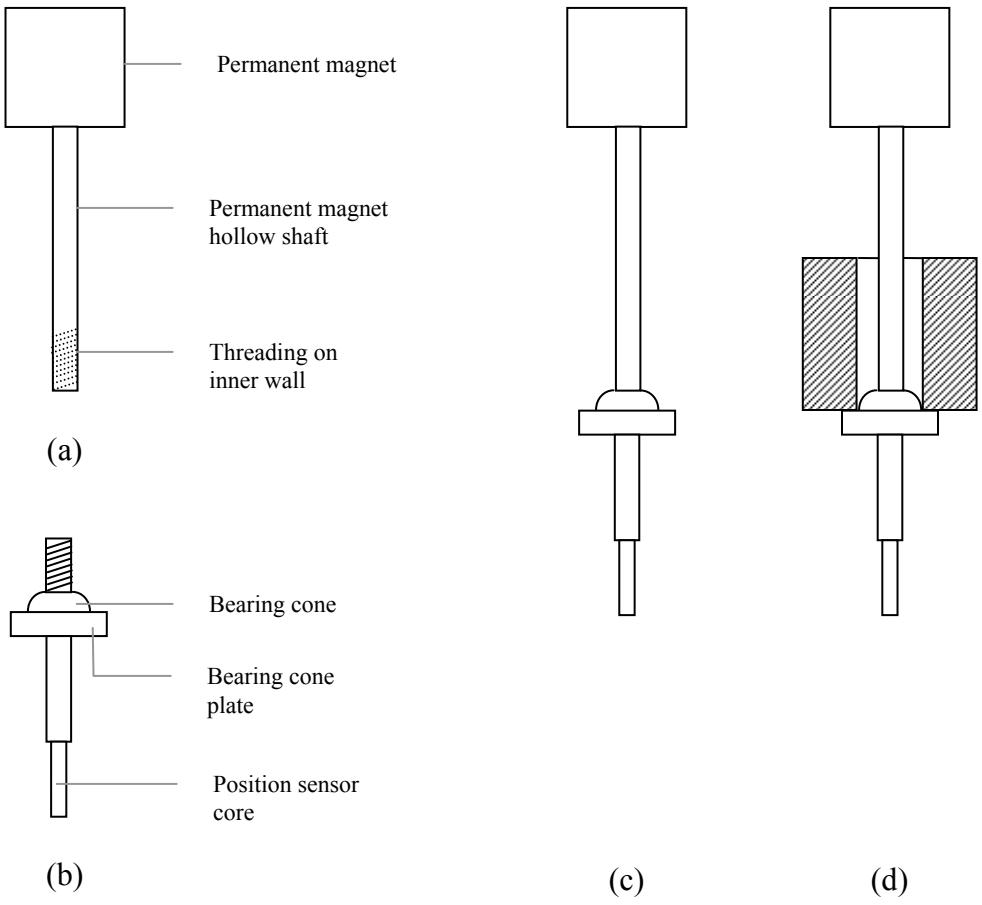

Figure 3.2. Details of the MSA Parts inside the Pressure Cell.
(a) The Permanent Magnet Piece
(b) The Bearing Cone Piece
(c) The Permanent Magnet Piece and the Bearing Cone Piece when Completely Engaged
(d) Sinker lifted by the Bearing Cone Piece when the Permanent Magnet is in a State of Levitation

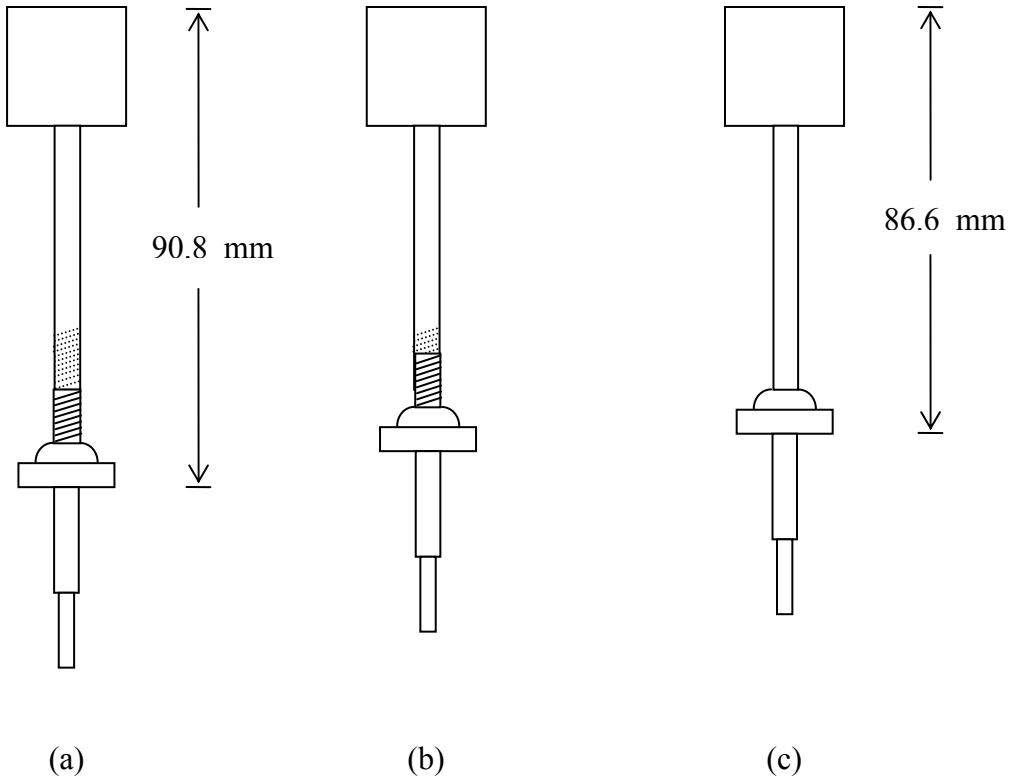

Figure 3.3. Relative Engagement of Permanent Magnet Piece with Bearing Cone Piece
(a) Completely Disengaged
(b) Partially Engaged
(c) Completely Engaged

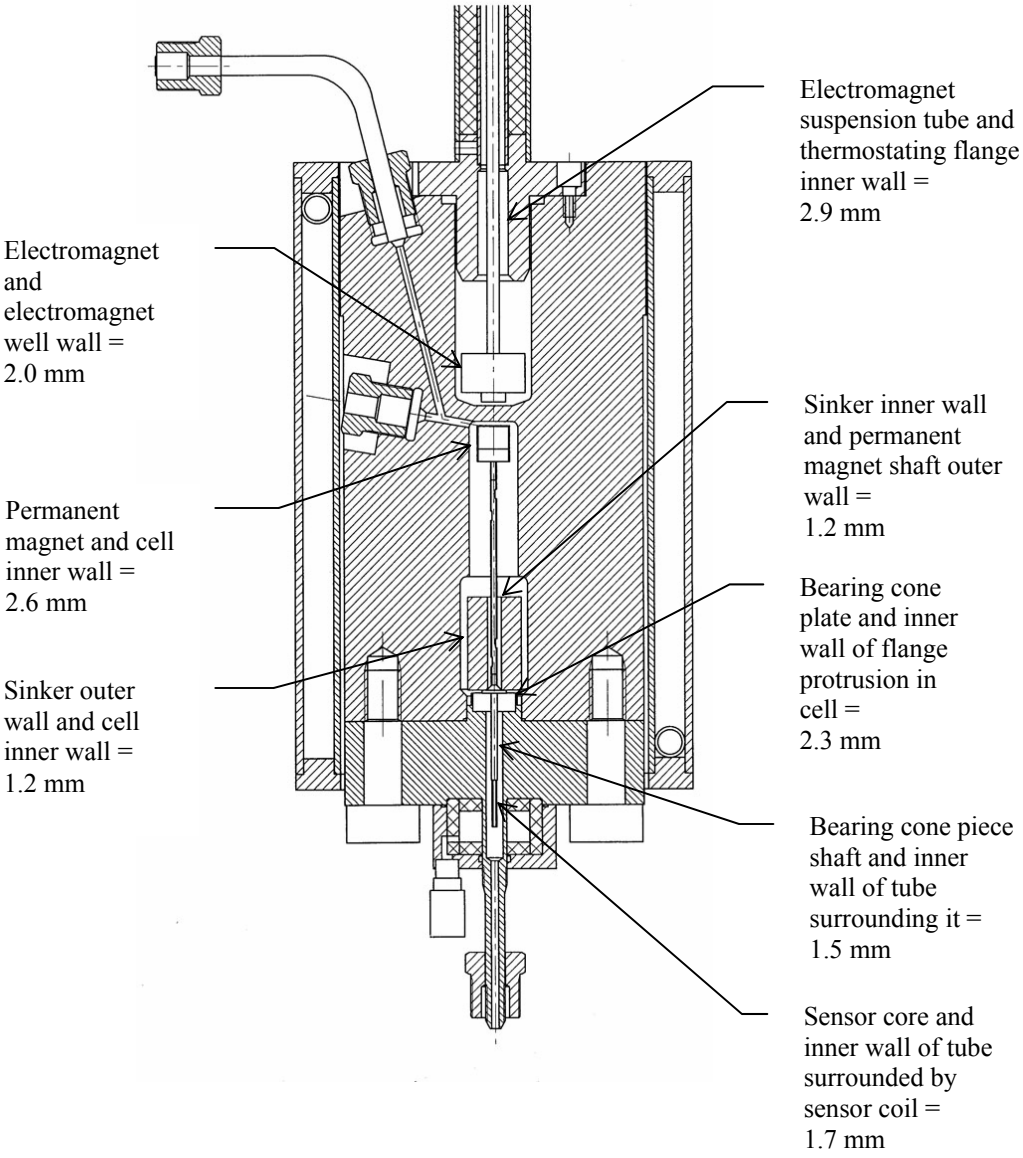

Figure 3.4. Horizontal Clearances along the Radius among the MSA Parts, the Sinker and the Cell Inner Walls. Scaled figure adapted from Rubotherm (1999), Lösch and Wagner (1998) and Lösch (2005).

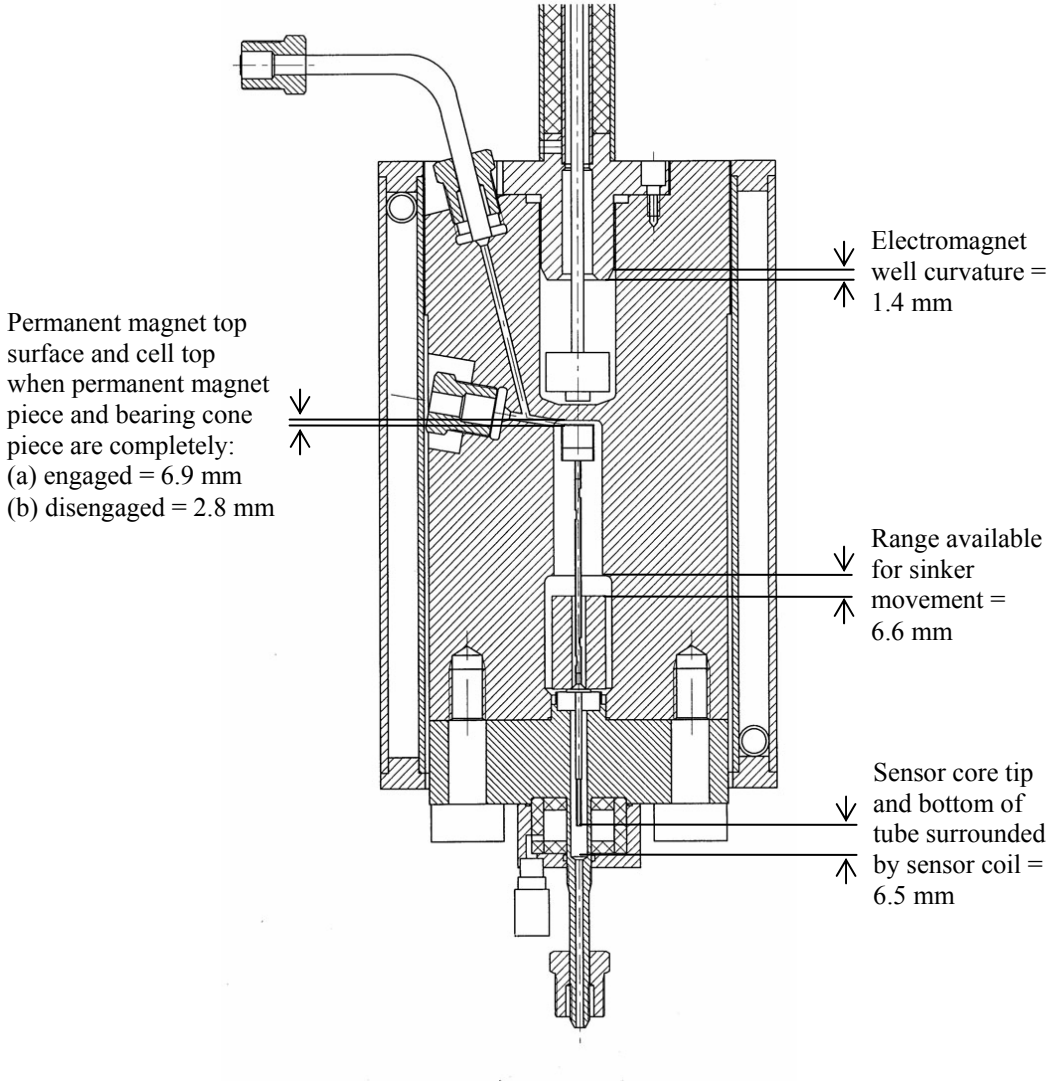

Figure 3.5. Vertical Clearances among the MSA Parts, the Sinker and the Cell Inner Walls along the Axis. Scaled figure adapted from Rubotherm (1999), Lösch and Wagner (1998) and Lösch (2005).

3.2.2 The Weighing Balance and the Magnetic Suspension Assembly

Figure 3.6 is a scaled, cross-sectional diagram with the cell attached to the weighing balance base plate through the thermostating tube. Dimensions in this figure adapted from Rubotherm (1999), Lösch and Wagner (1998) and Lösch (2005), are in mm. The weighing balance base plate is supported on four height-adjustable feet with threading and locking nuts. A bubble level indicator on the balance base plate ensures that the four feet and the balance base plate are horizontally level.

The weighing balance rests on a frame which in turn is attached to the balance base plate with knurled screws. These knurled screws can be loosened to move the balance frame so that the electromagnet suspension tube can be centered in the thermostating tube and retightened to prevent it from skewing during density measurements after initial centering. The space created by the balance frame between the balance and the balance base plate allows mechanical connection of the electromagnet suspension tube with the hook suspended from the balance pan as well as electrical connections for powering the electromagnet coil. This space is in an acrylic glass box that is split asymmetrically along a vertical axis into two parts so that the electromagnet suspension tube is not disturbed by air drafts that can cause the balance reading to become unstable. Both parts can slide on the balance base plate if the mechanical or electrical connections must be accessed. During initial adjustment of the vertical position of the electromagnet, both parts must slide from their normal positions that form an enclosure, whereas for lifting the electromagnet suspension tube gently through a small distance of about 2 to 3 mm, only the larger part needs to slide farther from its normal position. Figure 3.7 shows a scaled diagram adapted from Rubotherm (1999), Lösch and Wagner (1998) and Lösch (2005), for the relative positions of the weighing balance, the balance frame and the balance base plate.

A Mettler Toledo model AT 261 semi-micro analytical weighing balance is used as the force measuring device. Although the balance has a measuring range of

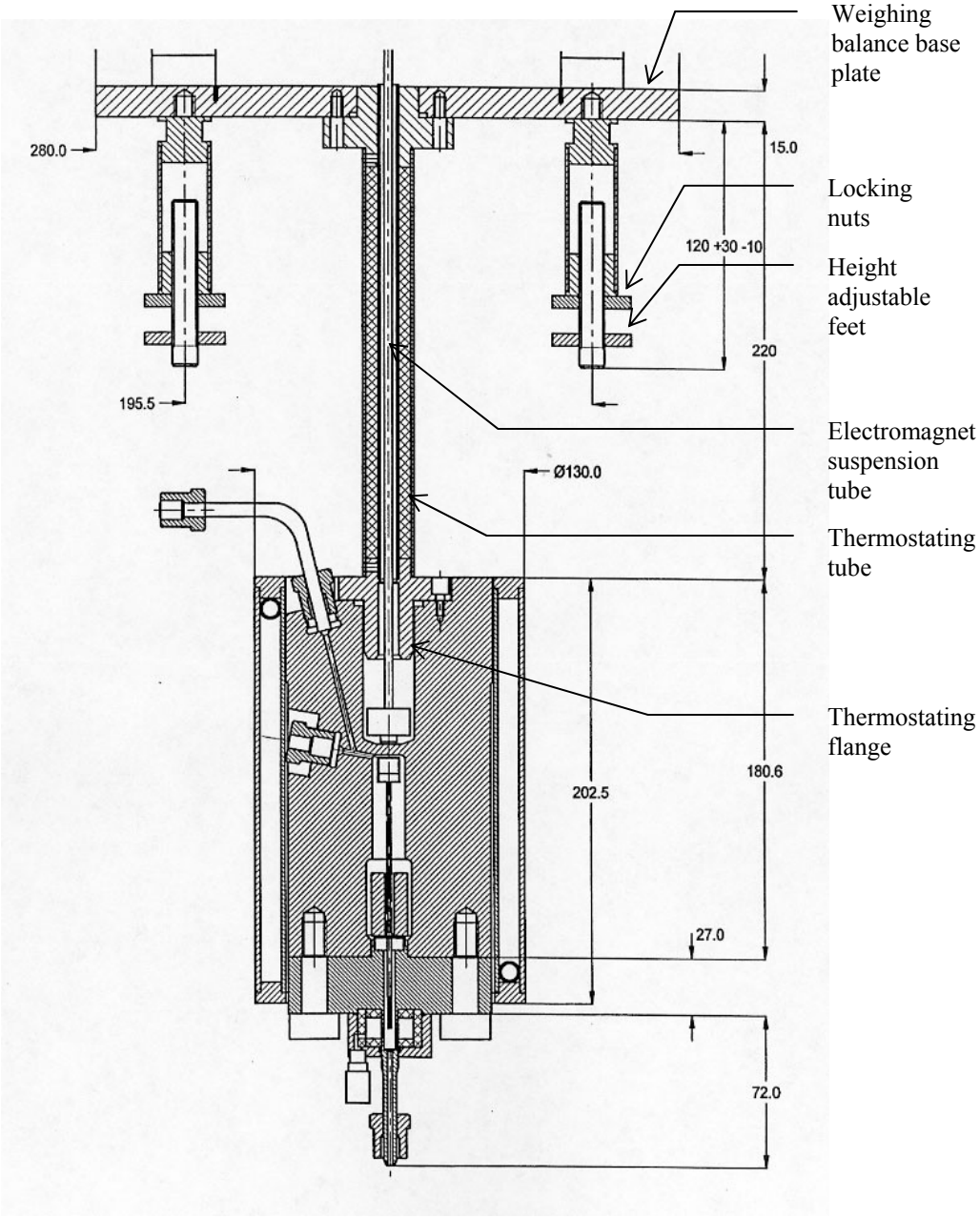

Figure 3.6. Attachment of the High Pressure Cell to the Weighing Balance Base Plate through the Thermostating Tube. Scaled figure adapted from Rubotherm (1999), Lösch and Wagner (1998) and Lösch (2005).

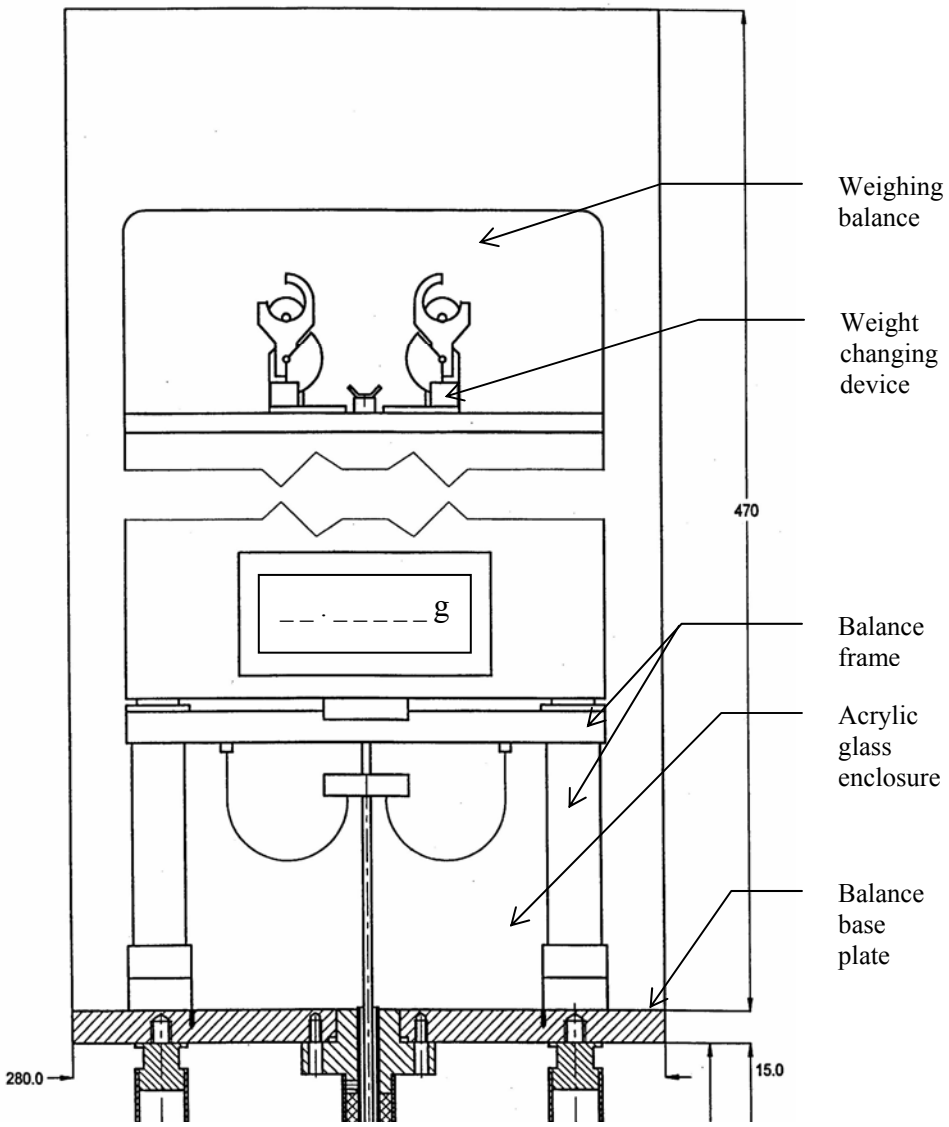

Figure 3.7. Attachment of the Weighing Balance to the Balance Base Plate through the Balance Frame. Scaled figure adapted from Rubotherm (1999), Lösch and Wagner (1998) and Lösch (2005).

200 g by itself, with the MSA attached under its pan the measuring load range is (10 to 30) g. In this finer range, the balance reading resolution is 0.01 mg and reproducibility is ±0.02 mg (Mettler Toledo, 1996). The weighing balance features can be accessed by computer commands through a RS-232 serial port of a personal computer (Mettler Toledo, 1990).

The balance stands on an aluminum plate 1.27 cm thick, 40 cm wide and 122 cm long [0.5 inch x 15.5 inch x 48 inch] with a 12.7 cm [5 inch] hole in the center for the thermostating tube. The aluminum plate is screwed along its length on top of two aluminum 'I' beams placed parallel to each other. The bottom surfaces of the 0.3175 cm [0.125 inch] thick and 10.5 cm [4.125 inch] tall 'I' beams are attached to two separate aluminum plates 40 cm long, 40 cm wide and 0.25 cm thick [15.5 inch x 15.5 inch x 0.25 inch] at each of their ends to form a rigid aluminum frame for the balance. The aluminum frame is supported on two towers with a 42.5 cm [16.75 inch] wide space between them formed by stacking six levels of cinder blocks with layers of carpet between every two levels to absorb vibrations. Figure 3.8 shows a schematic of the MSD support structure while Figure 3.9 shows the entire MSD apparatus that was supported on the support structure. The high pressure cell is suspended from the balance base plate by the thermostating tube into an aluminum bath with 51 cm [20 inch] depth, 23 cm [9 inch] outer diameter and 0.635 cm [0.25 inch] wall thickness. This cell bath is centrically suspended from the bottom surface around the 12.7 cm [5 inch] diameter opening in the half inch thick plate of the aluminum support frame. The heating/cooling liquid circulated into the bath causes thermostating of the cell. The heating/cooling liquid level was maintained at a distance of approximately 1 cm from the cell bath rim. The cell is immersed in the cell bath liquid such that the wetted depth along the thermostating tube between the cell top surface and the liquid surface is at least 5 cm [1.97 inch]. The cell and the thermostating tube can be lowered or raised into the cell bath with the help of the height adjustable feet of the balance base plate. An insulation layer is compressed between the rim of the cell bath and the bottom of the aluminum plate to prevent conduction of heat between them. The screws and washers used for fastening the two are

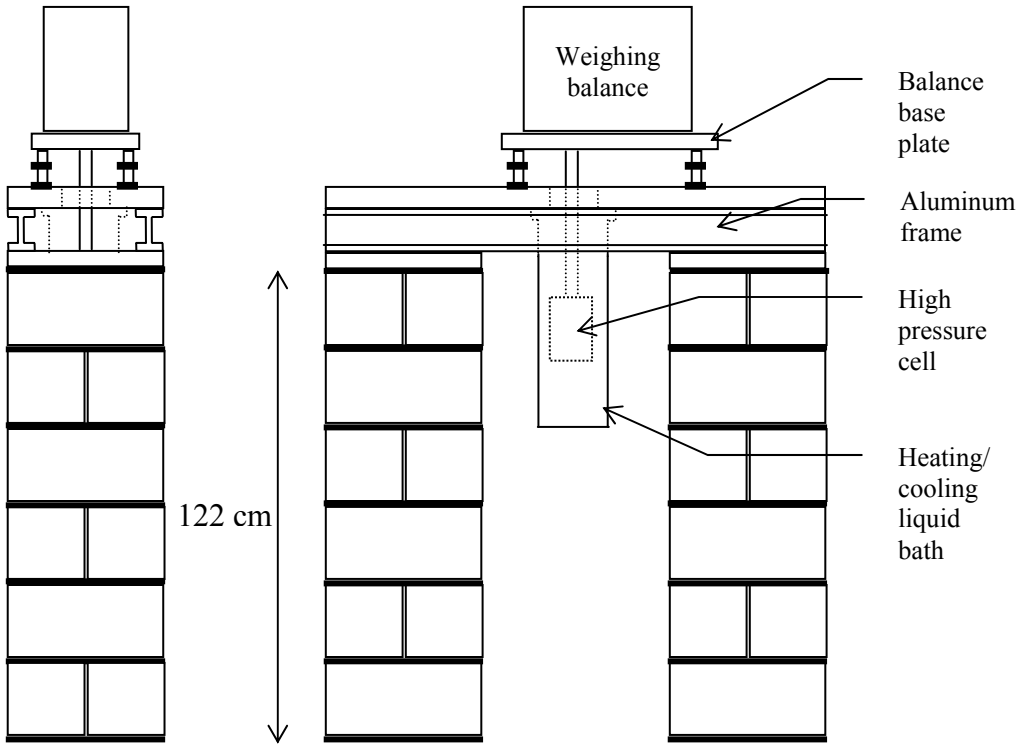

Figure 3.8. Magnetic Suspension Densitometer Support Structure

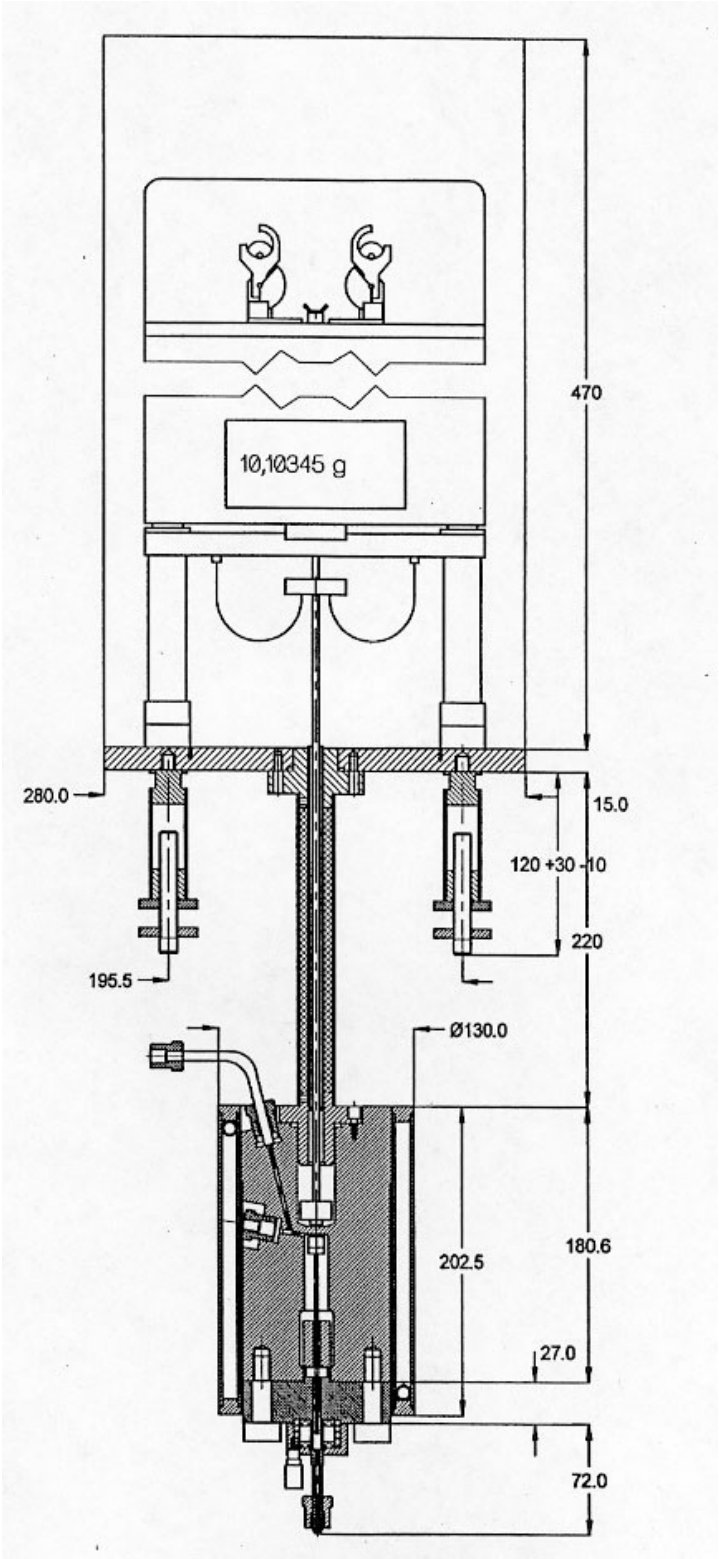

Figure 3.9. The Entire MSD Apparatus to be Supported on the Support Structure. Scaled figure adapted from Rubotherm (1999), Lösch and Wagner (1998) and Lösch (2005)

also sleeved with insulation for the same purpose. The 12.7 cm [5 inch] diameter hole in the aluminum support plate is covered with two semicircular pieces of styrofoam insulation around the thermostating tube to reduce temperature gradients between the cell bath liquid and ambient conditions. The length of the thermostating tube between the balance base plate and the cell is such that the weighing balance is thermally isolated from the temperature changes that the cell bath liquid could experience because of the presence of ambient conditions between the balance base plate and the aluminum support plate. Such isolation is important because the weighing balance calibration curve is sensitive to changes in temperature.

Auto-calibration during a density measurement and the ability to zero or tare the balance reading are two of the most notable features of the weighing balance. A weighing balance has an ideal characteristic curve between its display reading and the actual load that is a straight line over the range between zero and maximum load. However, the real characteristic curve deviates significantly from being linear because of external influences such as changes in ambient temperature, pressure, humidity, location and altitude of the balance that affects the force measured by the balance and the leveling of the balance (Mettler Toledo, 1988). The balance can perform a linearity check of its calibration automatically with the help of two 100 g reference calibration weights located internally within the balance. While this auto-calibration feature could be invoked by the balance itself when it sensed drastic changes in conditions, it was not used during density measurements. Instead, the linearity of the calibration was checked only once before every density measurement because: (a) the ambient conditions surrounding the apparatus were not expected to change drastically over the duration of a density measurement (b) there was no change in the acceleration due to gravity once the balance was installed at an approximate floor altitude of 43 m [142 feet] and (c) the balance leveling was not intentionally disturbed.

The balance works on the principle of electromagnetic force compensation where electrical energy is converted to mechanical energy to support the weight of a body on the balance pan. The strength of the permanent magnet of the

electromagnetic force compensation system of the balance is influenced by the temperature so that its magnetic field becomes weaker when the temperature increases. The error caused by a temperature change on the measurement result of the balance is specified with the temperature coefficient of sensitivity that is only 0.0001% per ^{o}C. Even if this low sensitivity to temperature could have been nullified by auto-calibrating the balance whenever the liquid bath temperature was changed, the length of the thermostating tube designed by Rubotherm may have been influenced by the need to separate the electromagnetic force compensation system of the weighing balance from the MSA used for density measurements.

While installing the apparatus, the electromagnet suspension tube must be inserted from the bottom of the thermostating tube and raised through it until its threaded end appears in the acrylic glass box. The high pressure cell along with its internal MSA parts is attached to the thermostating flange after this step. The internally threaded end of the electromagnet suspension tube engages with a screw at the bottom of an electromagnet connection assembly that is suspended from the bottom of the balance pan. The vertical separation of the electromagnet from the electromagnet well bottom, and hence also from the permanent magnet, is adjusted by mechanically screwing the electromagnet connection assembly into the electromagnet suspension tube. A locking nut on the screw of the electromagnet connection assembly prevents change in the vertical height of the electromagnet from the electromagnet well bottom during measurements. It is important that this vertical height be the same during measurement of the sinker weight in vacuum and under pressure in the presence of a fluid. If the apparatus assembly is left physically undisturbed, this vertical height of the electromagnet need not be readjusted after initial adjustment during installation of the apparatus. The electromagnet connection assembly also has two vertically held acrylic glass plates with two sockets embedded in each for electrical connections. The plate closer to the weighing balance connects the freely suspended, semicircular electromagnet wires from the balance frame to the electromagnet connection assembly. The plate closer to the balance base plate connects the electromagnet coil leads emerging

out of the electromagnet suspension tube to the electromagnet connection assembly. Insulated wires connect the sockets between the two plates, and the semicircular, 0.1 mm diameter electromagnet wires are made of silver. The electrical lugs engaging with the sockets in the plate closer to the balance base plate must be unplugged to enable free rotation of the electromagnet suspension tube on the screw of the electromagnet connection assembly for adjustment of the vertical height of the electromagnet.

3.2.3 The Magnetic Suspension Control and Operation of the Magnetic Suspension Assembly

Rubotherm (1999) provides a detailed description of the magnetic suspension control box connectors, switches and signal selection knob while Lösch (1987) has traced the evolution of the magnetic suspension control mechanism to its present state. The permanent magnet is brought to a state of levitation by a fast loop PID controller after its absolute position is detected by the position sensor. Soft upward or downward movements of the permanent magnet are achieved by means of a superimposed set-point controller and an additional control system (Klimeck *et al.*, 1998; Wagner *et al.* 1995). The vertical height of the electromagnet initially is adjusted with the threaded screw and locking nut on the electromagnet connection assembly to a position between 0.5 and 3 turns from the electromagnet well bottom while the cell is at ambient conditions. If the power to the MSA control box as well as the suspension control (SC) are switched ‘on’, the subsequent balance reading tared and the SC switched ‘off’, the balance reading is between (-5.6 and -7.0) g. This balance reading at ambient conditions called the ‘reference balance reading’ indicates an appropriate relative separation between the electromagnet and the permanent magnet and is used as a diagnostic tool before density measurements. After checking the reference balance reading at ambient conditions, the cell is evacuated to measure the true mass of the sinker at a T followed by pressurization of the cell to measure the apparent mass of the sinker at the same T in the presence of the gas whose density is to be measured.

Figure 3.10 shows the sequence of steps for the MSA operation when the cell is under vacuum. Figure 3.10 (a) shows the step where the MSA control box power is ‘on’ but the SC is ‘off’. Both the permanent magnet piece and the sinker are in their respective rest positions and the balance shows a reading close to the balance reference reading. The next step shown in Figure 3.10 (b) has the MSA control box as well as the SC ‘on’. The permanent magnet piece is lifted from its rest position by a small distance but the sinker continues to rest. The balance reading is expected to be close to 0 g but any weight that is indicated by the balance because of the reduction in the buoyant force acting on the permanent magnet piece when the cell is evacuated from ambient conditions after checking the balance reference reading is tared during this step. This is the zero point (ZP) position of the MSA. Figure 3.10 (c) shows the step attained by having the MSA control box and the SC ‘on’ and switching from the ZP position to the measuring point (MP) position. The permanent magnet piece is further lifted from its ZP position until it engages the inner diameter of the sinker which also lifts from its rest position as a result. Both the permanent magnet piece and the sinker are in a state of levitation during this step. However, because of the taring of the weight of the permanent magnet in the previous step, the balance reading gives the true weight of the sinker only. Switching from MP position to ZP position lowers the sinker to its rest position while the permanent magnet piece continues to be in levitation. This is essentially step (b) revisited. Switching the SC ‘off’ lowers the permanent magnet piece to its rest position, which is step (a) revisited. Several ZP and MP positions can be achieved at regular intervals of time to get an average value for the true mass of the sinker in vacuum in a discontinuous mode. However, in the continuous mode that was used for measurements as part of the present work, the sinker was held in the MP position continuously several times over 30 to 40 minute long periods with brief ZP position revisits of a minute to keep track of the drift in the balance zero reading. Averages of the stable balance readings over one such 30 to 40 minute interval during which the cell temperature had equilibrated were taken for the true mass of the sinker in vacuum.

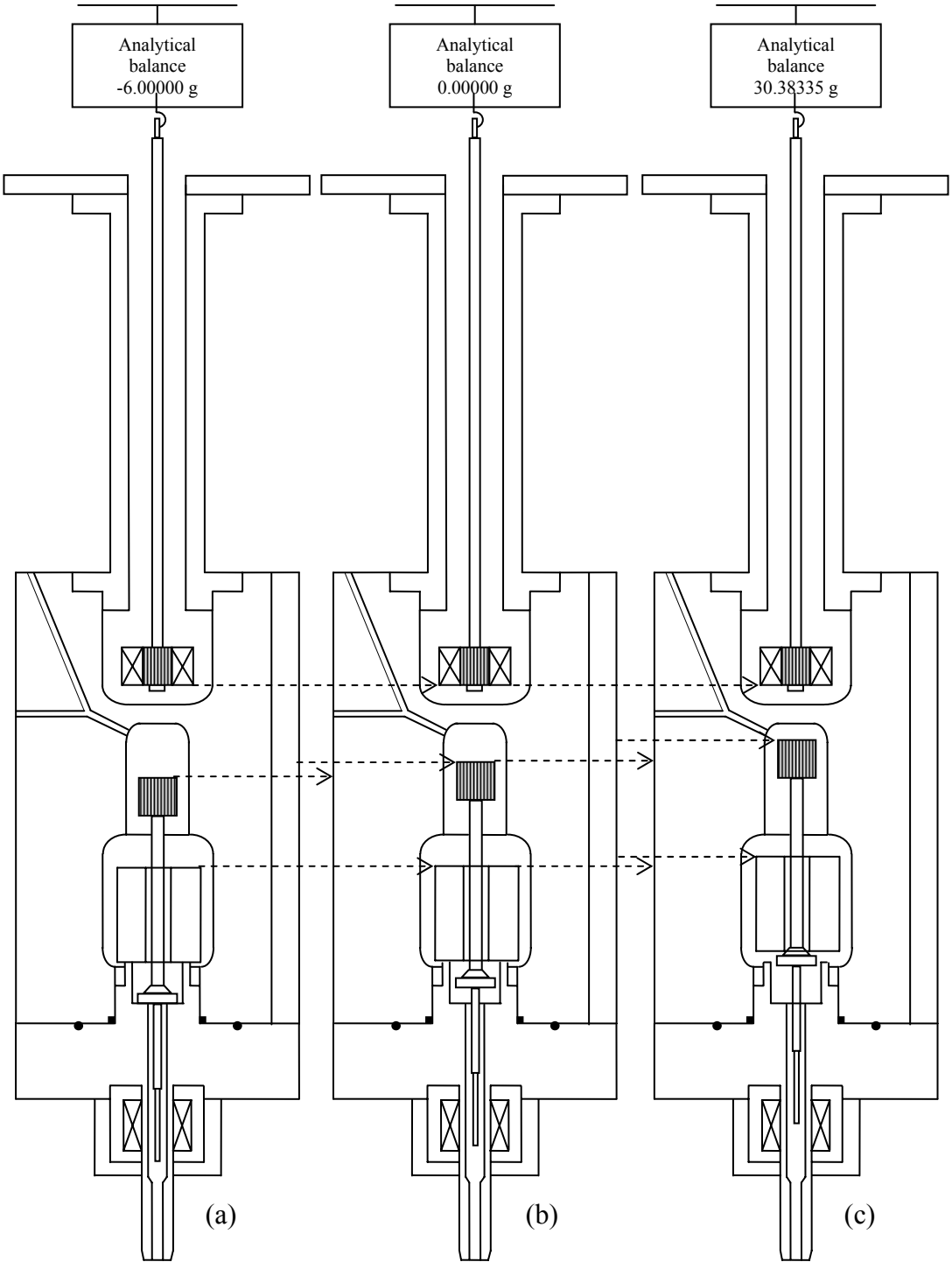

Figure 3.10. Operation of the MSA in Vacuum
(a) Suspension Control ‘off’
(b) Suspension Control ‘on’; Zero Point Position
(c) Suspension Control ‘on’; Measurement Point Position

Figure 3.11 shows a similar sequence of steps for the MSA operation when pressurized with the gas whose density is to be measured. Figure 3.11 (a) shows the equivalent of the step shown in Figure 3.10 (a). The balance readings are different but insignificant because both the permanent magnet and the sinker are in rest positions. Figure 3.11 (b) which is the equivalent of Figure 3.10 (b) shows the ZP position where only the permanent magnet piece is lifted from its rest position. Before taring the balance in the ZP position the balance readings in step (b) in vacuum and in the presence of gas are different because of the extra buoyant force experienced by the permanent magnet in the presence of gas. Upon taring the balance, this buoyant force difference is nullified. The extent to which the permanent magnet is lifted from its rest position is slightly larger in Figure 3.11 (b) than in Figure 3.10 (b). Figure 3.11 (c) which is the equivalent of Figure 3.10 (c) shows the MP position where the permanent magnet is raised from its ZP position so that it engages with the sinker and lifts it up too. The balance reads the apparent mass of the sinker in the presence of gas at the same temperature of the cell as during the true mass of the sinker in vacuum. The balance reading in Figure 3.11 (c) is different from that in Figure 3.10 (c) because of the upwardly acting buoyant force on the sinker. An average balance reading for the apparent mass of the sinker over a period of 30 to 40 minutes is taken in the continuous mode for density measurements.

The position sensor and the controller action are such that the attractive or repulsive electromagnetic force generated by the magnitude and direction of the current through the electromagnet coil powers the raising or lowering of the permanent magnet piece to achieve the ZP position and of the permanent magnet piece and the sinker to achieve the MP position in either vacuum or in the presence of gas. The electromagnetic force thus counters the force of gravity acting on the sinker or the weight of the sinker while raising it, but is aided by the buoyant force acting on the sinker in the presence of gas. The power requirement and hence the size of the electromagnet coil is reduced by winding the electromagnet coil on a magnetic core. Once the permanent magnet or the sinker is raised to a state of levitation the current flowing through the electromagnet coil is small enough to maintain the state of levitation and is near zero. If the stable position

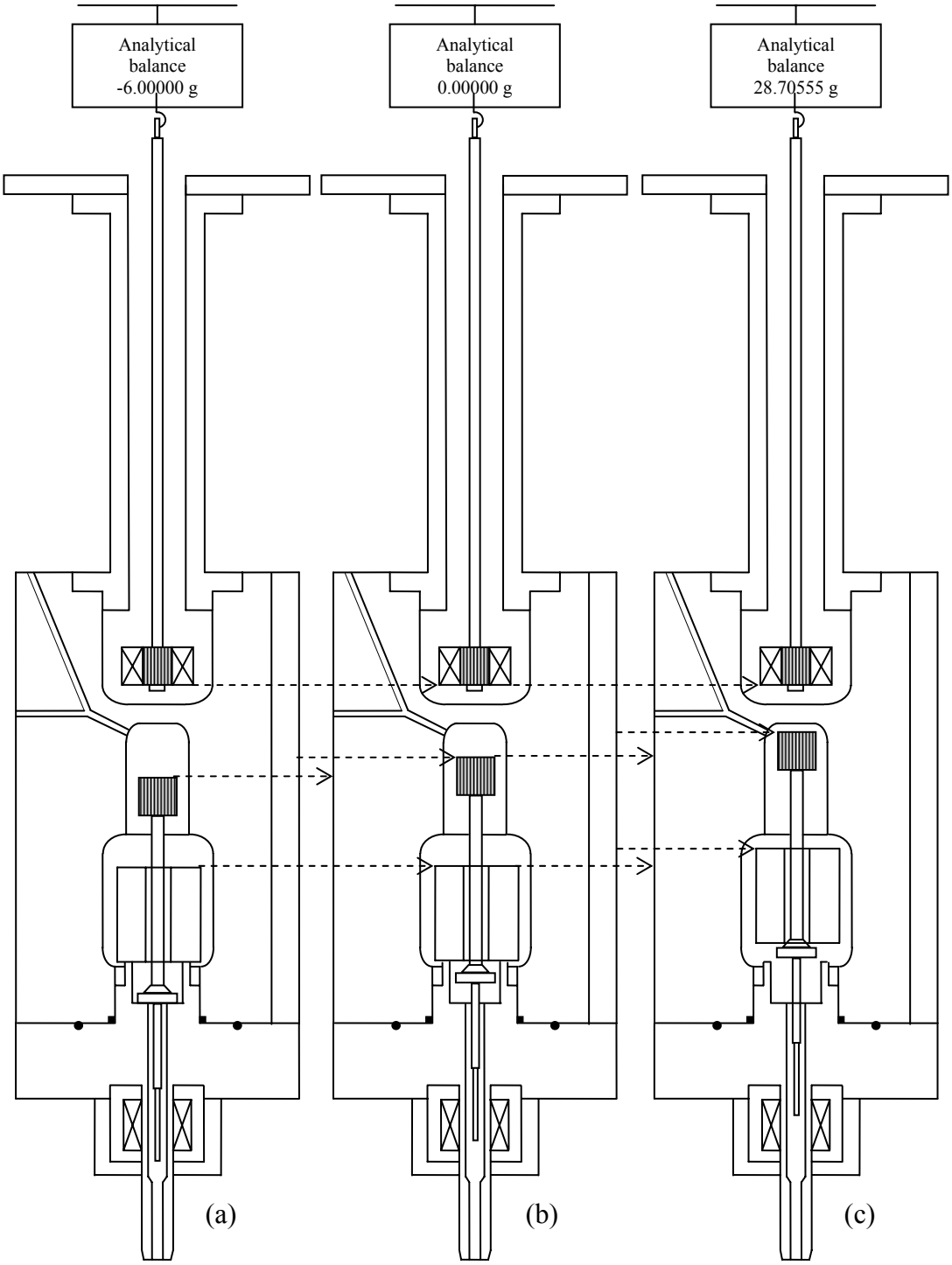

Figure 3.11. Operation of the MSA in Presence of Fluid under Pressure
(a) Suspension Control 'off'
(b) Suspension Control 'on'; Zero Point Position
(c) Suspension Control 'on'; Measurement Point Position

of the sinker in levitation is disturbed slightly, the position sensor detects such a disturbance and the controller sends current to the electromagnet coil to generate a high frequency motion of the permanent magnet so that it regains its stable levitation position. If however, the stable levitation position of the sinker experiences a large disturbance, the controller cannot send a large enough current to the electromagnet to counter the disturbance and regain the stable levitation position of the sinker, and the MSA goes out of control. In such a case the MSA control box has a safety provision that prevents overload of the electromagnet coil without blowout of the control box fuse. Examples of such large disturbances are a violent vibration of the MSA support structure, an external stray magnetic material or an electromagnetic force generating device such as a transformer that is brought too close to the MSA when the SC is 'on'. In the presence of such pre-existing, large, external disturbances, the MSA control is not able to raise the sinker.

3.2.4 The Weight Changing Device

Figure 3.12 shows the ideal and real calibration curves for a weighing balance with a range of 100 g. For the ideal straight line calibration the balance display reading is exactly the same as the actual load placed on the balance pan. For example, the sinker mass of approximately 30 g would be displayed by a balance with a linear calibration as 30 g as indicated by point A. However, a balance with a real calibration curve that deviates from linearity, the same 30 g sinker would be weighed with an error as indicated by point B. The magnitude of the error between the balance display readings increases as the actual load measured by the balance shifts away from zero. During density measurement, the ZP position is measured as a zero balance reading because the balance is tared to nullify the mass of the permanent magnet piece. However, the MP position is measured as a balance display reading of approximately 30 g which is the mass of the sinker in levitation. If the linearity of the calibration curve of the balance is not ensured by auto-calibrating the balance before a density measurement, the error in

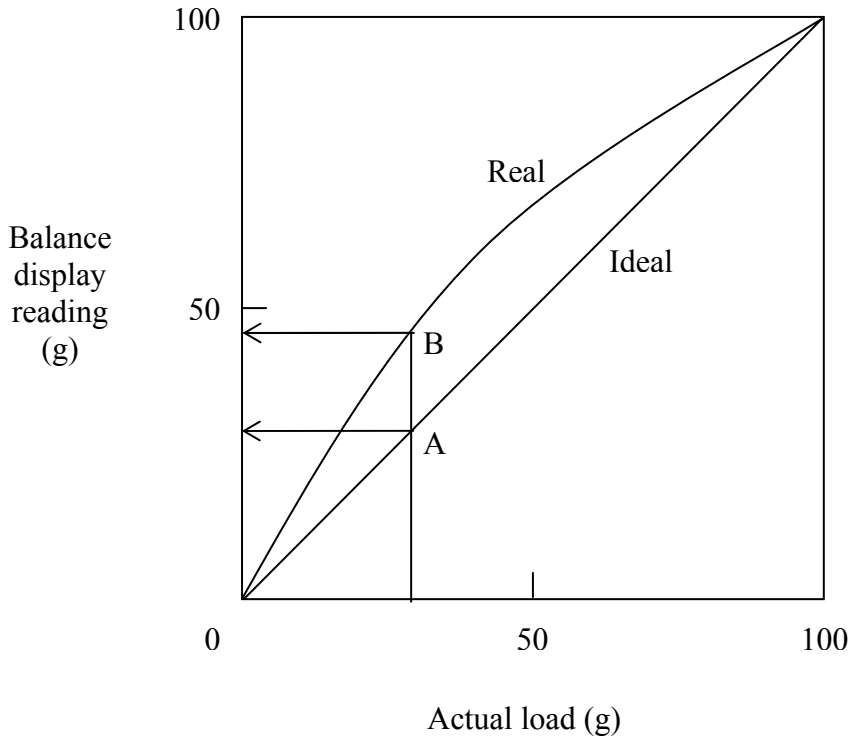

Figure 3.12. Ideal and Real Calibration Curves for the Weighing Balance and Need for the Weight Changing Device

the balance display readings between points A and B for the sinker mass leads to an inaccurate density measurement. Moreover, this error between points A and B for sinker mass measurement in vacuum may not be the same as the error under pressure causing a random error in density measurement. The solution to minimize the error in sinker mass in MP position caused by non-linearity of the balance calibration curve is to measure the MP position as closely as possible to a balance display reading of zero. This improves the accuracy of density measurements even at low densities and is achieved by using the basic load compensation device. This device consists of a titanium (Ti) weight and a tantalum (Ta) weight weighing approximately 10 g and 40 g respectively that can each be raised from or lowered upon the balance pan from the top with motors. The Ti sinker weighs approximately 30 g. The 16.7 g/cm^3 density of tantalum is approximately four times the 4.5 g/cm^3 density of titanium. This allows the balance reading of the sum of the titanium weight and the titanium sinker in the MP position as well as the balance reading of the tantalum weight in the ZP position to be close to zero. Figures 3.13 and 3.14 show the equivalent of Figures 3.10 and 3.11 respectively for the operation of the MSA using the weight changing device. After initial installation of the MSA, when the SC is switched 'on' with the cell at ambient conditions, only the permanent magnet is raised. Upon lowering the Ta weight on the balance pan, the balance display reading shows the weight of the Ta weight and the permanent magnet. If this weight is tared and the SC switched 'off', the balance display reading shows the 'balance reference reading' while using the weight changing device. Figure 3.13 (a) shows the step where the cell is under vacuum, the SC is 'off' and neither the Ta nor the Ti weight is lowered on the balance pan. Figure 3.13 (b) shows the step for the ZP position where the SC is switched 'on' so that only the permanent magnet is raised from its rest position and the Ta weight is lowered on the balance pan. The balance display reading should be close to zero and should be tared if it is not. Figure 3.13 (c) shows the MP position where the sinker is also raised from its rest position by the permanent magnet, the Ta weight is raised and the Ti weight is lowered on the balance pan. Figures 3.14 (a), (b) and (c) show the same sequence of steps in the presence of gas. As an example, the difference in the ZP and the

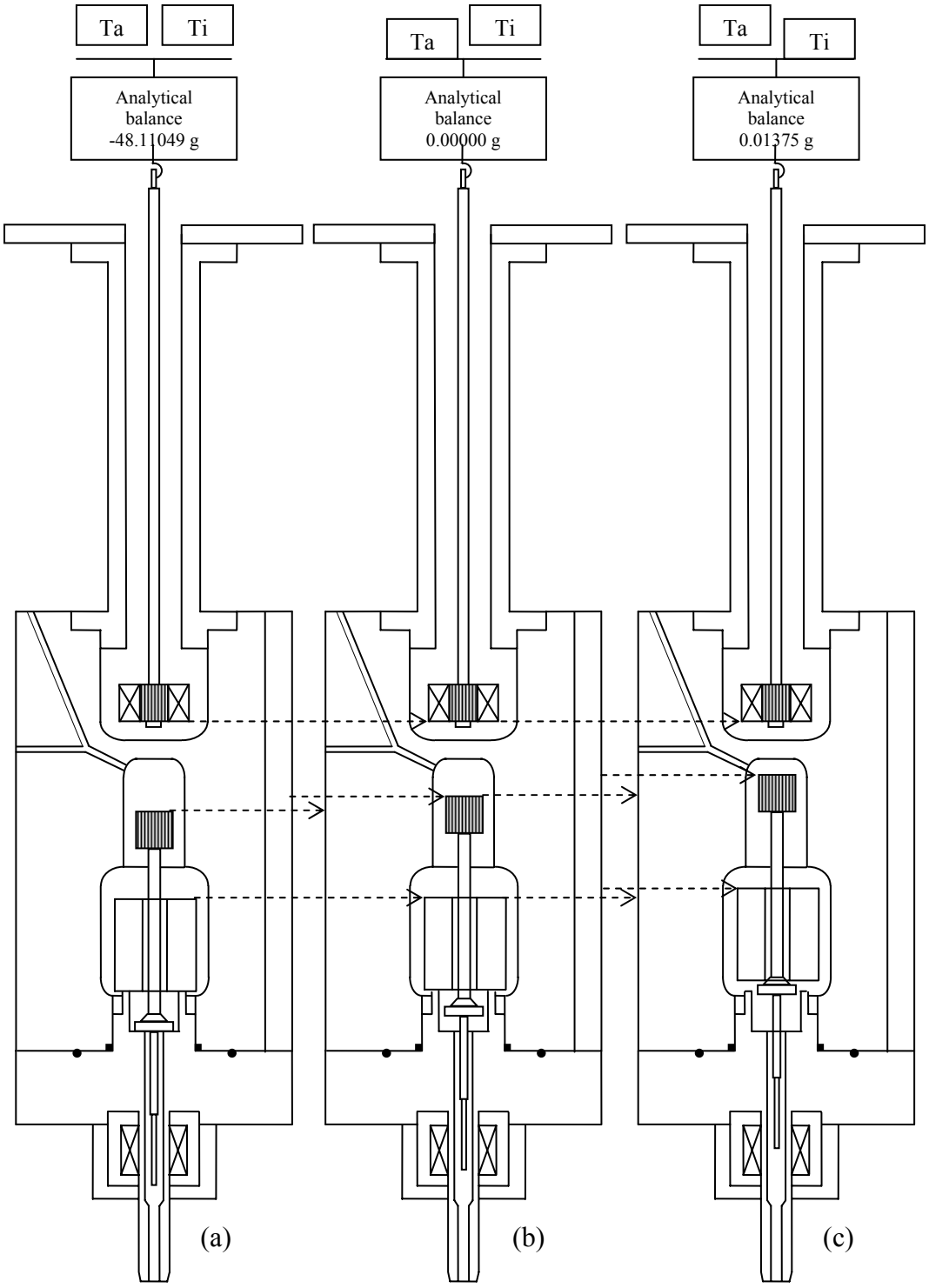

Figure 3.13. Operation of the MSA in Vacuum Using Weight Changing Device
(a) SC 'off', Ti and Ta both raised
(b) SC 'on'; ZP Position, Ta lowered, Ti raised
(c) SC 'on'; MP Position, Ta raised, Ti lowered

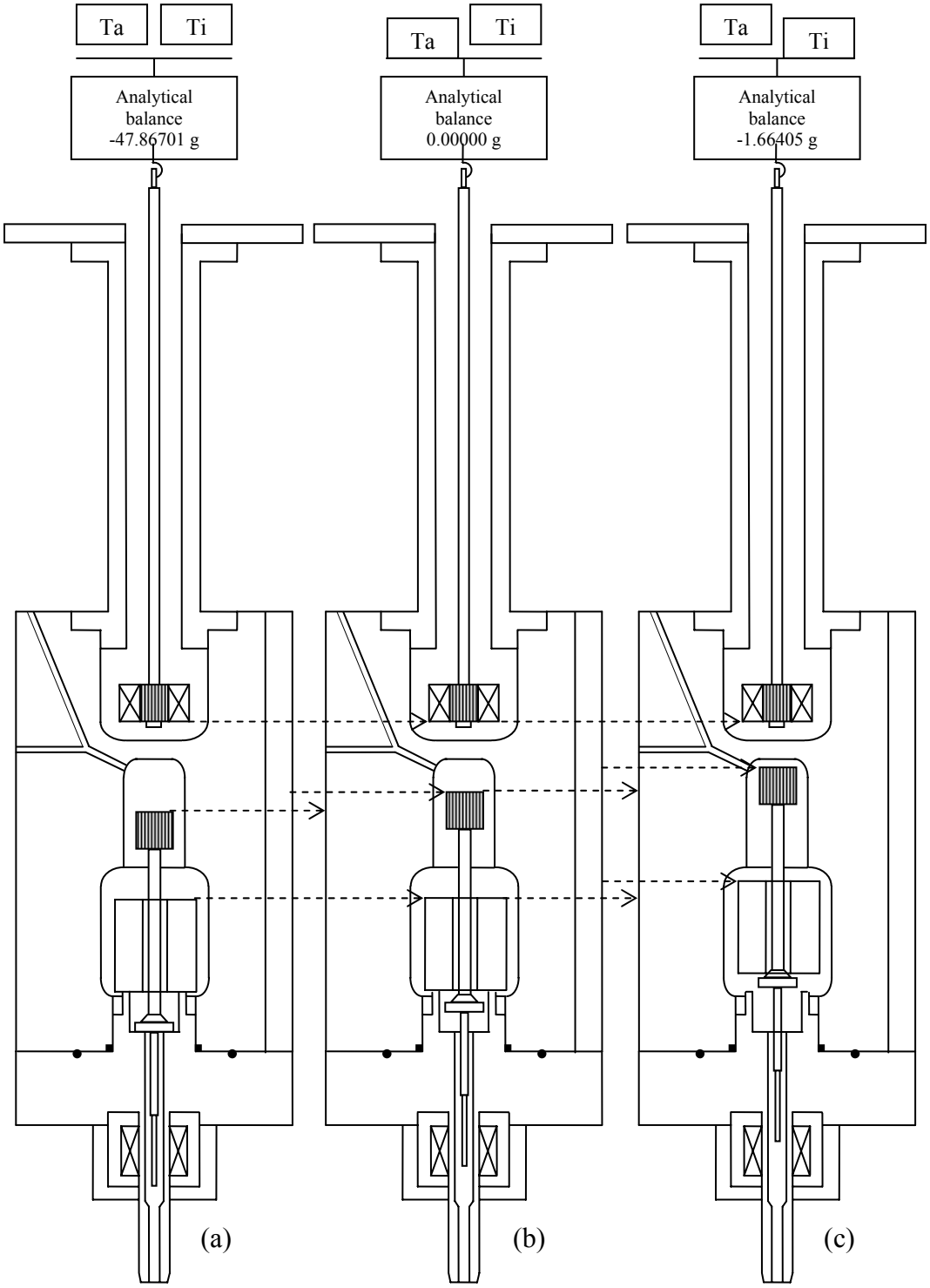

Figure 3.14. Operation of the MSA under Pressure Using Weight Changing Device
(a) SC 'off', Ti and Ta both raised
(b) SC 'on'; ZP Position, Ta lowered, Ti raised
(c) SC 'on'; MP Position, Ta raised, Ti lowered

MP position balance display readings for the sinker weight without using the weight changing device as shown in Figures 3.10 (c) and 3.11 (c) is (30.38335 - 28.70555) g = 1.67780 g. The same difference using the weight changing device as shown in Figures 3.13 (c) and 3.14 (c) is (0.01375-{-1.66405}) g = 1.67780 g. Thus, the same buoyant force difference between vacuum and pressure conditions is measured by weighing the sinker weight to values closer to zero. The Ta and Ti weights have the same volume so that the same buoyancy force from air acts on both and is compensated.

3.2.5 Temperature and Pressure Dependence of the Sinker Volume

The sinker volume appearing in equation (8) undergoes a change because of distortion of the sinker material at a temperature and pressure (T, P) other than the reference temperature and pressure (T_o, P_o) at which the reference sinker volume, v_{So}, is measured and can be determined using (Rubotherm, 1999):

$$v_S(T,P) = v_{So}(T_o,P_o) + v_{So}(T_o,P_o)\left[3\frac{\Delta L}{L_o}(T) - 3\frac{(P-P_o)}{E(T)}\{1-2\upsilon(T)\}\right] \qquad (9)$$

where, $\Delta L/L_o$ is the thermal expansion, E is the Young's modulus and υ is the Poisson's ratio of the sinker material at a temperature T. The thermal expansion was calculated using:

$$\frac{\Delta L}{L_o}(T) = \alpha(T - T_o) \qquad (10)$$

where, α is the thermal coefficient of expansion of the sinker material. For titanium, α is 8.8 x 10^{-6} K^{-1} as measured by Rubotherm in the range (193.15 to 533.15) K [(-112 to 500) ^oF, (-80 to 260) ^oC]. The reference sinker volumes for the two titanium sinkers used during the present project were measured by Rubotherm at 293.15 K [68 ^oF, 20 ^oC] and

0.1 MPa [14.504 psia, 1 bar] and are provided in Chapter IV. Table 3.1 shows the three material properties in the range (263.15 to 523.15) K [(14 to 482) ^{o}F, (-10 to 250) ^{o}C] for titanium.

3.3 Description of Ancillary Equipment

The ancillary equipment include a cylinder storage hot box, feed charging and discharging manifolds, pressure and temperature measurement systems, a compressor, a vacuum system, a heating/cooling liquid constant temperature circulation bath and a personal computer for data acquisition and control. In addition, a differential pressure indicator (DPI) and a dead weight gauge (DWG) are used for pressure transducer calibrations and a triple point of water (TPW) cell is used to check the calibration of the PRT.

In its original location, the MSD and the ancillary equipment were surrounded by walls on three sides and could be accessed only from the fourth side of the space approximately 2.6 m [8.5 feet] long and 1.83 m [6 feet] wide. However, in this location the MSA was separated from the nearest wall by a distance of 53 cm, from the nearest side of the constant temperature circulation bath by a distance of 68 cm and from the floor by a distance of 86 cm. Figure 3.15 (a) shows the relative position of the MSD with respect to the ancillary equipment in its original location. The steel struts in the wall, the constant temperature bath enclosure and the steel reinforcement in the concrete floor, which were all magnetic materials, interfered with the smooth operation of the MSA. Tests to simulate the presence of these stray magnetic sources were done and are presented in subsection 3.4.1. It was found that any stray magnet within an imaginary sphere of 1 m diameter around the MSA adversely affected the MSA operation. The adverse effect manifested itself as an unstable balance reading, a constant offset from the true balance reading, inability to raise the sinker or loss of control of the MSA. For this reason, the MSD was moved to a new location in May 2002, where it was separated from any stray magnetic effect by a distance of at least 1 m. The height of the two cinder

Table 3.1. Temperature Dependence of Thermal Expansion, Young's Modulus and Poisson's Ratio for Titanium

T	$\Delta L/L_o$	E	υ
K		GPa	
263.15	-0.000264	116.000	0.302
270.00	**-0.000204**	**115.486**	**0.303**
273.15	-0.000176	115.250	0.304
280.00	**-0.000116**	**114.736**	**0.305**
283.15	-0.000088	114.500	0.306
290.00	**-0.000028**	**114.158**	**0.308**
293.15	**0.000000**	**114.000**	**0.309**
303.15	0.000088	113.500	0.312
305.00	**0.000104**	**113.361**	**0.312**
313.15	0.000176	112.750	0.314
320.00	**0.000236**	**112.236**	**0.315**
323.15	0.000264	112.000	0.316
333.15	0.000352	111.250	0.317
340.00	**0.000412**	**110.736**	**0.318**
343.15	0.000440	110.500	0.318
353.15	0.000528	109.500	0.320
363.15	0.000616	108.500	0.322
373.15	0.000704	107.750	0.323
383.15	0.000792	107.000	0.324
393.15	0.000880	106.250	0.325
403.15	0.000968	105.500	0.326
413.15	0.001056	104.750	0.327
423.15	0.001144	104.000	0.328
433.15	0.001232	103.250	0.329
443.15	0.001320	102.500	0.329
453.15	0.001408	102.000	0.330
463.15	0.001496	101.500	0.330
473.15	0.001584	101.000	0.331
483.15	0.001672	100.500	0.331
493.15	0.001760	100.000	0.332
503.15	0.001848	99.500	0.333
513.15	0.001936	98.750	0.334
523.15	0.002024	98.000	0.335

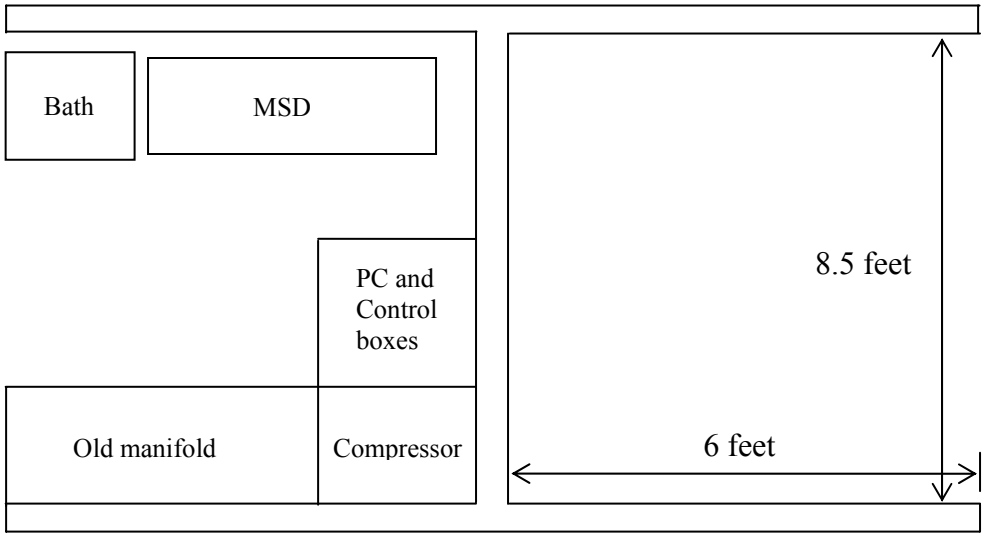

(a) Old location

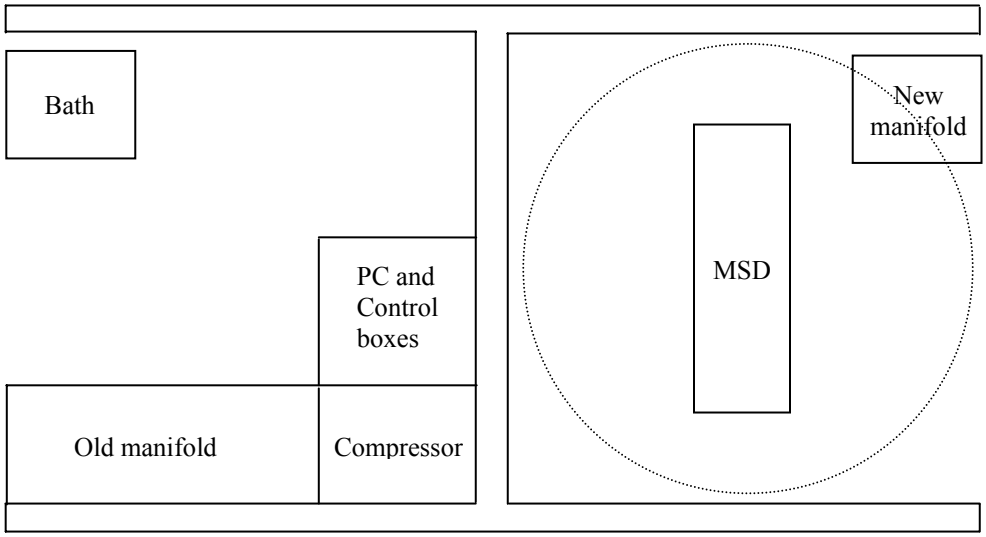

(b) New location

Figure 3.15. Old and New Locations of the MSD and Relative Positions of the Old and New Feed Manifolds

block supporting towers was increased by one more level and also centered in a neighboring space of the same dimensions as the original space. A new manifold was constructed later in January 2003 in an effort to increase the accuracy of density measurements. Although, the new manifold slightly overlaps the 1 m isolation sphere of the MSD, care was taken to ensure that neither the new manifold structure nor its fittings were magnetic. Figure 3.15 (b) shows the new location of the MSD along with the relative positions of the ancillary equipment.

3.3.1 Feed Manifolds

Densities of pure argon, methane and nitrogen were measured to determine the sign and magnitude of any systematic bias error associated with the apparatus before measuring densities of natural gas samples M94C1 and M91C1. Such pure component density measurements between natural gas sample density measurements were necessary as a test of repeatability of the apparatus for internal consistency. Table 3.2 lists the 26 isotherms for pure component and natural gas sample density measurements in a chronological order over the period between March 2003 and February 2004. Several modifications were made to the experimental setup before as well as during this period to ascertain repeatability and increase the accuracy of density measurements. Not all the isotherms were measured with the same feed manifold. Table 3.2 also lists the state of the experimental setup during each isotherm measurement. The isotherm nomenclature has been described in Chapter V.

Figure 3.16 is a schematic flow diagram of the old feed manifold with the MSD in its old location. The old manifold consists of high pressure, stainless steel 316 tubing, ‘Tee’ and ‘Cross’ fittings, needle valves and safety heads capable of withstanding 413.686 MPa [60,000 psia] supplied by the High Pressure Equipment (HIP) Company. Safety rupture discs with pressure limits of 206.843 MPa [30,000 psia] and 41.369 MPa [6,000 psia] were used to protect the pressure transducers PT30K and PT06K from damage by over-pressurization. High pressure coned-and-threaded joints

Table 3.2. State of the Experimental Setup during Isotherm Measurements

Isotherm No.	Isotherm identity	Figure number for manifold	Average internal temperature of pressure transducer over duration of isotherm (K)			Approximate temperature of manifold (K)		Approximate temperature of sample cylinder (K)	Approximate temperature of tubing (K) between:					
			2,000 psia	6,000 psia	30,000 psia	Old	New		Sample cylinder and T1	V5 and MSD cell	MSD cell and VI1	MSD cell and PT06K	MSD cell and T11	(T12 and PT06K) and (T13 and PT02K)
1	Ar 1 270K 03192003			295.084										
2	Ar 1 340K 03252003			295.629										
3	Ar 1 270K 03262003			294.839										
4	CH4 1 270K 03292003			294.103										
5	CH4 1 340K 03312003			294.751										
6	CH4 2 270K 04042003	3.16 (b)	NU	295.195	NU	A	A	A	A	A	A	A	NA	NA
7	CH4 3 270K 04082003			294.096										
8	CH4 3 340K 04162003			297.164										
9	Ar 1 340K 04182003			295.463										
10	Ar 2 340K 04222003			294.476										
11	N2 1 340K 04252003			295.048										
12	N2 1 270K 04272003			294.760										
13	M94C1 340K 05212003			304.344										
14	M94C1 305K 05252003			304.289										
15	M94C1 270K 05292003	3.16 (b)	NU	305.194	NU	331.15	A	333.15	373.15	348.15	348.15	348.15	NA	NA
16	M94C1 320K 06022003			305.142										
17	M94C1 280K 06062003			304.763										
18	M94C1 290K 06112003			304.603										
19	N2 1 340K 08182003	3.16 (c)	NU	323.353	NU	323.15	323.15	A	A	348.15	348.15	348.15	NA	NA
20	N2 1 270K 08272003			323.350										
21	N2 2 340K 12212003	3.16 (d)	339.290	325.334	NU	315.15	332.15	A	A	348.15	348.15	NA	332.15	332.15
22	N2 2 270K 12282003		339.280	325.359										
23	M91C1 340K 01202004		339.288	325.332										
24	M91C1 305K 01282004	3.16 (d)	339.281	325.350	NU	315.15	332.15	333.15	A	348.15	348.15	NA	332.15	332.15
25	M91C1 290K 02032004		339.293	325.375										
26	M91C1 270K 02102004		339.290	325.379										

A: Average ambient temperature = 295.15 K [22 ^{o}C]; NA: Not applicable; NU: Not used

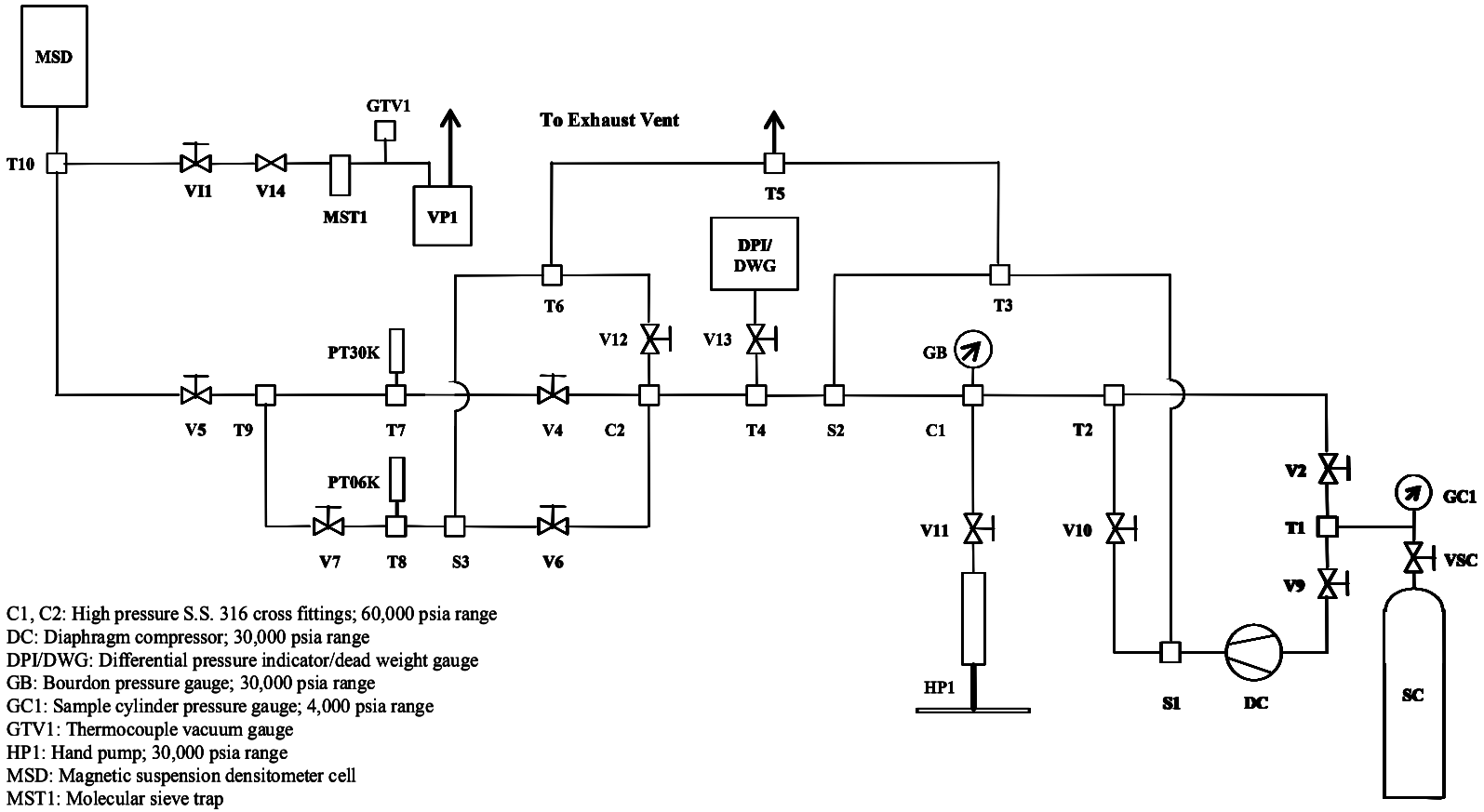

C1, C2: High pressure S.S. 316 cross fittings; 60,000 psia range
DC: Diaphragm compressor; 30,000 psia range
DPI/DWG: Differential pressure indicator/dead weight gauge
GB: Bourdon pressure gauge; 30,000 psia range
GC1: Sample cylinder pressure gauge; 4,000 psia range
GTV1: Thermocouple vacuum gauge
HP1: Hand pump; 30,000 psia range
MSD: Magnetic suspension densitometer cell
MST1: Molecular sieve trap
PT06K, PT30K: Pressure transducers; 6,000 and 30,000 psia range
S1, S2 and S3: Safety rupture disc heads with 40,000 psia, 30,000 psia and 6,000 psia range respectively
SC: Gas sample cylinder
T1 – T10: High pressure S.S. 316 tee fittings; 60,000 psia range
V14: Brass block valve for rough vacuum
VI1, V2, V4 – V7, V9 – V13: High pressure S.S. 316 needle valves; 60,000 psia range
VP1: Mechanical vacuum pump
VSC: Sample cylinder valve; CGA 580 for argon and nitrogen, CGA 350 for methane and natural gas samples

Figure 3.16. Schematic Flow Diagram of the Old Manifold with the MSD in the Old Location

were prepared in-house for metal-to-metal, leak proof seals between the 0.3175 cm [0.125 inch] outer diameter x 0.0508 cm [0.02 inch] inner diameter tubing and the other fittings. The small inner and outer diameters for the tubing were deliberately chosen to keep the volume of the sample in the manifold minimum without compromising on the ease of machinability. The smaller volume not only allowed faster equilibration of the temperature and pressure but also minimized the surface area available for adsorption of the heavier components of the natural gas mixture samples and made the manifold safer to work with even in the case of an accidental leak. A piston screw hand pump with a pressure rating of 206.843 MPa [30,000 psia] and capacity per stroke of 11 cm^3 was also provided as a receptacle of the gas sample between the sample cylinder and the MSD cell for fine adjustments of the pressure. A Bourdon gauge with a range of 206.843 MPa [30,000 psia] was used for crude adjustment of the pressure in the feed manifold using the diaphragm compressor. The section of the feed manifold between T1 and V5 was mounted on an aluminum panel and could be enclosed as a box with a half inch thick polycarbonate sheet on one side. The diaphragm compressor was placed within this feed manifold box. The section between V5 and the MSD cell was outside the feed manifold box. The sample inlet/outlet port at the top of the MSD cell was plugged, while the port at the bottom of the cell was used for feeding as well as discharging the cell.

After moving the MSD to its new location a test of the range of operation of the MSA was done with the experimental setup similar to that shown in Figure 3.16. Results of this test appear in subsection 3.4.2. After the range test, PT06K was moved to the new manifold and connected to the sample charge/discharge port at the top of the cell as shown in Figure 3.17 with a tubing approximately 1 m long. The distance between PT06K and the MSD cell as shown in Figure 3.16 was more than 6.7 m [22 feet] because of which the pressure indicated by PT06K was not the true cell pressure. Isotherms 1 through 12 for pure components were performed with the experimental setup as shown in Figure 3.17.

However, during density measurement of sample M94C1 with a CT of 303.882 K [87.318 ^oF, 30.732 ^oC] and a CB of 11.137 MPa [1,615.285 psia], the feed

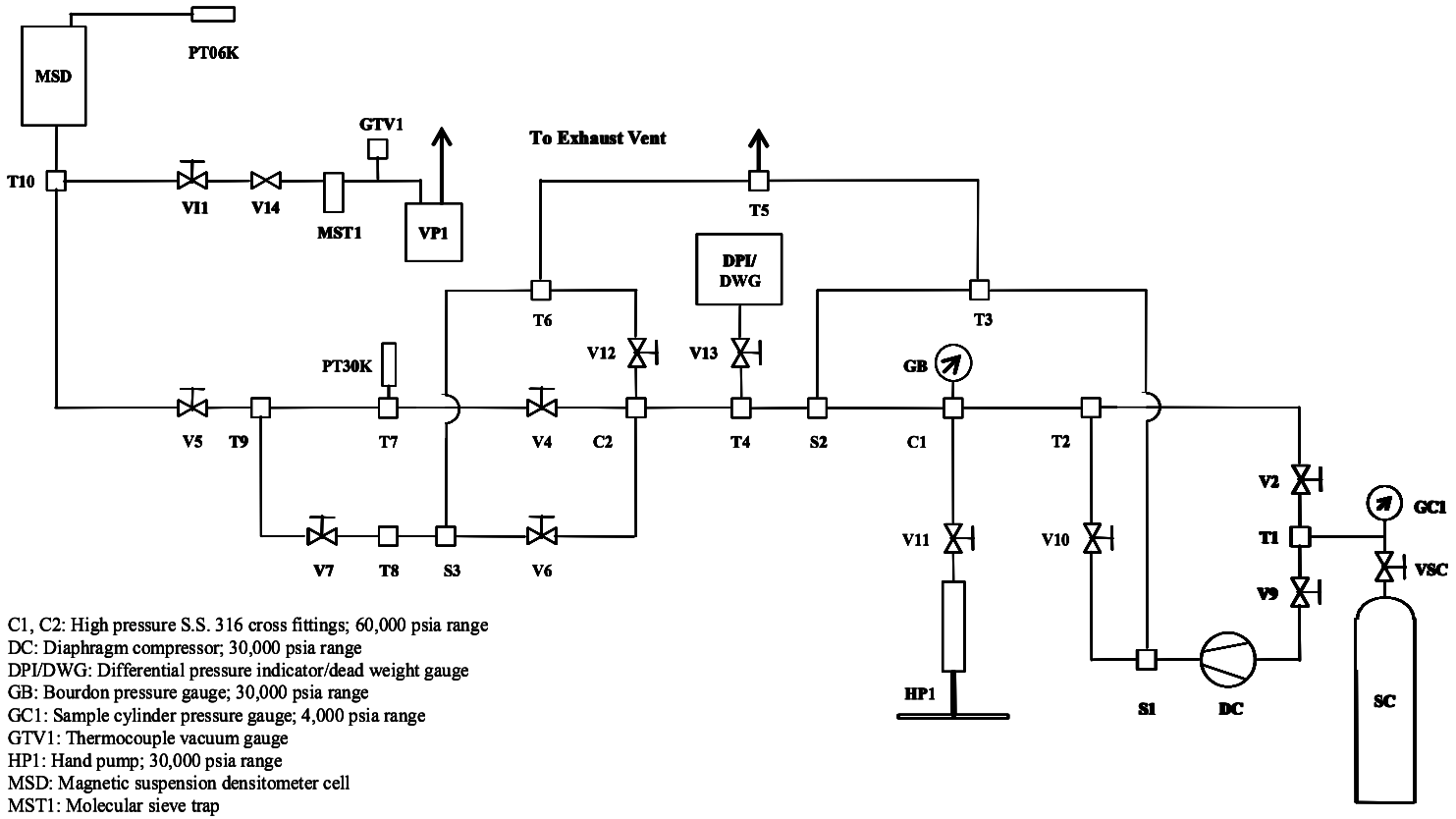

C1, C2: High pressure S.S. 316 cross fittings; 60,000 psia range
DC: Diaphragm compressor; 30,000 psia range
DPI/DWG: Differential pressure indicator/dead weight gauge
GB: Bourdon pressure gauge; 30,000 psia range
GC1: Sample cylinder pressure gauge; 4,000 psia range
GTV1: Thermocouple vacuum gauge
HP1: Hand pump; 30,000 psia range
MSD: Magnetic suspension densitometer cell
MST1: Molecular sieve trap
PT06K, PT30K: Pressure transducers; 6,000 and 30,000 psia range
S1, S2 and S3: Safety rupture disc heads with 40,000 psia, 30,000 psia and 6,000 psia range respectively
SC: Gas sample cylinder
T1 – T10: High pressure S.S. 316 tee fittings; 60,000 psia range
V14: Brass block valve for rough vacuum
VI1, V2, V4 – V7, V9 – V13: High pressure S.S. 316 needle valves; 60,000 psia range
VP1: Mechanical vacuum pump
VSC: Sample cylinder valve; CGA 580 for argon and nitrogen, CGA 350 for methane and natural gas samples

Figure 3.17. Schematic Flow Diagram of the Old and New Manifolds with the MSD in the New Location, with PT06K Moved to the New Manifold

could not be charged with the manifold at ambient temperature as this would have caused condensation (see Figure 2.2). The old manifold box was heated by radiation from infra-red bulbs as discussed earlier in subsection 2.2.1. The tubing sections outside the old feed manifold between the sample cylinder hot box and T1, V5 and T10, T10 and VI1 and the MSD cell and PT06K were heat-traced and insulated as discussed in subsection 2.2.1. Parts of the tubing between V5 and T10, T10 and VI1 and the MSD cell and PT06K, closest to the cell and T10 were immersed in the heating/cooling liquid of the cell bath and hence were at the temperature of the isotherm rather than the temperature of the heat traced sections. These sections of the tubing were purposely kept flexible by silver soldering 0.1588 cm [0.0625 inch] outer diameter x 0.0508 cm [0.02 inch] inner diameter stainless steel tubing axially to the main 0.3175 cm [0.125 inch] outer diameter x 0.0508 cm [0.02 inch] inner diameter tubing so that the additional stress because of the stiffness of the 0.3175 cm outer diameter tubing did not interfere with the vertical and horizontal alignment of the MSD. Isotherms 13 through 18 for M94C1 were measured with the experimental set-up as shown in Figure 3.17 but with the old feed manifold heated and the tubing sections that were exposed to ambient temperature, heat traced and maintained above the CT.

The stability of the pressure readings from PT06K could be improved by maintaining its temperature at a constant value much higher than ambient temperature. It was also necessary to quantify the temperature dependence of the calibration curve of PT06K by performing calibrations against a DPI/DWG assembly while maintaining PT06K at different temperatures. For these reasons, PT06K was enclosed in a thermostated aluminum heater block. Isotherms 19 and 20 were measured with the experimental setup as shown in Figure 3.18.

It was thought that the accuracy of density measurements at pressures below 13.790 MPa [2,000 psia] may have been restricted by the accuracy of pressure measurements made with PT06K. It was therefore decided to include another pressure transducer with a lower pressure range of 13.790 MPa [2,000 psia] (PT02K), in parallel with PT06K. Moreover, it was surmised that the offset of the calibration curve of PT06K

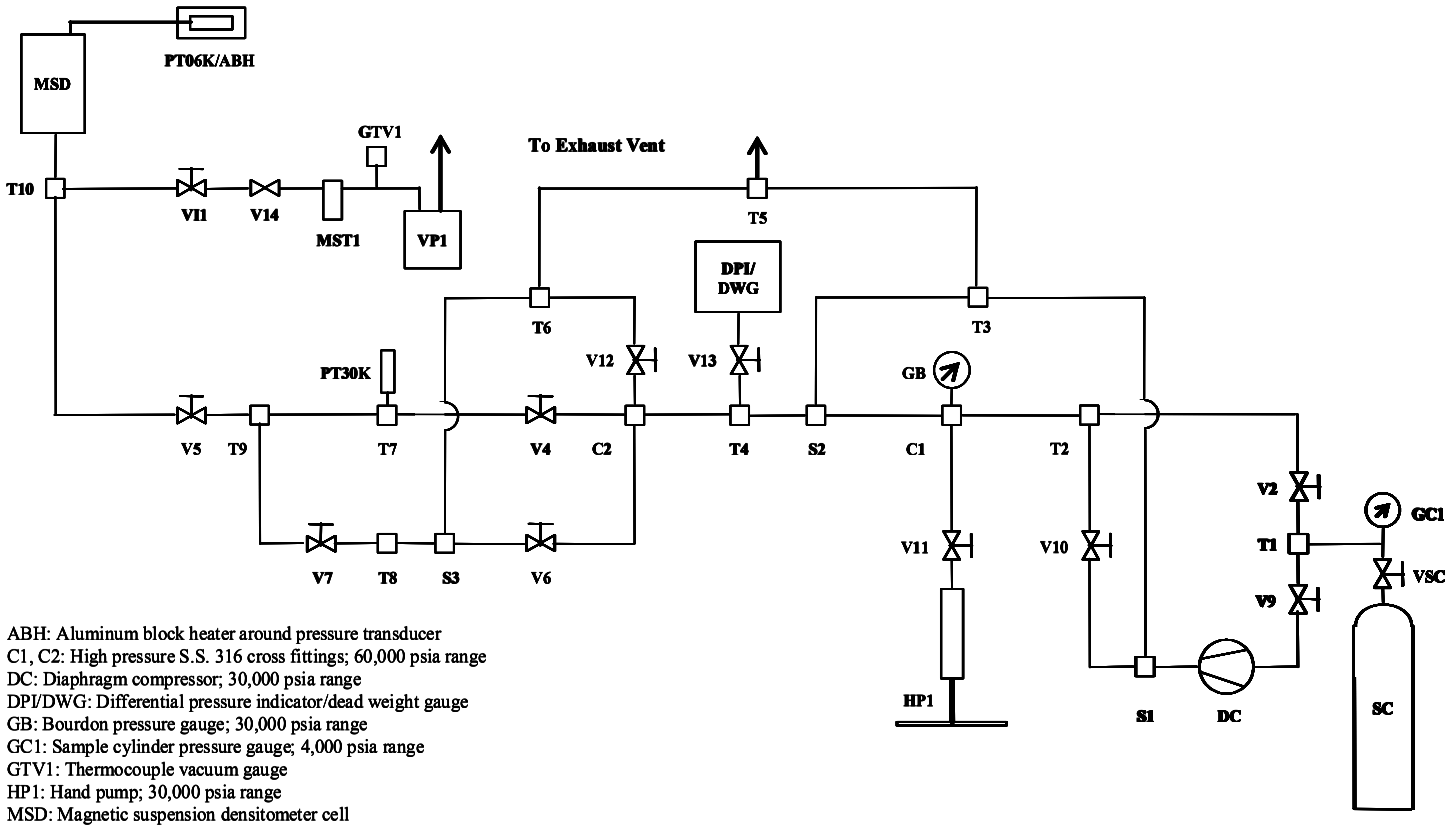

ABH: Aluminum block heater around pressure transducer
C1, C2: High pressure S.S. 316 cross fittings; 60,000 psia range
DC: Diaphragm compressor; 30,000 psia range
DPI/DWG: Differential pressure indicator/dead weight gauge
GB: Bourdon pressure gauge; 30,000 psia range
GC1: Sample cylinder pressure gauge; 4,000 psia range
GTV1: Thermocouple vacuum gauge
HP1: Hand pump; 30,000 psia range
MSD: Magnetic suspension densitometer cell
MST1: Molecular sieve trap
PT06K, PT30K: Pressure transducers; 6,000 and 30,000 psia range
S1, S2 and S3: Safety rupture disc heads with 40,000 psia, 30,000 psia and 6,000 psia range respectively
SC: Gas sample cylinder
T1 – T10: High pressure S.S. 316 tee fittings; 60,000 psia range
V14: Brass block valve for rough vacuum
VI1, V2, V4 – V7, V9 – V13: High pressure S.S. 316 needle valves; 60,000 psia range
VP1: Mechanical vacuum pump
VSC: Sample cylinder valve; CGA 580 for argon and nitrogen, CGA 350 for methane and natural gas samples

Figure 3.18. Schematic Flow Diagram of the Old and New Manifolds with the MSD in the New Location, with PT06K Moved to the New Manifold and Thermostated with an Aluminum Block Heater

depended upon the ambient pressure. Hence, it was decided to include the ambient pressure point, measured with a barometer, as well during its calibration. Provision was made to expose PT06K to atmospheric pressure intermittently during density measurements to keep track of how it responded to atmospheric pressure changes daily. The distance between the DWG assembly and PT06K as shown in Figure 3.17 or 3.18 was more than 15 m [50 feet] with relatively large volumes of the gas chamber of the DPI, the hand pump and the MSD cell between them. It was decided to shorten this distance and create the ability to calibrate PT06K against a force balance and to confirm that the calibration using the DPI/DWG assembly was reliable despite the long distance. The new manifold shown in Figure 3.19 was built to fulfill the above three requirements. It consists of medium pressure, taper seal, stainless steel 316 'Tee' and 'Cross' fittings and needle valves capable of withstanding 103.421 MPa [15,000 psia] pressure and 0.1588 cm [0.0625 inch] outer diameter x 0.0508 cm [0.02 inch] inner diameter, stainless steel 316 tubing with a pressure limit of approximately 75.842 MPa [11,000 psia] at ambient temperature. While the old manifold was built with the intention of measuring argon densities at pressures up to 206.843 MPa [30,000 psia], the new manifold was built to meet only the 34.474 MPa [5,000 psia] maximum pressure limit that would be encountered as part of the present project, mainly because of time and space limitations. Although both are metal-to-metal contact seals, the medium pressure taper-seal joints are much easier to achieve compared to the high pressure, coned-and-threaded joints. The new manifold box was small enough compared to the old manifold box that a couple of 60 watt bulbs could heat it to a temperature above the highest CT of 324.521 K [124.468 ^{o}F, 51.371 ^{o}C] for M78C1 among mixtures to be measured as part of the present project. The entire section between T11 and VC excluding PT02K, PT06K, the vacuum line arm extending from C3 and the force balance was enclosed in the new manifold box. PT02K and PT06K along with their respective thermostated aluminum block heaters were placed outside the new manifold box because their temperature and pressure stability would have been affected if they had been placed inside the uncontrolled new manifold box. Tubing sections between T12 and PT06K and

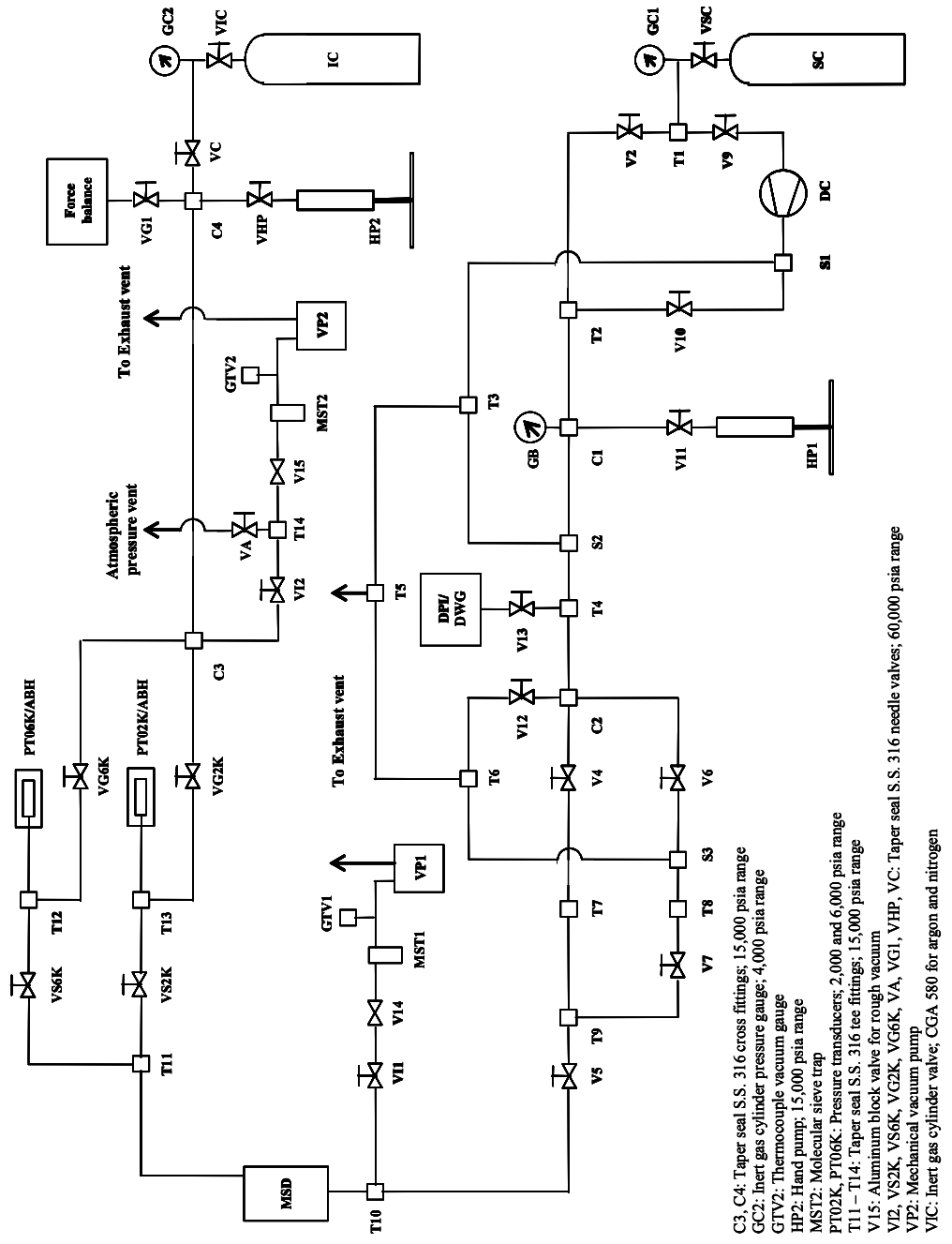

Figure 3.19. Schematic Flow Diagram of the Old and New Manifolds with the MSD in the New Location with PT02K and PT06K Thermostated with Aluminum Block Heaters

T13 and PT02K that were thus exposed to ambient temperature were heat traced with extensions of the trace heater used to heat the tubing section between the MSD cell top and T11. For pressure measurements in the range (13.790 to 34.474) MPa [(2,000 to 5,000) psia] using PT06K with VG6K and VS2K closed but VS6K open, VG2K was also kept open and VC, VHP and VG1 were kept closed. This setting eliminated the need for a safety rupture disc head to prevent PT02K from damage due to over-pressurization due to a potential leak from either VS2K or VG6K by keeping VI2 and VA open or by running VP2 with VA closed and VI2 and V15 open. Isotherms 21 through 26 were measured with the experimental set-up as shown in Figure 3.19.

3.3.2 The Diaphragm Compressor

A two-stage, diaphragm compressor, model 46-14021 manufactured by Newport Scientific Inc. was used to charge gas from the sample cylinder to the hand pump HP1 on the old manifold. The compressor required the suction pressure for the first stage to be at least 5.516 MPa [800 psia] and compressed up to 206.843 MPa [30,000 psia] at the discharge of the second stage. The reciprocating piston of the compressor was pneumatically driven with air at (0.552 to 0.689) MPa [(80 to 100) psia]. Although, the manufacturer's recommended working temperature for the compressor was at the most 323.15 K [122 ^{o}F, 50 ^{o}C], it had to be maintained at approximately 331.15 K [136.4 ^{o}F, 58 ^{o}C] when placed inside the old manifold box while measuring isotherms 13 through 18. There was the possibility of the oil from the hydraulic heads of the two stages seeping into the gas stream through the elastomeric 'O' rings of the diaphragm, if the compressor was maintained at temperatures higher than the manufacturer's recommended values. However, repeatability of the sinker mass reading in vacuum at ambient temperature before each isotherm, which was used as the criterion to ensure cleanness of the sinker, proved that there was no oil leakage from the compressor into the manifold or the MSD cell.

3.3.3 Sample Cylinder Storage Hot Box

A 1.83 m tall x 0.61 m deep x 0.81 m wide [6 feet x 2 feet x 2.67 feet] internally insulated, steel hot box was used to store the natural gas mixture sample cylinders at temperatures above their respective CT to prevent condensation and adsorption of the heavier components and homogenize the mixtures. The box was provided with a 600 watt heater and an adjustable analog thermostat with which cylinder temperatures between ambient and 366.48 K [200 ^{o}F, 93.33 ^{o}C] could be maintained with an accuracy of ±2 ^{o}F. Upon delivery and storage in the hot box at 333.15 K [140 ^{o}F, 60 ^{o}C], the M94C1 and M91C1 sample cylinder pressures were approximately 14.479 MPa [2,100 psia] and 11.032 MPa [1,600 psia] respectively. With usage of the mixture, even if the cylinder pressure dropped below the CB, there was no possibility of condensation by passage through the two phase region because the cylinder was maintained at a temperature above the CT of the mixture. The pure gas cylinders for argon, methane and nitrogen were stored at ambient conditions outside the hot box.

3.3.4 Vacuum System

A mechanical vacuum pump, VP1 with the ability to create a vacuum of 0.13 Pa [1 mTorr] at its inlet port was used as a roughing pump to evacuate the MSD cell by closing V5 and opening VI1 shown in Figures 3.16 through 3.19 for the old manifold. The approximately 4.6 m [15 feet] long section between T10 and V5 and the 2.1 m [7 feet] long section between T10 and VI1 were either medium or high pressure tubing with 0.0508 cm [0.02 inch] inner diameter, whereas, all sections between VI1 and the inlet of VP1 were 2.54 cm [1 inch] inner diameter stainless steel, flexible tubing with clamp joints. The very small diameter sections of the tubing between VP1 and V5 prolonged the period of evacuation of the MSD cell as compared to the case where large diameter tubing had been used throughout the length. Typically an 8 to 10 hour long period was required for evacuation of the MSD cell to a pressure of approximately (1.33 to 2.67) Pa

[(10 to 20) mTorr] from atmospheric or higher pressures. Any further reduction in the buoyancy force acting on the sinker caused by application of a higher vacuum using either a diffusion or a turbo-molecular pump would not have caused a change in the true mass of the sinker that could have been detected by the balance because of a limit on its resolution of 0.01 mg. A thermocouple vacuum gauge tube was used as a sensor for vacuum measurement with an analog vacuum gauge controller with a range of (0.13 to 267) Pa [(1 to 2,000) mTorr]. A molecular sieve trap was provided between the MSD cell and VP1 to prevent back-migration of vapors of the vacuum pump oil to the MSD cell that could contaminate the sinker. The molecular sieve particles were regenerated by heating the trap with an axially placed rod heater that caused desorption of the vacuum pump oil, closing the brass block valve V14 and running VP1.

A second vacuum system similar to the first shown in Figures 3.16 through 3.18 was built on the new manifold as shown in Figure 3.19. The second vacuum system allowed much faster evacuation of the MSD cell with V5, VI1, VA VG1, VHP and VC closed and VS2K, VS6K, VG2K, VG6K, VI2 and V15 open, despite using 0.0508 cm [0.02 inch] inner diameter tubing because of the much shorter lengths of such tubing on the new manifold. Typically 2 to 3 hours were required for evacuation of the MSD cell to a pressure of approximately (1.33 to 2.67) Pa [(10 to 20) mTorr] from atmospheric or higher pressures using the second vacuum system. The second vacuum system also allowed daily checks of the calibration curves of PT02K and PT06K at ambient pressure and under vacuum amidst density measurements, without contaminating the natural gas sample in the MSD cell.

3.3.5 Pressure Measurement

Oil-free, resonating quartz crystal, absolute pressure measuring transducers supplied by Paroscientific Inc. with NIST traceable calibrations were used for pressure measurements. The 206.843 MPa [30,000 psia] range transducer (PT30K: model 430K-101, serial number 80872) was used for testing the range of operation of the

MSA, the 41.369 MPa [6,000 psia] range transducer (PT06K: model 46K-101, serial number 84267) was used during density measurements and the 13.790 MPa [2,000 psia] range transducer (PT02K: model 42K-101, serial number 82703) was used to check if the accuracy of density measurements at lower pressures could be improved by using a lower pressure range transducer.

The accuracy of pressure measurement is better from a transducer whose accuracy is expressed as a percentage of the pressure reading rather than as a percentage of its full scale. Table 3.3 shows this along the columns for each one of the three transducers. The manufacturer's specified accuracy was ±0.01% of the full scale for all three transducers. If a high pressure range transducer is used to measure a low pressure, the accuracy of pressure measurement is lower than if the same low pressure was measured using a low pressure range transducer, because of this reason. This is observed under 'Measured P with 0.01% of full scale' of Table 3.3, along a row for the 3.447 MPa [500 psia] pressure point in moving from PT30K to PT06K to PT02K.

The frequency of oscillation of the quartz crystal resonator of the transducer varies with pressure induced stress (Paroscientific, 2001). The transducer also has an internal temperature signal that thermally compensates the pressure calculated from the frequency of oscillation so that pressure can be measured with high accuracy over a wide range of temperatures. PT02K and PT06K could be used over a temperature range of (273.15 to 398.15) K [(32 to 257) ^{o}F, (0 to 125) ^{o}C] while PT30K had a lower temperature range of (273.15 to 323.15) K [(32 to 122) ^{o}F, (0 to 50) ^{o}C]. The transducers could be used up to 1.2 times the full scale pressure with neither permanent damage nor a change in the calibration. However, use beyond 1.2 times the full scale pressure or outside the recommended range of temperature would disturb the original calibration of the transducer done by the manufacturer. Each transducer sends the pressure, internal temperature, pressure period/frequency and internal temperature period/frequency output to an accompanying model 730, intelligent electronics and digital display box.

A temperature gradient existed between PT06K held at ambient temperature for isotherms 1 through 18 and the MSD cell held at the temperature of the

Table 3.3. Accuracy of Pressure Transducers as a Percentage of Full Scale and of the Reading

PT02K			PT06K			PT30K		
True P	**Measured P**		**True P**	**Measured P**		**True P**	**Measured P**	
	0.01% of full scale	**0.01% of reading**		**0.01% of full scale**	**0.01% of reading**		**0.01% of full scale**	**0.01% of reading**
MPa								
3.447	0.00138	0.00034	3.447	0.00414	0.00034	3.447	0.02068	0.00034
6.895	0.00138	0.00069	6.895	0.00414	0.00069	6.895	0.02068	0.00069
10.342	0.00138	0.00103	10.342	0.00414	0.00103	10.342	0.02068	0.00103
13.790	0.00138	0.00138	13.790	0.00414	0.00138	13.790	0.02068	0.00138
			20.684	0.00414	0.00207	20.684	0.02068	0.00207
			27.579	0.00414	0.00276	27.579	0.02068	0.00276
			34.474	0.00414	0.00345	34.474	0.02068	0.00345
			41.369	0.00414	0.00414	41.369	0.02068	0.00414
						68.948	0.02068	0.00689
						103.421	0.02068	0.01034
						137.895	0.02068	0.01379
						172.369	0.02068	0.01724
						206.843	0.02068	0.02068

isotherm along the approximately 1 m long tubing between them as shown in Figure 3.17. This temperature gradient could have caused convective flow of the sample in the cell, thus adversely affecting the stability of the pressure as well as the balance reading. Immersion of PT06K in the cell bath liquid very close to the MSD cell to hold it at the same temperature as the isotherm and thus eliminate potential convection due to temperature gradients was considered. However, because of the manufacturer's advice against immersing the transducers in liquid, they were not placed in the cell bath, very close to the MSD cell despite not having any magnetic components.

PT02K and PT06K were maintained at temperatures higher than ambient temperature to improve the stability of their pressure readings. Each transducer was placed in a cylindrical hole slightly larger than the outer diameter of the transducer bored into a solid aluminum cylinder with 4 inch diameter and 9 inch length. The aluminum cylinder weighing approximately 3 kg after boring the hole was cut into two halves held together with screws to facilitate easy insertion and removal of the transducer. The bottom half of the aluminum cylinder was cut along a plane to prevent the cylinder from rolling. The aluminum block was maintained at a temperature higher than ambient with a thermostating scheme that included a three-lead PRT, an auto-tune PID temperature controller, a solid state relay (SSR) switch, a cartridge heater; all supplied by Omega Engineering, Inc. and a variable AC power supply. Figure 3.20 shows a schematic diagram of this thermostating scheme for the aluminum block. The three lead, ceramic encapsulated, 100 Ω PRT (model: RTD-2-1PT100KN2528-108-T) with a temperature coefficient of resistance (TCR) of 0.00385 Ω/Ω/^{o}C and an accuracy of ±0.3 ^{o}C at 0 ^{o}C and ±0.8 ^{o}C at 100 ^{o}C was used to measure the temperature of the aluminum block. The measured temperature was sent as an input to the auto tuning PID temperature controller (model: CNi3244) capable of controlling temperature with an accuracy of ±0.5 ^{o}C. The 10 V DC pulse, output signal from the controller was sent as the input control signal for the DC voltage input/ AC voltage output SSR switch (model: SSRL240DC25). The SSR was specified for an input DC signal of 3 to 32 V and an AC output voltage across the load heater of 24 to 280 V. However, the 500 W, 1.27 cm [0.5 inch] diameter and 12.7

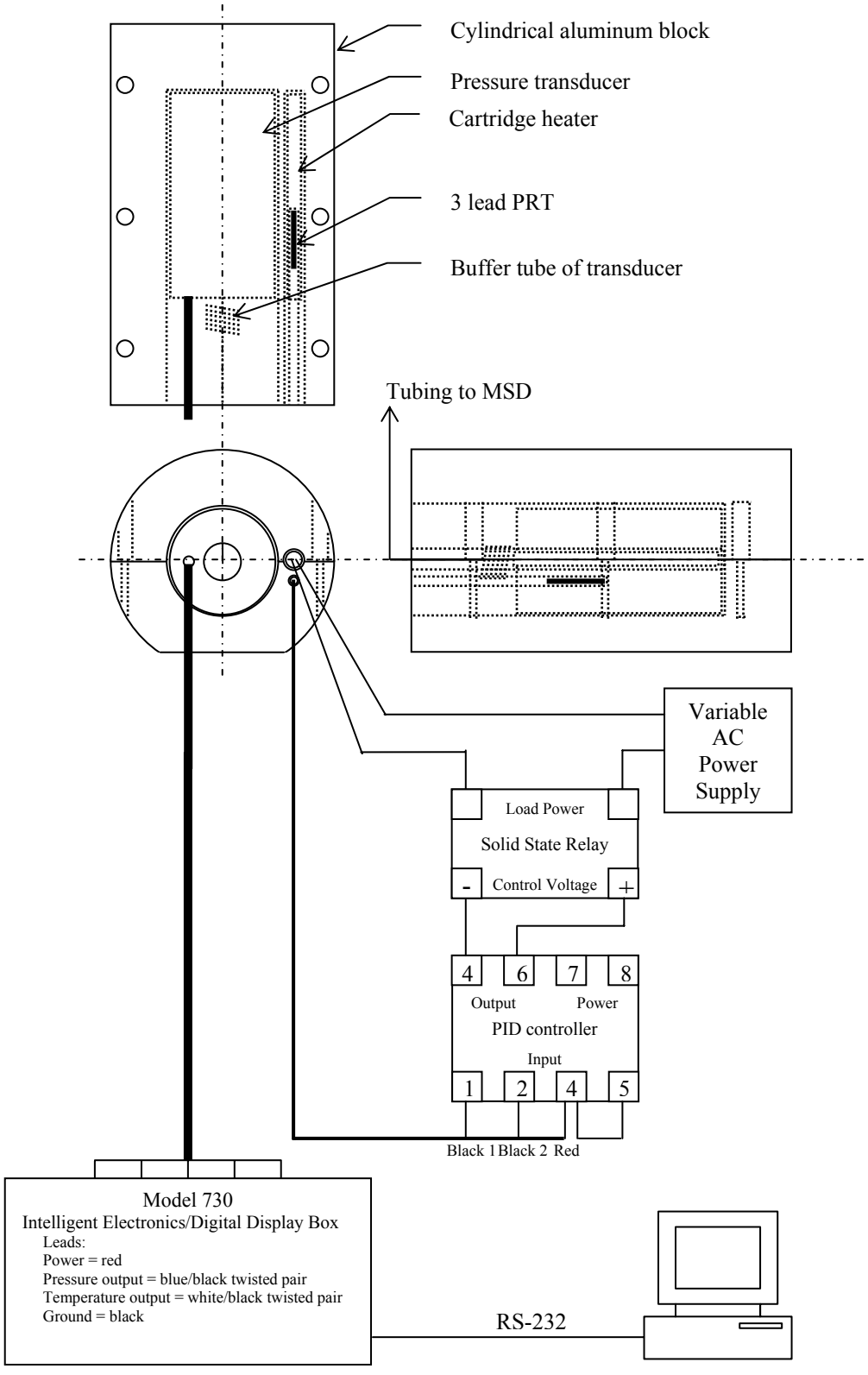

Figure 3.20. Thermostating Scheme for Pressure Transducers

cm [5 inch] long cartridge heater (model: CSH-305500/120V) was powered from a 120 V input/ (0 to 140) V output variable AC power supply. The voltage across the variable power supply was maintained closer to the higher end of its range while increasing the temperature of the aluminum block from ambient to the set-point temperature in order to increase the rate of heating but was lowered once the set-point temperature was reached to a value that allowed the most stable control action from the PID temperature controller. The controller performance was improved by insulating the aluminum blocks with glass-wool and polyisocyanurate rigid foam sheets. The stabilities and accuracies of pressure transducer readings without the thermostated aluminum block heaters for isotherms 1 through 18 as well as with them for isotherms 19 through 26 are presented in Chapter V. The internal temperatures of PT06K during isotherms 13 through 18 are higher than ambient temperature despite not using the aluminum block heaters because of conduction of heat from the heat traced tubing between the MSD cell and PT06K. During these isotherms PT06K was insulated with glass-wool and a polystyrene/styrofoam box only.

The temperature sensitivity of the pressure had to be known *a priori* for both PT02K and PT06K in order to decide the higher than ambient temperature at which each was to be held. For this, the pressure periods τ, over the entire pressure range from vacuum to the maximum pressure of the transducer at different internal temperature periods X, ranging over the temperature range of the transducer had to be known. Table C.1 of Appendix C shows the observed pressure periods between vacuum and approximately 12.066 MPa [1,750 psia] for PT02K and 34.474 MPa [5,000 psia] for PT06K when each was held at ambient temperature and at 353.15 K [176 ^{o}F, 80 ^{o}C] using the aluminum block heaters along with the corresponding internal temperature periods. The temperature dependence of pressure was determined by using the manufacturer's original calibration coefficients and the calibration equations provided in Table C.2 of Appendix C. Tables C.3.1 and C.3.2 show the pressure readings for PT02K and PT06K respectively over intervals between the observed internal temperature periods and pressure periods given in Table C.1. The bold numbers in these tables

represent $P_{minimum}$ among P values for different X. The 'P-$P_{minimum}$' column in these tables is presented particularly to highlight the quadratic dependence of pressure on the transducer internal temperature which is clearly seen in Figures C.1 and C.2 of Appendix C. While using the transducers with the model 730 intelligent electronics and digital display box, the pressure output of the transducers is fully temperature compensated using the output of the transducer internal temperature probe and the provided pressure calibration equations, so that no manual correction is required to account for the temperature dependency of pressure. Figures C.1 and C.2 also show that the temperature dependence of pressure is least at approximately 339.15 K [150.8 ^{o}F, 66 ^{o}C] for PT02K and at 325.15 K [125.6 ^{o}F, 52 ^{o}C] for PT06K. For this reason, the transducers were maintained at these temperatures during isotherms 21 through 26 after installing them in their respective aluminum block heaters.

The pressure transducer calibrations had to be checked periodically because the slope and the offset could vary to different values from the original, with time and use at different temperatures. A DPI/DWG assembly was used for *in-situ* calibration of the transducers at different temperatures. Details of the transducer calibrations are presented in Chapter IV.

3.3.6 Magnetic Suspension Densitometer Cell Thermostating Scheme

The cell bath introduced in subsection 3.2.2 and shown in Figure 3.8 held a pool of the constant temperature heating/cooling liquid around the cell and thus maintained the cell at a constant temperature during an isotherm. The heating/cooling liquid in turn was maintained at the temperature of the isotherm with a constant temperature circulator bath (model: Presto LH 85) manufactured by Julabo USA, Inc. A 50:50 mixture by volume of antifreeze coolant grade ethylene glycol and distilled water that could cover the temperature range (248.15 to 373.15) K [(-13 to 212) ^{o}F, (-25 to 100) ^{o}C] was used as the circulating heating/cooling liquid. Figure 3.21 shows the MSD cell thermostating scheme. The constant temperature bath pumped the heating/cooling

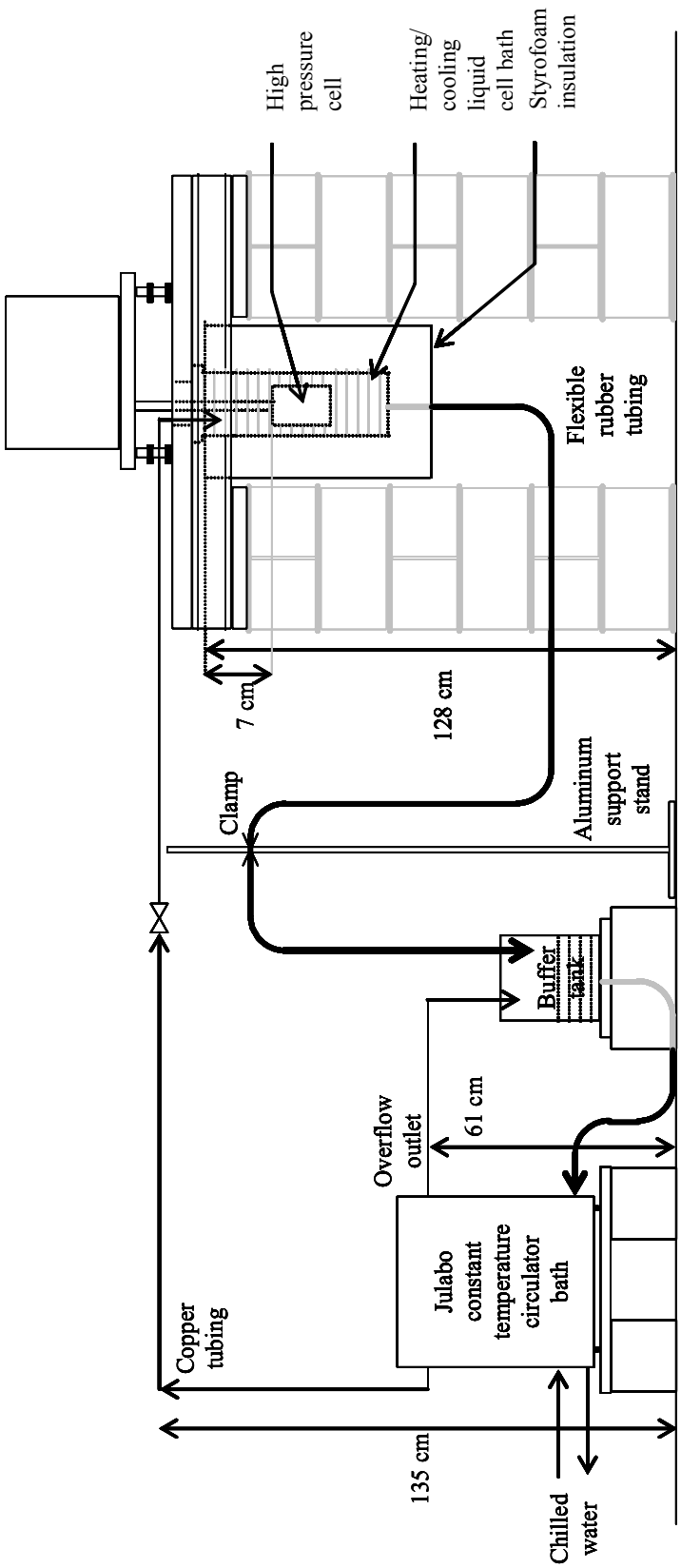

Figure 3.21. MSD Cell Thermostating Scheme

liquid through the 0.95 cm [0.375 inch] diameter insulated, copper tubing that entered into the cell bath. The bottom of the cell bath had a 2.54 cm [1 inch] diameter opening connected to an insulated, flexible, plastic tubing through which the liquid drained by gravity from the cell bath. The level in the cell bath was maintained by manually raising or lowering a clamp holding the plastic tubing along an aluminum support stand. The liquid was collected in a plastic buffer tank to absorb the increase or decrease in flow rates of liquid draining out of the cell bath as a result of lowering or raising the clamp. In addition, the buffer tank also provided a liquid head on the suction side of the constant temperature bath as well as acted as a receptacle for liquid overflow caused by expansion (especially at higher temperatures) from the constant temperature bath. Cylindrical holes slightly larger than the outer diameter of the cell bath were cut along the axis of a polystyrene/styrofoam sheet stack for insulation approximately 34cm wide, 29 cm deep and 61 cm tall [13.5 inch x 11.5 inch x 24 inch]. With this arrangement, it was possible to maintain the liquid level in the cell bath such that the thermostating tube was immersed to 7 cm in the bath liquid between the top surface of the cell and the meniscus of the bath liquid.

Although, the constant temperature circulator bath was used only over the range (270 to 343.15) K [(26.33 to 158) ^{o}F, (-3.15 to 70) ^{o}C] required for the present project, it could cover a wide range of (188.15 to 523.15) K [(-121 to 482) ^{o}F, (-85 to 250) ^{o}C] with corresponding stabilities of ±(50 to 100) mK. The high thermal conductivity of the copper beryllium cell and the high flow rate of the heating/cooling liquid of approximately 50 cm^3/s from the constant temperature circulator bath to the cell bath allowed rapid thermal equilibration of the MSD cell while the large material mass of the cell weighing approximately 11 kg without its flange and its immersion in the insulated cell bath together prevented any sudden changes in the cell temperature. For this reason, the cell temperature stability was expected to be ± 10 mK which is better than that of the constant temperature circulation bath. A heating/cooling liquid volume of approximately (0.016 to 0.018) m^3 [(16 to 18) liters] circulated in the MSD cell thermostating system. Although stability at a temperature and the rate of heating to reach

temperatures above ambient temperature were acceptable, the rate of cooling was extremely low because of the much larger volume of the circulating liquid than the specified capacity of 0.006 m^3 [6 liters] of the constant temperature circulation bath that used air or chilled water for cooling. The slower cooling at the rate of 4 K/hour [7.2 ^oF/hour, 4 ^oC/hour] slowed the rate at which isotherms were measured especially with natural gas mixtures where the cell had to be maintained at a temperature above the CT while charging gas to the cell until the cell pressure exceeded the CB and then cooled for measurement of lower temperature isotherms.

The liquid level in the cell bath required frequent monitoring in transition between isotherms because of the change in flow rate as a result of change in viscosity of the ethylene glycol/water mixture from that at ambient temperature. In approaching 270 K [26.33 ^oF, -3.15 ^oC] from ambient temperature, the flow rate from the cell bath decreased because of increase in viscosity of the liquid causing an overflow, while in approaching 340 K [152.33 ^oF, 66.85 ^oC] from ambient temperature, it increased because of decrease in viscosity of the liquid causing the thermostating tube to recede below the required 5 cm immersed depth. The clamp on the aluminum support stand was either lowered or raised respectively to maintain the required liquid level.

In the initial stages of the project, a double pipe heat exchanger jacket provided by Rubotherm was used around the MSD cell for thermostating. The accuracies of +0.2% with pure methane and +0.1% with pure argon for density measurements in the range (270 to 340) K [(26.33 to 152.33) ^oF, (-3.15 to 66.85) ^oC] during this period were much worse than the expected ±0.03% despite moving the apparatus to the new location. It was concluded that use of the jacket thermostating scheme was one of the factors leading to lower accuracies by allowing axial and radial thermal gradients in the cell walls such that the cell temperature measured by the PRT placed at the lower end of the groove on the cylindrical surface of the cell was different from the actual temperature of the gas sample in the cell high pressure chamber. However, the stabilities of measured cell temperatures with the jacket thermostat were as good as those with the cell liquid bath. As a better alternative to the jacket thermostat, the cell liquid bath and a two stage

thermostat similar to those used by Klimeck *et al*. (1998) Wagner *et al.* (1995) and Zhou (2002) were considered as thermostating schemes. The cell liquid bath option was preferred because of its relative simplicity, low cost, and quick implementation with the MSD apparatus that offered compatibility through its design.

3.3.7 Temperature Measurement

A four-lead, capsule PRT (model: S1059-2, serial number 204) with a range of (84.15 to 533.15) K [(-308.2 to 500) ^{o}F, (-189 to 260) ^{o}C] manufactured by Minco Products, Inc. was used for temperature measurements. A resistance thermometer works on the principle that there is a change in the resistance of the sensing element with temperature. For the 100 Ω, platinum element of the PRT used, the temperature sensitivity was 0.3925 Ω /^{o}C, leading to a TCR of 0.003925 Ω / Ω /^{o}C. The TCR is the change in the resistance of an element from that at a base temperature per unit change in temperature from the base temperature per unit of its resistance at the base temperature. The resistance at 0^{o}C, normally chosen as the base temperature is used to describe the PRT.

The 15.24 cm [6 inch] long leads of the PRT were too short to allow dry connections between the four PRT leads with their extension wires upon immersing the cell in the liquid of the cell bath. An isolation tube (shown in Figure 3.22) was prepared by soldering a copper pipe and a copper tube axially, through which the PRT and its leads with the extension joints were passed. The joints between the PRT leads and their approximately 2 m long, 22 AWG copper extension wires were established by crimping them on either end of a copper tubing approximately 1 cm long. Copper tubes were used to avoid introducing spurious voltages (called thermoelectric EMFs) as a result of a thermocouple effect at a joint between two dissimilar metals. The joints were insulated from each other with thermoplastic heat shrink tubes and glass cloth electrical insulation tape and bundled together so that any temperature changes could act equally on all four leads. High conductivity copper extension wires of equal length were used despite lead

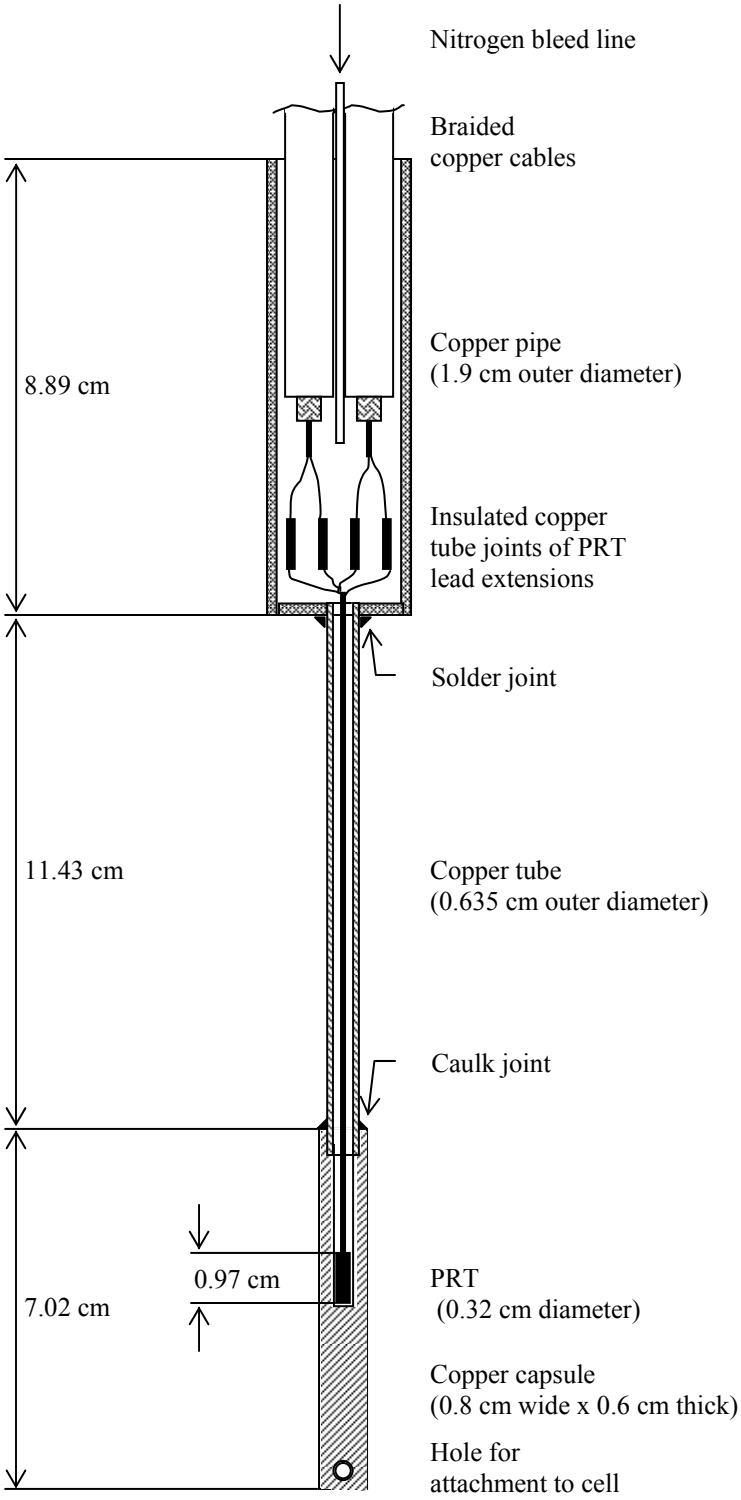

Figure 3.22. Isolation Tube between PRT and Cell Bath Liquid

wire and contact resistance not being of concern with a four-lead PRT. After inserting the PRT into the cylindrical hole drilled in the copper capsule, briefly described in subsection 3.2.1, the joint between the isolation tube and the capsule was sealed with silicone caulk to prevent the bath liquid from seeping into the isolation tube. This step was necessary because it would have been difficult to align the PRT into the axial cylindrical hole in the capsule if it had been lowered from the open end of the copper pipe, because of the flexible PRT lead wires. Any attempt to push the PRT downwards through the isolation tube with a stiff long object would have stressed the lead wire joints at the epoxy potting of the PRT, because of a snug fit between the PRT and the diameter of the hole drilled in the copper capsule for good thermal contact. The entire assembly shown in Figure 3.22 could then be held in the groove on the cylindrical surface of the MSD cell shown in Figure 3.1. with a copper screw such that the capsule and the copper tube parts of the assembly spanned the height of the MSD cell but the copper pipe expanded above the cell top surface and protruded out of the heating/cooling liquid meniscus to an extent of 5 cm. At 270 K [26.33 ^{o}F, -3.15 ^{o}C], atmospheric moisture condensed along the PRT lead wire joints with the extension cables because the copper pipe was open to atmospheric air. At temperatures higher than ambient temperature, the cell bath liquid vapors condensed on the cooler, copper pipe part of the isolation tube wetting the PRT leads through the insulated joints. To displace moisture laden atmospheric air from the PRT isolation tube, nitrogen was continuously bled into it.

Figure 3.23 shows a circuit diagram for accurate measurement of resistance of a four-lead PRT, R_{PRT}. A constant current, I, passes through the PRT through one pair of its leads, 1 and 2, while the other pair, 3 and 4, measures the voltage drop, V_{PRT} across it. The resistance value is then calculated simply by dividing the measured voltage with the current value as:

$$R_{\mathrm{PRT}} = \frac{V_{\mathrm{PRT}}}{I} \tag{11}$$

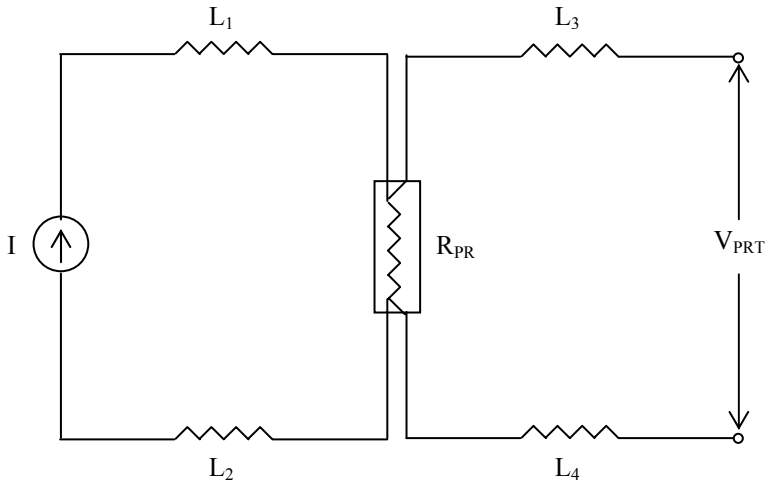

Figure 3.23. Four-lead Resistance Measurement

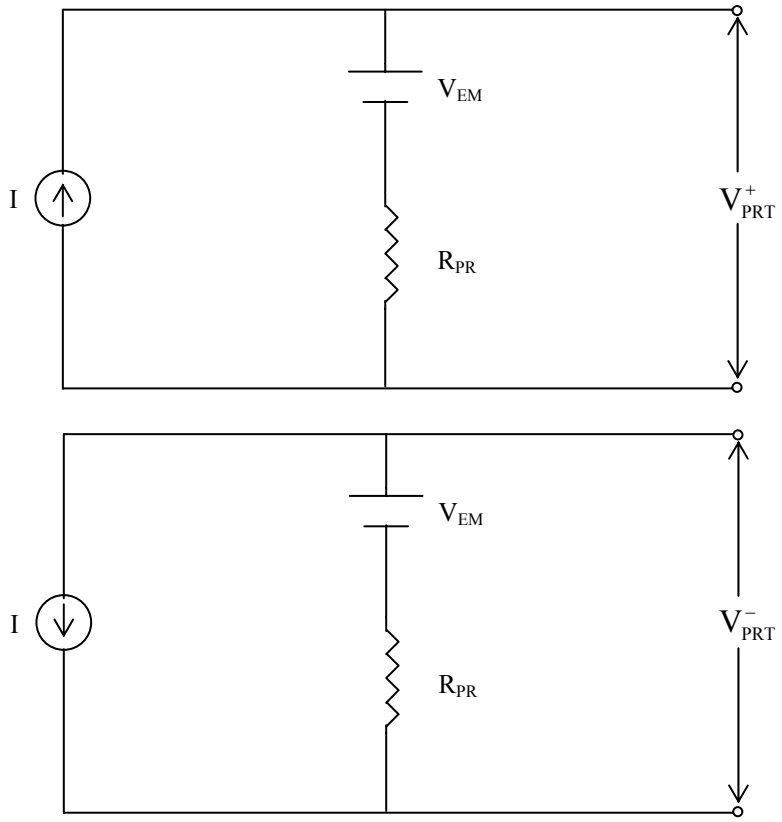

Figure 3.24. Current Reversal for Thermoelectric EMF Elimination

The measured voltage across a two-lead PRT is different from the actual voltage across it because of the voltage drops across lead resistances L_1 and L_2. However, the measured and actual voltages across a four-lead PRT are the same because the current through the voltage sensing leads with lead resistances L_3 and L_4 is negligible. Hence four-lead resistance measurement is preferred for more accurate temperature measurements. Figure 3.24 shows the circuit diagrams for a strategy to eliminate errors in resistance measurements due to thermoelectric EMFs. These can be cancelled by measuring the voltage drop twice with currents of opposite polarity through the PRT. With the positive current applied, the measured voltage is:

$$V_{\mathrm{PRT}}^{+} = V_{\mathrm{EMF}} + IR_{\mathrm{PRT}} \tag{12}$$

With the direction of current through the PRT reversed, the measured voltage is:

$$V_{\mathrm{PRT}}^{-} = V_{\mathrm{EMF}} - IR_{\mathrm{PRT}} \tag{13}$$

The average of the measured voltages with positive and negative currents then eliminates the thermoelectric EMFs such that:

$$V_{\mathrm{PRT}} = \frac{V_{\mathrm{PRT}}^{+} - V_{\mathrm{PRT}}^{-}}{2} = IR_{\mathrm{PRT}} \tag{14}$$

Equation (14) is then the same as equation (11) for calculating resistance.

In the present work, a 6 ½ digit digital multimeter (DMM) with a scanning card (model: 2000-20, serial number 0832694) manufactured by Keithley Instruments was used for accurately measuring the voltage drop across the four-lead, 100 Ω PRT as well as to supply a stable 1 mA DC current through it. Out of the 20 channels in the two pole mode or the 10 channels in four pole mode available through the scanning card, channels 1 and 11 were used in the four pole mode for supplying constant

current to the PRT and measuring the voltage drop across it, respectively. A double pole double throw (DPDT), mechanical switch enclosed in an insulated aluminum box was used on the constant current supply leads to the PRT for alternating the direction of the current through the PRT. Figure 3.25 shows a schematic circuit diagram for accurate, four-lead PRT resistance measurement without thermoelectric effects described in principle in Figures 3.23 and 3.24. All the connections with the DPDT switch were made with low thermal connection silver solder. The copper braiding of the two cables with the extension leads of the PRT and the braiding of the scanner card cable were connected to a junction inside the aluminum box housing the DPDT switch, in order to reduce interference from noise signals. The scanner card cable shell into which the braiding terminated was instead connected to the DMM ground terminal.

The measured resistance of the PRT given by equation (11) or (14) was converted to temperature according to the International Temperature Scale of 1990 (ITS-90) described by Preston-Thomas (1990) and the calibration constants for the PRT determined by Minco (2000). The deviation equations and reference equations of ITS-90 along with their constants are presented in Appendix D.

For temperature measurement with accuracy of ±10 mK with the PRT temperature sensitivity of 0.3925 mΩ/mK, R_{PRT} had to be measured with an accuracy of ±3.925 mΩ. For a stable current of 1 mA used to measure approximately 100 Ω, V_{PRT} had to be measured with an accuracy of ±3.925 μV. Thus, the effect of noise or current reversal could have been tolerated only with an uncertainty smaller than ±3.925 μV. The temperature thermostating and measurement system was tested by performing several tests at constant temperatures in the range (270 to 340) K [(26.33 to 152.33) ^{o}F, (-3.15 to 66.85) ^{o}C] with the cell either under vacuum or at atmospheric pressure. Results from these tests have been presented in Appendix E. R_{PRT} was measured while alternating the current direction every minute over a 20 minute period. An average value with positive and negative current over the entire 20 minute period, average$^{+/-}$, an average value with only positive current during the 20 minute period, average^{+}, and an average value with only negative current, average^{-}, during the 20 minute period along with their standard

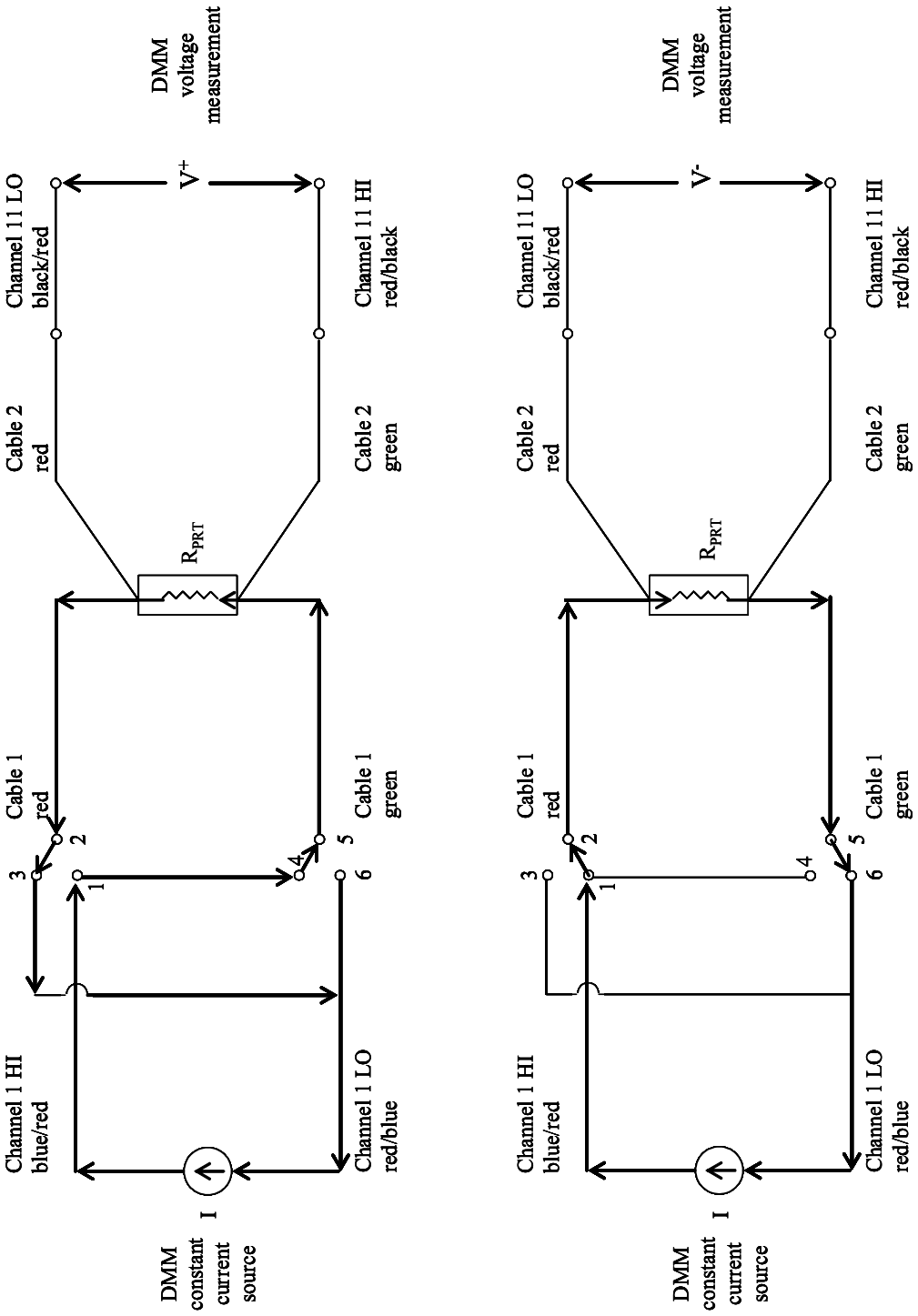

Figure 3.25. Temperature Measurement Scheme with Four-lead PRT and Current Reversal

deviations are shown in Table E.1. Tables E.2 and E.3 present corresponding values for V_{PRT} and T. The difference between resistance values with positive and negative currents, (average^{+}-average^{-})/2 was found to be smaller than ±3.925 mΩ. The corresponding voltage differences were smaller than ±3.925 μV and the temperature differences were smaller than ±10 mK. Stabilities of measured temperatures during density measurements for pure components and natural gas mixtures are presented in Chapter V.

The resistance of the PRT at TPW, R (273.16 K) which appears in equation D.1 of Appendix D, was measured twice over the density measurement period to ensure that it had not drifted with time from its original value given by Minco (2000). The temperature measurement accuracy of better than ±10 mK was based upon the assumption that the current was so stable that its contribution to temperature measurement uncertainty was zero. For this reason, the long-term stability/drift of the 1 mA DC current source of the Keithley DMM was checked by measuring the resistance of a standard four lead resistor. Results of the TPW test, the test for stability of the current source and details regarding the original calibration of the PRT and subsequent calibration checks are presented in Chapter IV. A thermopile with six, type T, copper-constantan thermocouple junctions and a Keithley DMM (model 195) were used to measure the thermoelectric voltage difference, ΔV, generated by any small axial temperature gradient, ΔT, between the top and the bottom of the MSD cell. ΔV in μV was converted to ΔT in ^{o}C using:

$$\Delta T = \left(\frac{\Delta V}{S} \right) \frac{1}{n} \tag{15}$$

where, n = 3 and S is the Seebeck coefficient in μV/ ^{o}C for the copper-constantan thermocouple. Burns *et al.* (1993) have given the reference functions according to ITS-90 for type T thermocouples which express the thermoelectric voltage as a function of temperature. S was calculated at the cell temperature measured by the PRT as the first

derivative of the reference function. Temperature gradients in the range (0 to100) mK at 340 K [152.33 ^{o}F, 66.85 ^{o}C] and (0 to -100) mK at 270 K [26.33 ^{o}F, -3.15 ^{o}C] were observed between the top and the bottom of the MSD cell.

3.3.8 Data Acquisition and Computer Control

A Dell Optiplex GX240 desktop computer with a Pentium® 4 processor was used for data acquisition and control purposes. A PCI-GPIB and a PCI-232/4 card manufactured by National Instruments were used for interfacing the IEEE 488 and RS-232 communication ports. The model 730 intelligent electronics and digital display boxes could communicate through the RS-232 serial port. Digiquartz® Assistant version 1 and Digiquartz® Interactive programs provided by Paroscientific Inc. were used for data acquisition and initial configuration of the pressure transducers respectively. The Keithley DMM with scanner card could communicate through the IEEE 488 bus. A program was written for acquisition of PRT resistance data using National Instruments LabVIEW version 6i software. The MSA operation control and weighing balance data acquisition were accomplished through the LPT port of the computer using the Messpro program provided by Rubotherm. Emergency back-up power supplies were used to keep the experimental set-up powered in case of a power shut-down so that the MSA did not lose control of the sinker position.

The forerun feature of Messpro allowed three transitions between the ZP and the MP positions for initial alignment of the MSA parts upon being newly installed or to remove any misalignments because of disturbances caused by rapidly charging or discharging gas to and from the cell. A settling time of at least one minute was allowed after a transition from a ZP or a MP position or upon turning the SC ‘on’. Typically a 30 to 40 minute period was allowed after thermal and pressure equilibration for each density measurement. An average of the 30 to 40 pressure, temperature and balance readings over this period collected at a frequency of one datum per minute was then used for density measurement. Messpro also made provision for auto-calibration of the

weighing balance with the SC 'on' before every density measurement, for taring the balance in the ZP position at the beginning of a measurement, for adjusting the frequency of revisiting the ZP position to check the drift in the balance reading and for applying a correction to the balance reading in the MP position to account for the balance drift.

3.4 Specific Tests and Observations with the Magnetic Suspension Densitometer Operation

Several peculiarities about the operation of the compact single-sinker MSD that affect the accuracy of density measurements were observed.

3.4.1 Effect of Proximity of a Stray Magnetic Source to the Magnetic Suspension Densitometer

For calculation of the measured density from the MSD, equation (8) can be expressed as:

$$\rho = \frac{\left(m_{\mathrm{v}}^{\mathrm{MP}} - m_{\mathrm{v}}^{\mathrm{ZP}}\right) - \left(m_{\mathrm{a}}^{\mathrm{MP}} - m_{\mathrm{a}}^{\mathrm{ZP}}\right)}{v_{\mathrm{S}}} \tag{16}$$

where,

$m_{\mathrm{v}}^{\mathrm{MP}}$ = balance reading in MP position with cell under vacuum

$m_{\mathrm{v}}^{\mathrm{ZP}}$ = balance reading in ZP position with cell under vacuum

$m_{\mathrm{a}}^{\mathrm{MP}}$ = balance reading in MP position with cell under pressure and

$m_{\mathrm{a}}^{\mathrm{ZP}}$ = balance reading in ZP position with cell under pressure

If e is the error in the balance reading introduced because of the presence of a stray magnetic source close to the MSA, equation (16) becomes:

$$\rho = \frac{\left(\left(m_{\mathrm{v}}^{\mathrm{MP}} + e_{\mathrm{v}}^{\mathrm{MP}}\right) - \left(m_{\mathrm{v}}^{\mathrm{ZP}} + e_{\mathrm{v}}^{\mathrm{ZP}}\right)\right) - \left(\left(m_{\mathrm{a}}^{\mathrm{MP}} + e_{\mathrm{a}}^{\mathrm{MP}}\right) - \left(m_{\mathrm{a}}^{\mathrm{ZP}} + e_{\mathrm{a}}^{\mathrm{ZP}}\right)\right)}{v_{\mathrm{S}}} \tag{17}$$

or

$$\rho = \frac{\left(\left(m_{\mathrm{v}}^{\mathrm{MP}} - m_{\mathrm{v}}^{\mathrm{ZP}}\right) - \left(m_{\mathrm{a}}^{\mathrm{MP}} - m_{\mathrm{a}}^{\mathrm{ZP}}\right)\right) + \left(\left(e_{\mathrm{v}}^{\mathrm{MP}} - e_{\mathrm{v}}^{\mathrm{ZP}}\right) - \left(e_{\mathrm{a}}^{\mathrm{MP}} - e_{\mathrm{a}}^{\mathrm{ZP}}\right)\right)}{v_s} \tag{18}$$

where, the subscripts and superscripts of *e* follow those of *m*. The differences between errors in balance readings in the ZP and MP positions in vacuum and under pressure are:

$$\Delta e_{\mathrm{v}} = e_{\mathrm{v}}^{\mathrm{MP}} - e_{\mathrm{v}}^{\mathrm{ZP}} \tag{19}$$

and $$\Delta e_{\mathrm{a}} = e_{\mathrm{a}}^{\mathrm{MP}} - e_{\mathrm{a}}^{\mathrm{ZP}} \tag{20}$$

If the errors in the balance readings in the ZP and MP positions caused by stray magnetism are the same, both in vacuum and under pressure, then $\Delta e_{\mathrm{v}} = \Delta e_{\mathrm{a}} = 0$ and equation (18) would reduce to equation (16).

The errors in the balance readings may be introduced by either a fixed or a variable stray magnetic source. $e_{\mathrm{a}}^{\mathrm{ZP}}$ is the error in the balance reading when only the permanent magnet weighing 8.72713 g and the bearing cone weighing 1.48958 g at ambient pressure and temperature are in suspension under pressure as a single piece weighing 10.21671 g. $e_{\mathrm{a}}^{\mathrm{MP}}$ is the error in the balance reading when the titanium sinker weighing 30.37391 g at ambient *T* and *P* is also in suspension in addition to the permanent magnet/bearing cone assembly under pressure. These two errors would be unequal at all pressures in the presence of a fixed, stray magnetic source because of the different weights being measured. Moreover, they would also be a function of density

because the buoyant force acting on the permanent magnet/bearing cone assembly or the sinker is a function of density. Among pure methane, nitrogen and argon as experimental fluids for density measurements in the pressure and temperature ranges of interest for the present project, the maximum buoyant force on the sinker of 4.17097 g and on the permanent magnet/bearing cone assembly of 1.40546 g is exerted by argon at 270 K [26.33 ^{o}F, -3.15 ^{o}C] and 34.474 MPa [5,000 psia] at a density of 619.044 kg/m^3. On the lower end, the buoyancy force on the sinker of 0.00388 g and on the permanent magnet/bearing cone assembly of 0.00131 g is exerted by methane at 340 K [152.33 ^{o}F, 66.85 ^{o}C] and atmospheric pressure at a density of 0.576 kg/m^3. Even if the permanent magnet/bearing cone assembly only and the sinker in addition to the permanent magnet/bearing cone assembly are in suspension in vacuum with and without a fixed stray magnetic source, the respective errors e_v^{ZP} and e_v^{MP} would be different because of different weights being measured. Thus, not only are Δe_a and Δe_v non-zero values for a fixed stray magnetic source but they also are unequal. The difference between them is a function of the density and can lead to a systematic error in the measured density.

A test was performed to simulate the presence of a few fixed stray magnetic sources close to the MSD cell in its old location as shown in Figure 3.15. The struts in the wall, the Julabo constant temperature circulator bath wall, the cinder block supports, a high pressure fitting gland nut, a ring on the PRT lead connector and the concrete reinforcement grid in the floor were potential stray magnetic sources. An 86 cm tall unistrut was held parallel to the axis of the MSD cell at different distances to simulate the struts in the wall. The top end of the unistrut was approximately at the height of the permanent magnet inside the cell. A magnetic steel sheet 58 cm wide and 48 cm high, the top edge of which was held at 70 cm from the floor was held at different distances to simulate the wall of the Julabo constant temperature circulation bath. A stack of cinder blocks was held 20 cm away from the cell axis and 10 cm below the MSD cell. The steps followed and the corresponding balance readings have been summarized in Table 3.4 for the test with the unistrut and in Table 3.5 for the test with the metal sheet and cinder blocks. The test was performed with the MSD cell at ambient

Table 3.4. Effect of Unistrut as a Stray Magnetic Source on the Balance Readings

Step No.	Description of step and balance reading	Distance of unistrut from cell axis (cm)								
		110	**100**	**90**	**80**	**70**	**60**	**50**	**40**	**30**
1	No source of stray magnetism ZP position (g) and balance tared	0.00000	0.00000	0.00000	0.00000	0.00000	0.00000	0.00000	0.00000	0.00000
2	No source of stray magnetism MP position (g)	30.37560	30.37562	30.37562	30.37563	30.37564	30.37562	30.37559	30.37558	30.37556
3	Source of stray magnetism introduced MP position (g)	30.37559	30.37562	30.37561	30.37560	30.37558	30.37552	30.37543	30.37531	30.37505
4	Source of stray magnetism continued to be held ZP position (g)	0.00000	0.00001	0.00000	-0.00001	-0.00003	-0.00009	-0.00015	-0.00027	-0.00050
5	Source of stray magnetism removed ZP position (g)	0.00002	0.00003	0.00003	0.00003	0.00004	0.00001	-0.00001	-0.00003	-0.00003
2 - 3	Error in MP position balance reading (mg) due to stray magnetism	0.01	0.00	0.01	0.02	0.06	0.10	0.16	0.27	0.51
1 - 4	Error in ZP position balance reading (mg) due to stray magnetism	0.00	-0.01	0.00	0.01	0.03	0.09	0.15	0.27	0.50

Table 3.5. Effect of Cinder Blocks and a Metal Sheet as Stray Magnetic Sources on the Balance Readings

Step No.	Description of step and balance reading	Distance of cinder blocks from cell axis (cm)	Distance of metal sheet from cell axis (cm)				
		20	110	90	70	50	30
1	No source of stray magnetism ZP position (g) and balance tared	0.00000	0.00000	-0.00001	-0.00001	0.00000	0.00000
2	No source of stray magnetism MP position (g)	30.37561	30.37557	30.37556	30.37557	30.37558	30.37557
3	Source of stray magnetism introduced MP position (g)	30.37563	30.37557	30.37554	30.37550	30.37544	30.37528
4	Source of stray magnetism continued to be held ZP position (g)	0.00005	0.00000	-0.00003	-0.00006	-0.00012	-0.00027
5	Source of stray magnetism removed ZP position (g)	0.00005	0.00000	0.00000	0.00000	0.00003	0.00001
2 - 3	Error in MP position balance reading (mg) due to stray magnetism	-0.02	0.00	0.02	0.07	0.14	0.29
1 - 4	Error in ZP position balance reading (mg) due to stray magnetism	-0.04	0.00	0.02	0.05	0.12	0.27

temperature and pressure. Figure 3.26 shows increasing errors in the balance readings in the ZP and MP positions upon holding the unistrut and metal sheet closer to the MSD cell axis while the cinder blocks had no effect even if placed as close as 20 cm. The different fixed stray magnetic sources within 1 m of the MSD cell in its old location are also shown. The combined effect of these fixed stray magnetic sources went undetected during acquisition of the balance readings as these were stable but became evident as a constant percentage offset in comparing the experimental and predicted densities for pure methane and argon in the range (270 to 340) K [(26.33 to 152.33) ^{o}F, (-3.15 to 66.85) ^{o}C] and (3.447 to 34.474) MPa [(500 to 5,000) psia].

A variable stray magnetic source that is within 1 m of the MSD could cause a random error in density depending upon the intensity, and period over which either e_{a}^{ZP}, e_{a}^{MP}, e_{v}^{ZP} or e_{v}^{MP} is introduced. A person passing/standing within 1 m of the MSD with a magnetic object would be an example of such a variable stray magnetic source.

3.4.2 Test for Optimum Vertical Distance of the Electromagnet from the Electromagnet Well Bottom and for the Range of Operation of the Magnetic Suspension Assembly

A test with the MSD cell and the old sinker at an ambient *T* of 297.15 K [75.2 ^{o}F, 24 ^{o}C] and ambient *P* was performed without using the weight changing device to decide the optimum vertical distance of the electromagnet from the electromagnet well bottom. The vertical position of the electromagnet was varied between half and four turns by rotating the electromagnet suspension tube while holding the electromagnet connection assembly fixed, after having lowered the electromagnet completely so as to touch the electromagnet well bottom. This was equivalent to moving the electromagnet through a vertical distance of only 2 mm because of the electromagnet suspension tube screw pitch of approximately 0.5 mm per turn. The reference position for zero turns of the electromagnet was sensed physically as well as by an ‘underload’ balance display.

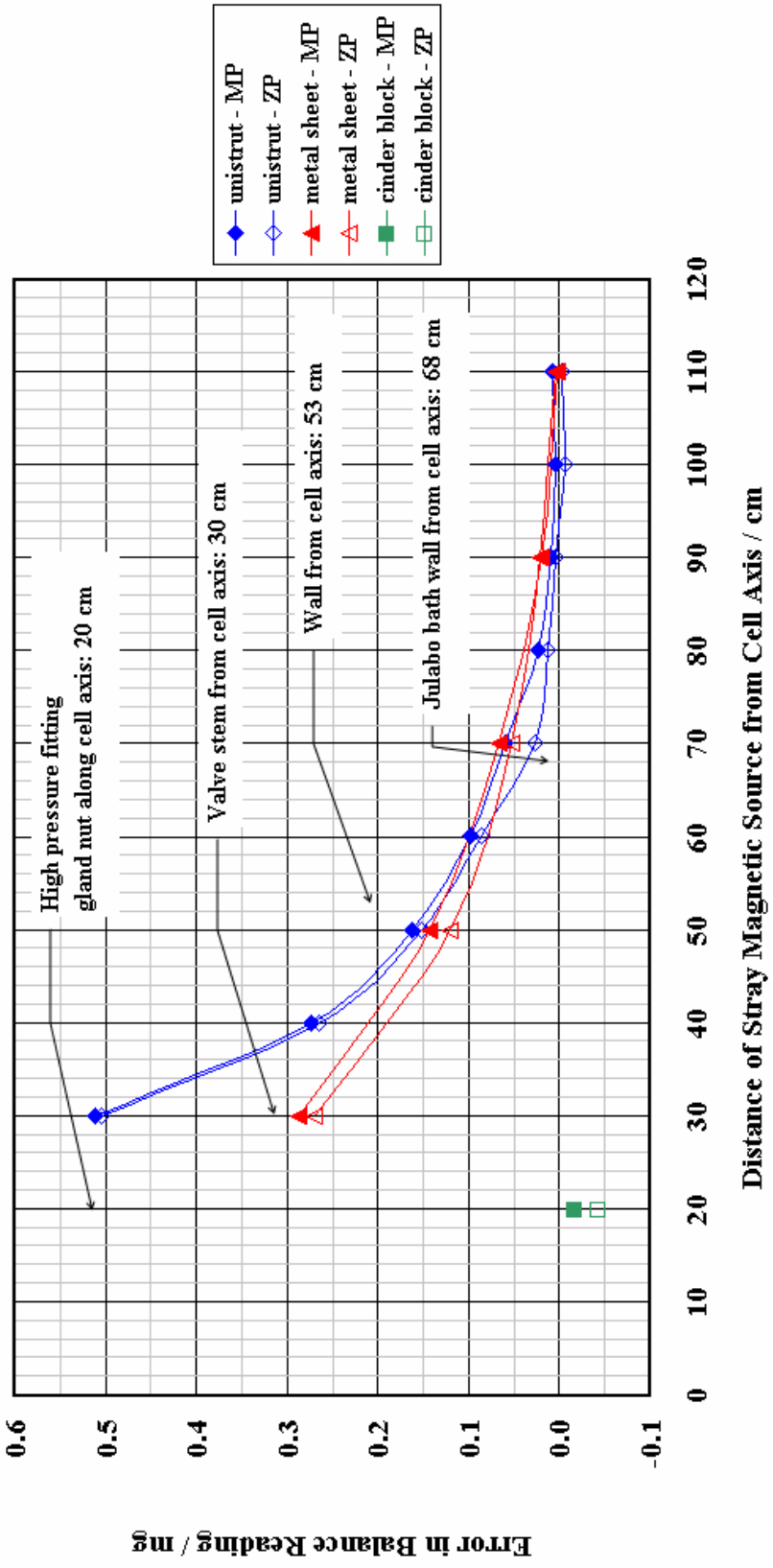

Figure 3.26. Effect of Stray Magnetic Sources on Magnetic Field of Electromagnet in the Old Location of the MSD

Table 3.6 shows the observed balance readings and the sensor signal, U_a values with the SC 'off' and for the ZP and MP positions with the SC 'on'. Figure 3.27 shows the balance reference reading and Figure 3.28 shows the U_a signals from the MSA control box at different vertical positions of the electromagnet from the bottom of the electromagnet well. The U_a signals for both the ZP and the MP positions with the SC 'on', increased with increase in the number of turns of the electromagnet from the electromagnet well bottom, but the with the SC 'off' it remained unaffected.

If the electromagnet was positioned between half and one turn from the electromagnet well bottom so as to get a balance reference reading of approximately -5.9 g as instructed by Rubotherm (1999), the MSA went out of control more frequently. This was evident as unstable and non-repeatable balance readings in the ZP and MP positions caused by the MSA parts touching the MSD cell walls because of small clearances between them, as shown earlier in Figures 3.4 and 3.5. Another indication that the MSA parts were touching the cell walls was the inability of the balance to auto-calibrate with the SC 'on'. The clearest indications of the MSA going out of control were unusual balance readings and U_a signals and subsequent inability to transition between ZP and MP positions. On the other hand, if the electromagnet was positioned at more than three turns from the electromagnet well, the MSA control was able to raise the permanent magnet and bearing cone assembly to the ZP position but unable to raise the sinker to the MP position. The electromagnet was therefore positioned at approximately two turns from the electromagnet well bottom while measuring isotherms 1 through 26. Thus, the decision to maintain the vertical position of the electromagnet at two rather than at half a turn from the electromagnet well bottom led to fewer occasions when the MSA went out of control and required less frequent horizontal and vertical alignments of the balance base plate, the aluminum frame and the electromagnet suspension tube in the thermostating tube.

While the operation of the MSA with a vertical position of the electromagnet of two turns from the electromagnet well bottom has been tested for stability, accuracy and range of operation for densities up to 620 kg/m^3 with pure

Table 3.6. Effect of Changing Vertical Distance of Electromagnet from the Electromagnet Well Bottom with the Old Sinker

Number of turns of electromagnet from electromagnet well bottom	SC 'off'		SC 'on' - ZP position		SC 'on' - MP position	
	Balance reference reading	U_a signal	Balance reading	U_a signal	Balance reading	U_a signal
	g	V	g	V	g	V
0.5	-5.64810	6.00947	0.00003	6.56978	30.37437	8.63229
0.5	-5.55736	6.01812	0.00001	6.57131	30.37483	8.59298
0.5	-	-	-0.00003	6.56801	30.37480	8.58005
1.0	-6.14857	6.00870	0.00003	6.72668	30.37512	8.91270
1.5	-6.27983	6.01541	0.00000	6.76718	30.37538	8.96419
2.0	-6.53057	6.00305	-0.00002	6.85462	30.37583	9.11904
3.0	-7.06323	6.02935	0.00005	7.11203	30.37724	9.39680
3.5	-7.20017	6.05190	0.00000	7.23414	-7.04024	6.05316
4.0	-7.44874	6.01818	0.00001	7.36877	-7.27612	6.06314

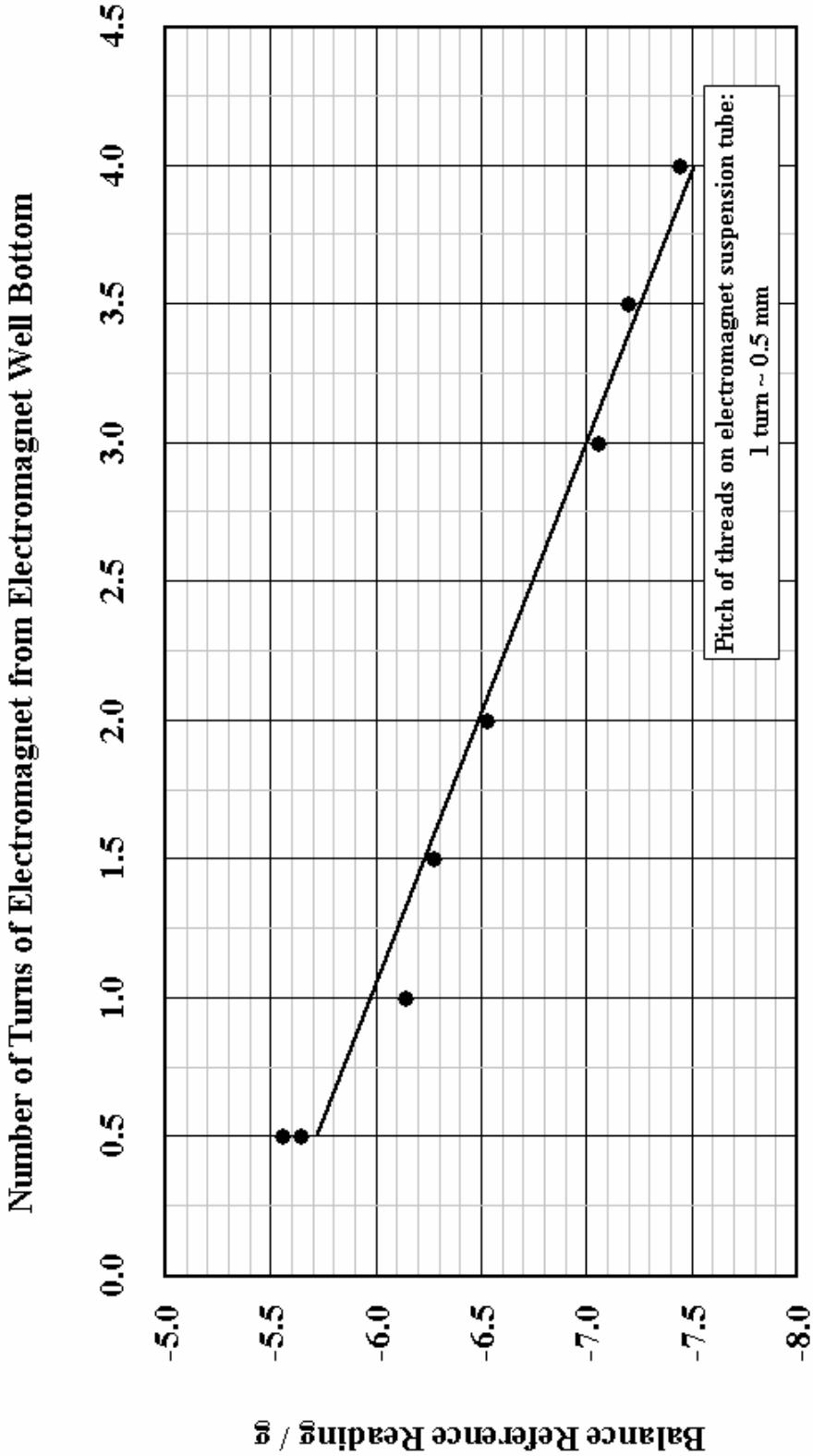

Figure 3.27. Effect of Changing Vertical Position of the Electromagnet on the Balance Reference Reading at Ambient Temperature and Pressure

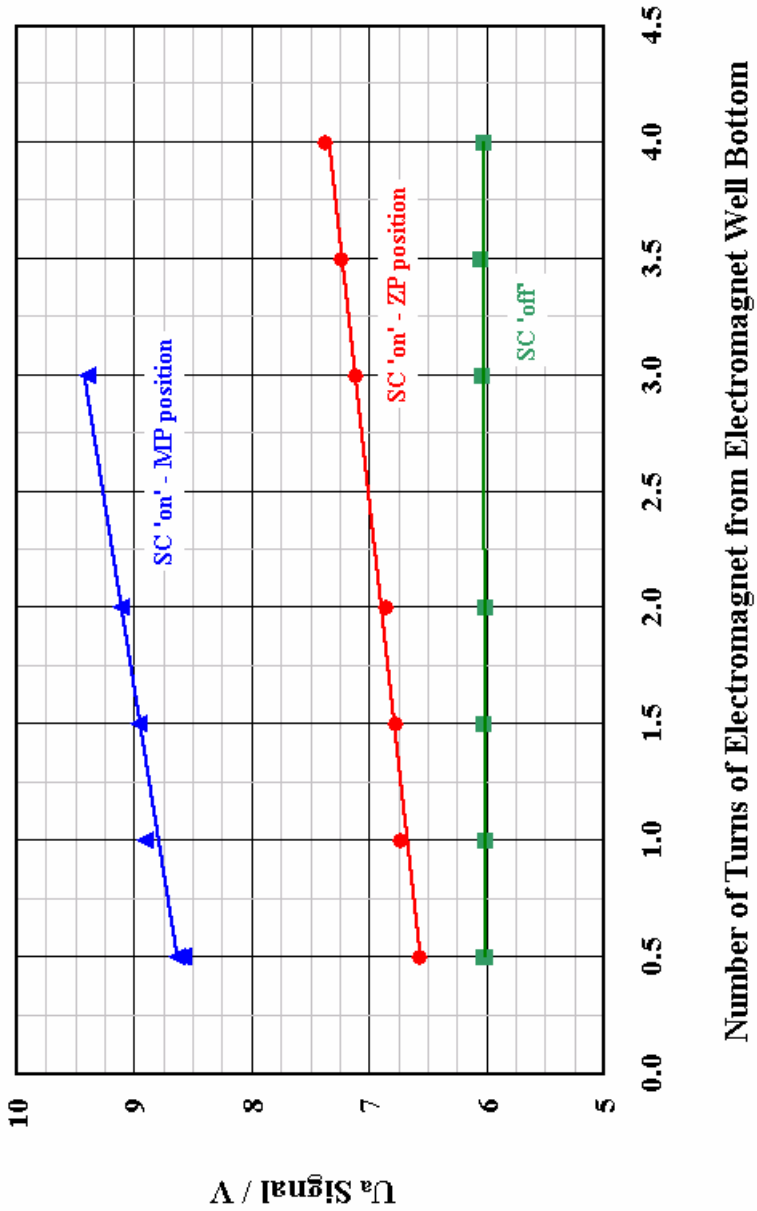

Figure 3.28. Effect of Changing Vertical Position of the Electromagnet on the U_a Signal with the SC 'on' and 'off' at Ambient Temperature and Pressure

methane, nitrogen, argon and the natural gas mixtures M91C1 and M94C1 over the range (270 to 340) K [(26.33 to 152.33) ^{o}F, (-3.15 to 66.85) ^{o}C] and up to 34.474 MPa [5,000 psia], its operation for measurement of higher densities remains largely untested. The MSD cell was tested twice over the entire range of operation of the MSA up to 206.843 MPa [30,000 psia] with argon at ambient T without thermostating, with the electromagnet vertical position of half a turn from the electromagnet well bottom and without using the weight-changing device. During the first test performed in January 2002 with the MSD in its old location, the MSA control could raise and lower the sinker for the MP and ZP positions respectively up to 68.948 MPa [10,000 psia] but went out of control at higher pressures especially while lowering the sinker from the MP position to the ZP position. The balance reading failed to return to the tared zero value assumed in the ZP position before raising the sinker and instead displayed a value between zero and the MP position reading. The second test was performed in September 2002 in the new location of the MSD. Figure 3.29 shows the balance readings for the sinker mass when it was held continuously in the MP position and the corresponding U_a signals of the MSA control box. A similar test at ambient T over the entire P range up to 206.843 MPa [30,000 psia] where the sinker was raised to the MP position and lowered to the ZP position several times at each P also confirmed smooth operation of the MSA. However, the effect of expansion of the MSA parts at higher temperatures on their clearances with the cell internal walls and the corresponding stabilities and operation of the MSA control have not been tested. The more frequent failure of the MSA control above 68.948 MPa [10,000 psia] during the January 2002 test may have been not only because of the vertical distance of the electromagnet being half a turn from the electromagnet well bottom but also because of stray magnetic sources in the old location of the MSD, inaccurate horizontal and vertical alignments of the MSA parts and incorrect gas charging/discharging procedure. The axial centrality of the MSA parts is disturbed if the cell pressure is rapidly increased or decreased by direct compression in to the cell or by opening the cell discharge valve while the SC is ‘on’ and the MSA parts are either in ZP or MP positions.

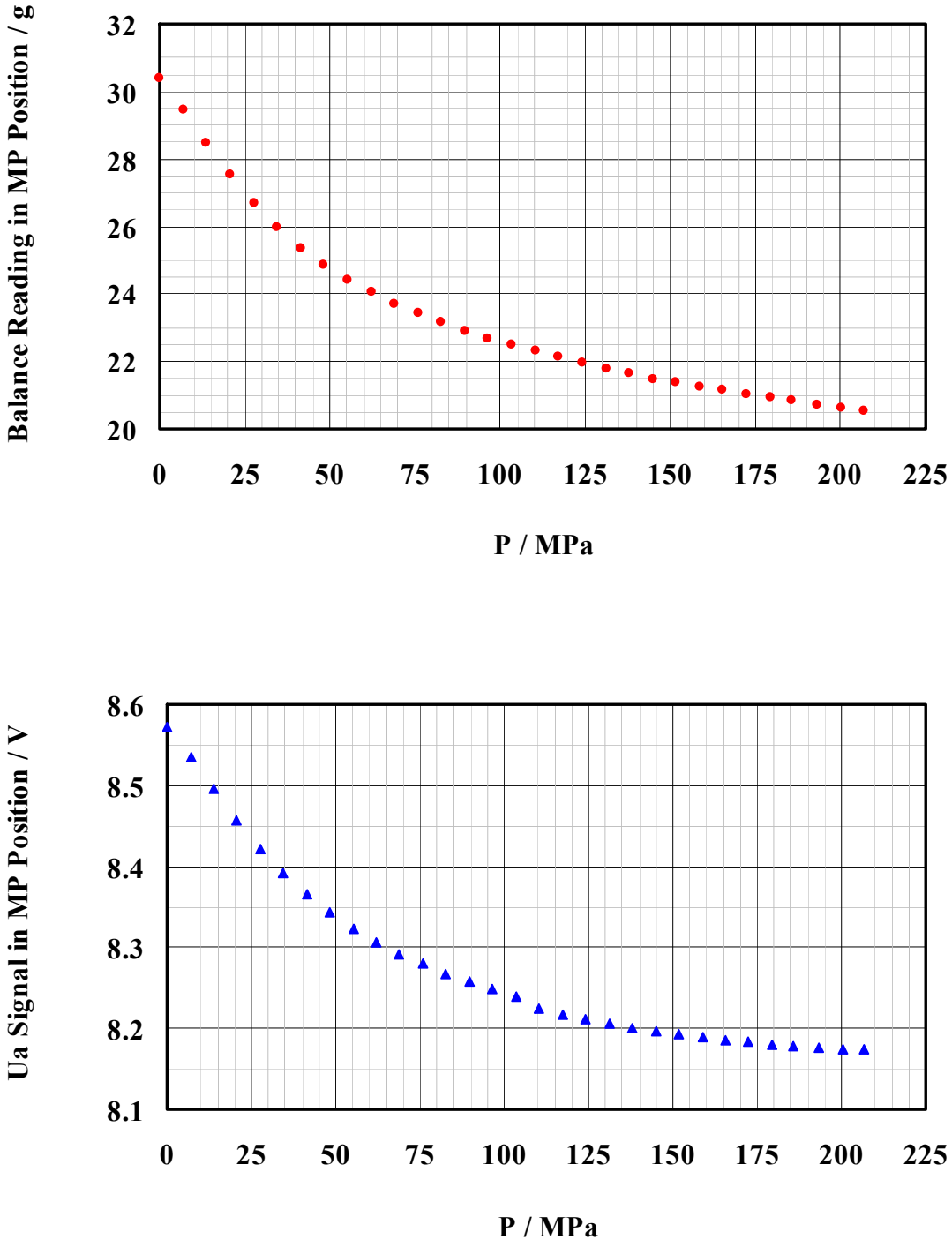

Figure 3.29 Balance Readings and Corresponding U_a Signals in MP Position over the Entire Pressure Range of Operation of the MSA

3.4.3 Loss of Magnetic Suspension Assembly Control

When aligning the MSD assembly the following steps were performed sequentially: (i) horizontal leveling of the balance base plate with a Hahn and Kolb Stuttgart liquid bubble level with an accuracy of 0.1 mm/m (ii) horizontal leveling of the balance on the aluminum frame using the leveling screws of the balance (iii) adjustment of the vertical distance of the electromagnet at two turns from the electromagnet well bottom (iv) centering of the electromagnet suspension tube in the thermostating tube by horizontally moving the aluminum frame (v) gentle tightening of the two screws under the balance base plate to prevent the frame from moving horizontally, without changing the electromagnet vertical position substantially. Following such an initial adjustment, stable balance readings in the MP position were observed in the continuous mode of operation with periodic revisits to the ZP position, to check for balance drift. Most often, it was immediately following such ZP revisits that the MSA went out of control gradually over a period of a few minutes. The balance readings and U_a signal readings during this period that were between those for ZP and MP positions implied that the permanent magnet/bearing cone assembly was still in a state of levitation until the permanent magnet reached its final position where it became stuck at the top of the high pressure chamber top while the sinker had dropped down to its rest position.

Such occasions at the new location of the MSD, when the MSA went out of control despite having adjusted the electromagnet at a vertical position of two turns from the electromagnet well bottom, having aligned horizontally and vertically the MSD assembly, not having any stray magnetic sources within a distance of 1 m of the MSD and having used a slow rate of gas charging or discharging, arose possibly because the MSA parts touched the cell internal walls caused by swaying of the building through several inches. For intense swaying, the MSA probably went completely out of control while for mild swaying it destabilized over the duration of the swaying and recovered stability thereafter.

Table 3.7 shows comparisons of the expected and observed values of signals from the MSA control box immediately following such occasions when the MSA went out of control and also after taking remedial steps. If the MSA went out of control, the following remedial steps were taken: (i) the signals at the back of the control box were observed (ii) the MSA control box power was switched 'off' (iii) the electromagnet suspension tube was gently raised through a distance of two to three mm to separate the permanent magnet from the electromagnet and the cell wall (iv) the electromagnet tube was centered in the thermostating tube (v) the MSA control box power was switched 'on' again and (vi) the signals at the back of the control box were observed again according to instructions 7.2 and 7.2.1 of Rubotherm (1999). An audible 'click' when the electromagnet suspension tube was raised and attainment of the expected value of the U_a signal confirmed that the permanent magnet/bearing cone assembly had fallen down to its rest position. Switching the control box power 'off' and 'on' again was necessary to reset the U_R and U_{KSH} signals.

The electromagnet voltage, U_m, was observed to detect and quantify instabilities in the balance reading in the ZP and MP positions because of the MSA parts touching the cell walls as a result of mild swaying of the building. Table 3.8 shows a sequence of steps followed along with the corresponding U_a signals and the range of the U_m signal while operating the MSA in the manual mode with the weight changing device, the vertical position of the electromagnet at two turns from the electromagnet well bottom and the new sinker while the cell was under vacuum at 340 K [152.33 ^{o}F, 66.85 ^{o}C]. The average U_m signal was found to be in the range (-8 to -9) mV for stable balance readings in the ZP or MP position of the MSA.

Table 3.7. Signals after Loss of MSA Control and after Remedial Steps

Isotherm identity		21	23	24
Observations after MSA went out of control				
Signal identity	**Expected value (V)**	**Observed value (V)**		
- 15 V (power supply)	- (15 ± 0.5)	-15.1127	-15.0993	-15.1043
+15 V (power supply)	+ (15 ± 0.5)	14.8792	14.8870	14.8868
+18 V (power supply)	+ (18 ± 0.5)	17.8631	17.8564	17.8650
- 18 V (power supply)	- (18 ± 0.5)	-18.0631	-18.0638	-18.0653
U_s (initial set-point)	~ - 5.5	-13.3938	13.5780	13.5898
U_a (sensor signal)	~ + 5.5	7.3653	5.6054	7.5710
U_{ag} (control difference)	0	6.0438	-13.0500	-13.0425
U_R (controller output)	~ - 0.2	-13.4248	13.5689	13.5683
U_m (electromagnet voltage)	0	-0.0001	0.0014	0.0033
U_{KSH}	0	2.0456	-2.0438	-2.0444
U_{KSR}	0	0.0003	-0.0009	-0.0003
Observations after remedial steps				
Signal identity	**Expected value (V)**	**Observed value (V)**		
- 15 V (power supply)	- (15 ± 0.5)	-15.0989	-15.1022	-15.0996
+15 V (power supply)	+ (15 ± 0.5)	14.8901	14.8881	14.8893
+18 V (power supply)	+ (18 ± 0.5)	17.8788	17.8717	17.8797
- 18 V (power supply)	- (18 ± 0.5)	-18.0521	-18.0605	-18.0528
U_s (initial set-point)	~ - 5.5	-5.6387	-5.5888	-5.8080
U_a (sensor signal)	~ + 5.5	5.6514	5.6005	5.8213
U_{ag} (control difference)	0	0.0162	0.0148	0.0157
U_R (controller output)	~ - 0.2	-0.4022	-0.3641	-0.3790
U_m (electromagnet voltage)	0	-0.0013	-0.0006	-0.0036
U_{KSH}	0	0.0033	0.0032	0.0032
U_{KSR}	0	-0.0002	-0.0018	-0.0002

Table 3.8. U_a and U_m Signals during Stable Operation of MSA in Vacuum at 340 K with the New Sinker

Description of step	Position of MSA	Balance reading	U_a	U_m range	
				from	to
		g	V	mV	
Control box main power 'off'		-48.10999	-0.00002		0.0
Power to control boxes switched 'on' but SC 'off'		-48.11049	5.63389		0.9
SC switched 'on'	ZP	-41.61796	6.49037	-6.9	-6.9
Balance tared	ZP	0.00000	6.49120	-11.9	-12.4
Ta weight lowered on balance pan	ZP	41.61844	6.48514	-12.8	-13.0
Balance tared	ZP	0.00000	6.48511	-6.7	-7.6
Ta weight raised from balance pan	ZP	-41.61842	6.50345	-7.0	-9.0
Ti weight lowered on balance pan	ZP	-30.38507	6.49810	-6.8	-7.0
Sinker raised	MP	0.01372	8.69500	-2.0	-15.0
Sinker lowered	ZP	-30.38508	6.49500	-6.2	-8.8
Sinker raised	MP	0.01375	8.71297	-4.8	-12.0
Sinker lowered	ZP	-30.38508	6.49760	-6.4	-8.4
Sinker raised	MP	0.01376	8.70000	-1.7	-15.2
Sinker lowered (balance tared accidentally)	ZP	0.00000	6.49724	-5.8	-8.5
Ti weight raised from balance pan	ZP	-11.23334	6.50244	-9.8	-11.6
Ta weight lowered on balance pan	ZP	30.38511	6.47953	-10.6	-12.7
Balance tared	ZP	0.00000	6.47912	-6.2	-8.2
Ta weight raised from balance pan	ZP	-41.61845	6.49665	-6.3	-8.1
Ti weight lowered on balance pan	ZP	-30.38510	6.49348	-6.4	-8.2
Sinker raised	MP	0.01377	8.69500	-5.9	-14.2
Sinker lowered	ZP	-30.38510	6.50222	-7.0	-7.4
Ti weight raised from balance pan	ZP	-41.61843	6.50688	-9.0	-9.6
SC switched 'off'		-48.11843	5.67926		0.9
SC switched 'on'	ZP	-41.61840	6.49357	-9.8	-10.5
SC switched 'off'		-48.12331	5.67162		1.1
Control box main power switched 'off'		-48.12292	-0.00002		0.0

3.4.4 Test for Magnetic Suspension Assembly Buoyancy Force Transmission Error

An error of up to ±0.003% can be introduced in transmitting the buoyancy force through the MSA because the copper beryllium material of the cell around the MSA is not magnetically neutral but slightly diamagnetic (International Union of Pure and Applied Chemistry, 2003). The apparent sinker weights measured directly over the balance pan and through the MSA at ambient *T* and *P* were compared to ascertain that the non-physical contact force transmission through the MSA did not introduce errors in the balance readings during density measurements. The weighing balance of the MSD was used for direct measurements after dismantling the MSA from the hook under it. Similarly, the sinker true weights were measured at ambient *T* and under vacuum to remove the effect of ambient air buoyancy force on the sinker. Table 3.9 shows the results of this test performed over a period of eight months approximately three years since the MSD was manufactured. Although the observed uncertainty of ±0.006% over this period was larger than the manufacturer's original uncertainty of ±0.003% it was small compared to the intended ±0.03% uncertainty in density measurement. The small increase in uncertainty of force transmission may have been caused by weakening of the magnetic field of the permanent magnet because of aging. The results also show that the uncertainty in force transmitted by the MSA increases with increase in the vertical distance of the electromagnet from the electromagnet well bottom. Table 3.9 also shows the weights of the titanium and tantalum masses measured directly over the balance pan at ambient temperature and pressure.

The force transmission error (FTE) is also a weak function of temperature that can introduce errors in the balance reading (Rubotherm, 1999). The true weight of the sinker in vacuum at 340 K [152.33 ^{o}F, 66.85 ^{o}C] was found to be larger than that at 270 K [26.33 ^{o}F, -3.15 ^{o}C] by up to 0.15 mg leading to an error of 0.0005%. The *T* dependence of the FTE can be measured by evacuating the cell with the sinker in the MP position and increasing the cell *T* in stages, allowing time for equilibration at each *T*.

Table 3.9. Sinker Weights Measured Directly over Balance Pan and through MSA

Weights measured and conditions	Old sinker				New sinker			
	over balance pan	through MSA			over balance pan	through MSA		
Date test performed	06/22/02	06/21/02	10/23/02	01/17/03	03/11/03	03/14/03	03/17/03	03/17/03
Vertical position of electromagnet (turns)	-	two	two	half	-	half	one	two
Ambient temperature and pressure								
Sinker weight (g)	30.37391	30.37560	30.37572	30.37485	30.38812	30.38916	30.38940	30.39000
Temperature (K)	297.15	293.15	293.53	293.65	297.039	296.483	295.15	295.15
Pressure (MPa)	0.1	0.1	0.1	0.1	0.1	0.1	0.1	0.1
Buoyancy due to air (g)	0.00790	0.00801	0.00794	0.00800	0.00780	0.00784	0.00787	0.00787
Error (%)		0.006	0.006	0.003		0.003	0.004	0.006
Ambient temperature and vacuum								
Sinker weight (g)	30.38181	30.38348	30.38351	30.38301	30.39592	30.39700	30.39727	30.39787
Error (%)		0.005	0.006	0.004		0.004	0.004	0.006
Ambient temperature and pressure								
Tantalum weight (g)	41.61804				41.61823			
Titanium weight (g)	11.23311				11.23328			

However, if the MSA went out of control from touching of the MSA parts to the cell inner walls as they expanded with increasing *T*, such a test would be inconclusive because of the slight change in the horizontal position of the electromagnet after lifting the electromagnet to separate it from the permanent magnet. Instead, the true mass of the sinker was weighed in vacuum at the beginning of each isotherm, the cell *P* increased for density measurements and the measurement for true mass of the sinker in vacuum repeated at the end of the isotherm. The repeated measurement was necessary to ensure that there was no addition of contaminants such as compressor oil during pure or gas mixture density measurements and no condensation in the cell during gas mixture density measurements.

3.4.5 Effect of Magnetic Suspension Densitometer Cell Temperature Gradients

Upon evacuating the cell with the sinker raised to the MP position for measurement of its true mass at a *T*, the balance reading was found to pass through fluctuations for a period of a few hours before it could stabilize. The fluctuations are similar to those caused by Knudsen forces acting on the balance through an object such as the sinker that experiences *T* gradients at low pressures (Massen *et al.*, 1984; Garcia Fierro and Alvarez Garcia, 1981). Not only is it important to keep the sinker in a state of levitation while evacuating the cell at a particular temperature but also to allow sufficient equilibrium time for dampening the Knudsen effect before accurately measuring the true mass of the sinker. Figure 3.30 shows the balance readings using the weight changing device with the new sinker in a state of levitation while the cell was being evacuated at 305 K. While measuring isotherms 1 through 26 periods of at least (8 to 10) hours were allowed for cell evacuation despite observing the Knudsen effect only during the first few hours.

During a density measurement, the volume of the gas sample under pressure within V5 on the old manifold, VI1 and either VS6K and VG2K or VS2K and VG6K on the new manifold was at the most 25 cm^3 of which approximately 19.5 cm^3

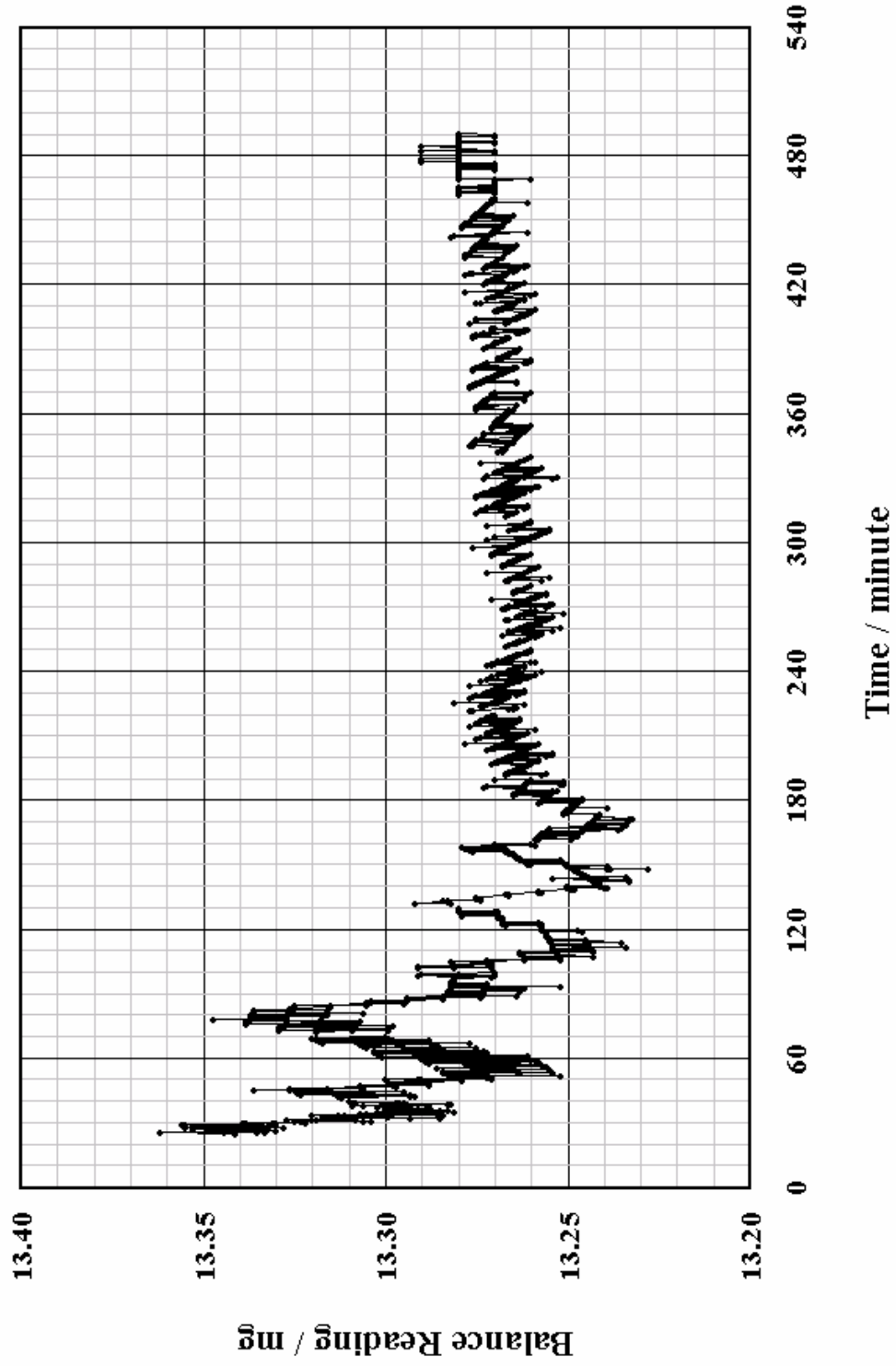

Figure 3.30. Fluctuations in the Balance Readings in MP Position during Cell Evacuation because of Knudsen Force

volume was that of the high pressure chamber of the MSD cell and the remaining 5.5 cm^3 was that from the tubing and fittings. The cell temperature either increased or decreased through a few hundred mK depending on the rate of charge of gas into or out of the cell. A predictive analysis with the sinker in levitation would have helped determine the time required for equilibrium after the sinker and cell experienced radial and/or axial *T* gradients following charging or discharging. Any *T* gradients would have introduced instabilities in the balance readings because of convective circulation of the gas in the cell. The observed stabilities of the balance readings were used as indicators of attaining equilibrium rather than the predictive analysis. Attaining equilibrium was confirmed through repeatable density measurements under similar conditions over two or three different 30 minute periods following the first 30 minute period after equilibration. The observed thermal and pressure equilibration period after charging the cell with gas was approximately two hours, but a systematic observation of the equilibration period after discharging gas was not performed.

3.4.6 Open Cage Test for Magnetic Suspension Assembly Operation

An aluminum cage equal in height to the copper beryllium cell was used to replace the cell between the thermostating flange and the stainless steel flange of the cell with the sinker rest and the sensor coil. The operation of the MSA was observed to relate the balance instability to the settling time of physical movements of the permanent magnet/bearing cone assembly in the ZP position or the permanent magnet/bearing cone assembly and the sinker in the MP position. Appendix F provides video clips of the MSA operation. Planar, axial and rotational oscillations while in levitation and rocking of the permanent magnet/bearing cone assembly when the SC was switched ‘off’ were observed. For a vertical and horizontal alignment of the MSD apparatus such that the MSA parts do not touch the cell inner walls, the oscillations dampen within a minute but can cause the MSA to go out of control if the MSA parts touch the walls. The rocking

motion on the other hand can cause the permanent magnet/bearing cone assembly to settle into a rest position that is not along the cell axis.

CHAPTER IV

INSTRUMENT CALIBRATION AND TRACEABILITY

4.1 Pressure Transducer Calibration and Traceability

The pressure transducers PT02K and PT06K were calibrated *in-situ* against a Ruska Instrument Corporation, manually operated DWG (model: 2450-701, serial number: 19851) using a Ruska, oil-gas DPI (model: 2411.1, serial number: 8886). The stainless steel diaphragm of the DPI separated the oil in its top chamber connected to the DWG and the gas in its bottom chamber connected to the old manifold and pressure transducers. Each chamber of the DPI had a maximum operating pressure of 103.421 MPa [15,000 psia] while the tungsten carbide piston cylinder assembly (serial number: V-519) of the DWG had an operating range of up to 275.790 MPa [40,000 psi]. The shift in the zero position of the DPI electronic null indicator of approximately 0.275 KPa [0.04 psia] when pressurized up to 103.421 MPa [15,000 psia] is large compared to pressure differentials as small as 0.689 Pa [0.0001 psia] that a DPI can detect (Ruska Instruments Corporation, 1961). Over the P range of (3.447 to 34.474) MPa [(500 to 5,000) psia] of interest for the present project, the shift in the zero point of the DPI null indicator could have introduced an uncertainty of at the most ±0.008 % which was smaller than the targeted uncertainty for P measurements of ±0.01 %. The shift in zero position caused by over pressurization was nullified electronically by using the zero adjustment knob of the DPI. To prevent shifts in the zero position of the DPI null indicator, the overpressure was always applied from the top chamber containing oil. A stainless steel 303, class 'S' weight set (model: 2450-707-00, serial number: 23353) manufactured by Ruska was used to balance the fluid pressure on the piston cylinder assembly. The cross sectional area of the piston cylinder assembly at 296.15 K [73.4 ^{o}F, 23 ^{o}C], A_o and the mass of each weight of the weight set were calibrated in June 2003

and are traceable to NIST standards (Ruska Instruments Corporation, 2003). A barometer manufactured by Paroscientific (model: 740-16B, serial number: 55782) with a NIST traceable calibration in the range (0.079 to 0.110) MPa [(11.5 to 16) psia] was used for measuring the atmospheric *P*. Figure 4.1 shows the schematic flow diagram for the DWG/DPI setup for calibrating the pressure transducers. The approximately 6.7 m [22 feet] long stainless steel tubing with an internal diameter of 0.0508 cm [0.02 inch] and outer diameter of 0.3175 cm [0.125 inch], connecting V13 of the old manifold shown in Figures 3.16 through 3.19 to the calibration setup, was always maintained at ambient *T* and was not heat-traced. A Ruska hand pump (model: 2427-801, serial number: 23940) and HP1 on the old manifold were used to manipulate the oil and gas pressures respectively. Corrections were applied to the pressure measured by the DWG/DPI setup to account for the temperature and elastic distortion of the piston and cylinder, the effect of gravity on the masses, the buoyant effect of air, the pressure head between the DWG reference plane of measurement and the DPI diaphragm, the taring components and oil surface tension effects as described by Ruska Instruments Corporation (1977). The DWG/DPI setup was expected to measure pressures with an uncertainty of ±0.005 % of the reading which was better than the uncertainty of ±0.01 % of full scale for pressure measurements using PT02K and PT06K.

4.1.1 May 15, 2003 Calibration of PT06K

PT06K was calibrated at an ambient *T* of approximately 298.15K [77 ^{o}F, 25 ^{o}C] while it was connected to the top of the cell as shown in Figure 3.17. The calibration data in units of MPa was fit to a simple linear regression model whose coefficients were determined by the method of least squares and can be expressed as:

$$P_{\mathrm{DWG/DPI}} = 0.9997966\, P_{\mathrm{PT06K}} + 0.0001716 \qquad (21)$$

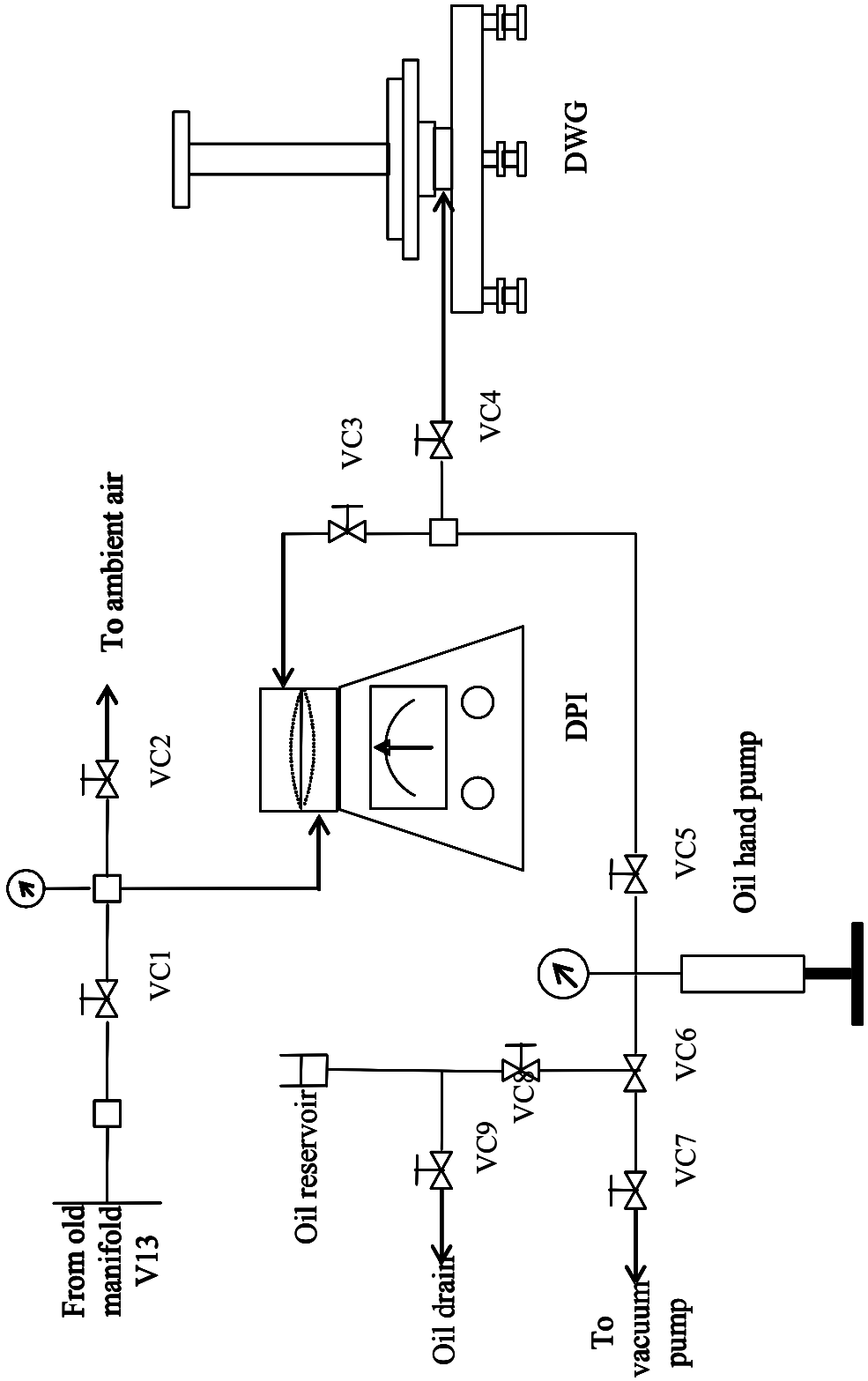

Figure 4.1. DWG/DPI Setup for Pressure Transducer Calibration

Equation (21) was used to calculate the true P from that measured by PT06K for isotherms 1 through 12.

4.1.2 July 25, July 28 and July 29, 2003 Calibrations of PT06K

PT06K was enclosed in the aluminum heater block described in subsection 3.3.5 and calibrated at an ambient T of approximately 298.15 K [77 ^{o}F, 25 ^{o}C], 323.15 K [122 ^{o}F, 50 ^{o}C] and 353.15 K [176 ^{o}F, 80 ^{o}C] while it was connected to the top of the cell as shown in Figure 3.18 to include the effect of temperature on its calibration. The calibration data in MPa at each temperature was fit to a simple linear regression model by the method of least squares and can be represented as:

$$P_{DWG/DPI} = 0.9999862\ P_{PT06K} - 0.0023817 \text{ at } 25\ ^{o}\text{C, (July 25, 2003)} \quad (22)$$

$$P_{DWG/DPI} = 1.0000418\ P_{PT06K} - 0.0022657 \text{ at } 50\ ^{o}\text{C, (July 28, 2003)} \quad (23)$$

$$P_{DWG/DPI} = 1.0000904\ P_{PT06K} - 0.0020396 \text{ at } 80\ ^{o}\text{C, (July 29, 2003)} \quad (24)$$

The intercept, I and slope, S of the linear fit for the calibrations were found to be a function of the internal temperature of PT06K, T_{PT06K}. Linear fits for the T dependence of the intercept and the slope can be represented as:

$$I\ (T_{PT06K}) = 0.0000062634\ T_{PT06K} - 0.0025526 \quad (25)$$

and

$$S\ (T_{PT06K}) = 0.000001885\ T_{PT06K} + 0.9999420 \quad (26)$$

where, T_{PT06K} is expressed in ^{o}C. Thus, the overall linear calibration equation including T dependence is:

$$P_{DWG/DPI} = S\,(T_{PT06K})\,P_{PT06K} + I\,(T_{PT06K}) \tag{27}$$

The equivalent of equation (27) for PT06K used for pure component isotherms 19 and 20 and for natural gas mixture isotherms 13 through 18 is:

$$P_{DWG/DPI} = -0.0025526 + 6.2634 \times 10^{-6}\,T_{PT06K} + (0.9999420 + 1.885 \times 10^{-6}\,T_{PT06K})\,P_{PT06K} \tag{28}$$

4.1.3 December 23 and 28, 2003 Calibrations of PT06K and PT02K

PT06K and PT02K were calibrated at 325.15 K [125.6 ^{o}F, 52 ^{o}C] and 339.15 K [150.8 ^{o}F, 66 ^{o}C] respectively while they were connected to the top of the cell as shown in Figure 3.19. PT06K and PT02K were simultaneously calibrated at pressures approximately 0.103 MPa [15 psia] above and below every pressure at which density was measured during pure component isotherms 21 and 22 on December 23 and 28, 2003. A linearly interpolated value between the calibration pressures was used to express the pressure for an experimental density measurement. For gas mixture isotherms 23 through 26, the two sets of calibrations performed on December 23 and 28, 2003 were combined and a simple least squares linear regression fit used to calculate the true P and can be represented in units of MPa as:

$$P_{DWG/DPI} = 1.0000855\,P_{PT06K} + 0.0001030 \tag{29}$$

The equivalent calibration equation for PT02K can be represented as:

$$P_{DWG/DPI} = 0.9996559\,P_{PT02K} - 0.0003569 \tag{30}$$

4.1.4 Discussion on Pressure Transducer Calibrations

Tables 4.1 and 4.2 summarize the data for six calibrations of PT06K and two calibrations of PT02K against the DWG/DPI setup respectively along with the temperatures of the transducers and values for the slope and intercept for the least squares simple linear regression fits. The plots along the left hand side of Figure 4.2 show the absolute residuals between the linear fit and the true pressure from the DWG/DPI setup at the 95% confidence level for all calibrations of PT06K and PT02K, while those on the right hand side show the corresponding relative residuals. In general, the relative residuals are within ±0.01% for PT06K except at pressures lower than approximately 6.998 MPa [1,015 psia] where they are within ±0.0125%. Similarly, the relative residuals for PT02K are in general within ±0.01% except at pressures lower than approximately 6.998 MPa [1,015 psia]. The reasons for the larger residuals between the true P measured by the DWG and the predicted P from the linear fit or the P measured by either PT02K or PT06K lower than approximately 7 MPa was the greater difficulty in balancing the pressures on the two sides of the DPI diaphragm and the DWG piston at the reference plane and the limitation in accuracy arising from the piston-cylinder assembly meant for pressure measurements up to 275.790 MPa [40,000 psia] being used to measure pressures as low as (3.447 to 6.998) MPa [(500 to 1,015) psia]. Balancing the DPI null indicator and the DWG were difficult because of higher compressibilities of argon and nitrogen used for calibrations at pressures lower than approximately 6.998 MPa [1,015 psia], the large tubing length of approximately 6.7 m between the old manifold and the DWG/DPI setup.

The pressure transducer readings under vacuum were close to the intercepts of the linear fits from the calibration data. Thus, the pressure transducer reading under vacuum could be used as a crude indicator of the change in the calibration for the short-term ranging over a few days. However, *in-situ* calibrations against the

Table 4.1. Calibration Data for PT06K against DWG/DPI

5/15/2003		7/25/2003		7/28/2003		7/29/2003		12/23/2003		12/28/2003	
298.15 K [25 °C]		298.15 K [25 °C]		323.15 K [50 °C]		353.15 K [80 °C]		325.15 K [52 °C]		325.15 K [52 °C]	
P_{PT06K}	$P_{DWG/DPI}$	P_{PT06K}	$P_{DWG/DPI}$	P_{PT06K}	$P_{DWG/DPI}$	P_{PT06K}	$P_{DWG/DPI}$	P_{PT06K}	$P_{DWG/DPI}$	P_{PT06K}	$P_{DWG/DPI}$
MPa											
3.338153	3.337418	3.340869	3.338212	3.340382	3.338212	3.339619	3.337801	3.337695	3.338365	3.337429	3.338194
3.544940	3.543967	3.547302	3.544769	3.546774	3.544778	3.546006	3.544352	3.544158	3.544929	3.544027	3.544751
6.781189	6.780304	6.783629	6.781076	6.783400	6.781091	6.781887	6.780598	6.780274	6.781436	6.781137	6.781484
6.988438	6.986855	6.990120	6.987620	6.989790	6.987651	6.988517	6.987136	6.986533	6.988004	6.987831	6.988028
10.224990	10.223174	10.226465	10.223998	10.225594	10.223966	10.224372	10.223440	10.223151	10.224305	10.223949	10.224477
10.431309	10.429702	10.432867	10.430547	10.432270	10.430514	10.431017	10.429983	10.429438	10.430839	10.430554	10.431039
13.667612	13.666088	13.669508	13.666942	13.668729	13.666892	13.667196	13.666327	13.665992	13.667417	13.667012	13.667808
13.874944	13.872624	13.876323	13.873523	13.875227	13.873441	13.873882	13.872882	13.872517	13.874002	13.873631	13.874399
17.111903	17.108560	17.112078	17.109428	17.110953	17.109343	17.109431	17.108792	17.108948	17.109925	17.109824	17.110503
17.318642	17.315116	17.318773	17.315986	17.317422	17.315877	17.316114	17.315328	17.315429	17.316508	17.316122	17.317087
20.555814	20.551578	20.555069	20.552513	20.553534	20.552327	20.551621	20.551749	20.551074	20.553221	20.551946	20.553857
20.761512	20.758145	20.761175	20.759065	20.760184	20.758870	20.758525	20.758318	20.757686	20.759804	20.758523	20.760448
24.000553	23.994691	23.998173	23.995591	23.996251	23.995405	23.994689	23.994844				
24.206775	24.201259	24.204785	24.202141	24.203172	24.201946	24.201248	24.201413				
27.443947	27.437853	27.440769	27.438711	27.439408	27.438496	27.437466	27.437944	27.437177	27.439978	27.437331	27.440042
27.649652	27.644398	27.647822	27.645278	27.646033	27.645065	27.644044	27.644518	27.644298	27.646577	27.643721	27.646583
30.886797	30.880910	30.885572	30.881784	30.882577	30.881540	30.880197	30.880994				
31.093502	31.087473	31.091009	31.088371	31.089112	31.088102	31.087145	31.087577				
34.331005	34.324200	34.328454	34.325087	34.325912	34.324785	34.323071	34.324257	34.323186	34.326732	34.323259	34.326454
34.537041	34.530792	34.534384	34.531640	34.532373	34.531328	34.529609	34.530833	34.530167	34.533335	34.530353	34.533056
Slope =	0.9997966	0.9999862		1.0000418		1.0000904		1.0000780		1.0000930	
Intercept =	0.0001716	-0.0023817		-0.0022657		-0.0020396		0.0004194		-0.0002134	

Table 4.2. Calibration Data for PT02K against DWG/DPI

12/23/2003		12/28/2003	
339.15 K [66 °C]		339.15 K [66 °C]	
P_{PT02K}	$P_{DWG/DPI}$	P_{PT02K}	$P_{DWG/DPI}$
MPa			
3.340118	3.338363	3.340187	3.338205
3.546655	3.544923	3.546802	3.544758
6.783388	6.781434	6.784288	6.781494
6.989438	6.987993	6.990858	6.988037
10.228106	10.224317	10.228496	10.224483
10.434397	10.430860	10.435073	10.431047
13.672783	13.667438	13.673052	13.667807
13.878998	13.874004	13.880030	13.874395
Slope =	0.9996457	0.9996661	
Intercept =	-0.0000189	-0.0006950	

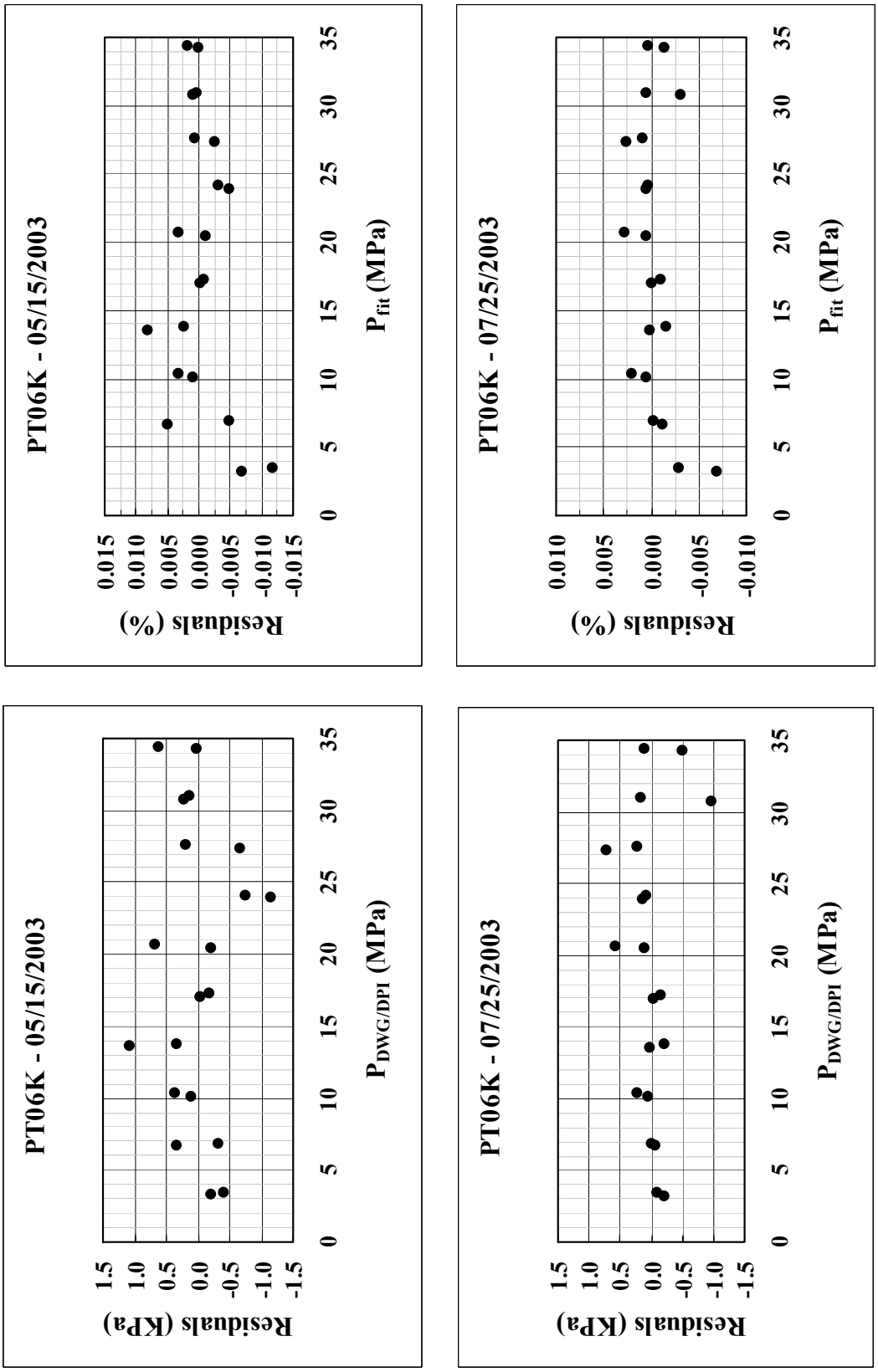

Figure 4.2. Absolute and Relative Residuals of Linear Fits for Calibrations of PT02K and PT06K against DWG/DPI

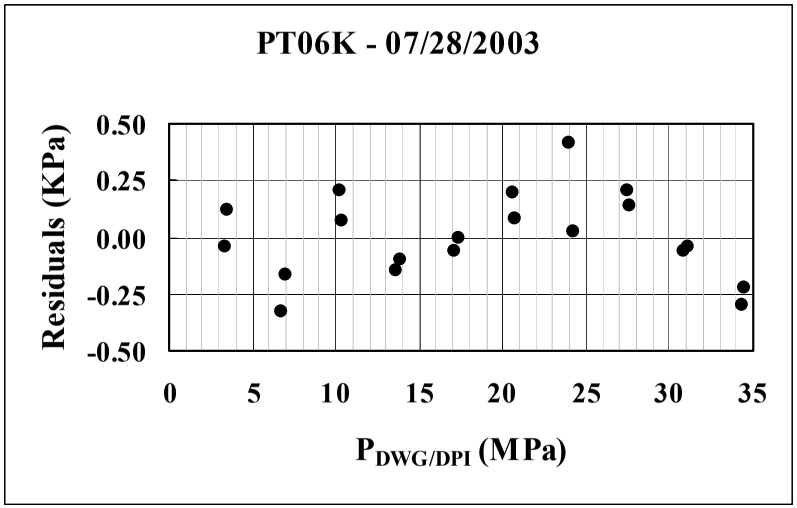

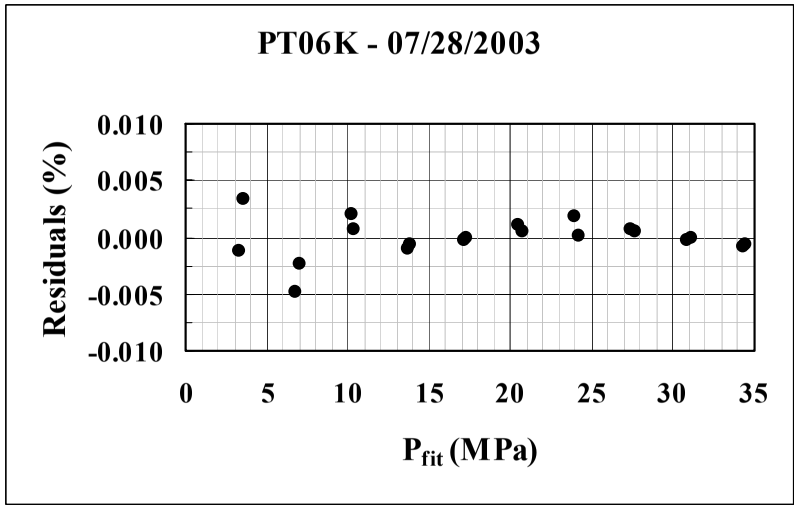

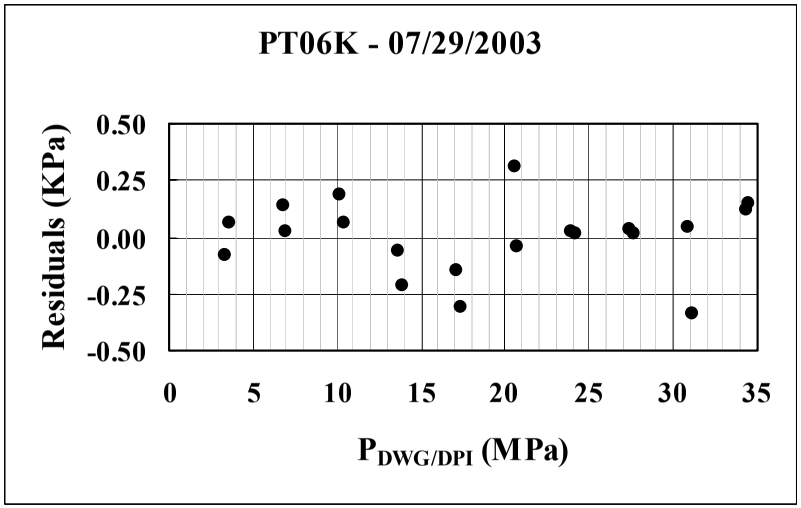

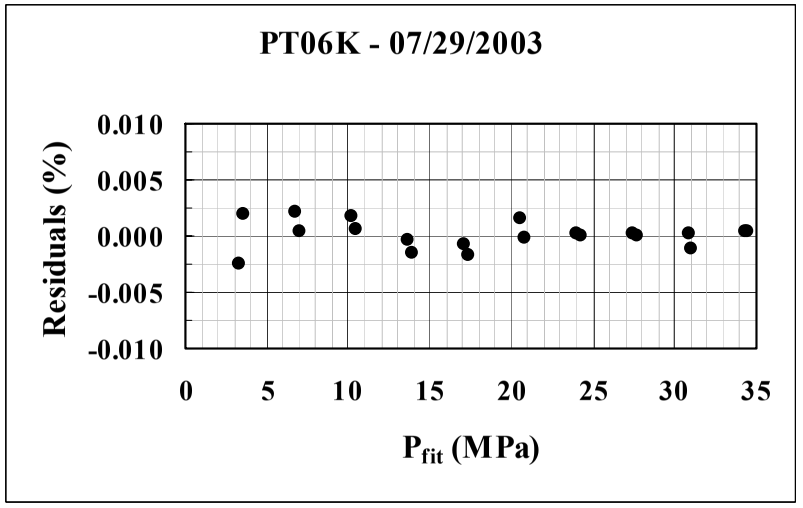

Figure 4.2. Absolute and Relative Residuals of Linear Fits for Calibrations of PT02K and PT06K against DWG/DPI (Continued)

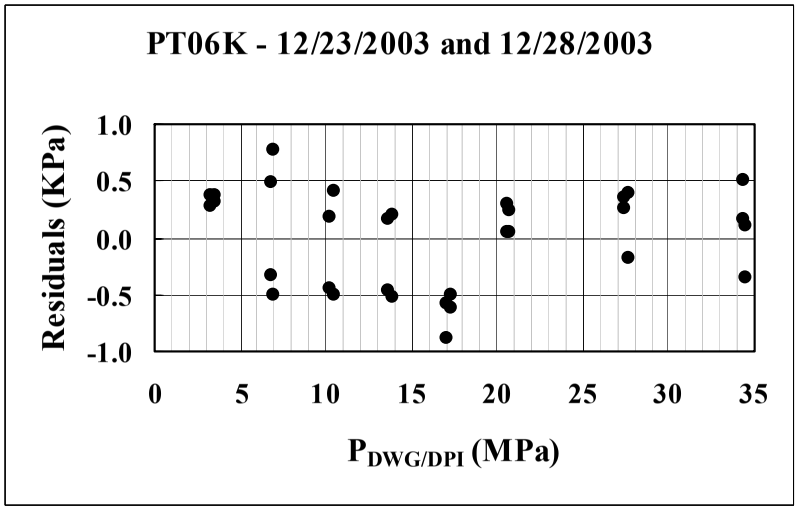

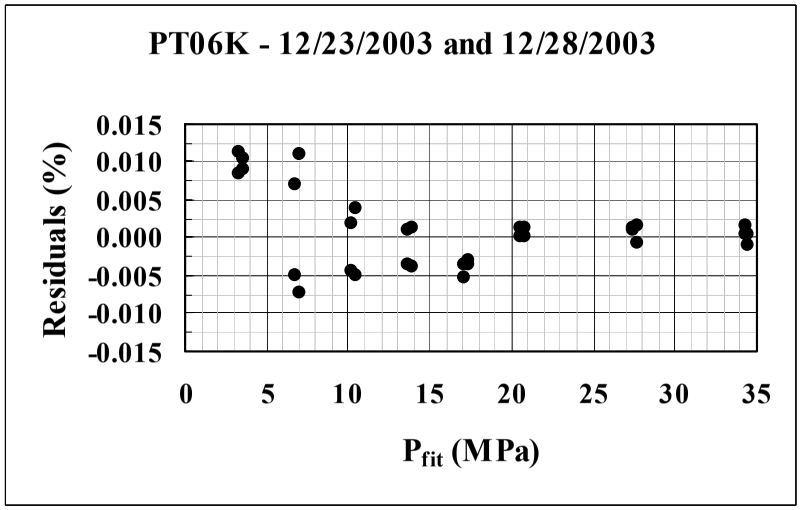

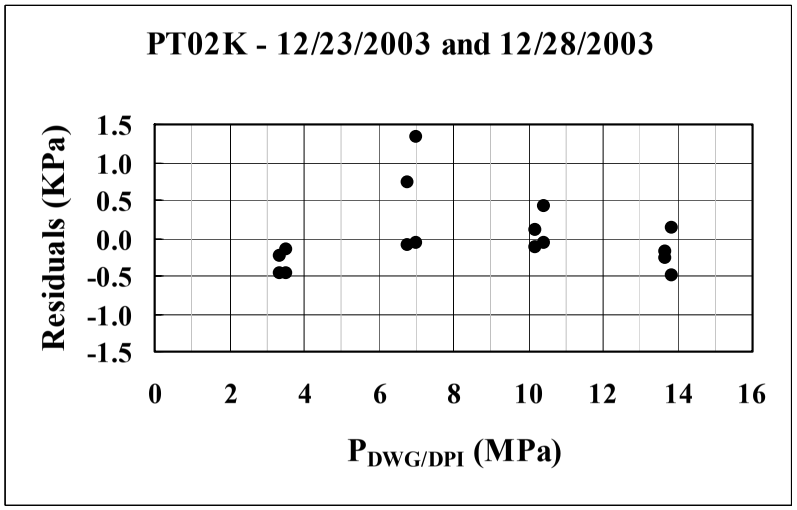

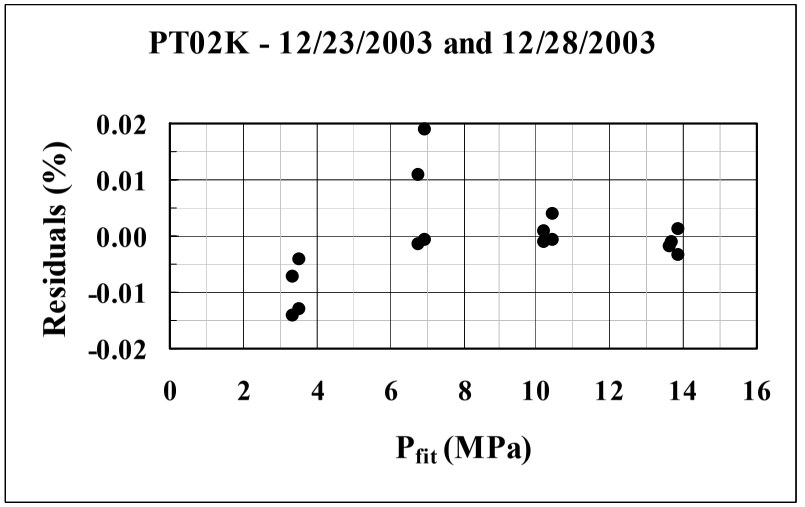

Figure 4.2. Absolute and Relative Residuals of Linear Fits for Calibrations of PT02K and PT06K against DWG/DPI (Continued)

DWG/DPI setup were still required to track changes in the slope of the calibration equation for the longer term, ranging over a few weeks.

The pressure transducer and barometer readings were monitored on a daily basis while measuring isotherms 21 and 22 with the goal of including the atmospheric pressure point in the transducer calibration data of December 23 and 28, 2003 presented in Tables 4.1 and 4.2. Simple linear regression fits including the atmospheric *P* point showed relative residuals as large as ±2.5% for PT06K and ±1% for PT02K at the atmospheric *P*. Comparison of linear fits including the atmospheric *P* point with those excluding it as given in subsection 4.1.3 and the observation of transducer readings under vacuum led to the conclusion that the linear calibration fit including the atmospheric *P* point should not be used.

4.2 Platinum Resistance Thermometer Calibration and Traceability

The PRT was calibrated by Minco (2000) according to ITS-90 at fixed *T* points or by comparison with a calibrated PRT traceable to NIST. Long-term drifts in the resistance of the PRT at the TPW, *R* (273.16 K) and the 1 mA DC current from the DMM were potential sources for inaccurate temperature measurements.

4.2.1 Drift in Resistance of Platinum Resistance Thermometer at the Triple Point of Water

The resistance of the PRT at the TPW, *R* (273.16 K) was measured twice using a TPW cell and the procedure described by Mangum and Furukawa (1990). If the newly measured *R* (273.16 K) was found to be different from its original value of 100.4244 Ω measured by Minco on November 16, 2000 such that the uncertainty of temperature measurement exceeded ±10 mK, the new value would need be used for subsequent temperature measurements. The first TPW cell test was done on May 16, 2002 with current reversal but with only the PRT suspended in the TPW cell. The

second TPW cell test was done on February 18, 2003 with current reversal and the copper isolation tubing of the PRT around it. A reproducible value of *R* (273.16 K) close to that of the original was indicative that the PRT calibration was undisturbed over its entire range.

Table 4.3 compares *R* (273.16 K) from the TPW cell tests with its original value. The May 16, 2002 test results show that *R* (273.16 K) had increased from its original value by only 0.748 mK and that the observed drift rate was also within the manufacturer's specified limit. However, the February 18, 2003 test results show that *R* (273.16 K) had increased from its original value by 17.376 mK which is much larger than the targeted ±10 mK uncertainty for temperature measurement. Figure 4.3 shows the temperature equivalent of the deviations of *R* (273.16 K) from its original value during the two tests. While the May 16, 2002 test shows stable deviations throughout the duration of the test indicating that the PRT had reached equilibrium, the February 18, 2003 test shows continuously increasing deviations. The increasing deviations with time of the test are indicative that the PRT did not reach equilibrium because of the continuous thermal conduction through the PRT isolation tube that was immersed in the TPW cell along with the PRT. For density measurements during the present work, the original value of *R* (273.16 K) given by the manufacture and confirmed through the May 16, 2002 test was used.

4.2.2 Drift in Constant Current Supplied to the Platinum Resistance Thermometer

A four-lead, standard 100 Ω resistor with an accuracy of ±0.01% and manufactured by Julie Research Laboratories (model: CH46T4 6AD4C) was used to check the stability of the Keithley DMM internal resistor and hence the current through the PRT. The standard resistor value was expected to vary over the range (99.990 to 100.010) Ω. The DMM was specified to measure a resistance in the 100 Ω range with an accuracy of ±(100 ppm of reading + 40 ppm of range) if maintained at (23 ± 5) ^{o}C over a

Table 4.3. TPW Cell Test Results Compared with Original Calibration of PRT

Description	Unit	Original	Present work	
		11/16/2000	**5/16/2002**	**2/18/2003**
R (273.16 K) original	Ω	100.424400	-	-
Average of measured R (273.16 K)	Ω	-	100.424695	100.431249
Period from original R (273.16 K) measurement	year	-	1.5	2.25
ΔR (273.16 K)	mΩ	-	0.295	6.849
TCR	Ω/Ω/K	0.003925	-	-
R (273.15 K)	Ω	100.4204	-	-
Sensitivity of R_{PRT} to temperature	mΩ/mK	0.3942	-	-
ΔT equivalent to ΔR (273.16 K)	mK	-	**0.748**	**17.376**
Standard deviation of ΔT	mK	-	**3.4**	**5.1**
ΔT per year	mK/year	-	0.5	7.7
		2.5	-	-

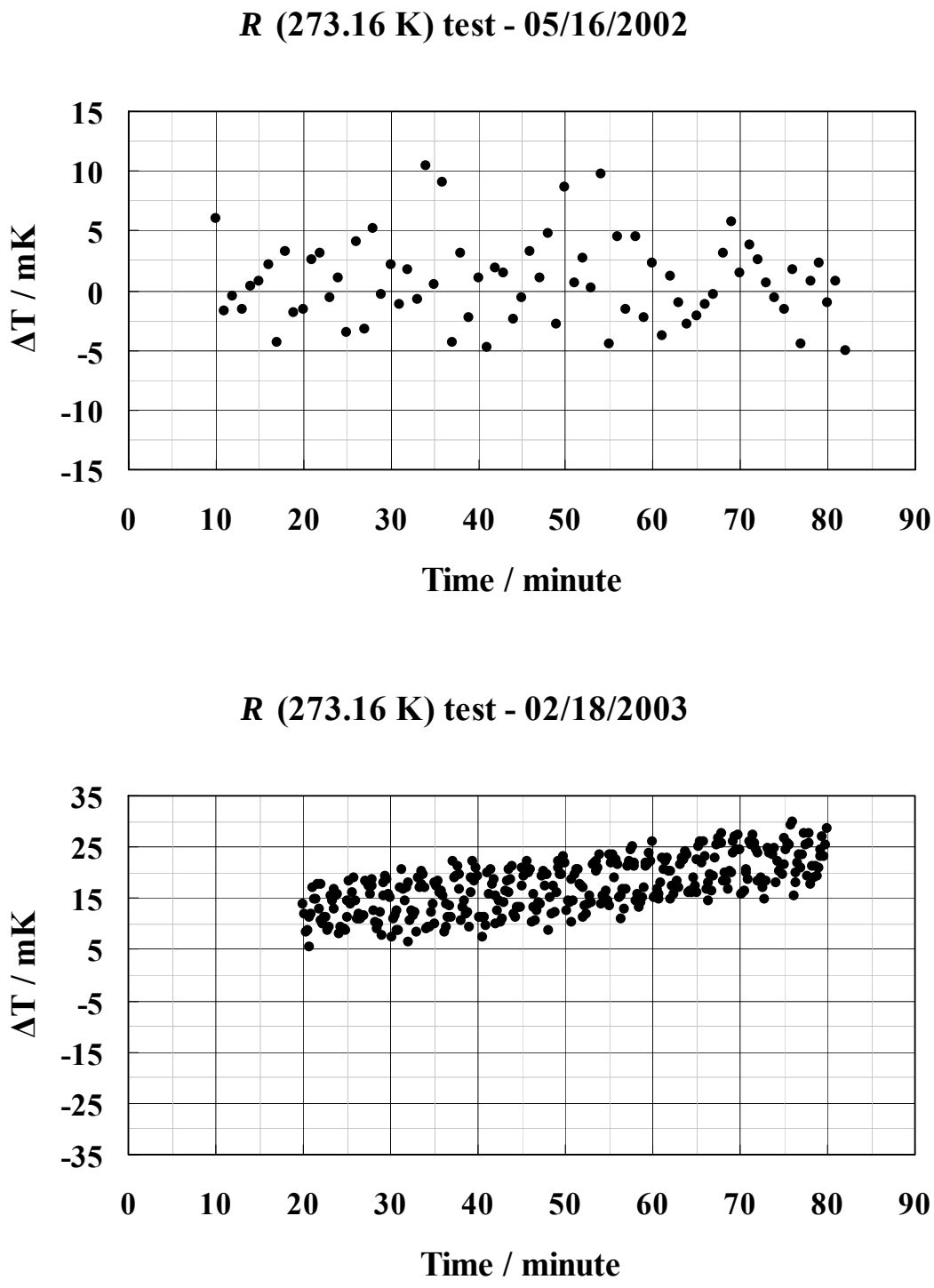

Figure 4.3. Temperature Equivalent of Deviations of the PRT Resistance at the TPW from Its Original Value

period of 1 year. Thus, for measuring an approximately 100 Ω resistance with the 100 Ω range, the DMM had an accuracy of ± 0.014 Ω and hence could measure the resistance as a value in the range (99.986 to 100.014) Ω. The standard resistor was wrapped in foam insulation and enclosed in an aluminum box to prevent temperature changes caused by air drafts. The resistor was connected directly to the DMM rather than through the scanner card, and its value was recorded periodically along with the corresponding ambient temperature. Between July 01, 2003 and December 10, 2003 when the DMM was maintained at (23.7 ± 2) ^{o}C, the average measured value of the standard resistor was 100.0058 Ω with an uncertainty of ±0.904 mΩ at the 68 % confidence level (1σ). The observed value of the standard resistor in the range (100.0049 to 100.0067) Ω confirmed that the DC current supplied to the PRT had not drifted.

4.3 Weighing Balance Calibration and Traceability

The weighing balance calibration was checked for linearity and range by Mettler Toledo (2002) on June 21, 2002. The weights used to test the balance calibration were traceable to NIST. The deviations of the observed balance readings over the range (0 to 200) g were found to be within the manufacturer's specification.

4.4 Sinker Volume Calibration and Traceability

The reference sinker volume referred to in subsection 3.2.5 was measured by Rubotherm for the two titanium sinkers used in the present work. The volume of the old sinker measured on November 6, 1998 was (6.73777 ± 0.0014) cm^3 (Rubotherm, 1998) and that of the new sinker measured on January 20, 2003 was (6.74083 ± 0.0034) cm^3 (Rubotherm, 2003) at the approximately 68% confidence level (1σ). The MSD uncertainty of ±0.03% at the 68% confidence level (1σ) for density measurements mentioned in subsection 3.1.3 was applicable with the old sinker reference volume uncertainty of ±0.02%. However, with the new sinker reference volume uncertainty of

±0.05% at the 68% confidence level (1σ), the uncertainty of density measurements cannot be expected to be better than ±0.05%. Density measurements for all the 26 isotherms of Table 3.2 were performed with the new sinker. The earliest density measurements for pure methane and argon with the old sinker showed a systematic apparatus bias error of greater than +0.1% when compared to EOS predictions for densities. After ensuring that the measurement uncertainties of pressure, temperature, the true mass of the sinker in vacuum, the apparent mass of the sinker under pressure and the sample purity could not lead to such a large, systematic apparatus bias error, it was concluded that the sinker volume uncertainty provided by Rubotherm (1998) may have been unreliable. The new sinker was used to check the validity of this conclusion. The inference drawn about the apparatus systematic bias error after using the new sinker for density measurements of pure methane, argon and nitrogen is presented in Chapter V.

4.5 Natural Gas Mixture Composition Traceability

The natural gas mixtures were synthesized gravimetrically by DCG Partnership Ltd. and their compositions verified by GC analysis and are NIST traceable by weight. Table 4.4 shows the standard deviations of the mole fraction compositions for natural gas mixtures M91C1 (DCG Partnership, 2003) and M94C1 (DCG Partnership, 2002) that have already been provided in Table 2.1. The mole fraction standard deviations in Table 4.4 for the mixture RR-NIST2 mole fraction compositions are those provided by Magee *et al.* (1997).

Table 4.4. Standard Deviations of Mole Fraction Compositions of Natural Gas Mixtures

Component	**RR-NIST2 (± 1σ)**	**M91C1 (± 1σ)**	**M94C1 (± 1σ)**
methane	0.0000028	0.0003200	0.0002900
ethane	0.0000015	0.0001707	0.0000000
propane	0.0000010	0.0000012	0.0000011
iso butane	0.0000008	0.0000009	0.0000008
n butane	0.0000008	0.0000009	0.0000008
iso pentane	0.0000006	0.0000007	0.0000006
n pentane	0.0000006	0.0000007	0.0000006
n hexane	0.0000005		0.0000005
n heptane			0.0000005
n octane			0.0000004
n nonane			0.0000000
methyl cyclopentane			0.0000000
2 methyl pentane			
3 methyl pentane			
benzene			
2, 3 dimethyl pentane			
3 methyl hexane			
toluene			
methyl cyclohexane			
2, 2, 4 trimethyl pentane			
nitrogen	0.0000016	0.0000018	0.0000017
carbon dioxide	0.0000011	0.0000012	0.0000011

CHAPTER V

PURE COMPONENT AND NATURAL GAS MIXTURE DENSITY MEASUREMENTS

5.1 Pure Component Density Measurements

Densities of pure argon, nitrogen and methane were measured to ensure correct operation of the MSD and also to determine the magnitude and sign of the systematic bias error of the apparatus, if it existed. These three pure components were selected with the aim of reproducing the abundant, high accuracy density data measured by previous workers. Tegeler *et al.* (1999), Span *et al*. (2000) and Setzmann and Wagner (1991) have used these data to develop reference quality EOS for argon, nitrogen and methane respectively. Relative deviations of the measured densities for the pure components as part of the present work from those predicted by the reference EOS would give the systematic bias error of the apparatus.

The 16 pure component isotherms numbered 1 through 12 and 19 through 22 measured during the present work have been assigned identities as shown in Table 3.2. The prefixes ‘Ar’, ‘N2’ or ‘CH4’ in the isotherm identity stand for argon, nitrogen and methane respectively. The numbers 1, 2 or 3 following the prefix identify different cylinder numbers of the pure component. The following ‘270K’ or ‘340K’ convey the isotherm temperature. The last part of the isotherm identity represents the date when the measurement was started in the format ‘mmddyyyy’. Table 5.1 shows the purities in mole percent of different cylinders of argon, nitrogen and methane along with the impurities and the supplier. The pure component purities were checked neither after receiving the cylinders from the suppliers nor after measuring the densities. Instead densities of samples of the same pure component from different cylinders were

Table 5.1. Purities of Argon, Nitrogen and Methane Gas Cylinders

Pure gas	Pure gas cylinder identity	Purity	Impurities	Supplier
		mole %		
argon	Ar 1	99.9990	CO_2 < 1ppm CO < 1 ppm O_2 < 3 ppm THC < 0.5 ppm H_2O < 5 ppm	Matheson TriGas
argon	Ar 2	99.9990	N_2 < 4 ppm O_2 < 1 ppm H_2 < 4 ppm CO_2 < 1 ppm THC < 0.5 ppm H_2O < 1 ppm	Scott Specialty Gas
methane	CH4 1	99.9900	O_2 = 2 ppm N_2 = 33 ppm C_2H_6 = 7 ppm C_2H_4 < 1 ppm CO < 1 ppm H_2O < 1 ppm	H.P. Gas Products
methane	CH4 2	99.9900	unknown	Matheson TriGas
methane	CH4 3	99.9851	N_2 = 74 ppm O_2 = 65 ppm CO_2 = 10 ppm	DCG Partnership
nitrogen	N2 1	99.9995	CO < 1 ppm CO_2 <1 ppm THC < 0.5 ppm H_2O < 2 ppm O_2 < 0.5 ppm	Scott Specialty Gas
nitrogen	N2 2	99.9995	CO < 1 ppm CO_2 < 1 ppm THC < 0.5 ppm H_2O < 2 ppm O_2 < 0.5 ppm	Scott Specialty Gas

measured. The general outline of the experimental procedure followed for pure component density measurements has been provided in Appendix G.

Table 5.2 provides the measured density data for each pure component isotherm with PT06K used for pressure measurement. Densities were measured at 26 points for argon, 45 points for nitrogen and 25 points for methane in the range (3.447 to 34.474) MPa [(500 to 5,000) psia] and at either 270 K [26.33 ^{o}F, -3.15 ^{o}C] or 340 K [152.33 ^{o}F, 66.85 ^{o}C] for a total of 96 points. The average, μ for temperature, pressure and weighing balance readings for either the true or apparent sinker mass over a period of 30 to 40 minutes are given at every measurement point and the corresponding standard deviations, σ are also provided as a measure of uncertainty. The average internal temperature of PT06K needed for temperature dependence of the calibration curve and its standard deviation quantifying the stability of the aluminum block heater temperature control are also provided. The measured mass density $\rho_{\text{measured}}^{\text{mass}}$ calculated using equation (8), was converted to molar density, $\rho_{\text{measured}}^{\text{molar}}$ using the molar masses given by Tegeler *et al.* for argon, Span *et al.* for nitrogen and Setzmann and Wagner for methane. The measured molar density was compared with the molar density predicted by the NIST-12 program (National Institute of Standards and Technology, 2000) for pure components. The percentage relative density deviation between the measured and predicted values was calculated as:

$$\frac{\Delta\rho^{\text{molar}}}{\rho^{\text{molar}}} = \frac{\left(\rho_{\text{measured}}^{\text{molar}} - \rho_{\text{predicted}}^{\text{molar}}\right)}{\rho_{\text{predicted}}^{\text{molar}}} \text{x100} \tag{31}$$

Figure 5.1 shows the observed relative density deviations for pure argon, nitrogen and methane isotherms. While the isotherms for each pure component were clustered, with methane showing the largest and argon the smallest relative density deviations, the isotherm ‘N2 1 340K 08182003’ clearly fell outside the cluster for nitrogen. The exact reason for the abnormal behavior of this isotherm was not clear but may have been the result of accidentally leaving one or more tubing trace heaters close to the cell, ‘off’

Table 5.2. Measured Density Data for Pure Components

Isotherm 1: Ar 1 270K 03192003											
T		P				m_v and m_a		v_s	ρ		
μ	σ	μ	σ	T_{PT06K} μ	T_{PT06K} σ	μ	σ		measured	NIST-12 predicted	Relative deviation
K	mK	MPa	KPa	K	mK	g	mg	cm^3	$kmole/m^3$	$kmole/m^3$	%
270.022	3.543	-0.000392	0.017	294.133	44.206	0.01297	0.005	-	-	-	-
270.013	3.853	7.024316	0.028	295.062	34.341	-0.88339	0.006	6.73623	3.33096	3.32920	0.053
270.015	5.000	13.883214	0.347	295.530	7.942	-1.82414	0.053	6.73576	6.82736	6.82360	0.055
270.014	2.655	20.739401	1.758	295.504	18.077	-2.73083	0.234	6.73529	10.19765	10.19152	0.060
270.024	2.389	27.496195	8.477	295.193	17.651	-3.50485	0.867	6.73482	13.07531	13.06743	0.060
270.024	2.991	34.501119	22.568	295.085	1.512	-4.16006	1.815	6.73434	15.51176	15.50290	0.057

Table 5.2. (Continued)

Isotherm 2: Ar 1 340K 03252003											
T		P				m_v and m_a		v_s	ρ		
μ	σ	μ	σ	T_{PT06K} μ	T_{PT06K} σ	μ	σ		measured	NIST-12 predicted	Relative deviation
K	mK	MPa	KPa	K	mK	g	mg	cm^3	$kmole/m^3$	$kmole/m^3$	%
340.010	3.174	-0.000844	0.018	295.108	20.021	0.01312	0.006	-	-	-	-
339.973	2.634	6.915530	0.111	295.582	34.276	-0.65648	0.012	6.74871	2.48370	2.48220	0.060
340.003	4.048	13.886717	0.156	295.877	11.092	-1.33296	0.019	6.74825	4.99329	4.99047	0.056
340.032	2.352	20.732242	0.387	295.846	6.731	-1.97097	0.038	6.74779	7.36047	7.35653	0.054
340.035	2.270	27.603607	0.581	295.768	6.572	-2.56296	0.042	6.74734	9.55724	9.55199	0.055
340.038	5.406	34.498250	0.996	295.595	11.318	-3.09647	0.103	6.74688	11.53733	11.53061	0.058

Table 5.2. (Continued)

Isotherm 3: Ar 1 270K 03262003											
T		P				m_v and m_a		v_s	ρ		
μ	σ	μ	σ	T_{PT06K} μ	T_{PT06K} σ	μ	σ		measured	NIST-12 predicted	Relative deviation
K	mK	MPa	KPa	K	mK	g	mg	cm^3	$kmole/m^3$	$kmole/m^3$	%
269.978	2.900	-0.000929	0.016	294.844	22.116	0.01292	0.004	-	-	-	-
269.974	3.270	6.988688	0.177	295.108	19.804	-0.87898	0.025	6.73624	3.31441	3.31205	0.071
269.973	1.859	13.852090	0.254	295.205	17.523	-1.82059	0.040	6.73576	6.81399	6.80933	0.068
269.992	4.034	20.747945	0.686	294.887	10.616	-2.73248	0.105	6.73529	10.20362	10.19680	0.067
269.993	3.029	20.766498	0.105	294.852	3.434	-2.73481	0.015	6.73529	10.21229	10.20533	0.068
270.011	3.711	27.621639	0.539	293.880	35.378	-3.51842	0.094	6.73482	13.12558	13.11678	0.067
269.956	3.392	34.518944	0.420	295.097	23.336	-4.16329	0.038	6.73434	15.52361	15.51368	0.064

Table 5.2. (Continued)

Isotherm 4: CH4 1 270K 03292003											
T		P				m_v and m_a		v_s	ρ		
μ	σ	μ	σ	T_{PT06K} μ	T_{PT06K} σ	μ	σ		measured	NIST-12 predicted	Relative deviation
K	mK	MPa	KPa	K	mK	g	mg	cm^3	$kmole/m^3$	$kmole/m^3$	%
269.998	3.235	-0.000914	0.013	294.265	3.367	0.01289	0.003	-	-	-	-
270.002	2.296	6.965019	0.045	294.069	23.229	-0.39022	0.005	6.73624	3.73010	3.72430	0.156
269.987	3.168	34.729441	2.018	294.036	48.547	-1.74809	0.039	6.73433	16.29974	16.28030	0.119
269.987	3.531	27.712224	0.240	294.230	4.443	-1.57210	0.008	6.73481	14.66964	14.65218	0.119
269.984	3.081	20.925920	0.148	294.249	3.543	-1.32033	0.008	6.73528	12.33856	12.32432	0.116
269.994	3.593	13.789554	0.158	294.080	19.492	-0.89565	0.009	6.73577	8.40763	8.39756	0.120
270.006	6.172	6.834334	0.174	293.795	18.675	-0.38125	0.008	6.73625	3.64713	3.64172	0.149

Table 5.2. (Continued)

Isotherm 5: CH4 1 340K 03312003											
T		P				m_v and m_a		v_s	ρ		
μ	σ	μ	σ	T_{PT06K} μ	T_{PT06K} σ	μ	σ		measured	NIST-12 predicted	Relative deviation
K	mK	MPa	KPa	K	mK	g	mg	cm^3	$kmole/m^3$	$kmole/m^3$	%
340.020	4.414	-0.000995	0.025	294.478	25.604	0.01311	0.006	-	-	-	-
340.017	4.411	6.955254	0.208	294.849	21.079	-0.27132	0.011	6.74871	2.62705	2.62320	0.147
340.005	3.332	13.826201	0.200	294.949	6.571	-0.57258	0.011	6.74825	5.40995	5.40260	0.136
340.013	3.894	20.733750	0.869	294.246	50.137	-0.86006	0.038	6.74779	8.06589	8.05515	0.133
340.006	4.246	27.643588	0.548	294.794	38.774	-1.10363	0.021	6.74733	10.31662	10.30342	0.128
339.991	4.192	34.454589	0.937	295.189	28.312	-1.29694	0.042	6.74688	12.10326	12.08765	0.129

Table 5.2. (Continued)

Isotherm 6: CH4 2 270K 04042003											
T		P				m_v and m_a		v_s	ρ		
μ	σ	μ	σ	T_{PT06K} μ	T_{PT06K} σ	μ	σ		measured	NIST-12 predicted	Relative deviation
K	mK	MPa	KPa	K	mK	g	mg	cm^3	$kmole/m^3$	$kmole/m^3$	%
269.949	3.022	-0.000567	0.017	294.748	12.990	0.01301	0.005	-	-	-	-
269.967	3.240	6.905708	0.056	294.748	12.990	-0.38615	0.012	6.73624	3.69362	3.68767	0.161
269.886	8.876	13.806413	0.681	295.061	15.360	-0.89773	0.025	6.73577	8.42808	8.41716	0.130
269.953	2.454	20.673950	0.221	295.457	22.763	-1.30882	0.013	6.73529	12.23316	12.21859	0.119
269.949	4.630	27.563967	0.644	295.625	3.097	-1.56787	0.009	6.73482	14.63162	14.61411	0.120
269.956	3.478	34.548479	0.988	295.445	16.151	-1.74439	0.010	6.73434	16.26659	16.24685	0.122
269.945	2.108	6.778310	0.082	295.285	6.317	-0.37749	0.011	6.73625	3.61345	3.60796	0.152

Table 5.2. (Continued)

Isotherm 7: CH4 3 270K 04082003											
T		P				m_v and m_a		v_s	ρ		
μ	σ	μ	σ	T_{PT06K} μ	T_{PT06K} σ	μ	σ		measured	NIST-12 predicted	Relative deviation
K	mK	MPa	KPa	K	mK	g	mg	cm^3	$kmole/m^3$	$kmole/m^3$	%
270.095	3.221	-0.000657	0.016	293.967	8.834	0.01304	0.007	-	-	-	-
269.989	3.605	7.018243	0.078	294.070	6.177	-0.39368	0.006	6.73623	3.76362	3.75836	0.140
269.973	2.719	13.895146	0.077	294.243	9.365	-0.90324	0.011	6.73576	8.47936	8.46991	0.112
269.979	3.655	20.753411	0.164	294.232	2.772	-1.31203	0.009	6.73529	12.26322	12.25069	0.102
269.977	2.831	26.878279	0.538	293.969	27.616	-1.54627	0.006	6.73487	14.43195	14.41713	0.103

Table 5.2. (Continued)

Isotherm 8: CH4 3 340K 04162003											
T		P				m_v and m_a		v_s	ρ		
μ	σ	μ	σ	T_{PT06K} μ	T_{PT06K} σ	μ	σ		measured	NIST-12 predicted	Relative deviation
K	mK	MPa	KPa	K	mK	g	mg	cm^3	$kmole/m^3$	$kmole/m^3$	%
340.004	5.896	-0.000264	0.015	294.685	13.412	0.01329	0.008	-	-	-	-
340.038	5.907	6.968711	0.111	296.467	22.480	-0.27158	0.013	6.74871	2.63111	2.62833	0.106
339.995	8.923	13.879164	0.174	297.214	41.020	-0.57461	0.028	6.74825	5.43041	5.42419	0.115
340.003	3.338	20.757004	0.364	297.804	31.252	-0.86062	0.018	6.74779	8.07281	8.06385	0.111
339.997	3.075	27.539234	0.608	298.149	12.725	-1.09994	0.016	6.74734	10.28423	10.27329	0.106

Table 5.2. (Continued)

Isotherm 9: Ar 1 340K 04182003											
T		P				m_v and m_a		v_s	ρ		
μ	σ	μ	σ	T_{PT06K} μ	T_{PT06K} σ	μ	σ		measured	NIST-12 predicted	Relative deviation
K	mK	MPa	KPa	K	mK	g	mg	cm^3	$kmole/m^3$	$kmole/m^3$	%
339.929	4.669	-0.000364	0.019	294.924	20.154	0.01329	0.009	-	-	-	-
339.944	5.474	6.941460	0.264	295.828	54.613	-0.65899	0.013	6.74871	2.49364	2.49182	0.073
339.963	6.224	13.888609	0.253	296.190	1.833	-1.33328	0.013	6.74825	4.99510	4.99186	0.065
339.951	4.872	17.199149	0.195	296.037	10.883	-1.64692	0.015	6.74803	6.15873	6.15485	0.063
339.912	3.416	27.642727	0.920	294.852	3.521	-2.56725	0.065	6.74733	9.57377	9.56823	0.058
339.899	2.683	34.535319	0.588	294.945	1.170	-3.10063	0.051	6.74687	11.55340	11.54635	0.061

Table 5.2. (Continued)

Isotherm 10: Ar 2 340K 04222003											
T		P				m_v and m_a		v_s	ρ		
μ	σ	μ	σ	T_{PT06K} μ	T_{PT06K} σ	μ	σ		measured	NIST-12 predicted	Relative deviation
K	mK	MPa	KPa	K	mK	g	mg	cm^3	$kmole/m^3$	$kmole/m^3$	%
340.099	3.489	-0.000240	0.015	294.325	5.322	0.01327	0.007	-	-	-	-
340.069	3.684	6.936001	0.076	294.441	13.825	-0.65807	0.011	6.74871	2.49016	2.48881	0.054
340.080	3.838	13.834205	0.093	294.673	1.634	-1.32736	0.013	6.74825	4.97303	4.97043	0.052
340.079	2.247	20.730657	0.275	294.579	1.883	-1.97024	0.026	6.74779	7.35829	7.35471	0.049
340.076	2.848	27.594570	0.524	294.474	13.258	-2.56157	0.041	6.74734	9.55262	9.54780	0.051
340.097	2.432	34.500323	0.610	294.367	9.954	-3.09570	0.050	6.74688	11.53501	11.52874	0.054

Table 5.2. (Continued)

Isotherm 11: N2 1 340K 04252003											
T		P				m_v and m_a		v_s	ρ		
μ	σ	μ	σ	T_{PT06K} μ	T_{PT06K} σ	μ	σ		measured	NIST-12 predicted	Relative deviation
K	mK	MPa	KPa	K	mK	g	mg	cm^3	$kmole/m^3$	$kmole/m^3$	%
340.001	2.940	-0.000315	0.016	294.479	10.303	0.01327	0.011	-	-	-	-
339.957	2.680	6.996853	0.081	295.104	16.117	-0.44895	0.009	6.74871	2.44491	2.44320	0.070
339.960	3.050	13.911771	0.110	295.247	4.039	-0.88064	0.009	6.74825	4.72866	4.72515	0.074
339.954	3.366	20.700612	0.238	295.175	12.306	-1.26643	0.018	6.74779	6.76985	6.76480	0.075
339.952	2.457	27.710474	0.357	295.137	2.362	-1.61971	0.016	6.74733	8.63939	8.63269	0.078
339.951	3.979	34.559344	2.586	295.148	2.678	-1.92190	0.025	6.74687	10.23884	10.23119	0.075

Table 5.2. (Continued)

Isotherm 12: N2 1 270K 04272003											
T		P				m_v and m_a		v_s	ρ		
μ	σ	μ	σ	T_{PT06K} μ	T_{PT06K} σ	μ	σ		measured	NIST-12 predicted	Relative deviation
K	mK	MPa	KPa	K	mK	g	mg	cm^3	$kmole/m^3$	$kmole/m^3$	%
269.966	2.808	-0.000254	0.015	294.119	12.816	0.01299	0.008	-	-	-	-
269.965	2.558	6.966050	0.080	294.541	14.721	-0.58493	0.005	6.73624	3.16855	3.16599	0.081
269.961	2.766	13.845764	0.210	294.806	10.841	-1.16018	0.018	6.73576	6.21736	6.21199	0.087
269.959	2.426	20.728037	0.371	295.037	5.801	-1.66996	0.017	6.73529	8.91969	8.91170	0.090
269.967	2.774	27.612029	0.286	295.113	9.822	-2.09551	0.016	6.73482	11.17586	11.16581	0.090
269.969	3.519	34.485036	0.345	294.943	20.651	-2.44405	0.020	6.73434	13.02415	13.01298	0.086

Table 5.2. (Continued)

Isotherm 19: N2 1 340K 08182003											
T		P				m_v and m_a		v_s	ρ		
μ	σ	μ	σ	T_{PT06K} μ	T_{PT06K} σ	μ	σ		measured	NIST-12 predicted	Relative deviation
K	mK	MPa	KPa	K	mK	g	mg	cm^3	$kmole/m^3$	$kmole/m^3$	%
339.906	3.539	-0.002395	0.008	323.333	1.675	0.01393	0.007	-	-	-	-
339.948	2.344	3.447080	0.026	323.354	2.115	-0.21566	0.006	6.74894	1.21438	1.21413	0.020
339.947	2.808	3.446939	0.029	323.333	1.761	-0.21565	0.007	6.74894	1.21431	1.21409	0.018
339.970	2.860	6.901222	0.024	323.369	1.015	-0.44179	0.008	6.74871	2.41053	2.41039	0.006
339.989	2.379	6.901841	0.030	323.353	1.015	-0.44181	0.006	6.74871	2.41062	2.41045	0.007
339.971	2.370	13.805757	0.043	323.343	1.792	-0.87325	0.005	6.74825	4.69302	4.69142	0.034
339.966	2.664	13.805662	0.061	323.361	4.671	-0.87326	0.008	6.74825	4.69307	4.69147	0.034
340.000	3.298	13.804197	0.107	323.368	2.734	-0.87310	0.007	6.74825	4.69221	4.69048	0.037
340.000	2.686	20.694070	0.084	323.360	1.761	-1.26481	0.008	6.74780	6.76477	6.76192	0.042
340.002	2.384	20.694963	0.066	323.367	2.208	-1.26486	0.010	6.74780	6.76501	6.76213	0.043
339.988	2.702	27.610323	0.210	323.347	3.044	-1.61372	0.018	6.74733	8.61114	8.60672	0.051
340.019	1.976	34.507002	0.216	323.347	2.123	-1.91837	0.011	6.74688	10.22362	10.21767	0.058
340.018	2.782	34.511629	0.217	323.349	2.915	-1.91857	0.009	6.74687	10.22470	10.21871	0.059

Table 5.2. (Continued)

Isotherm 20: N2 1 270K 08272003											
T		P				m_v and m_a		v_s	ρ		
μ	σ	μ	σ	T_{PT06K} μ	T_{PT06K} σ	μ	σ		measured	NIST-12 predicted	Relative deviation
K	mK	MPa	KPa	K	mK	g	mg	cm^3	$kmole/m^3$	$kmole/m^3$	%
269.976	2.325	-0.004149	0.013	323.370	7.530	0.01362	0.004	-	-	-	-
269.973	2.038	3.456941	0.018	323.373	3.465	-0.28140	0.004	6.73648	1.56334	1.56131	0.129
269.998	2.669	6.927457	0.036	323.340	1.015	-0.58103	0.005	6.73624	3.15120	3.14791	0.104
270.001	2.421	10.371838	0.237	323.328	2.626	-0.87465	0.015	6.73600	4.70735	4.70263	0.100
269.969	1.969	13.811624	0.174	323.362	1.068	-1.15689	0.013	6.73577	6.20331	6.19733	0.097
269.972	2.796	20.719738	0.351	323.354	1.502	-1.66873	0.014	6.73529	8.91647	8.90816	0.093
269.994	2.306	27.609557	0.368	323.333	1.633	-2.09448	0.018	6.73482	11.17377	11.16376	0.090
270.005	1.594	34.509092	0.282	323.343	6.527	-2.44407	0.022	6.73434	13.02763	13.01697	0.082

Table 5.2. (Continued)

Isotherm 21: N2 2 340K 12212003 with PT06K											
T		P				m_v and m_a		v_s	ρ		
μ	σ	μ	σ	T_{PT06K} μ	T_{PT06K} σ	μ	σ		measured	NIST-12 predicted	Relative deviation
K	mK	MPa	KPa	K	mK	g	mg	cm^3	$kmole/m^3$	$kmole/m^3$	%
339.977	2.429	-0.002607	0.017	325.319	2.209	0.01374	0.015	-	-	-	-
340.152	2.169	3.463590	0.024	325.337	3.155	-0.21698	0.011	6.74894	1.22019	1.21914	0.086
340.149	3.355	6.909779	0.090	325.342	1.353	-0.44263	0.011	6.74871	2.41380	2.41193	0.077
340.136	2.196	10.361997	0.125	325.354	3.573	-0.66244	0.015	6.74848	3.57662	3.57379	0.079
340.134	2.444	13.803025	0.095	325.329	1.824	-0.87321	0.011	6.74825	4.69166	4.68802	0.078
340.153	2.365	17.265804	0.199	325.308	5.602	-1.07537	0.019	6.74802	5.76124	5.75670	0.079
340.161	1.911	20.714612	0.263	325.342	8.547	-1.26591	0.017	6.74779	6.76943	6.76417	0.078
340.164	2.296	27.605495	0.167	325.331	7.160	-1.61328	0.013	6.74733	8.60767	8.60072	0.081
340.164	2.113	34.511282	0.419	325.325	2.647	-1.91840	0.021	6.74687	10.22261	10.21415	0.083
340.151	2.138	-0.002638	0.016	325.350	11.450	0.01369	0.008	-	-	-	-

Table 5.2. (Continued)

Isotherm 22: N2 2 270K 12282003 with PT06K											
T		P				m_v and m_a		v_s	ρ		
μ	σ	μ	σ	T_{PT06K} μ	T_{PT06K} σ	μ	σ		measured	NIST-12 predicted	Relative deviation
K	mK	MPa	KPa	K	mK	g	mg	cm^3	$kmole/m^3$	$kmole/m^3$	%
269.948	1.889	-0.002771	0.022	325.309	2.418	0.01325	0.013	-	-	-	-
269.988	2.150	3.460498	0.027	325.308	4.675	-0.28200	0.006	6.73648	1.56459	1.56284	0.112
269.955	2.077	6.897271	0.081	325.349	1.562	-0.57892	0.007	6.73624	3.13810	3.13474	0.107
269.953	2.095	10.350689	0.092	325.348	3.199	-0.87343	0.008	6.73600	4.69896	4.69429	0.099
269.979	2.207	13.799986	0.135	325.313	9.078	-1.15626	0.009	6.73577	6.19798	6.19211	0.095
269.959	3.093	-0.002703	0.015	325.559	17.559	0.01325	0.008	-	-	-	-
269.984	2.615	17.247061	0.092	325.332	11.737	-1.42185	0.016	6.73553	7.60579	7.59934	0.085
269.972	1.932	20.700589	0.318	325.357	8.585	-1.66765	0.022	6.73529	8.90880	8.90127	0.085
269.983	2.153	27.603984	0.218	325.384	8.729	-2.09451	0.016	6.73482	11.17197	11.16264	0.084
269.975	1.946	34.497937	0.644	325.353	3.966	-2.44417	0.030	6.73434	13.02622	13.01581	0.080
269.990	2.433	-0.003018	0.019	325.341	7.095	0.01326	0.005	-	-	-	-

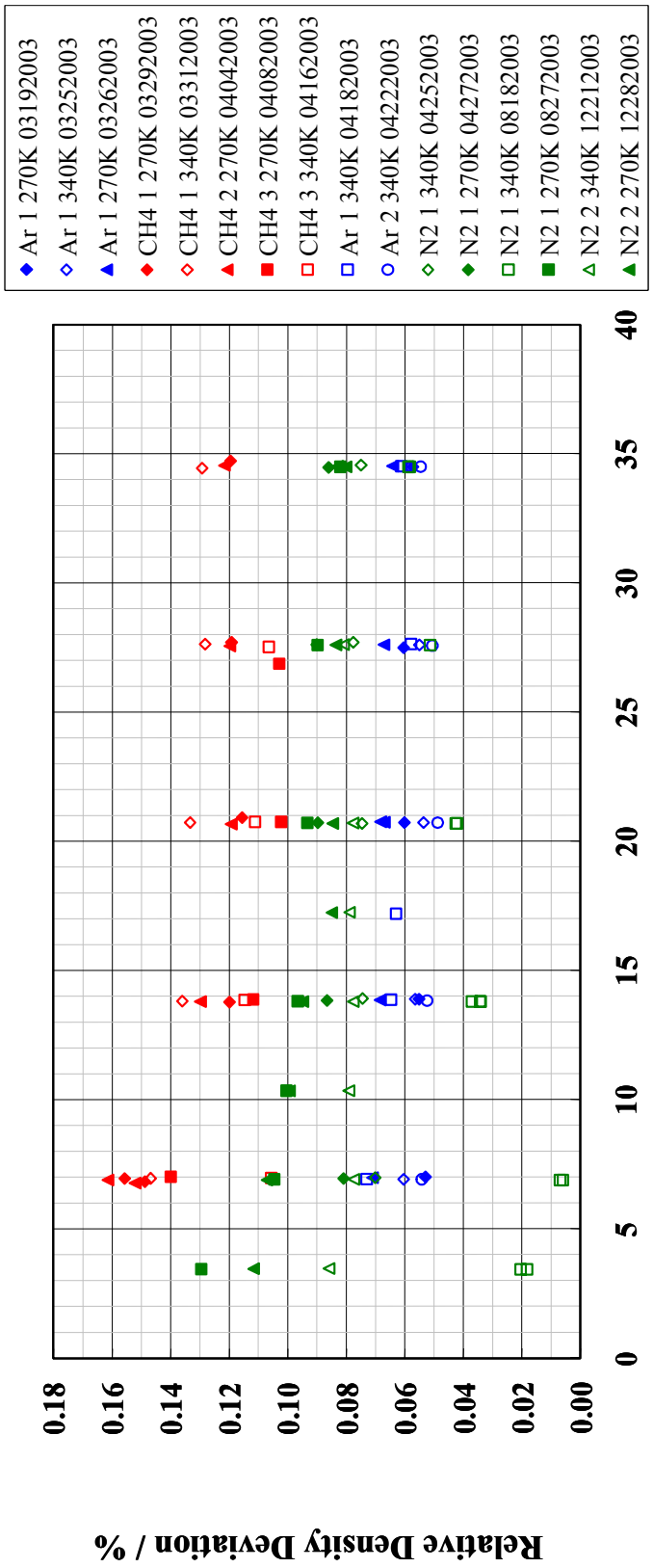

Figure 5.1. Relative Deviations between Measured and Predicted Molar Densities for Pure Components

during measurements. The 12 points of this isotherm were excluded from further data analysis.

Based on 84 pure component data points, temperatures were measured with an uncertainty of ±3.2 mK, pressures with an uncertainty of ±0.003%, the weighing balance readings for the true mass of the sinker in vacuum with an uncertainty of ±0.01 mg and the weighing balance readings for the apparent mass of the sinker under pressure with an uncertainty of ±0.06 mg at the approximately 68% confidence level (1σ).

P measurements without the aluminum block heaters for PT06K had an uncertainty of ±0.004% while those with it had an uncertainty of ±0.001%. Thus, the uncertainty of *P* measurements improved only slightly when using the aluminum block heaters. While measuring isotherms 21 and 22, below 13.790 MPa [2,000 psia], the *P* readings from PT06K were on an average larger than those measured by PT02K by 0.002%. The data analyses with *P* readings from PT02K have not been included because no significant improvements exist in the relative density deviations in the lower *P* range because of using PT02K.

5.1.1 Systematic Bias Error of the Magnetic Suspension Densitometer

Figure 5.2 shows the observed relative density deviations for 15 pure component isotherms after excluding the 'N2 1 340K 08182003' isotherm data. The observed relative density deviations from the MSD would have been close to zero for all pure components in the absence of a systematic bias error. However, the non-zero, positive values for relative density deviations in Figure 5.2 lead to the conclusion that the MSD has a simple average systematic bias error of +0.090% based on all 84 pure component points. Additionally, the relative density deviation appears to be an inverse function of the density or the molar mass of the pure components. The average relative density deviations for the 26 points of argon, 33 points of nitrogen and 25 points of methane are +0.060%, +0.087% and +0.126% respectively. Figure 5.3 shows the

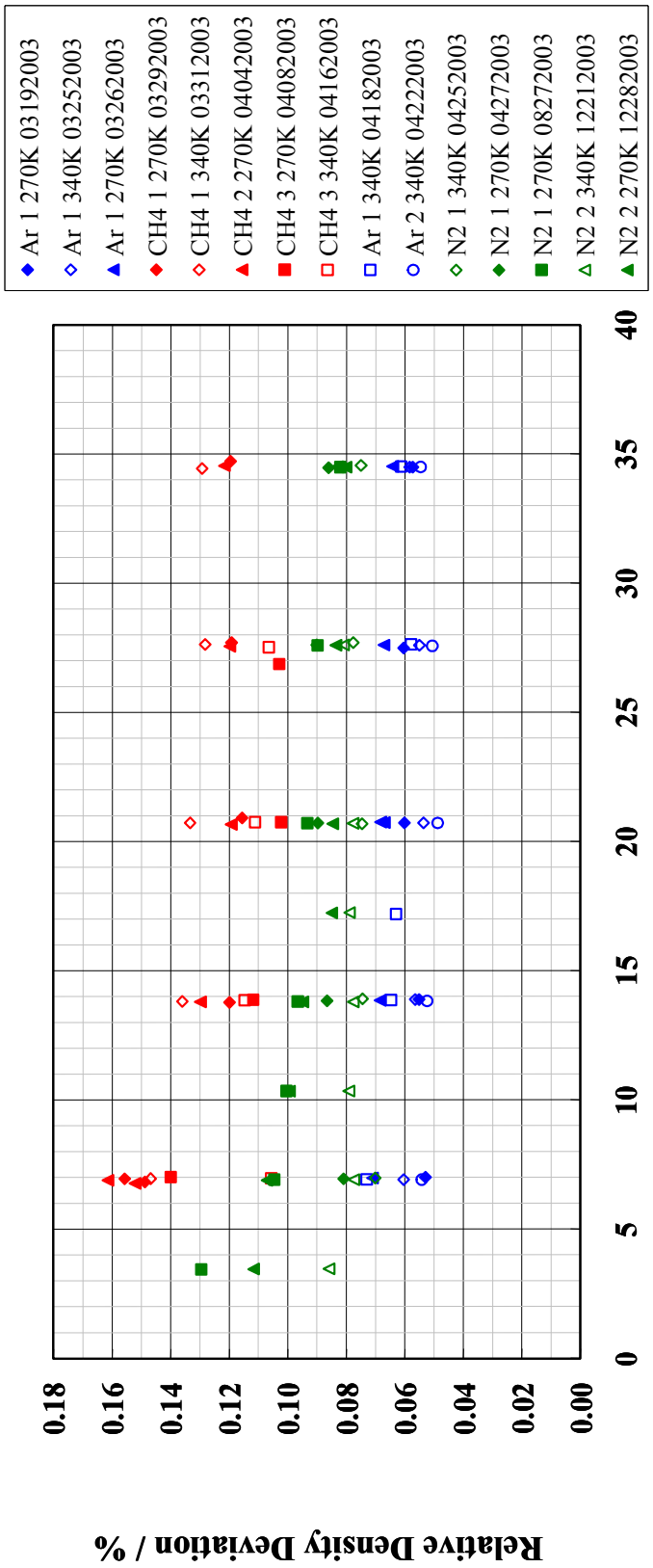

Figure 5.2. Relative Deviations between Measured and Predicted Molar Densities for Pure Components Excluding Isotherm 'N2 1 340K 08182003' data

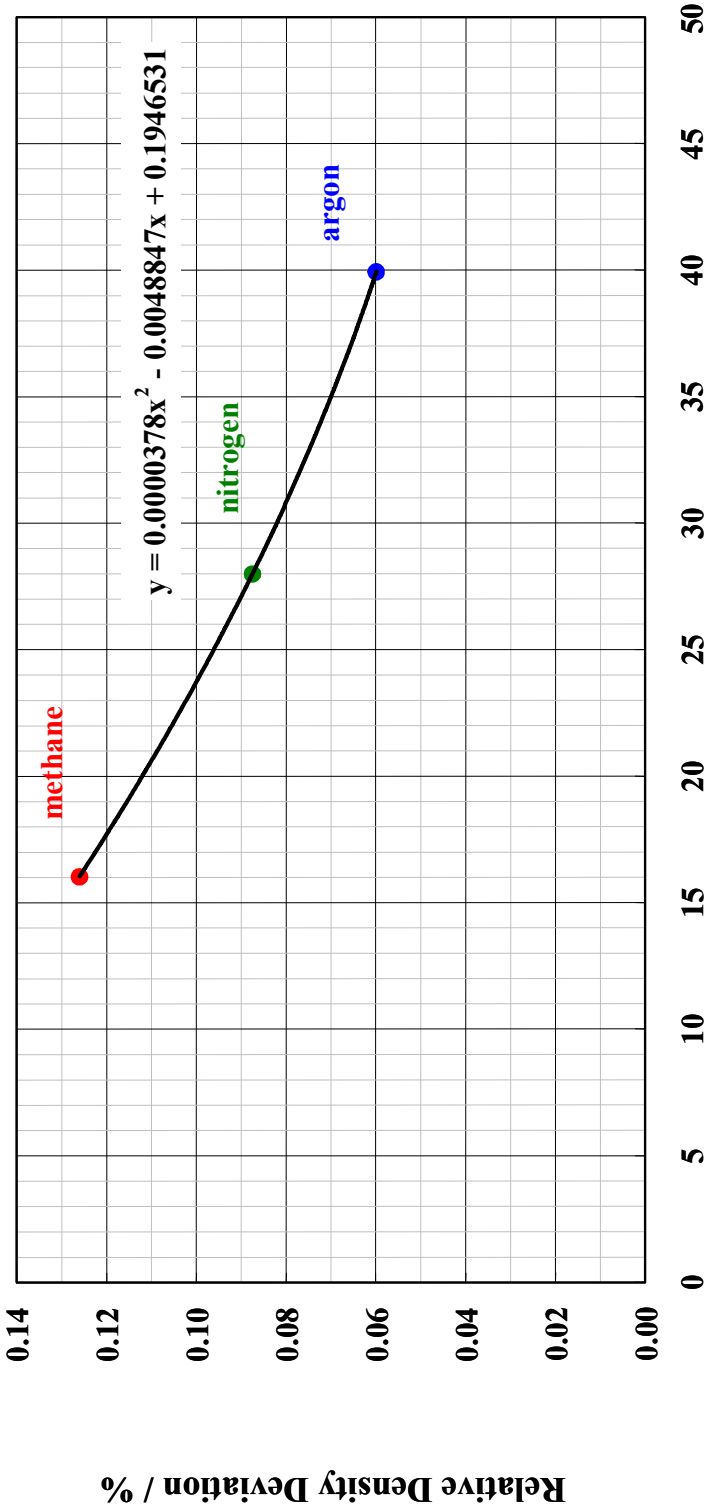

Figure 5.3. Molar Mass Dependence of the Observed Pure Component Relative Density Deviations

dependence of the observed pure component relative density deviations on the pure component molar mass. A quadratic equation fit to the three points was found to be:

$$\text{Relative density deviation \%} = 0.0000378\, M^2 - 0.0048847\, M + 0.1946531 \qquad (32)$$

where, M is the molar mass of the sample fluid whose density is measured. Additional density measurement data for fluids with molar mass lower than that of methane and higher than that of argon are required to confirm the dependence of the relative density deviation or the apparatus bias error on the molar mass. Examples of pure components with reference quality EOS for density predictions that satisfy this requirement along with their molar masses in units of kg/kmole are: helium {4.0026}, butane {58.1222}, pentane {72.14878}, krypton {83.80423}, xenon {131.3} and sulfur hexafluoride {146.06042}. The molar masses of the four natural gas mixtures whose densities were to be measured as part of the present project are: M91C1 {18.21068}, M94C1 {17.88784}, M88C1 {19.15424} and M78C1 {21.77743}. Additional data to confirm the shape of the apparatus bias error curve outside the range of molar mass covered by methane and argon were not necessary for the present work because the natural gas mixture molar masses lie between those of methane and nitrogen. Thus, equation (32) can be used to get the systematic bias error of the apparatus knowing the molar mass of the natural gas mixture.

If the molar mass dependent apparatus bias errors of +0.060% for argon, +0.087% for nitrogen and +0.126% for methane are subtracted from the observed relative density deviations, the data shown in Figure 5.2 collapse to values closer to zero as shown in Figure 5.4. The relative density deviations after applying the molar mass dependent correction for the apparatus bias error are the ‘true’ values that could have been expected if the MSD were not to have any systematic bias error.

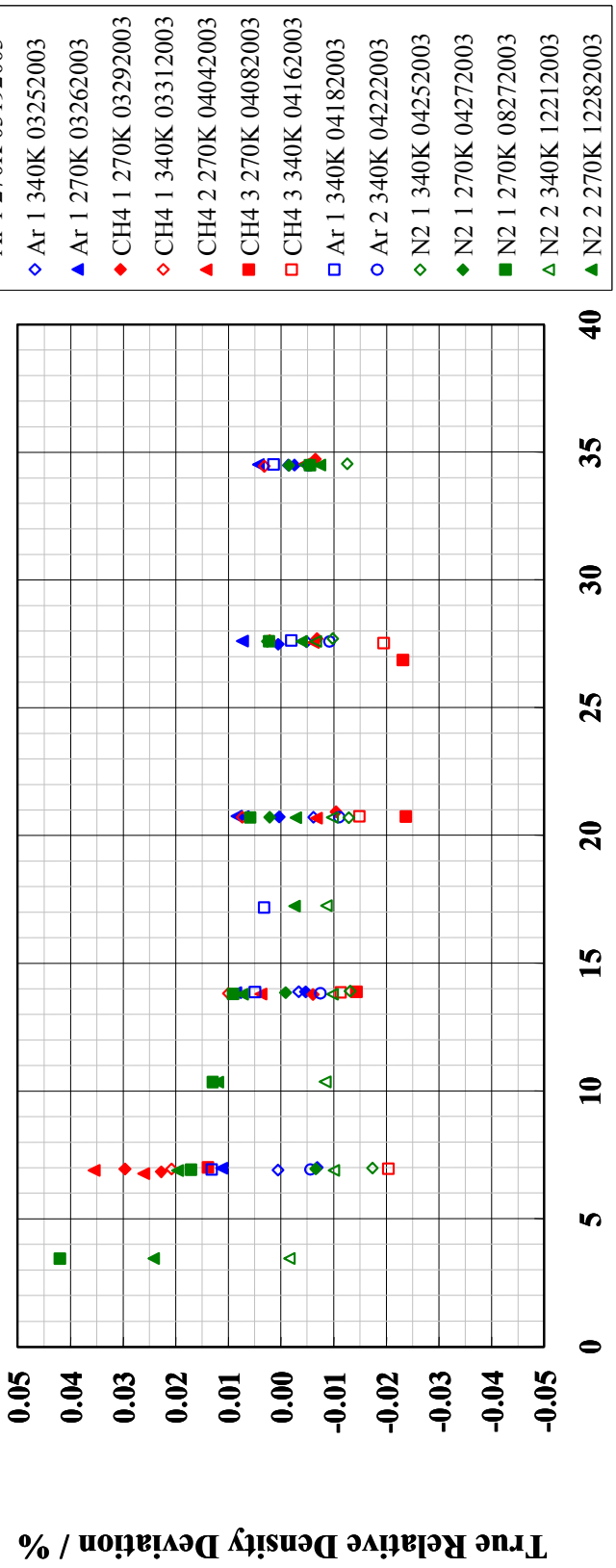

Figure 5.4. True Relative Density Deviations for Pure Components after Applying the Molar Mass Dependent Correction for the Apparatus Bias Error

5.1.2 Comparison of Pure Component Density Measurements with Literature Data

The pure component densities measured with the compact single-sinker MSD as part of the present work were compared to those previously measured by other workers using other apparatuses or methods. The true relative density deviations for each pure component were plotted along with the relative density deviations of the measured data appearing in the literature with those predicted by NIST-12 as given by equation (31). An agreement between the true and literature relative density deviations within each other's experimental uncertainty would validate the method of determination of the systematic bias error of the apparatus.

Data sets from the literature with density measurements on pure components with 99.990 mole percent purity or better were chosen. Preference was given to those data sets with the smallest experimental uncertainties, measured using the most recent advances in density measurement techniques and which were used by Tegeler *et al.*, Span *et al.* and by Setzmann and Wagner to validate their reference EOS. If the temperatures from the literature data sets were measured on the International Practical Temperature Scale of 1968 (IPTS-68) (Barber, 1969), they were converted to the ITS-90 using the difference table given by Preston-Thomas (1990). The maximum difference between temperatures measured on the two scales can be 20 mK in the range (263.15 to 343.15) K [(14 to 158) ^{o}F, (-10 to 70) ^{o}C]. If the data sets had isotherms at several temperatures in the range (260 to 340) K [(8.33 to 152.33) ^{o}F, (-13.15 to 66.85) ^{o}C], only those close to 270 K [26.33 ^{o}F, -3.15 ^{o}C] or 340 K [152.33 ^{o}F, 66.85 ^{o}C] were chosen for comparison with the isotherms measured during the present work. However, if no data were available close to 270 K [26.33 ^{o}F, -3.15 ^{o}C] or 340 K [152.33 ^{o}F, 66.85 ^{o}C], isotherms at any temperature in the range (260 to 340) K [(8.33 to 152.33) ^{o}F, (-13.15 to 66.85) ^{o}C] were also selected.

Figure 5.5 compares the true relative density deviations for argon from the present work with the relative density deviations for the measurements done by

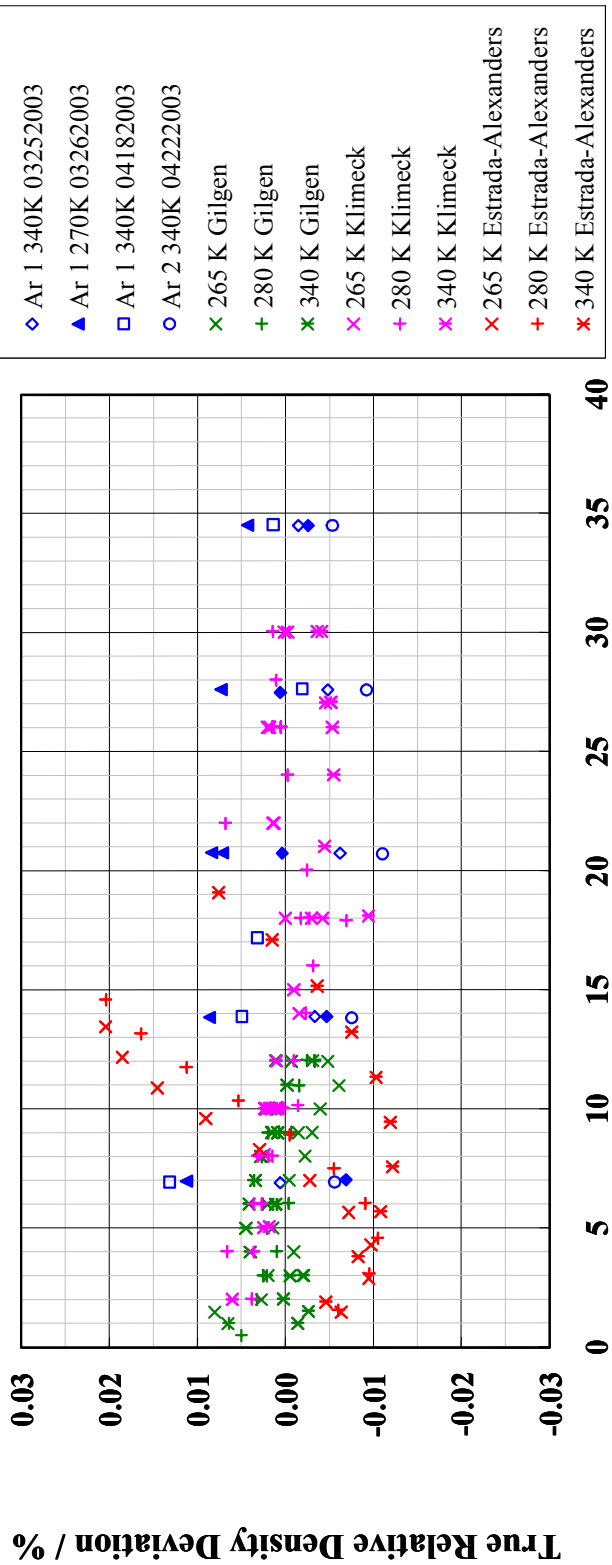

Figure 5.5. Comparison of True Relative Density Deviations from the MSD with Literature Data for Argon
(Only first author names appear in legend; for complete citations refer text)

Gilgen *et al.* (1994) using a two-sinker MSD, Klimeck *et al.* (1998) using a single-sinker MSD and of Estrada-Alexanders and Trusler (1996) from the speed of sound method. Figure 5.6 shows a similar comparison for nitrogen with density measurements of Nowak *et al.* (1997) using a two-sinker MSD, Klimeck *et al.* (1998) using a single-sinker MSD, Pieperbeck *et al.* (1991) using a two-sinker MSD built especially for natural gas mixture density measurements, Fenghour *et al.* (1993) and Straty and Diller (1980) using an isochoric apparatus and Achtermann *et al.* (1986) using the refractive index method. Figure 5.7 compares the true relative density deviations for methane from the present work with the relative density deviations for measurements done by Kleinrahm *et al.* (1988) using a two-sinker MSD, Klimeck *et al.* (2001) using a single-sinker MSD, Pieperbeck *et al.* (1991) using a two-sinker MSD built especially for natural gas mixture density measurements, Achtermann *et al.* (1986) using the refractive index method, Trappeniers *et al.* (1979) using a piezometer, and Mollerup (1985) using a Burnett apparatus.

Table 5.3 summarizes the comparison of densities measured during the present work with the literature data. Argon, nitrogen and methane densities shown in Figure 5.4 were measured with an uncertainty of ±0.007%, ±0.013% and ±0.017% respectively. In general, the uncertainties of density data measured during the present work are slightly larger than those measured at Ruhr University but equal to or smaller than those of others, except the measurements of Mollerup *et al.* and Achtermann *et al.* for methane. The reason for the smaller uncertainties from the workers at Ruhr University is associated with the range and type of MSD used. Gilgen *et al.* and Nowak *et al.* have used a two-sinker MSD with a range of 11.997 MPa [1,740 psia] for argon and nitrogen measurements respectively, while Kleinrahm *et al.* have also used a two-sinker MSD but with a range of only 7.998 MPa [1,160 psia] for methane measurements. Klimeck *et al.* (1998) measured argon and nitrogen densities and Klimeck *et al.* (2001) measured methane densities with a single-sinker MSD with a range of 29.992 MPa [4,350 psia]. Pieperbeck *et al.* measured nitrogen and methane densities with a two-sinker MSD with a range of 11.997 MPa [1,740 psia], built especially for measurement

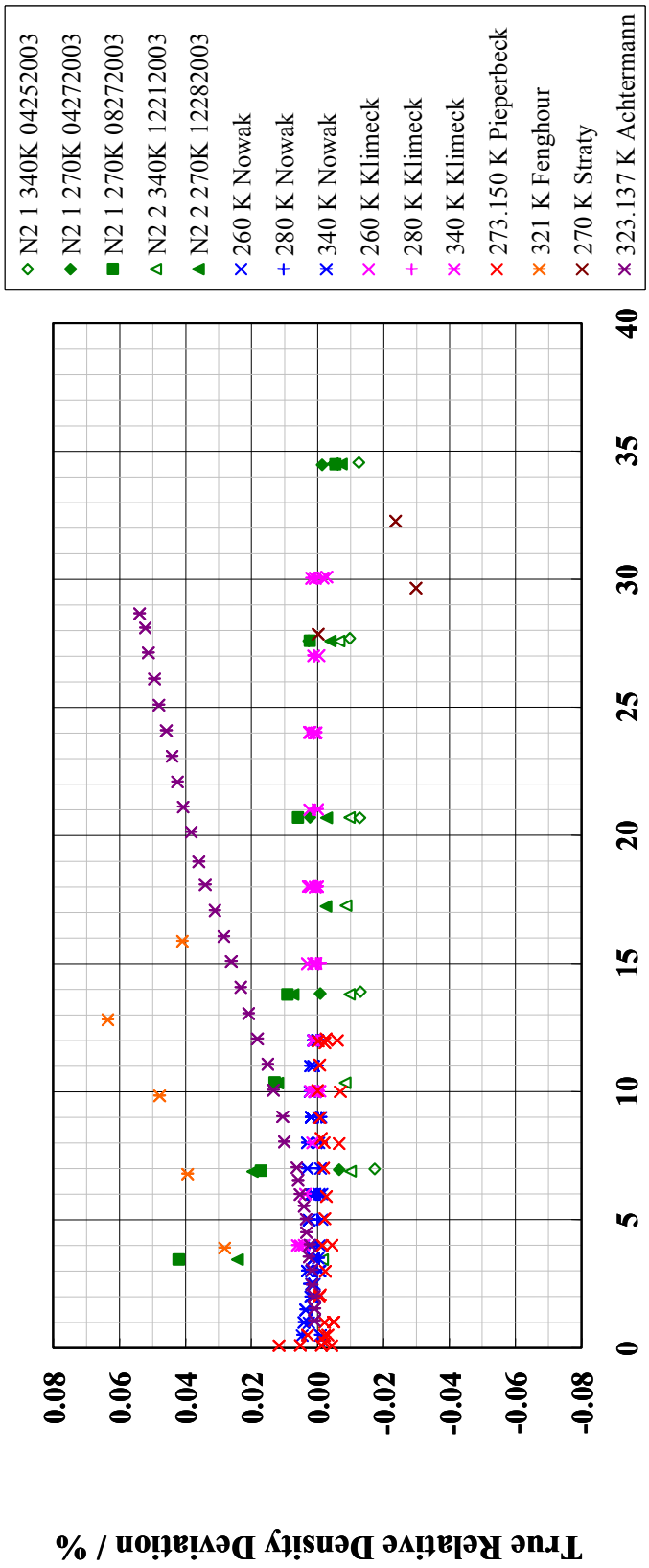

Figure 5.6. Comparison of True Relative Density Deviations from the MSD with Literature Data for Nitrogen
(Only first author names appear in legend; for complete citations refer text)

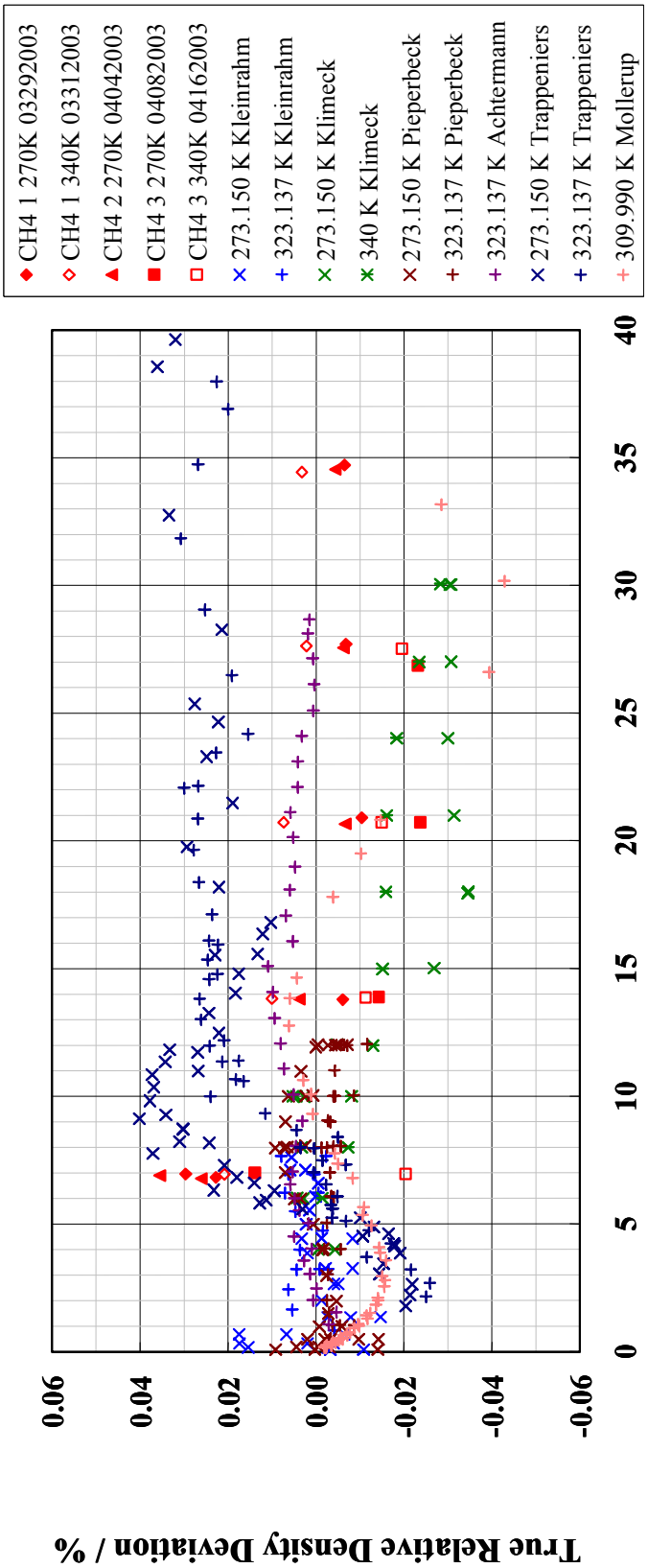

Figure 5.7. Comparison of True Relative Density Deviations from the MSD with Literature Data for Methane
(Only first author names appear in legend; for complete citations refer text)

Table 5.3. Comparison of Measured and Literature Density Data for Pure Components
(Only first author names appear in table; for complete citations refer text)

argon							
Data source	**Present work**	Ruhr University			Other		
		Gilgen	Klimeck		Estrada-Alexanders		
Average	**0.000**	0.001	0.000		-0.001		
Standard deviation	**0.007**	0.003	0.003		0.011		
nitrogen							
Data source	**Present work**	Ruhr University			Other		
		Nowak	Klimeck	Pieperbeck	Fenghour	Straty	Achtermann
Average	**0.000**	0.001	0.001	-0.002	0.044	-0.018	0.022
Standard deviation	**0.013**	0.002	0.002	0.004	0.013	0.016	0.019
methane							
Data source	**Present work**	Ruhr University			Other		
		Kleinrahm	Klimeck	Pieperbeck	Trappeniers	Mollerup	Achtermann
Average	**0.000**	0.001	-0.014	-0.002	0.013	-0.009	0.004
Standard deviation	**0.017**	0.007	0.014	0.005	0.018	0.010	0.003

of natural gas mixture densities. However, the present work up to 34.998 MPa [5,076 psia] was done with a compact, single-sinker MSD with a range of 200 MPa [29,007.54 psia]. Despite the larger range of the compact single-sinker MSD, the agreement of data measured with it even at lower pressures with those measured with the lower range MSD apparatuses at Ruhr University is good. The uncertainty of density measurements using the compact single-sinker MSD has been observed to increase at pressures below approximately 6.998 MPa [1,015 psia]. The agreement between the true relative density deviations from the present work and the relative density deviations of literature data validate the dependence of the relative density deviation or the apparatus bias error on the molar mass of the sample fluid. The density measurement uncertainty for the entire set of 84 pure component data points shown in Figure 5.4 is ±0.013%.

5.1.3 Discussion on Pure Component Density Measurement Results

In determining the systematic bias error of the MSD apparatus from the data shown in Figure 5.2, two other approaches were also evaluated. One was based upon a simple average of the relative density deviations of all 84 data points for the pure components, and the other was based upon a weighted average to include the contribution of each pure component relative density deviation to the total apparatus bias error. The simple average and standard deviation of data shown in Figure 5.2 were found to be 0.09% and ±0.029% respectively. This would have meant that the MSD had a fixed bias error of +0.09%. The other approach summed the contribution of each pure component to the overall apparatus bias error based upon weighting factors proportional to the inverse of their respective observed variances. The agreement with literature data with neither of these other two approaches for the apparatus bias error was as good as the molar mass dependent apparatus bias error approach. The molar mass based apparatus bias error approach was chosen because it was too conspicuous to be ignored.

The simple average bias error of +0.09% shown in Figure 5.2 could have also been caused by an erroneous reference volume measurement by Rubotherm for the

new sinker. Therefore, it was decided to calibrate the new sinker reference volume independently at NIST (McLinden and Holste, 2003) against a silicon sinker. The density of silicon is accurately known and the volume of a sinker of any other material can be accurately determined by weighing the two sinkers in the same fluid without needing to know the density of the fluid. With the good agreement between the true relative density deviations and the relative density deviations of literature data, it appears unlikely that the sinker reference volume was measured erroneously. Despite this, an independent calibration of the new sinker reference volume from NIST is recommended. Such a calibration along with density measurements for fluids with molar masses lower than methane and higher than argon together can help confirm or negate the dependence of the apparatus bias error upon molar mass of the fluid.

The molar mass dependence of the apparatus bias error may be the result of the fluid specificity of the FTE described in subsection 3.4.4, which in turn depends upon the sinker mass according to Wagner *et al.* (International Union of Pure and Applied Chemistry, 2003). Wagner and Kleinrahm (2004) have reported force transmission errors of +0.011% and +0.004% for diamagnetic fluids such as methane and nitrogen respectively and Kuramoto *et al.* (2004) have reported an FTE of +0.006% for n-tridecane depending upon the magnetic susceptibilities of the fluids during density measurements with their respective single-sinker MSD. These are small compared to the observed +0.126% and +0.087% errors observed in the present work for methane and nitrogen respectively. The observation of the FTE of 0.006% in the present work caused by diamagnetism of the copper beryllium cell (was described in subsection 3.4.4) includes the effect of the thick cell walls, but it still fails to explain relative density deviations as large as those observed with methane, nitrogen and argon. Thus, the observed molar mass dependent relative density deviations may be caused by the titanium sinker weighing below a critical mass.

The sinker details used in different MSD apparatuses at Ruhr University are provided by Wagner *et al.* (International Union of Pure and Applied Chemistry, 2003) and have been summarized in Table 5.4. The titanium sinker used during the

Table 5.4. Details of Sinkers Used in Different MSD Apparatuses

MSD description	P range	Sinker details			
		material and shape	mass	volume	density
	MPa		g	cm^3	kg/m^3
Ruhr University, Germany - two sinker	12	gold coated quartz glass sphere	54	24.5	2200
		solid gold disk	54	2.8	19300
Ruhr University, Germany - two sinker for natural gas	12	gold coated stainless steel sphere	123	107.0	1160
		gold coated solid stainless steel ring	123	15.6	7900
National Engineering Laboratory, UK - two sinker	30	gold coated quartz glass sphere	54	24.0	2200
		solid gold ring	54	2.8	19300
National Institute of Standards and Technology, USA - two sinker	35	single crystal silicon cylinder	60	25.7	2330
		tantalum ring	60	3.6	16600
Ruhr University, Germany - single sinker	30	quartz glass cylinder	60	26.5	2200
Ruhr University, Germany - compact single sinker	100	titanium cylinder	90	20.0	4500
		or			
		quartz glass cylinder	44	20.0	2200
Ruhr University, Germany - compact single sinker combined viscometer densitometer	30	titanium cylinder	60	13.0	4500
University of Valladolid, Spain - single sinker	35	titanium cylinder	60	13.0	4500
Texas A&M University, USA - compact single sinker	200	titanium cylinder	30	6.7	4500

present work weighed approximately 30 g, and had an approximate volume and density of 6.7 cm^3 and 4,500 kg/m^3 and is lighter than those previously used. In an effort to increase the P and T range of operation of the MSD, the mechanical design considerations may have required reduction in the size of the MSD cell and the sinker. Once the cell dimensions are decided, the sinker volume may become fixed as well, leaving only the sinker material density or the sinker mass as the adjustable parameters. It may be possible that the choice of 30 g for the titanium sinker is such that the measurements show molar mass dependent relative density deviations as shown in Figure 5.2.

Density measurements with different fluids as suggested in subsection 5.1.1 with the present sinker weighing 30 g can establish the shape of the curve for the molar mass dependence of the relative density deviations. Similar density measurements with sinkers of different materials or weights but with the same volume as the present sinker will determine the sharpness or the sensitivity of the curve for the molar mass dependence of the relative density deviation. The sinker which becomes completely insensitive to the molar mass of the fluid being measured at the lowest possible molar mass should then be used for density measurements. If either a stainless steel or tantalum or gold sinker of volume equal to the present sinker is used, it will weigh approximately 53 g or 111 g or 130 g respectively. However, tests with heavier sinkers than the present one may be hindered by the strength of the electromagnetic field generated by the electromagnet current that raises or lowers the sinker. It is for this reason that tests with a sinker lighter than the present one would be informative. A silicon or quartz glass sinker with the same volume as the present titanium sinker would weigh 15 g each. The relative density deviations with a lighter sinker can be expected to be larger than the ones shown in Figure 5.2 with the present titanium sinker. Wagner and Kleinrahm (2004) have reported the work of Klimeck for the determination of the correction factor for the fluid specific FTE by measuring methane densities with two sinkers each weighing 60 g but of different materials and hence different volumes. If the density measurements with sinkers of the same volume but different masses do not provide an explanation for the

observed relative density deviations, measurements with sinkers of the same mass but different volumes will be needed.

As a summary, the simple average bias error of +0.09% shown in Figure 5.2 could either be entirely because of the molar mass dependence of the apparatus bias error or because of a combination of the molar mass dependence and the sinker reference volume error.

The true measured densities for pure components, calculated from the true relative density deviations shown in Figure 5.4 after applying the correction for the molar mass dependent apparatus bias error, are given in Table 5.5.

5.2 Natural Gas Mixture Density Measurements

Density measurements for the two gas mixtures, M91C1 and M94C1, are presented as part of the present work. M91C1 is similar in composition to the mixture RR-NIST2 whose densities have been measured as part of a round-robin project. Densities of M91C1 have been measured with the aim of comparing the RR-NIST2 density measurements and further validating the operation of the MSD apparatus. After validating the MSD operation with density measurements of pure components and M91C1, densities of the mixture M94C1 containing C_{6+} components could be considered reliable. The nomenclature for natural gas mixture isotherms 23 through 26 for M91C1 and isotherms 13 through 18 for M94C1 shown in Table 3.2 includes the name of the natural gas mixture, the isotherm temperature in K and the date in 'mmddyyyy' format. The number between the name and the isotherm temperature used in pure component isotherm identities to represent the cylinder number was dropped because only one cylinder each for M91C1 and M94C1 was used. The mole fraction compositions of the mixtures have been provided in Table 2.1 and the corresponding mole fraction uncertainties in Table 4.4. The compositions were verified neither after receiving the cylinders from DCG Partnership nor after measuring the densities.

Table 5.5. Pure Component True Measured Density Data

T	P	ρ
		True measured
K	MPa	kmole/m^3
Isotherm 1: Ar 1 270K 03192003		
270.013	7.024316	3.32897
270.015	13.883214	6.82327
270.014	20.739401	10.19155
270.024	27.496195	13.06750
270.024	34.501119	15.50249
Isotherm 2: Ar 1 340K 03252003		
339.973	6.915530	2.48221
340.003	13.886717	4.99030
340.032	20.732242	7.35607
340.035	27.603607	9.55153
340.038	34.498250	11.53044
Isotherm 3: Ar 1 270K 03262003		
269.974	6.988688	3.31243
269.973	13.852090	6.80991
269.992	20.747945	10.19753
269.993	20.766498	10.20619
270.011	27.621639	13.11774
269.956	34.518944	15.51434
Isotherm 4: CH4 1 270K 03292003		
270.002	6.965019	3.72540
269.987	34.729441	16.27922
269.987	27.712224	14.65118
269.984	20.925920	12.32303
269.994	13.789554	8.39705
270.006	6.834334	3.64254

Table 5.5. (Continued)

T	P	ρ
		True measured
K	MPa	kmole/m^3
Isotherm 5: CH4 1 340K 03312003		
340.017	6.955254	2.62374
340.005	13.826201	5.40314
340.013	20.733750	8.05574
340.006	27.643588	10.30364
339.991	34.454589	12.08803
Isotherm 6: CH4 2 270K 04042003		
269.967	6.905708	3.68897
269.886	13.806413	8.41748
269.953	20.673950	12.21777
269.949	27.563967	14.61321
269.956	34.548479	16.24612
269.945	6.778310	3.60890
Isotherm 7: CH4 3 270K 04082003		
269.989	7.018243	3.75888
269.973	13.895146	8.46869
269.979	20.753411	12.24778
269.977	26.878279	14.41378
Isotherm 8: CH4 3 340K 04162003		
340.038	6.968711	2.62780
339.995	13.879164	5.42358
340.003	20.757004	8.06265
339.997	27.539234	10.27129

Table 5.5. (Continued)

T	P	ρ
		True measured
K	MPa	kmole/m^3
Isotherm 9: Ar 1 340K 04182003		
339.944	6.941460	2.49215
339.963	13.888609	4.99211
339.951	17.199149	6.15505
339.912	27.642727	9.56805
339.899	34.535319	11.54650
Isotherm 10: Ar 2 340K 04222003		
340.069	6.936001	2.48867
340.080	13.834205	4.97006
340.079	20.730657	7.35390
340.076	27.594570	9.54692
340.097	34.500323	11.52812
Isotherm 11: N2 1 340K 04252003		
339.957	6.996853	2.44277
339.960	13.911771	4.72453
339.954	20.700612	6.76393
339.952	27.710474	8.63184
339.951	34.559344	10.22989
Isotherm 12: N2 1 270K 04272003		
269.965	6.966050	3.16578
269.961	13.845764	6.21193
269.959	20.728037	8.91189
269.967	27.612029	11.16609
269.969	34.485036	13.01277

Table 5.5. (Continued)

T	P	ρ
		True measured
K	MPa	kmole/m^3
Isotherm 20: N2 1 270K 08272003		
269.973	3.456941	1.56197
269.998	6.927457	3.14845
270.001	10.371838	4.70324
269.969	13.811624	6.19789
269.972	20.719738	8.90868
269.994	27.609557	11.16401
270.005	34.509092	13.01624
Isotherm 21: N2 2 340K 12212003		
340.152	3.463590	1.21912
340.149	6.909779	2.41169
340.136	10.361997	3.57349
340.134	13.803025	4.68756
340.153	17.265804	5.75620
340.161	20.714612	6.76351
340.164	27.605495	8.60015
340.164	34.511282	10.21368
Isotherm 22: N2 2 270K 12282003		
269.988	3.460498	1.56322
269.955	6.897271	3.13536
269.953	10.350689	4.69485
269.979	13.799986	6.19256
269.984	17.247061	7.59914
269.972	20.700589	8.90101
269.983	27.603984	11.16220
269.975	34.497937	13.01483

The procedure followed for natural gas mixture density measurements differs from that described in Appendix G for pure components in two ways. The first difference is that the calibration procedure for PT06K immediately following each density measurement point was not done while measuring natural gas densities. Instead, the calibrations of PT06K done with pure components and described in subsections 4.1.3 and 4.1.2 were used for M91C1 and M94C1 respectively. The second difference is that while measuring isotherms of M94C1 at temperatures below its CT, the mixture was not directly charged into the cell at the isotherm temperature in order to avoid the two phase region shown in Figure 2.2, at pressures below the CB. Instead, the cell was heated to a temperature above the CT of M94C1, the pressure increased above the CB of M94C1, the cell temperature decreased to the isotherm temperature with simultaneous increments in pressure to always maintain the cell pressure above the CB and subsequently, densities measured at increasingly higher pressures. Similar precautions were taken to avoid the two phase region while emptying the cell. Although the predicted phase envelope for M91C1 as shown in Figure 2.2 did not require a similar precautionary procedure while measuring its 270 K [26.33 ^{o}F, -3.15 ^{o}C] isotherm, the cell was maintained at ambient temperature, pressurized above the CB of M91C1, the cell temperature reduced to 270 K [26.33 ^{o}F, -3.15 ^{o}C] always maintaining the cell pressure above the CB of M91C1 and then densities measured at pressures above the CB. This precaution was taken to avoid passing through the two phase region in case the predicted phase envelope misleadingly suggested a CT lower than the actual. The lower pressure points of approximately 3.447 MPa [500 psia] and 6.895 MPa [1,000 psia] on the 270 K [26.33 ^{o}F, -3.15 ^{o}C] isotherm were measured towards the end just before emptying the cell.

5.2.1 Density Measurements with M91C1 Mixture

Densities of M91C1 were measured at 33 points in the range (270 to 340) K [(26.33 to 152.33) ^{o}F, (-3.15 to 66.85) ^{o}C] and (3.447 to 34.474) MPa [(500 to 5,000)

psia]. Based upon these 33 points, temperatures were measured with an uncertainty of ±3.8 mK, pressures with an uncertainty of ±0.002%, the weighing balance readings for the true mass of the sinker in vacuum with an uncertainty of ±0.01 mg and the weighing balance readings for the apparent mass of the sinker under pressure with an uncertainty of ±0.02 mg at the approximately 68% confidence level (1σ). The measured mass density calculated from equation (8) was converted to molar density using molar masses for the components shown in Table 2.2. The measured molar density was compared with the molar density predicted by the HY, AGA8-DC92 and REFPROP EOS each, using programs for gas mixtures mentioned in subsection 2.1.10. The percentage relative density deviations between the measured and predicted values were calculated according to equation (31). Table 5.6 shows the measured molar densities and the relative molar density deviations from the corresponding predictions from each of the three EOS. The relative mass density deviations are systematically larger than the relative molar density deviations calculated from the REFPROP EOS by 0.001% because of the small differences in molar masses of M91C1 used for the experimental densities and the HY EOS predicted densities on the one hand and those used by either AGA8-DC92 or REFPROP EOS predictions on the other hand because of the way the components are grouped as shown in Table 2.4. Mass densities were converted to molar densities using molar masses of M91C1 as shown in Table A.2.1 for the HY EOS prediction and the experimental density and in Tables A.2.2 and A.2.3 for the AGA8-DC92 and REFPROP predictions respectively. Figures 5.8, 5.9 and 5.10 respectively show the relative deviations of the measured densities from the HY, AGA8-DC92 and REFPROP EOS predicted densities given in Table 5.6. For the molar mass of 18.21068 kg/kmole of M91C1, an apparatus bias error of +0.118 % implied from equation (32) was deducted from the relative density deviations of Table 5.6 to get the true relative density deviations.

The true relative density deviations of data measured as part of the present work for M91C1 were compared with the relative density deviations of data measured by Hwang *et al.* (1997) and Magee *et al.* (1997) for RR-NIST2 as shown in

Table 5.6. Measured Density Data for M91C1 Mixture

Isotherm 23: M91C1 340K 01202004										
T	P	m_v and m_a	v_s	ρ						
μ	μ	μ		measured	predicted			Relative deviation		
					HY	AGA8-DC92	REFPROP	HY	AGA8-DC92	REFPROP
K	MPa	g	cm^3	$kmole/m^3$	$kmole/m^3$	$kmole/m^3$	$kmole/m^3$	%	%	%
340.018	-0.002669	0.01372	-	-	-	-	-	-	-	-
340.000	-0.002743	0.01372	-	-	-	-	-	-	-	-
340.016	-0.002671	0.01373	-	-	-	-	-	-	-	-
340.002	3.449669	-0.14327	6.74894	1.27752	1.28130	1.27615	1.27553	-0.295	0.107	0.156
339.999	6.901520	-0.31317	6.74871	2.65998	2.67735	2.65812	2.65576	-0.649	0.070	0.159
340.033	10.349619	-0.49205	6.74848	4.11558	4.15403	4.11387	4.10965	-0.926	0.042	0.144
340.027	13.798785	-0.67353	6.74825	5.59252	5.65437	5.59109	5.58566	-1.094	0.026	0.123
340.024	20.699339	-1.01182	6.74780	8.34584	8.42676	8.34015	8.33478	-0.960	0.068	0.133
340.025	27.587333	-1.28611	6.74734	10.57871	10.62306	10.56242	10.55527	-0.417	0.154	0.222
340.026	27.591119	-1.28623	6.74734	10.57968	10.62405	10.56344	10.55629	-0.418	0.154	0.222
339.995	34.486008	-1.49779	6.74688	12.30230	12.29251	12.28318	12.26999	0.080	0.156	0.263
339.997	-0.003700	0.01377	-	-	-	-	-	-	-	-

Table 5.6. (Continued)

Isotherm 24: M91C1 305K 01282004										
T	P	m_v and m_a	v_s	ρ						
μ	μ	μ		measured	predicted			Relative deviation		
					HY	AGA8-DC92	REFPROP	HY	AGA8-DC92	REFPROP
K	MPa	g	cm^3	$kmole/m^3$	$kmole/m^3$	$kmole/m^3$	$kmole/m^3$	%	%	%
304.994	-0.003436	0.01328	-	-	-	-	-	-	-	-
305.002	3.484438	-0.16792	6.74271	1.47820	1.48114	1.47524	1.47385	-0.199	0.201	0.295
304.999	6.898528	-0.37069	6.74248	3.12966	3.14654	3.12697	3.12176	-0.537	0.086	0.253
304.994	10.343093	-0.59658	6.74225	4.96954	5.00524	4.96934	4.95972	-0.713	0.004	0.198
305.001	13.791554	-0.82889	6.74202	6.86179	6.91690	6.86639	6.85331	-0.797	-0.067	0.124
305.007	20.707261	-1.23493	6.74156	10.16969	10.22967	10.17615	10.15754	-0.586	-0.063	0.120
305.001	27.586034	-1.52167	6.74109	12.50613	12.51451	12.50407	12.47536	-0.067	0.016	0.247
305.016	34.472145	-1.72361	6.74063	14.15209	14.10008	14.14469	14.11037	0.369	0.052	0.296
305.017	-0.002723	0.01371	-	-	-	-	-	-	-	-
305.014	-0.003575	0.01376	-	-	-	-	-	-	-	-

Table 5.6. (Continued)

Isotherm 25: M91C1 290K 02032004										
T	P	m_v and m_a	v_s	ρ						
μ	μ	μ		measured	predicted			Relative deviation		
					HY	AGA8-DC92	REFPROP	HY	AGA8-DC92	REFPROP
K	MPa	g	cm^3	$kmole/m^3$	$kmole/m^3$	$kmole/m^3$	$kmole/m^3$	%	%	%
290.002	-0.003465	0.01362	-	-	-	-	-	-	-	-
290.005	3.453465	-0.17800	6.74004	1.56239	1.56707	1.56108	1.55916	-0.299	0.084	0.207
290.007	6.902846	-0.40460	6.73981	3.40868	3.42656	3.40893	3.40133	-0.522	-0.007	0.216
290.006	10.354206	-0.66342	6.73957	5.51756	5.54754	5.52347	5.50863	-0.540	-0.107	0.162
290.003	13.788715	-0.92816	6.73934	7.67495	7.71780	7.69118	7.67047	-0.555	-0.211	0.058
290.008	20.693324	-1.36200	6.73887	11.21064	11.25574	11.23098	11.19764	-0.401	-0.181	0.116
290.012	27.600326	-1.64382	6.73840	13.50811	13.49987	13.51486	13.47129	0.061	-0.050	0.273
290.011	34.505487	-1.83499	6.73793	15.06697	14.99591	15.06576	15.01860	0.474	0.008	0.322
290.013	-0.003387	0.01392	-	-	-	-	-	-	-	-
290.039	-0.003504	0.01372	-	-	-	-	-	-	-	-
290.013	17.271107	-1.16854	6.73910	9.63350	9.68625	9.65574	9.62996	-0.545	-0.230	0.037

Table 5.6. (Continued)

Isotherm 26: M91C1 270K 02102004										
T	P	m_v and m_a	v_s	ρ						
μ	μ	μ		measured	predicted			Relative deviation		
					HY	AGA8-DC92	REFPROP	HY	AGA8-DC92	REFPROP
K	MPa	g	cm^3	$kmole/m^3$	$kmole/m^3$	$kmole/m^3$	$kmole/m^3$	%	%	%
270.014	-0.002961	0.01385	-	-	-	-	-	-	-	-
270.004	3.482523	-0.19960	6.73648	1.73926	1.74660	1.74074	1.73759	-0.420	-0.085	0.096
269.988	6.896953	-0.46542	6.73624	3.90622	3.92142	3.91408	3.90050	-0.388	-0.201	0.147
269.990	10.369826	-0.79451	6.73600	6.58914	6.59037	6.61736	6.58759	-0.019	-0.427	0.023
269.983	10.374792	-0.79506	6.73600	6.59359	6.59482	6.62190	6.59210	-0.019	-0.428	0.023
269.977	13.799264	-1.11901	6.73577	9.23482	9.24098	9.28506	9.24362	-0.067	-0.541	-0.095
269.990	17.260776	-1.37865	6.73553	11.35196	11.38322	11.40615	11.35042	-0.275	-0.475	0.014
269.985	20.698186	-1.56804	6.73529	12.89643	12.93042	12.94261	12.87813	-0.263	-0.357	0.142
269.989	27.617939	-1.82408	6.73482	14.98500	14.96764	15.00953	14.93995	0.116	-0.163	0.302
269.983	27.608389	-1.82387	6.73482	14.98326	14.96591	15.00774	14.93816	0.116	-0.163	0.302
269.991	34.542911	-1.99341	6.73434	16.36681	16.27933	16.38238	16.31182	0.537	-0.095	0.337
270.025	-	0.01367	-	-	-	-	-	-	-	-

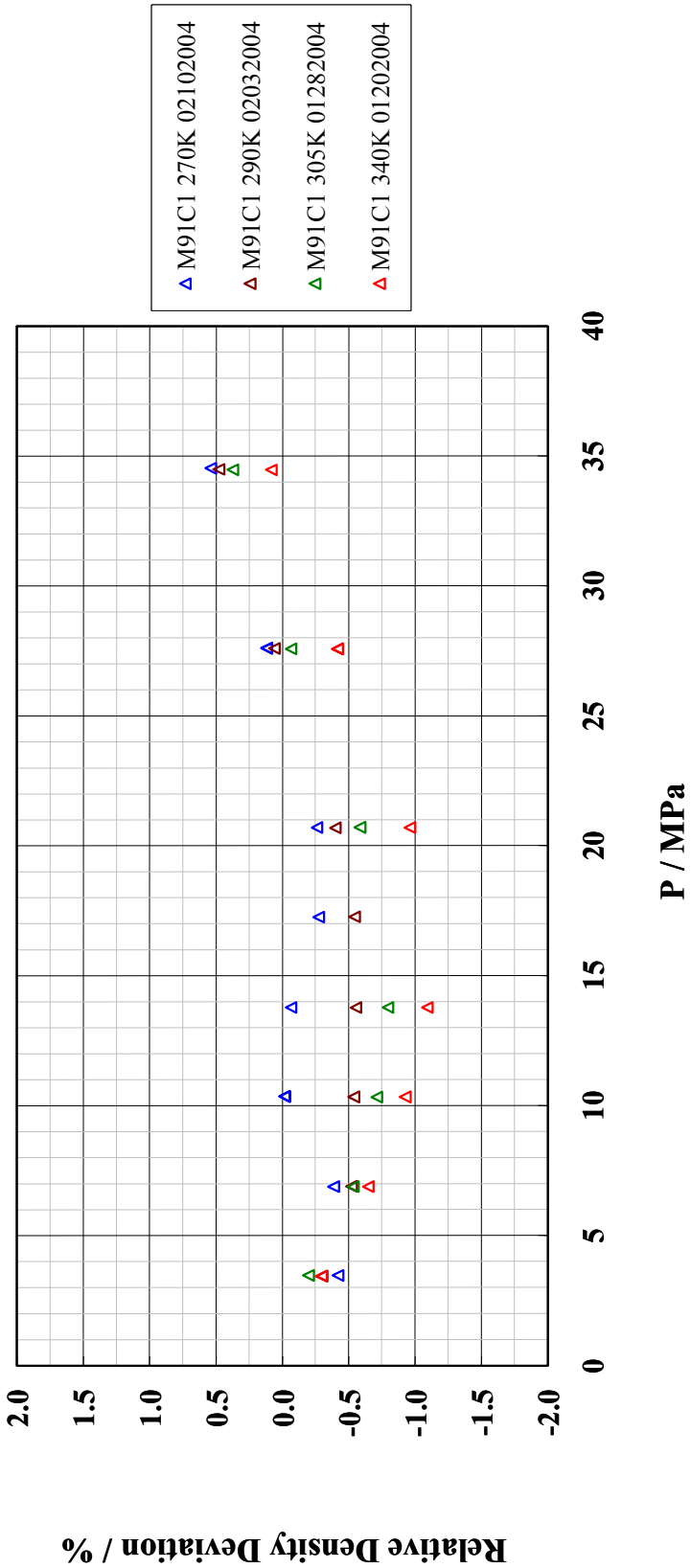

Figure 5.8. Relative Deviations between Measured and HY EOS Predicted Molar Densities for M91C1

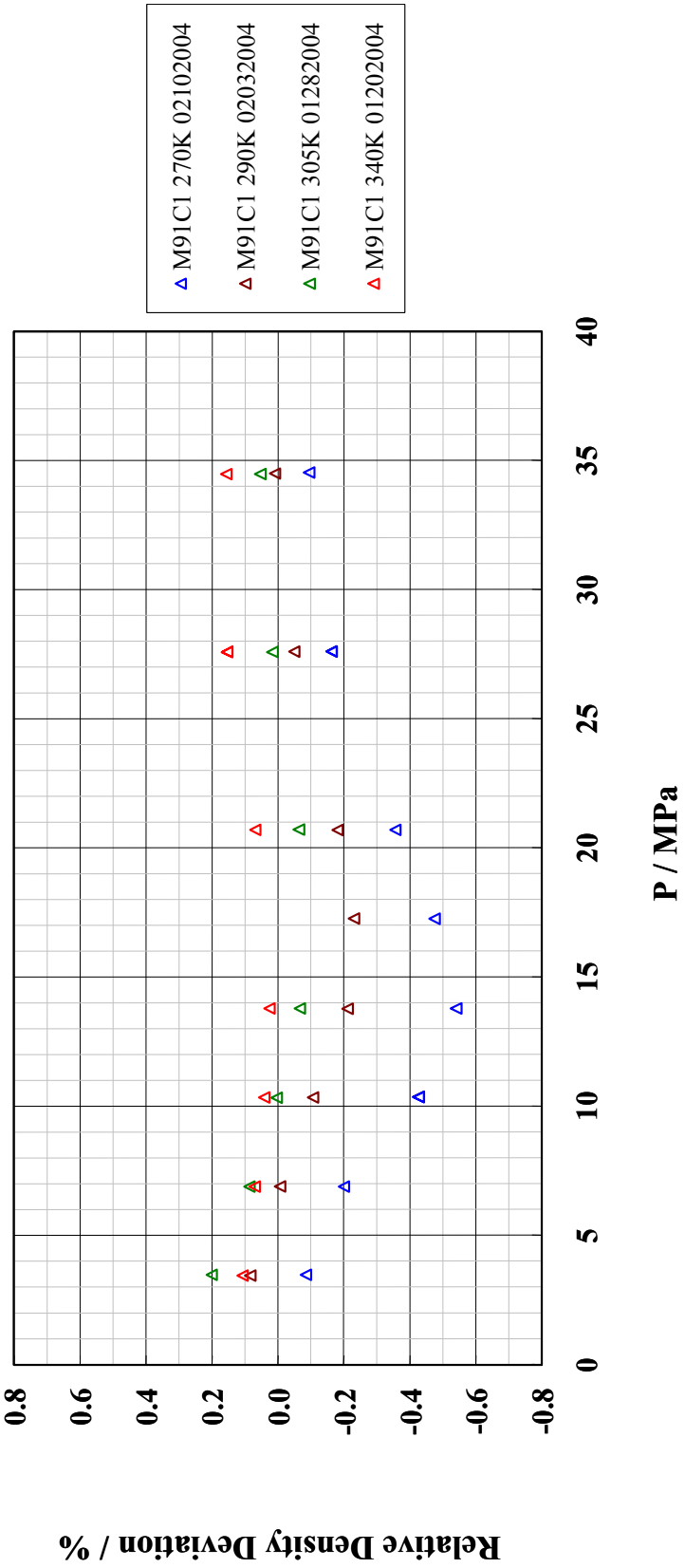

Figure 5.9. Relative Deviations between Measured and AGA8-DC92 EOS Predicted Molar Densities for M91C1

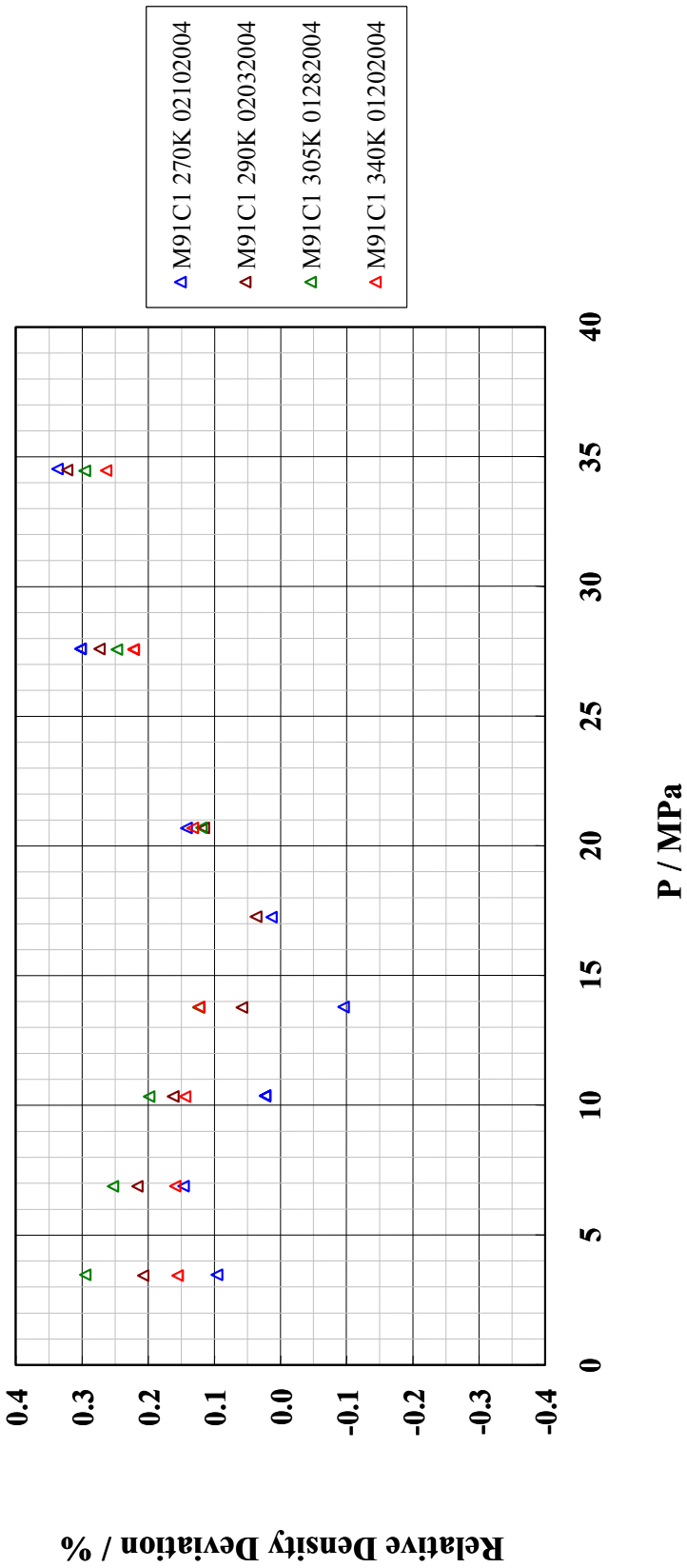

Figure 5.10. Relative Deviations between Measured and REFPROP EOS Predicted Molar Densities for M91C1

Figures 5.11, 5.12 and 5.13 for the HY, AGA8-DC92 and REFPROP EOS respectively. The ‘b’ and ‘p’ at the extreme end of the isotherm identities of the data of Hwang *et al.* represent the Burnett apparatus and the pycnometer respectively. Density data only over the range (263 to 350) K [(13.73 to 170.33) ^{o}F, (-10.15 to 76.85) ^{o}C] and up to approximately 37 MPa [5,366.395 psia] that overlaps with the range of interest of the present work were selected. The relative mass density deviations are systematically larger than the relative molar density deviations calculated from the REFPROP EOS by 0.002% because of the small differences in molar masses of RR-NIST2 used for the experimental densities and the HY EOS predicted densities on the one hand and those used by either AGA8-DC92 or REFPROP EOS predictions on the other hand because of the way the components are grouped as shown in Table 2.3. Mass densities were converted to molar densities using molar masses of RR-NIST2 as shown in Table A.1.1 for the HY EOS prediction and the experimental density and in Tables A.1.2 and A.1.3 for the AGA8-DC92 and REFPROP predictions respectively.

5.2.2 Discussion on M91C1 Density Measurement Results

In general, the entire measured data set shown deviates by ±2% from the HY EOS predictions, ±0.7% from the AGA8-DC92 EOS predictions and ±0.3% from the REFPROP EOS predictions; thus showing the improvements in the EOS predictions for natural gas custody transfer applications. Both RR-NIST2 and M91C1 have compositions that fall under the ‘normal range’ as defined by the AGA8-DC92 EOS report (American Gas Association, 1992) where the C_{6+} fraction is lower than 0.2%.

For data in region 1 of American Gas Association (1992) that spans over the range (265 to 335) K [(17.33 to 142.7) ^{o}F, (-8.15 to 61.85) ^{o}C] up to 11.997 MPa [1,740 psia], the relative density deviations from the AGA8-DC92 EOS predictions were expected to be lower than ±0.1% for both RR-NIST2 and M91C1. Out of the 9 points of M91C1 measured in this range, 3 points on the 270 K [26.33 ^{o}F, -3.15 ^{o}C] isotherm and one point on the 290 K [62.33 ^{o}F, 16.85 ^{o}C] isotherm, clearly neither lie within the

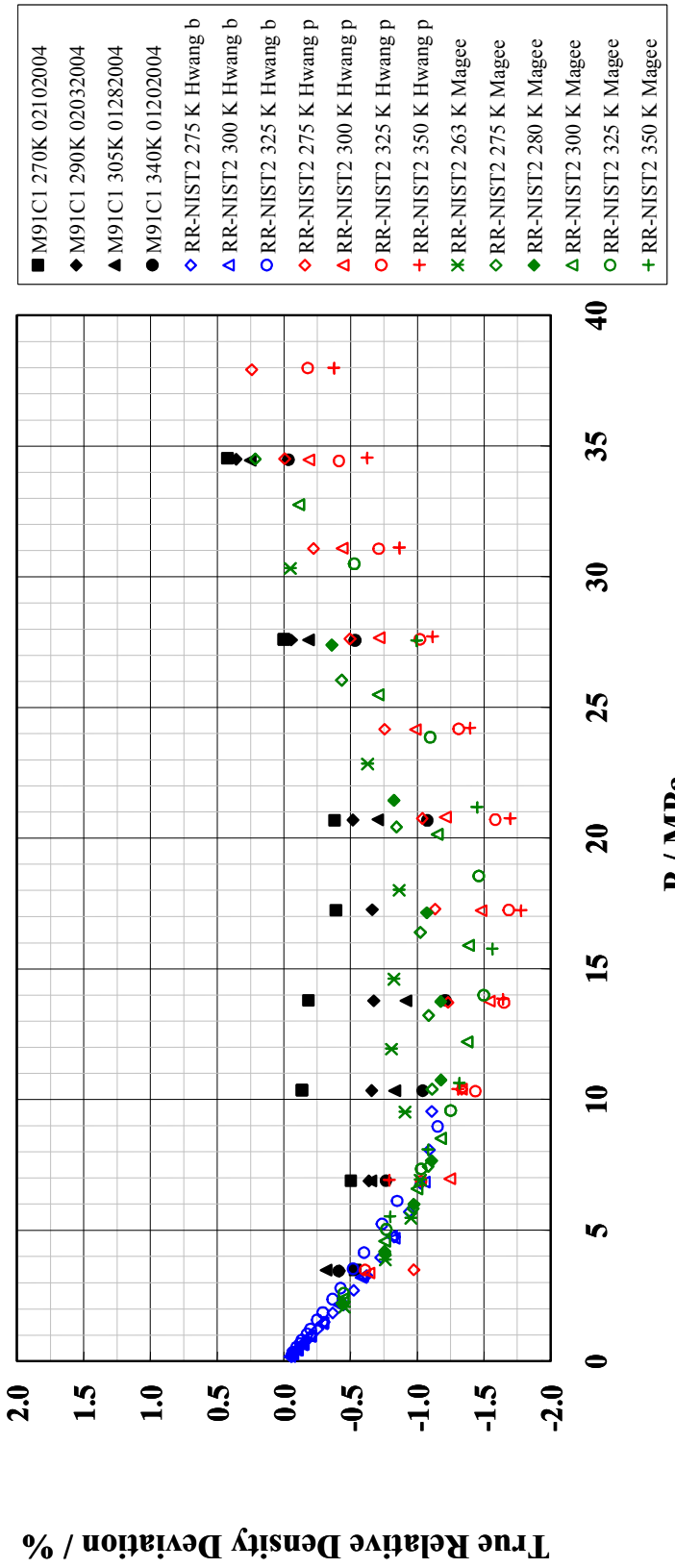

Figure 5.11. Comparison of True Relative Density Deviations from the HY EOS Predictions for M91C1 from the MSD Measurements, with Relative Density Deviations of Literature Data from the HY EOS Predictions for RR-NIST2. (Only first author names appear in legend; for complete citations refer text)

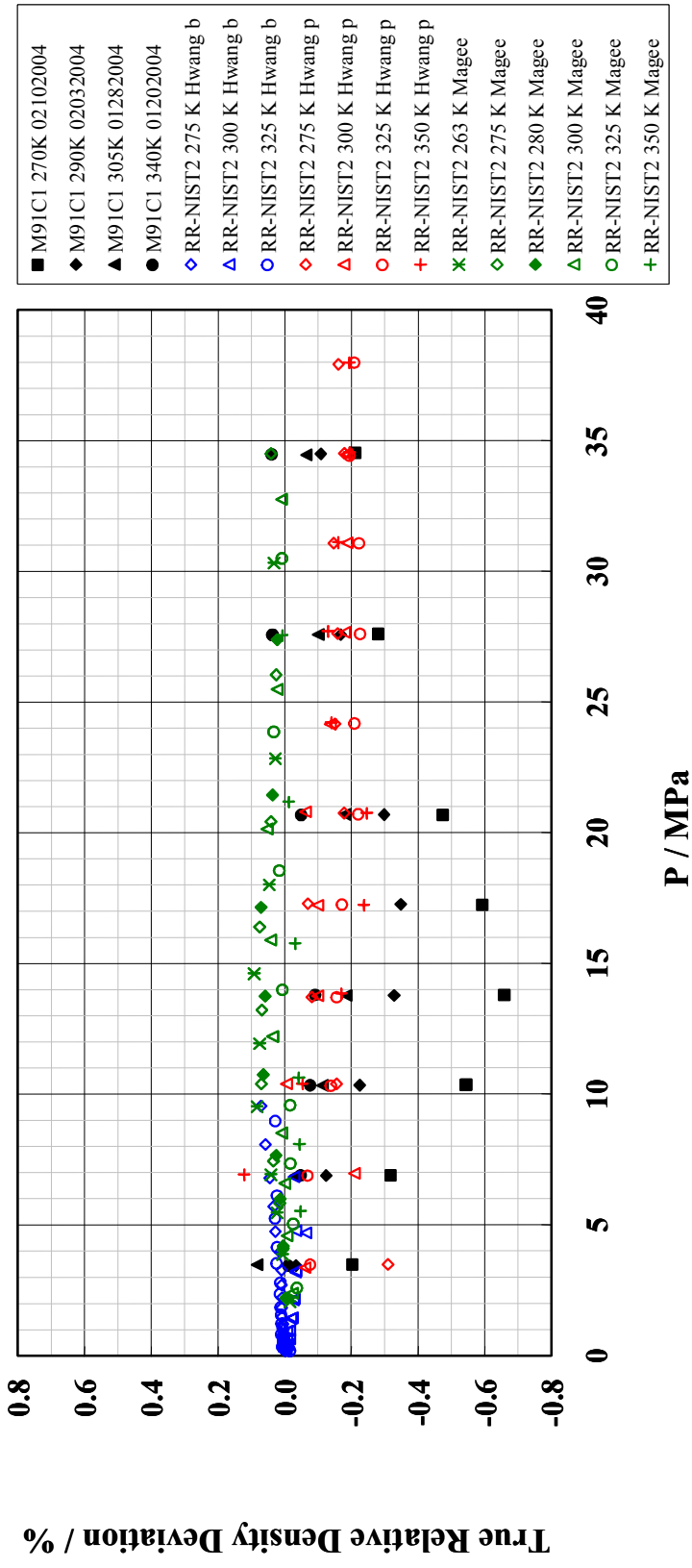

Figure 5.12. Comparison of True Relative Density Deviations from the AGA8-DC92 EOS Predictions for M91C1 from the MSD Measurements, with Relative Density Deviations of Literature Data from the AGA8-DC92 EOS Predictions for RR-NIST2. (Only first author names appear in legend; for complete citations refer text)

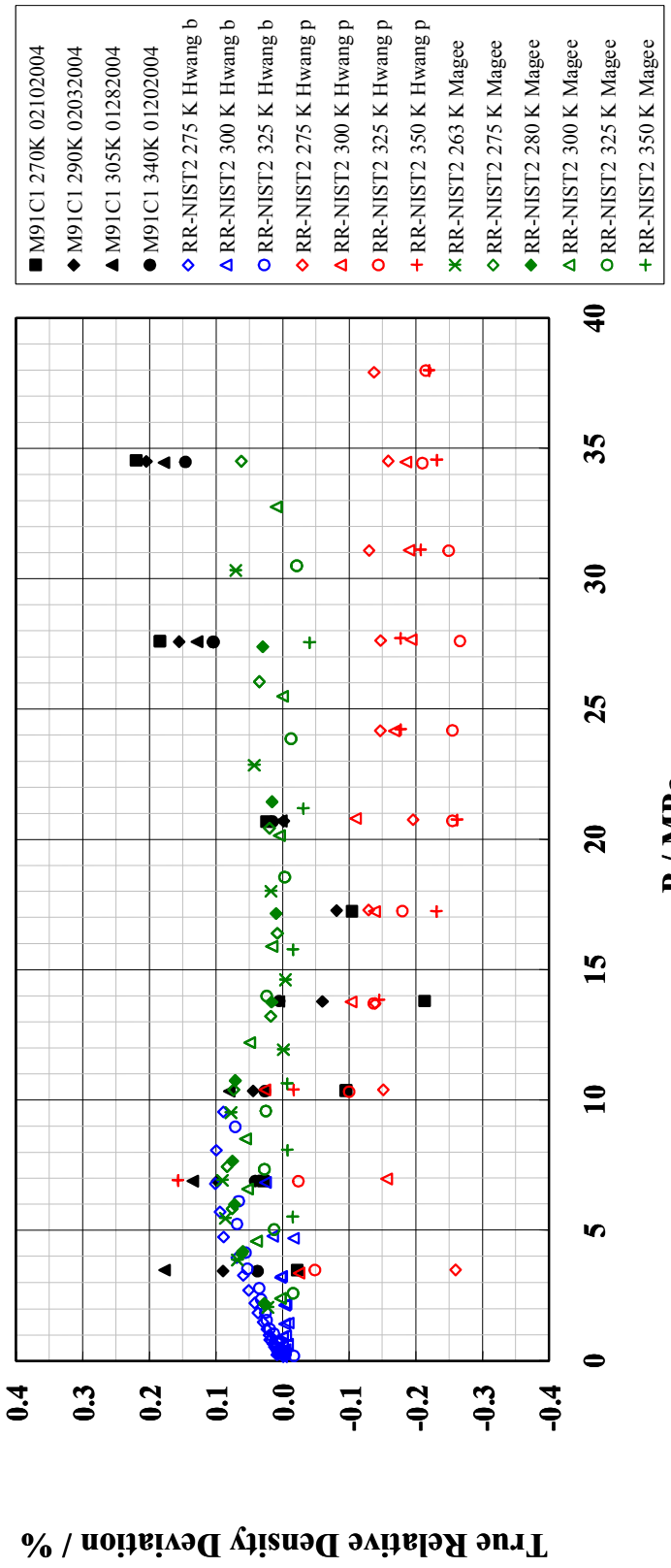

Figure 5.13. Comparison of True Relative Density Deviations from the REFPROP EOS Predictions for M91C1 from the MSD Measurements, with Relative Density Deviations of Literature Data from the REFPROP EOS Predictions for RR-NIST2. (Only first author names appear in legend; for complete citations refer text)

±0.1% uncertainty limit for region 1 nor match closely with the RR-NIST2 data as shown in Figure 5.12. Out of these four points, two on the 270 K [26.33 ^{o}F, -3.15 ^{o}C] isotherm at approximately 3.496 MPa [507 psia] and 6.998 MPa [1,015 psia] may not match because of the higher uncertainty of density measurement of the apparatus below approximately 6.998 MPa [1,015 psia] as mentioned earlier in subsection 5.1.2. The remaining two points of M91C1 at approximately 10.5 MPa [1,522.896 psia] on the 270 K [26.33 ^{o}F, -3.15 ^{o}C] and 290 K [62.33 ^{o}F, 16.85 ^{o}C] isotherms were expected to have same relative deviations as the corresponding points for RR-NIST2, but do not. However, the same four measured data have relative density deviations that match with those of RR-NIST2 when compared with the REFPROP EOS predictions as shown in Figure 5.13. Only one point of M91C1 that fell within the ±0.1% limit of region 1, when compared to AGA8-DC92 EOS predictions, does not agree with the RR-NIST2 data when compared with the REFPROP EOS predictions.

For data in region 2 of American Gas Association (1992) that covers the range of approximately (211 to 394) K [(-79.87 to 249.53) ^{o}F, (-62.15 to 120.85) ^{o}C] and (12 to 17) MPa [(1,740.452 to 2,465.641) psia], the relative density deviations from the AGA8-DC92 EOS predictions were expected to be lower than ±0.3% for both RR-NIST2 and M91C1. Out of the 9 points of M91C1 measured in this region, four points have relative density deviations from the AGA8-DC92 EOS predictions larger than the expected ±0.3% and do not match with the relative density deviations of RR-NIST2 as shown in Figure 5.12. However, eight out of the nine points of M91C1 have relative density deviations that match with those of RR-NIST2 points when compared with the REFPROP EOS predictions as shown in Figure 5.13.

For data in region 3 of American Gas Association (1992) that covers the range of approximately (144 to 477) K [(-200.40 to 398.93) ^{o}F, (-129.15 to 203.85) ^{o}C] and (17 to 35) MPa [(2,465.641 to 5,076.320) psia] , the relative density deviations from the AGA8-DC92 EOS predictions were expected to be lower than ±0.5% for both RR-NIST2 and M91C1. Figure 5.12 shows that the relative density deviations of the 12 measured points of M91C1 when compared with the AGA8-DC92 EOS predictions do

fall within the expected ±0.5% limit and that there is good agreement with the RR-NIST2 data except for one point on the 270 K [26.33 ^{o}F, -3.15 ^{o}C] isotherm at approximately 20.5 MPa [2,973.273 psia]. The same 12 points agree with the RR-NIST2 data to within ±0.3% when compared with the REFPROP EOS predictions as shown in Figure 5.13.

It can be summarized from the above discussion that the measured densities for M91C1 deviate from the AGA8-DC92 EOS predictions in regions 1 and 2 to much greater extents than expected but match in region 3. However, they match well with the REFPROP EOS predictions in all three regions. After taking into consideration the validation of the apparatus operation with pure component density measurements and the good agreement of the measured densities of M91C1 with the predicted densities from a recently developed EOS such as REFPROP, it can be concluded that the AGA8-DC92 EOS density predictions in the temperature and pressure range of most importance to the natural gas custody transfer business are unreliable.

The true measured densities for M91C1, calculated from the true relative density deviations shown in Figures 5.11, 5.12 and 5.13 after applying the correction for the molar mass dependent apparatus bias error for the MSD, are given in Table 5.7. Figure 5.14 shows a *P versus* ρ plot for the true measured densities of M91C1 along with the measured densities of Hwang *et al.* and Magee *et al.* for RR-NIST2. The systematic order among isotherms of M91C1 and RR-NIST2 in the absence of any major composition difference between the two natural gas mixtures further corroborates the true measured density data using the MSD.

5.2.3 Density Measurements with M94C1 Mixture

Densities of M94C1 were measured at 56 points in the range (270 to 340) K [(26.33 to 152.33) ^{o}F, (-3.15 to 66.85) ^{o}C] and (3.447 to 34.474) MPa [(500 to 5,000) psia]. Based upon these 56 points, temperatures were measured with an uncertainty of ±3.3 mK, pressures with an uncertainty of ±0.002%, the weighing balance readings for

Table 5.7. M91C1 True Measured Density Data

T	P	ρ
		True measured
K	MPa	kmole/m^3
Isotherm 23: M91C1 340K 01202004		
340.002	3.449669	1.27600
339.999	6.901520	2.65682
340.033	10.349619	4.11067
340.027	13.798785	5.58584
340.024	20.699339	8.33587
340.025	27.587333	10.56615
340.026	27.591119	10.56712
339.995	34.486008	12.28776
Isotherm 24: M91C1 305K 01282004		
305.002	3.484438	1.47645
304.999	6.898528	3.12594
304.994	10.343093	4.96363
305.001	13.791554	6.85361
305.007	20.707261	10.15760
305.001	27.586034	12.49133
305.016	34.472145	14.13542

Table 5.7. (Continued)

T	P	ρ
		True measured
K	MPa	kmole/m^3
Isotherm 25: M91C1 290K 02032004		
290.005	3.453465	1.56054
290.007	6.902846	3.40463
290.006	10.354206	5.51100
290.003	13.788715	7.66583
290.008	20.693324	11.19734
290.012	27.600326	13.49215
290.011	34.505487	15.04924
290.013	17.271107	9.62205
Isotherm 26: M91C1 270K 02102004		
270.004	3.482523	1.73719
269.988	6.896953	3.90158
269.990	10.369826	6.58134
269.983	10.374792	6.58579
269.977	13.799264	9.22389
269.990	17.260776	11.33850
269.985	20.698186	12.88114
269.989	27.617939	14.96731
269.983	27.608389	14.96557
269.991	34.542911	16.34757

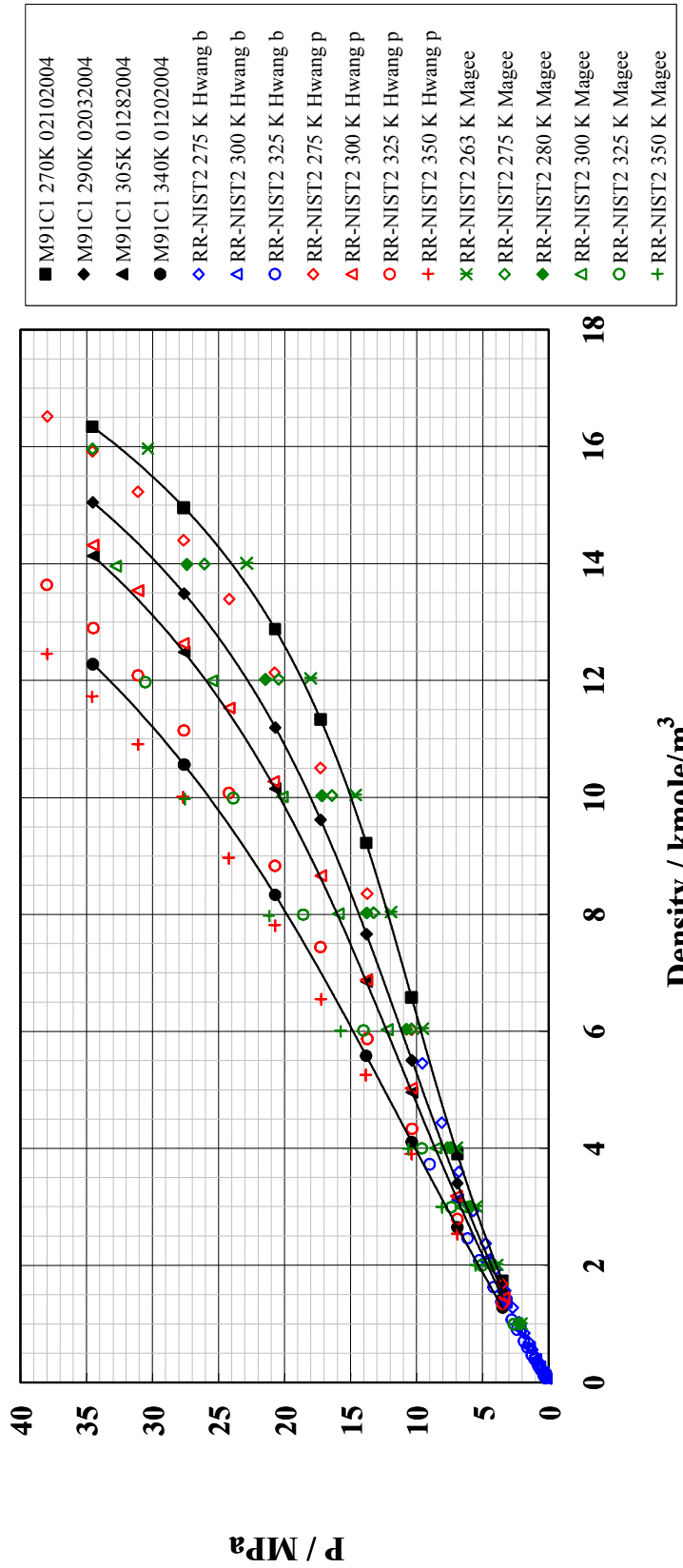

Figure 5.14. Comparison of True Measured Densities for M91C1 from the MSD with Measured Densities for RR-NIST2 from Literature on a Pressure versus Density Plot. (Only first author names appear in legend; for complete citations refer text)

the true mass of the sinker in vacuum with an uncertainty of ±0.01 mg and the weighing balance readings for the apparent mass of the sinker under pressure with an uncertainty of ±0.03 mg at the approximately 68% confidence level (1σ). A procedure similar to that described for M91C1 in subsection 5.2.1 was followed for the M94C1 measured data. Table 5.8 shows the measured molar densities and the relative molar density deviations from the corresponding predictions from each of the three EOS for M94C1. The relative mass density deviations are systematically smaller than the relative molar density deviations calculated from the AGA8-DC92 EOS by 0.001% and larger than the relative molar density deviations calculated from the REFPROP EOS by 0.020% because of the differences in molar masses of M94C1 used for the experimental densities and the HY EOS predicted densities on the one hand and those used by either AGA8-DC92 or REFPROP EOS predictions on the other hand in grouping the components as shown in Table 2.5. Mass densities were converted to molar densities using molar masses of M94C1 as shown in Table A.3.1 for the HY EOS prediction and the experimental density and in Tables A.3.2 and A.3.3 for the AGA8-DC92 and REFPROP predictions respectively. For the molar mass of 17.88784 kg/kmole of M94C1, an apparatus bias error of + 0.119% implied from equation (32) was deducted from the relative density deviations of Table 5.8 to get the true relative density deviations. Figures 5.15, 5.16 and 5.17 respectively show the true relative deviations of the measured densities from the HY, AGA8-DC92 and REFPROP EOS predicted densities given in Table 5.8. The true measured densities for M94C1, calculated from the true relative density deviations shown in Figures 5.15, 5.16 and 5.17 after applying the correction for the molar mass dependent apparatus bias error for the MSD, are given in Table 5.9. Figure 5.18 shows a plot of pressure *versus* the true measured density for M94C1.

Figure 5.19 shows the results of a test to evaluate if the MSD can be used for identification of the two phase envelope by observing a sudden change in the slope of the relative density deviation versus pressure curve for an isotherm at the inception of liquid condensate. This test was done for the 280 K [44.33 ^{o}F, 6.85 ^{o}C] and 290 K [62.33

Table 5.8. Measured Density Data for M94C1 Mixture

Isotherm 13: M94C1 340K 05212003										
T	P	m_v and m_a	v_s	ρ						
μ	μ	μ		measured	predicted			Relative deviation		
					HY	AGA8-DC92	REFPROP	HY	AGA8-DC92	REFPROP
K	MPa	g	cm^3	$kmole/m^3$	$kmole/m^3$	$kmole/m^3$	$kmole/m^3$	%	%	%
340.028	-0.007053	0.01330	-	-	-	-	-	-	-	-
340.025	3.499658	-0.14286	6.74894	1.29355	1.30083	1.29586	1.29543	-0.559	-0.178	-0.145
340.020	6.929327	-0.30857	6.74871	2.66627	2.68968	2.67114	2.67012	-0.870	-0.182	-0.144
340.023	10.393377	-0.48544	6.74848	4.13150	4.17578	4.13586	4.13591	-1.060	-0.105	-0.107
340.020	12.114931	-0.57481	6.74837	4.87191	4.92774	4.87535	4.87694	-1.133	-0.071	-0.103
340.026	13.818562	-0.66285	6.74825	5.60136	5.66799	5.60313	5.60684	-1.176	-0.032	-0.098
340.030	15.528452	-0.74971	6.74814	6.32103	6.39742	6.32106	6.32729	-1.194	-0.001	-0.099
339.995	17.286678	-0.83669	6.74802	7.04170	7.12518	7.03919	7.04818	-1.172	0.036	-0.092
339.998	19.002277	-0.91810	6.74791	7.71629	7.80353	7.71106	7.72258	-1.118	0.068	-0.081
339.994	20.701856	-0.99500	6.74779	8.35349	8.44104	8.34554	8.35911	-1.037	0.095	-0.067
339.996	27.544327	-1.26241	6.74734	10.56969	10.63092	10.55548	10.56893	-0.576	0.135	0.007
340.061	34.520557	-1.47232	6.74687	12.30964	12.31950	12.29302	12.29603	-0.080	0.135	0.111

Table 5.8. (Continued)

Isotherm 14: M94C1 305K 05252003										
T	P	m_v and m_a	v_s	ρ						
μ	μ	μ		measured	predicted			Relative deviation		
					HY	AGA8-DC92	REFPROP	HY	AGA8-DC92	REFPROP
K	MPa	g	cm^3	$kmole/m^3$	$kmole/m^3$	$kmole/m^3$	$kmole/m^3$	%	%	%
304.998	-0.007411	0.01316	-	-	-	-	-	-	-	-
305.006	13.809135	-0.81623	6.74202	6.87719	6.93568	6.87447	6.88681	-0.843	0.040	-0.140
305.005	15.534073	-0.92615	6.74190	7.78883	7.85519	7.78340	7.80181	-0.845	0.070	-0.166
305.008	17.286057	-1.03156	6.74179	8.66301	8.73371	8.65402	8.67723	-0.810	0.104	-0.164
305.003	18.970681	-1.12569	6.74167	9.44370	9.51502	9.43180	9.45731	-0.750	0.126	-0.144
305.002	20.712540	-1.21501	6.74156	10.18457	10.25262	10.17055	10.1957	-0.664	0.138	-0.109
305.015	12.085573	-0.70252	6.74213	5.93424	5.98236	5.93278	5.93916	-0.804	0.025	-0.083
305.016	10.340341	-0.58609	6.74225	4.96875	5.00752	4.96935	4.97098	-0.774	-0.012	-0.045
305.015	6.895333	-0.36342	6.74248	3.12237	3.14615	3.12722	3.12507	-0.756	-0.155	-0.087
305.063	27.640767	-1.49755	6.74109	12.52833	12.55283	12.50921	12.51800	-0.195	0.153	0.082
304.894	34.425965	-1.69450	6.74063	14.16265	14.12865	14.13979	14.13139	0.241	0.162	0.221

Table 5.8. (Continued)

Isotherm 15: M94C1 270K 05292003										
T	P	m_v and m_a	v_s	ρ						
μ	μ	μ		measured	predicted			Relative deviation		
					HY	AGA8-DC92	REFPROP	HY	AGA8-DC92	REFPROP
K	MPa	g	cm^3	$kmole/m^3$	$kmole/m^3$	$kmole/m^3$	$kmole/m^3$	%	%	%
270.055	-0.007714	0.01310	-	-	-	-	-	-	-	-
270.019	13.841947	-1.10594	6.73576	9.28754	9.29021	9.27022	9.32589	-0.029	0.187	-0.411
270.021	15.523501	-1.23940	6.73565	10.39539	10.41330	10.37219	10.43040	-0.172	0.224	-0.336
270.024	17.235790	-1.35647	6.73553	11.36723	11.39818	11.34087	11.39164	-0.272	0.232	-0.214
270.026	18.970225	-1.45756	6.73541	12.20648	12.24507	12.17959	12.21876	-0.315	0.221	-0.101
270.036	20.702053	-1.54384	6.73529	12.92282	12.96310	12.89693	12.92401	-0.311	0.201	-0.009
270.010	27.608542	-1.79437	6.73482	15.00337	15.00286	14.97945	14.96723	0.003	0.160	0.241
270.025	34.543934	-1.96125	6.73434	16.38976	16.31700	16.36404	16.32798	0.446	0.157	0.378

Table 5.8. (Continued)

Isotherm 16: M94C1 320K 06022003										
T	P	m_v and m_a	v_s	ρ						
μ	μ	μ		measured	predicted			Relative deviation		
					HY	AGA8-DC92	REFPROP	HY	AGA8-DC92	REFPROP
K	MPa	g	cm^3	$kmole/m^3$	$kmole/m^3$	$kmole/m^3$	$kmole/m^3$	%	%	%
320.031	-0.007882	0.01324	-	-	-	-	-	-	-	-
320.056	3.482568	-0.15388	6.74538	1.38501	1.39319	1.38794	1.38726	-0.588	-0.211	-0.163
320.057	6.912216	-0.33705	6.74515	2.90318	2.92773	2.90861	2.90704	-0.839	-0.187	-0.133
320.054	10.362430	-0.53638	6.74492	4.55536	4.59948	4.55910	4.55968	-0.959	-0.082	-0.095
320.056	12.086935	-0.63856	6.74481	5.40239	5.45714	5.40426	5.40768	-1.003	-0.035	-0.098
320.054	13.799866	-0.73948	6.74469	6.23894	6.30386	6.23855	6.24570	-1.030	0.006	-0.108
320.051	15.521374	-0.83849	6.74458	7.05971	7.13349	7.05694	7.06827	-1.034	0.039	-0.121
320.055	17.252039	-0.93400	6.74446	7.85151	7.93137	7.84616	7.86148	-1.007	0.068	-0.127
320.053	18.978038	-1.02425	6.74435	8.59976	8.68133	8.59113	8.60952	-0.940	0.100	-0.113
320.049	20.706337	-1.10880	6.74423	9.30077	9.38059	9.28968	9.30968	-0.851	0.119	-0.096
320.012	27.610790	-1.38902	6.74377	11.62433	11.66664	11.60783	11.62014	-0.363	0.142	0.036
320.001	34.491161	-1.59398	6.74331	13.32424	13.30921	13.30405	13.30159	0.113	0.152	0.170

Table 5.8. (Continued)

Isotherm 17: M94C1 280K 06062003										
T	P	m_v and m_a	v_s	ρ						
μ	μ	μ		measured	predicted			Relative deviation		
					HY	AGA8-DC92	REFPROP	HY	AGA8-DC92	REFPROP
K	MPa	g	cm^3	$kmole/m^3$	$kmole/m^3$	$kmole/m^3$	$kmole/m^3$	%	%	%
280.018	-0.007527	0.01311	-	-	-	-	-	-	-	-
279.998	13.829140	-1.00073	6.73755	8.41216	8.44018	8.40452	8.43986	-0.332	0.091	-0.328
280.002	15.519426	-1.12866	6.73743	9.47381	9.51026	9.46087	9.50377	-0.383	0.137	-0.315
280.006	17.597771	-1.26736	6.73729	10.62490	10.66929	10.60740	10.64940	-0.416	0.165	-0.230
280.018	18.973628	-1.34773	6.73719	11.29197	11.33879	11.27343	11.31048	-0.413	0.164	-0.164
280.028	20.696135	-1.43695	6.73708	12.03250	12.07872	12.01415	12.04295	-0.383	0.153	-0.087
279.999	12.065543	-0.85579	6.73767	7.20939	7.22907	7.20509	7.22666	-0.272	0.060	-0.239
280.018	27.608680	-1.70340	6.73660	14.24448	14.24788	14.22270	14.21938	-0.024	0.153	0.177
280.026	34.512871	-1.88137	6.73613	15.72250	15.65977	15.69753	15.67187	0.401	0.159	0.323

Table 5.8. (Continued)

Isotherm 18: M94C1 290K 06112003										
T	P	m_v and m_a	v_s	ρ						
μ	μ	μ		measured	predicted			Relative deviation		
					HY	AGA8-DC92	REFPROP	HY	AGA8-DC92	REFPROP
K	MPa	g	cm^3	$kmole/m^3$	$kmole/m^3$	$kmole/m^3$	$kmole/m^3$	%	%	%
290.021	-0.007789	0.01314	-	-	-	-	-	-	-	-
290.041	13.787352	-0.91325	6.73934	7.68459	7.72787	7.67878	7.70122	-0.560	0.076	-0.216
290.018	15.515802	-1.03605	6.73922	8.70333	8.75385	8.69375	8.72429	-0.577	0.110	-0.240
289.987	17.272759	-1.15077	6.73910	9.65516	9.70969	9.64102	9.67531	-0.562	0.147	-0.208
290.097	18.980951	-1.24991	6.73898	10.47773	10.53337	10.46129	10.49435	-0.528	0.157	-0.158
290.067	20.727719	-1.34163	6.73887	11.23880	11.29151	11.22128	11.24971	-0.467	0.156	-0.097
290.055	12.063759	-0.78387	6.73946	6.61119	6.64594	6.60721	6.61986	-0.523	0.060	-0.131
290.057	10.350536	-0.65209	6.73957	5.51800	5.54936	5.51886	5.52316	-0.565	-0.015	-0.093
290.059	27.618779	-1.61700	6.73840	13.52418	13.53351	13.50281	13.50561	-0.069	0.158	0.137
290.081	34.501559	-1.80417	6.73793	15.07804	15.02539	15.05296	15.03566	0.350	0.167	0.282

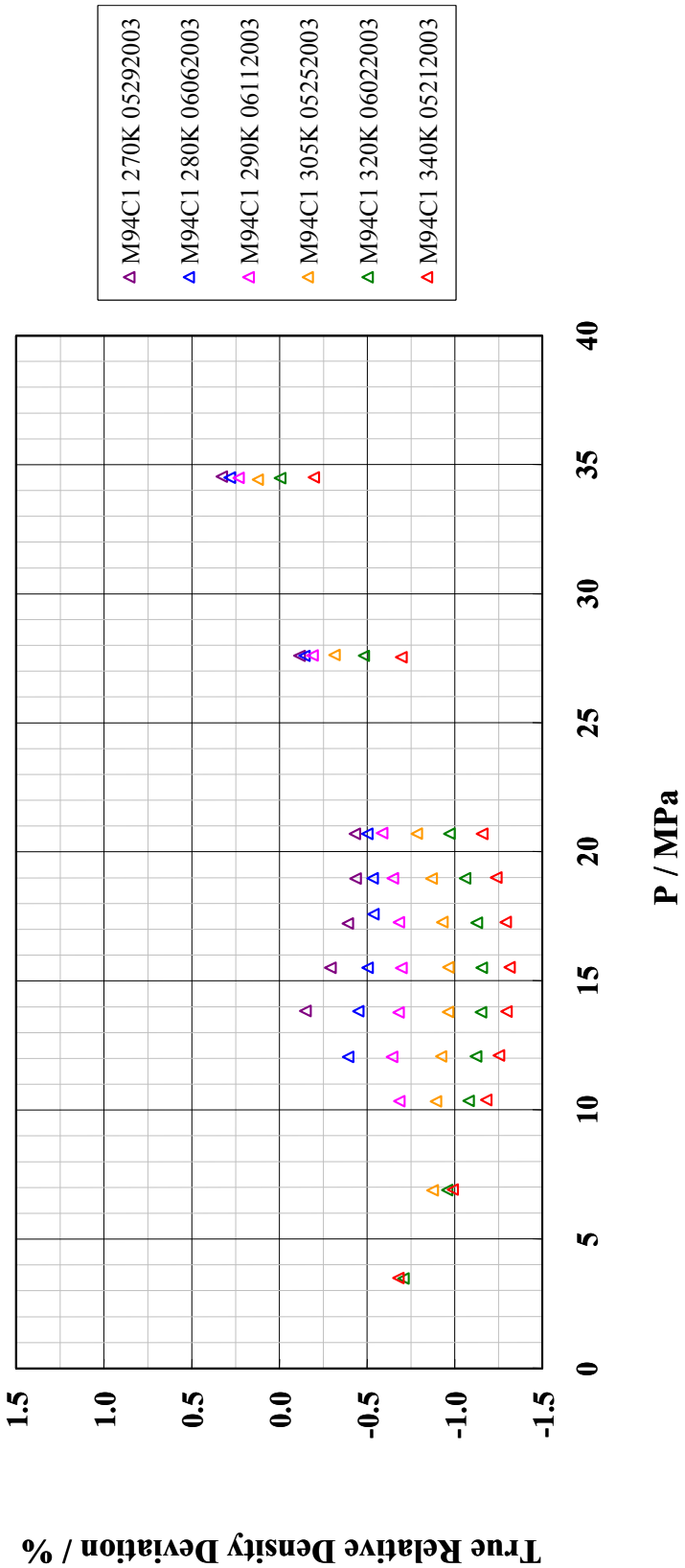

Figure 5.15. True Relative Density Deviations from the HY EOS Predictions for M94C1

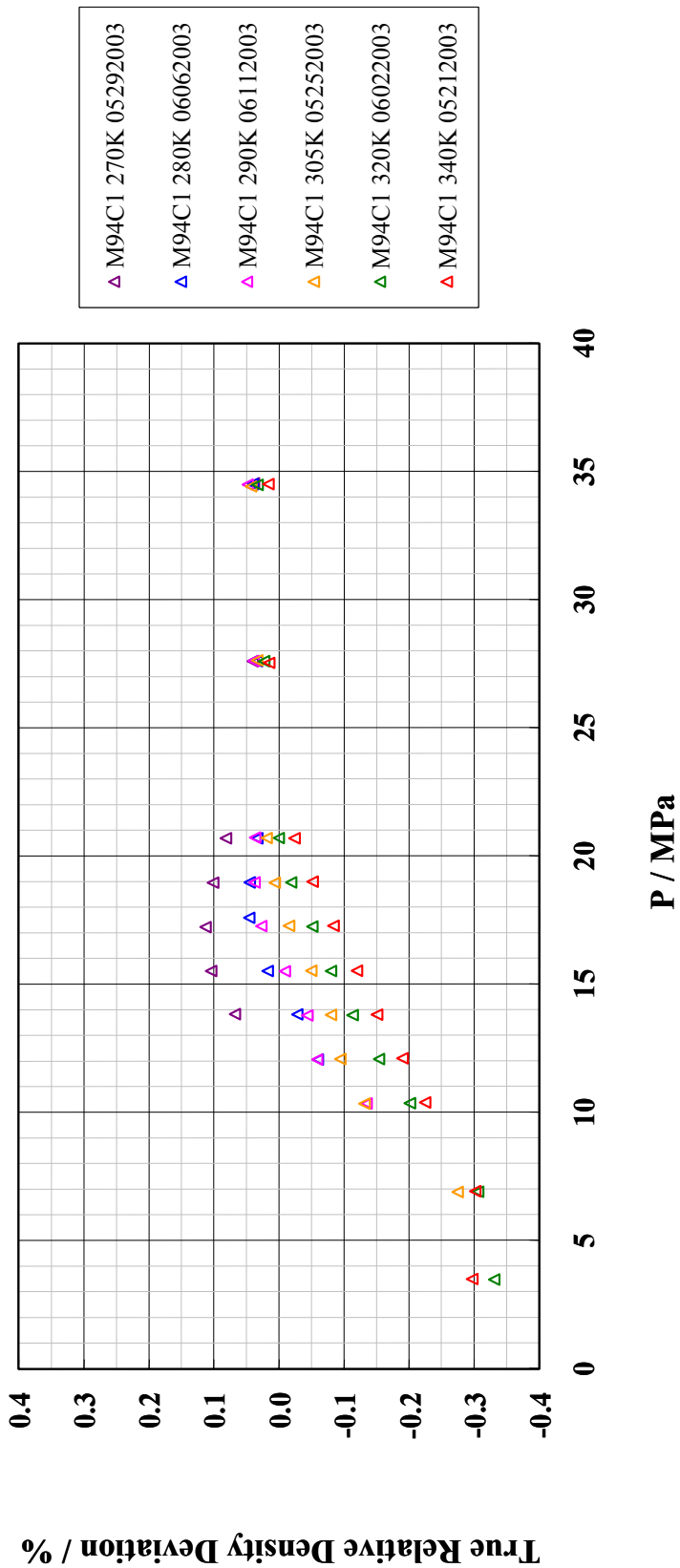

Figure 5.16. True Relative Density Deviations from the AGA8-DC92 EOS Predictions for M94C1

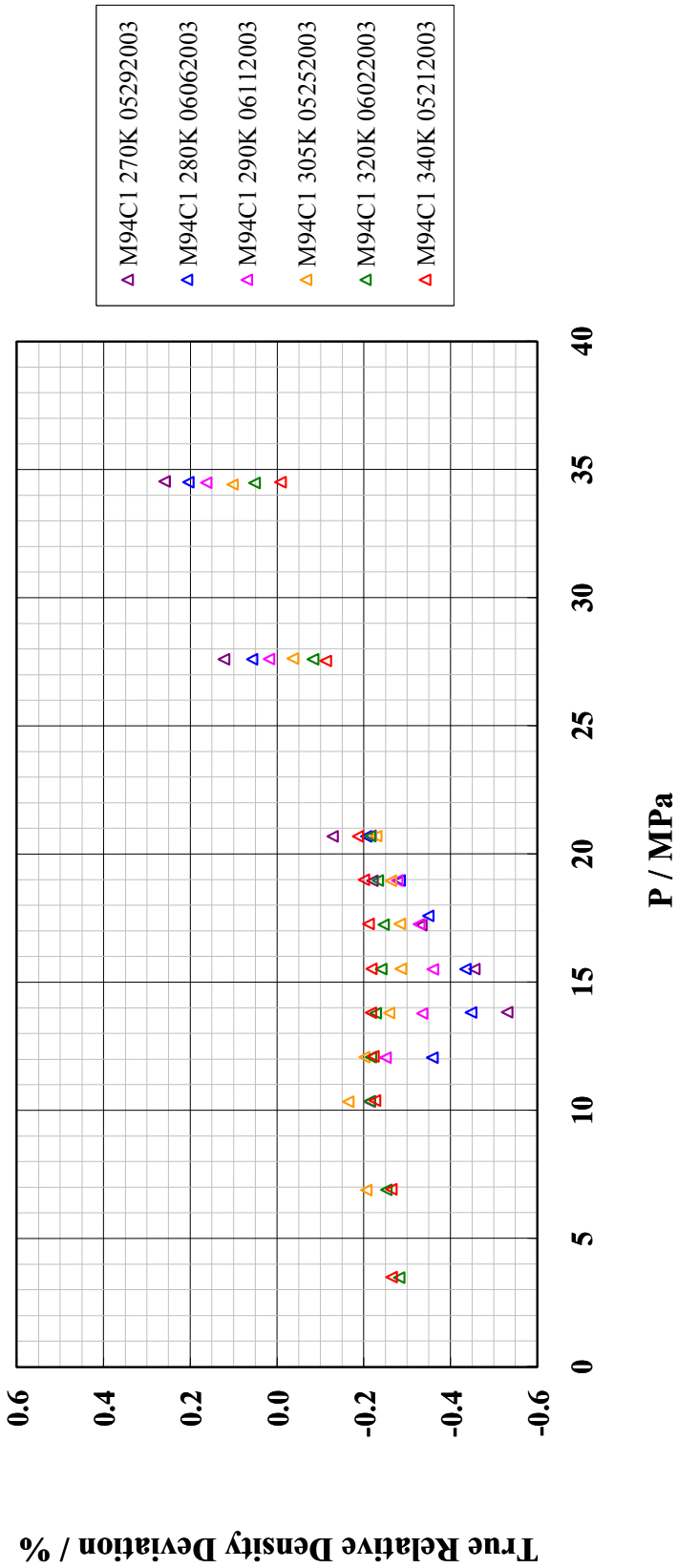

Figure 5.17. True Relative Density Deviations from the REFPROP EOS Predictions for M94C1

Table 5.9. M94C1 True Measured Density Data

T	P	ρ
		True measured
K	MPa	kmole/m^3
Isotherm 13: M94C1 340K 05212003		
340.025	3.499658	1.29200
340.020	6.929327	2.66306
340.023	10.393377	4.12652
340.020	12.114931	4.86603
340.026	13.818562	5.59459
340.030	15.528452	6.31339
339.995	17.286678	7.03320
339.998	19.002277	7.70698
339.994	20.701856	8.34341
339.996	27.544327	10.55700
340.061	34.520557	12.29493
Isotherm 14: M94C1 305K 05252003		
305.006	13.809135	6.86891
305.005	15.534073	7.77946
305.008	17.286057	8.65258
305.003	18.970681	9.43234
305.002	20.712540	10.17233
305.015	12.085573	5.92710
305.016	10.340341	4.96277
305.015	6.895333	3.11861
305.063	27.640767	12.51334
304.894	34.425965	14.14578

Table 5.9. (Continued)

T	P	ρ
		True measured
K	MPa	kmole/m^3
Isotherm 15: M94C1 270K 05292003		
270.019	13.841947	9.27645
270.021	15.523501	10.38296
270.024	17.235790	11.35362
270.026	18.970225	12.19186
270.036	20.702053	12.90735
270.010	27.608542	14.98546
270.025	34.543934	16.37028
Isotherm 16: M94C1 320K 06022003		
320.056	3.482568	1.38334
320.057	6.912216	2.89968
320.054	10.362430	4.54987
320.056	12.086935	5.39588
320.054	13.799866	6.23142
320.051	15.521374	7.05120
320.055	17.252039	7.84205
320.053	18.978038	8.58940
320.049	20.706337	9.28957
320.012	27.610790	11.61040
320.001	34.491161	13.30836

Table 5.9. (Continued)

T	P	ρ
		True measured
K	MPa	kmole/m^3
Isotherm 17: M94C1 280K 06062003		
279.998	13.829140	8.40208
280.002	15.519426	9.46246
280.006	17.597771	10.61216
280.018	18.973628	11.27843
280.028	20.696135	12.01808
279.999	12.065543	7.20076
280.018	27.608680	14.22747
280.026	34.512871	15.70381
Isotherm 18: M94C1 290K 06112003		
290.041	13.787352	7.67536
290.018	15.515802	8.69288
289.987	17.272759	9.64357
290.097	18.980951	10.46515
290.067	20.727719	11.22532
290.055	12.063759	6.60326
290.057	10.350536	5.51138
290.059	27.618779	13.50802
290.081	34.501559	15.06011

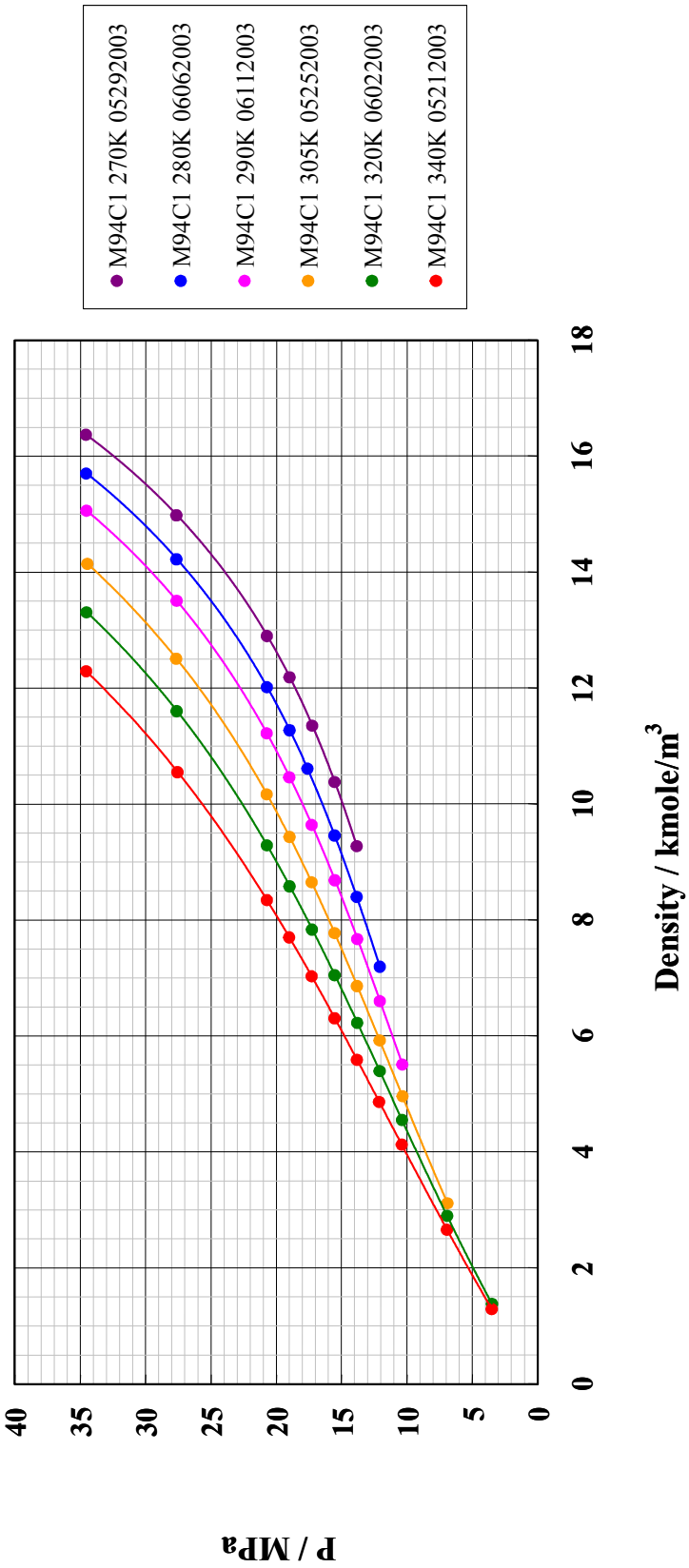

Figure 5.18. Pressure versus True Measured Densities from the MSD for M94C1

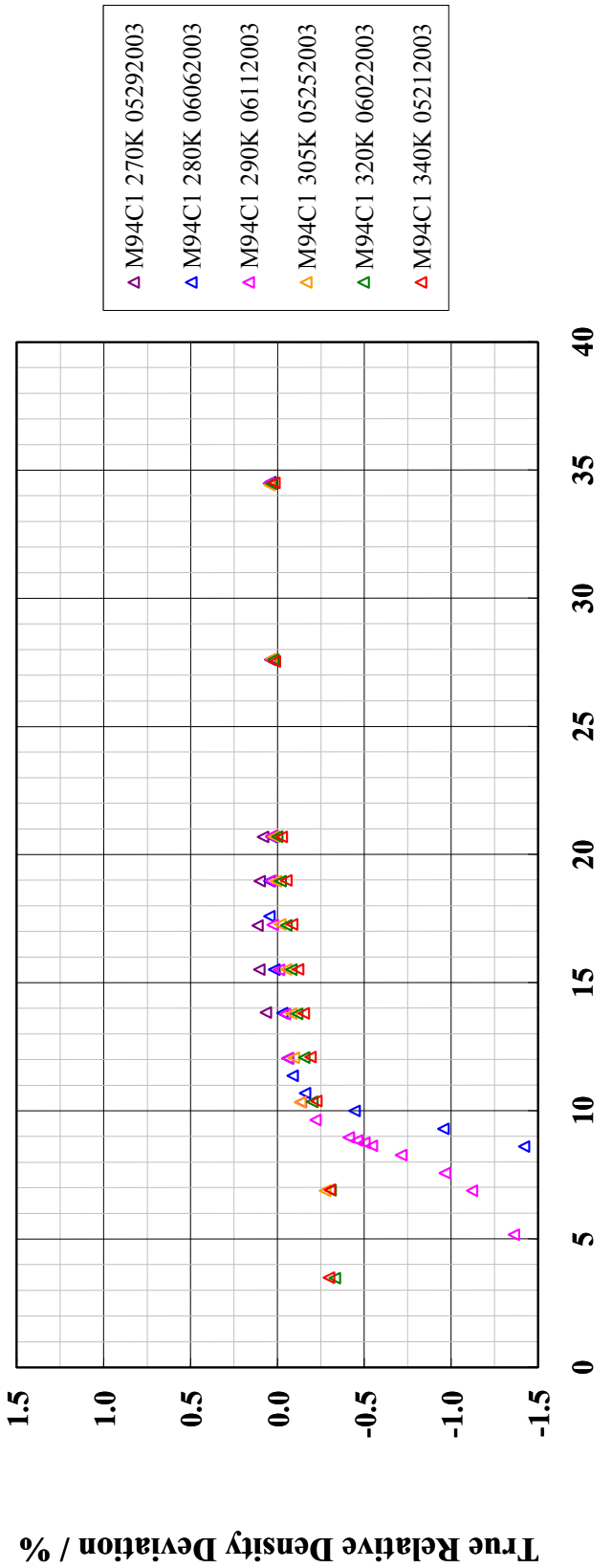

Figure 5.19. Test for Detection of the Two-phase Envelope by Sudden Change in Slope of Isotherms

^{o}F, 16.85 ^{o}C] isotherms after measuring gas densities up to 35 MPa [5,076.320 psia] and deliberately reducing the MSD cell pressure to different values below the CB of M94C1.

5.2.4. Discussion on M94C1 Density Measurement Results

The true measured densities for M94C1 deviate by ±1.5% from the HY EOS predictions, ±0.4% from the AGA8-DC92 EOS predictions and ±0.6% from the REFPROP EOS predictions, again showing the improvements in the density prediction capabilities of recent EOS. M94C1 has a composition that falls under the 'extended range' as defined by the American Gas Association (1992), where its C_{6+} fraction of 0.382% is higher than the 0.2% limit for the 'normal range'. For this reason, the relative density deviations of M94C1 from the AGA8-DC92 EOS predictions may not necessarily meet the expected limits of ±0.1%, ±0.3% and ±0.5% in regions 1, 2 and 3 respectively of the American Gas Association (1992), although, in reality, this has been the rigid expectation as mentioned earlier in subsection 2.1.8 and the practice currently followed in the custody transfer business.

Out of the 6 points of M94C1 measured in region 1, none lies within the ±0.1% expected deviation but the 26 points measured in region 2 and the 24 points measured in region 3 do lie within the expected ±0.3% and ±0.5% deviation limits for the two regions. As a result of the validation of the apparatus operation with pure component density measurements and the inference drawn from M91C1 density measurements, the relative density deviations from REFPROP are more reliable. In region 1, the deviations of the measured data from REFPROP EOS predictions are almost of the same magnitude as those from the AGA8-DC92 EOS predictions, which confirms that the AGA8-DC92 EOS cannot be expected to give deviations with measured densities within ±0.1% for M94C1. In region 3, the deviations of the measured data from REFPROP EOS predictions are of almost the same magnitude as those from the AGA8-DC92 EOS predictions, which confirm that the AGA8-DC92 EOS is reliable in region 3 for M94C1. However, the deviations of the measured data from the AGA8-

DC92 and REFPROP EOS differ the most in region 2. In region 2, the observation that there is agreement between the measured and the AGA8-DC92 EOS predicted densities for M94C1 within ±0.3%, despite the presence of C_{6+} fraction higher than the 'normal range' is thus misleading. As a summary, the M94C1 measurements lead to the conclusion that the AGA8-DC92 predictions for density in region 1 cannot be expected to be within the expected ±0.1% limit and in region 2 are unreliable because of the presence of the heavier C_{6+} fraction.

A literature search for measured density data in the *P* and *T* range of interest in the present work, for gas mixtures similar in composition to M94C1 proved to be mostly futile. Li and Guo (1991) have measured densities of a natural gas mixture with 94.53% methane and 0.38% C_{6+} fraction which is similar to the composition of M94C1, at only seven pressures up to 6.998 MPa [1,015 psia] at approximately 312 K [101.93 ^{o}F, 38.85 ^{o}C]. These data were not used for comparison with measured densities of M94C1 because they were at lower pressures where the MSD density measurement uncertainty is higher. A joint industrial project was undertaken between the National Engineering Laboratory, UK and the Gas Research Institute in the US to investigate the magnitude of the deviations between the densities predicted by AGA8-DC92 EOS and those measured with a two-sinker MSD for rich natural gas mixtures and if needed to provide reference quality data for refinement of the AGA8-DC92 EOS (Watson, 1998). Rich natural gas mixtures having higher densities because of higher contents of heavier hydrocarbons such as ethane, propane and the C_{6+} fraction do not fall under the 'normal range' of composition but in the 'expanded range' as defined by the American Gas Association (1992). Out of the ten natural gas mixtures measured as part of the joint industrial project, seven had ethane and propane compositions in the 'expanded range' but C_{6+} compositions in the 'normal range' and the remaining 3 had neither ethane nor propane but C_{6+} fraction composition in the 'expanded range'. Thus, the rich natural gas mixtures of Watson and M94C1, M88C1 and M78C1 mixtures that were to be measured as part of the present project were similar because of their compositions being in the 'expanded range' as shown in Table 2.1. As a result of this investigation, Watson has

concluded that: (i) the deviations between the measured densities and those predicted by the AGA8-DC92 EOS for rich natural gas mixtures do not necessarily fall within the expected limits given by the American Gas Association (ii) the maximum deviations occur for mixtures with compositions close to the upper limit of the 'expanded range' and (iii) the AGA8-DC92 EOS parameters need to be modified so as to make it applicable for mixtures with compositions over the 'expanded range' as well, containing more than 0.5% C_{6+} fraction.

The conclusions drawn from density measurements of M94C1 containing 0.382% C_{6+} fraction are so similar to those of Watson that they corroborate each other and emphasize the need for measurements on more mixtures with compositions in the 'expanded range' such as M88C1 and M78C1. The newly measured reference quality data can then be used to modify the parameters of the AGA8-DC92 EOS so that it becomes applicable over a wider range of compositions or to validate an entirely new EOS such as the one being developed by Hall (2000) and Atilhan (2004).

5.2.5 Inferences from Natural Gas Mixture Density Measurements

If the virial EOS is restricted to the first order term in density assuming that the gas mixtures to be measured during the present project have 12 components, 12 second virial coefficients for the pure components and 66 cross second virial coefficients would be required to characterize the two body interactions. Although, knowledge of all the 78 second virial coefficients would be required to represent the (P - ρ - T) behavior of each natural gas mixture most accurately, this is practically impossible. Instead, emphasis is laid upon knowing only those second virial coefficients for which the density is most sensitive. Knowing second virial coefficients involving methane, ethane, propane, nitrogen and carbon dioxide is in general important for natural gas mixtures with compositions in the 'expanded range' because of their relatively higher contents. More specifically, for gas mixtures to be measured as part of the present project the interactions between lower hydrocarbons such as methane and ethane with higher

hydrocarbons such as hexane, heptane, octane *etc*. are important because of differences between them and so are the interactions between nitrogen and carbon dioxide and those of both with hydrocarbons. Figure 5.20 shows a matrix of two body interactions for a mixture representative of gas mixtures in the present project and the status of each binary interaction as inferred from American Gas association (1992), Savidge *et al.* (1995) and Jaeschke *et al*. (1989). In validating the AGA8-DC92 EOS, the second virial coefficients representing the important interactions mentioned above for natural gas mixtures with compositions in the 'expanded range' were either not accounted for at all or accounted for based only upon sparse data or estimates that may not have been verified through measurements. The larger than expected relative density deviations for M91C1 with the AGA8-DC92 EOS but good agreement with REFPROP EOS predictions may be caused by inclusion of more data to validate the REFPROP EOS which was not available while developing the AGA8-DC92 EOS. The relative density deviations for M94C1 from the AGA8-DC92 EOS may not be reliable because it was not validated against data that was truly representative of the M94C1 composition. If the second order term in density is added in the virial EOS, the third virial coefficients representing like and unlike three body interactions also are required. A systematic study for the identification of those second and third virial coefficients that most sensitively affect the density of natural gas mixtures must be undertaken to narrow the vast amount experimental data that would otherwise be required.

In addition to the experimental measurements and the EOS predictions for density, availability of computational resources has made predictions from molecular simulations a new avenue that can be considered. Neubauer *et al.* (1999) have demonstrated the use of Monte Carlo simulations for predicting densities of three natural gas mixtures; one of which has a composition close to that of M88C1 to be measured as part of the present project. While the deviations of the molecular simulation predictions from experimentally measured data are smaller than those of predictions from cubic EOS such as the PR EOS, they are larger than those of the AGA8-DC92 EOS predictions and in the worst case as large as ±5%. Thus, the acknowledgement that more

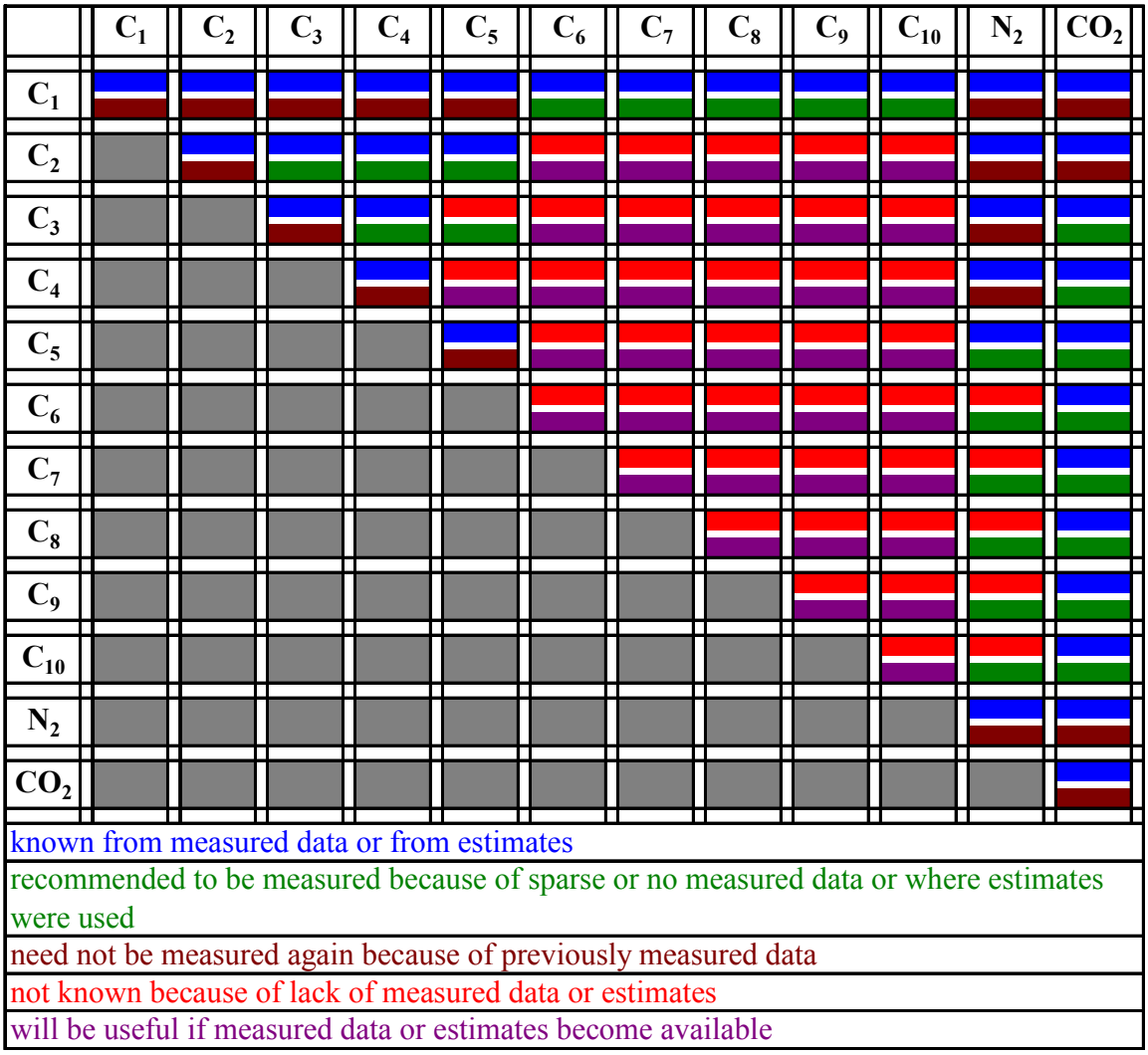

Figure 5.20. Matrix Summarizing Status of Two Body Interactions for Natural Gas Mixtures with Compositions in the 'Expanded Range'

systematic work is needed for accurate density predictions by molecular simulations implies that the experimentally measured density data are still indispensable.

5.3 Density Measurement Uncertainty Analysis

The relative uncertainty for density measurement has been expressed as a combination of the random error in the buoyant force measurement by the weighing balance and the systematic error in measuring the sinker volume (Brachthauser *et al.*, 1993). The total uncertainty for density measurement however, is a combination of the random errors in measuring pressure, temperature, the balance readings for the true mass of the sinker in vacuum and the apparent mass of the sinker under pressure and the molar composition in case of mixtures and the systematic error in measuring the sinker volume. The random error in density measurement can be expressed as:

$$\Delta\rho = \left\{ \begin{array}{l} \left[\left(\frac{\partial \rho}{\partial P} \right)_{T,m_{\mathrm{v}},m_{\mathrm{a}},x} .\Delta P \right]^2 + \left[\left(\frac{\partial \rho}{\partial T} \right)_{P,m_{\mathrm{v}},m_{\mathrm{a}},x} .\Delta T \right]^2 + \\ \left[\left(\frac{\partial \rho}{\partial m_{\mathrm{v}}} \right)_{P,T,m_{\mathrm{a}},x} .\Delta m_{\mathrm{v}} \right]^2 + \left[\left(\frac{\partial \rho}{\partial m_{\mathrm{a}}} \right)_{P,T,m_{\mathrm{v}},x} .\Delta m_{\mathrm{a}} \right]^2 + \\ + \sum_{i=1}^{N} \left[\left(\frac{\partial \rho}{\partial x_i} \right)_{P,T,m_{\mathrm{v}},m_{\mathrm{a}},x_{j\neq i}} .\Delta x_i \right]^2 \end{array} \right\}^{1/2} \tag{33}$$

where, N is the number of components in the natural gas mixture. Dividing throughout by ρ and using equation (8) for the partial derivatives in the third and fourth terms of equation (33), the relative uncertainty for density measurement becomes:

$$\frac{\Delta\rho}{\rho}=\left\{\begin{array}{l}\left[\left(\frac{\partial\rho}{\partial P}\right)_{T,m_{\mathrm{v}},m_{\mathrm{a}},x}.\frac{1}{\rho}.(\Delta P)\right]^2+\left[\left(\frac{\partial\rho}{\partial T}\right)_{P,m_{\mathrm{v}},m_{\mathrm{a}},x}.\frac{1}{\rho}.(\Delta T)\right]^2+\\ \left[\frac{1}{v_{\mathrm{S}}}.\frac{1}{\rho}.(\Delta m_{\mathrm{v}})\right]^2+\left[(-\frac{1}{v_{\mathrm{S}}}).\frac{1}{\rho}.(\Delta m_{\mathrm{a}})\right]^2+\\ +\sum_{i=1}^{N}\left[\left(\frac{\partial\rho}{\partial x_i}\right)_{P,T,m_{\mathrm{v}},m_{\mathrm{a}},x_{j\neq i}}.\frac{1}{\rho}.(\Delta x_i)\right]^2\end{array}\right\}^{1/2} \qquad (34)$$

The partial derivatives in the first, second and last terms of equation (34) can be calculated from an EOS such as the AGA8-DC92.

The P, T and the balance readings for the true and apparent mass of the sinker were expected to be measured with uncertainties of $\Delta P = \pm 0.0001P$, $\Delta T = \pm 10$ mK, $\Delta m_{\mathrm{v}} = \Delta m_{\mathrm{a}} = \pm 0.02$ mK for a total expected uncertainty of better than ±0.1% for density measurements of pure components. The observed uncertainties for each measured parameter given in section 5.1 during pure component density measurements are much better than their expected uncertainties causing the total uncertainty for density measurement of ±0.013% to be much better than the expected uncertainty of ±0.1%.

In addition, gas mixture molar compositions were expected to be measured with uncertainties comparable with the ±0.007% or ±0.001% uncertainties of gas mixtures measured by Watson and Magee *et al.* respectively. M91C1 and M94C1 prepared gravimetrically by DCG Partnership have molar composition uncertainties of approximately ±0.05% and greater than ±0.03% respectively. The true measured density data represented in Figures 5.11 through 5.13 for M91C1 and Figures 5.15 through 5.17 for M94C1, thus have larger than expected uncertainties despite smaller uncertainties than expected for the other parameters as described in subsections 5.2.1 and 5.2.3. However, a comparison of the composition uncertainties with the scale of the true relative density deviations shows that the large deviations between the predicted and measured densities are real and much larger than the uncertainty of density measurement.

Figure 5.21 shows the absolute deviations from the average of the weighing balance readings for the true mass of the sinker in vacuum over the entire period when pure component and gas mixture densities were measured. Such a tracking was necessary to ensure that the sinker was not contaminated by either oil leakages from the compressor, gas condensate or other impurities. The observed deviations of ±0.6 mg are because of differences in horizontal and vertical alignments of the MSA parts and lead to an error of up to ±0.002% in the true mass of the sinker in vacuum, which is smaller than the observed FTE of ±0.006%.

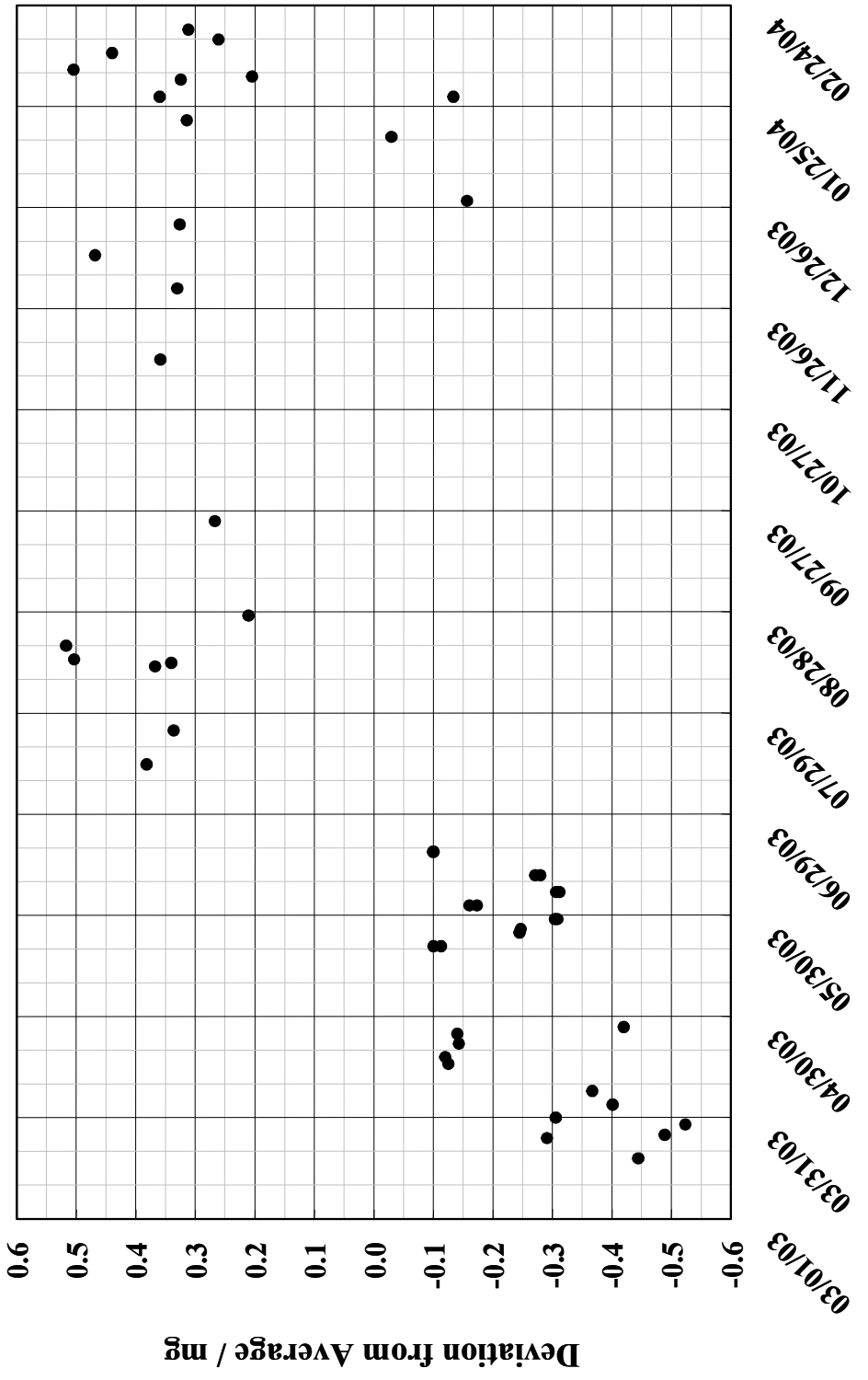

Figure 5.21 Deviations from the Average of the Weighing Balance Readings for the True Mass of the Sinker in Vacuum over the Period of Density Measurements

CHAPTER VI

CONCLUSIONS AND RECOMMENDATIONS

6.1 Conclusions

(1) A facility for accurate density measurements of fluids using a state-of-the-art, high pressure, high temperature, compact single-sinker magnetic suspension densitometer designed and built by Rubotherm has been commissioned and tested by measuring densities of pure argon, nitrogen and methane in the range (270 to 340) K [(26.33 to 152.33) ^{o}F, (-3.15 to 66.85) ^{o}C] and (3.447 to 34.474) MPa [(500 to 5,000) psia], which is of interest to the natural gas custody transfer business. The relative deviations of measured pure component densities from reference quality EOS predictions show a molar mass dependent apparatus bias error. The true densities for pure components after applying the empirically determined correction factor for the apparatus bias error have been measured with an uncertainty of ±0.013 %.

(2) Measured densities of the natural gas mixture M91C1 with a composition in the 'normal range' of the American Gas Association (1992) show larger than the expected deviations of ±0.1% and ±0.3% from the AGA8-DC92 EOS predictions in regions 1 and 2 respectively, which cover the most relevant ranges of pressure and temperature for natural gas custody transfer. The measured densities agree with predictions from the recently developed REFPROP EOS within ±0.3%. The measured data suggest that the AGA8-DC92 EOS considered a standard in natural gas custody transfer since the early 90s may be unreliable because of insufficient data in validating its parameters. The AGA8-DC92 EOS may need to be re-calibrated with more accurate data from newly developed density

measurement techniques or a new EOS such as the REFPROP EOS adopted for custody transfer purposes.

(3) After validating the operation of the apparatus through pure component density measurements and finding the reliability of the REFPROP EOS predictions for natural gas mixture density measurements better than those of the AGA8-DC92 EOS through M91C1 density measurements, the measured data for the natural gas mixture M94C1 with a composition in the 'expanded range' of the American Gas Association (1992) was evaluated against the REFPROP EOS predictions rather than the AGA8-DC92 EOS. The larger than expected deviations of the measured data for M94C1 from the AGA8-DC92 EOS predictions in region 1 are not surprising because of the presence of the heavier C_{6+} fraction but the agreement with expected deviations from the AGA8-DC92 EOS in region 2 is misleading as can be seen from the deviations with the REFPROP EOS.

6.2 Recommendations

(1) More data are needed for accurate density measurements of natural gas mixtures with compositions in the 'expanded range' of the American Gas Association (1992). Density measurements on binary and ternary mixtures emphasizing those components that occur in natural gas mixtures to the greatest extent such as methane, ethane and propane form the first part, binary and ternary mixtures of vastly different components such as methane - hexane, methane - heptane, nitrogen - hexane, carbon dioxide - hexane etc. form the second part and multi-component natural gas mixtures such as M88C1 and M78C1 and rich natural gas mixtures such as those of Watson form the third part of the required data set. Together, such a data set will allow either re-calibration of the existing AGA8-DC92 EOS to extend its applicability over a wider range of compositions or development of an entirely new EOS that is more accurate than the AGA8-DC92 EOS over wider ranges of temperature, pressure and composition.

(2) Densities of helium, carbon dioxide, propane, butane, pentane, krypton, xenon and sulfur hexafluoride should be measured to determine the molar dependence of the apparatus bias error over a wide range of molar masses practically encountered.

(3) The sinker volume and its uncertainty measured by Rubotherm must be re-measured and confirmed by NIST.

(4) Provision should be made for accurate compositional analysis of the natural gas mixtures after receiving them from the supplier and after density measurement to track any possible compositional changes caused because of adsorption or retrograde condensation of the heavier components of the natural gas mixtures or the natural gas mixtures should be prepared gravimetrically using a mixture apparatus in-house.

(5) A force balance or an automatic dead weight gauge should be used to calibrate the pressure transducers instead of the DWG/DPI assembly to reduce uncertainties because of human error and to increase the rate of data production.

(6) A two stage cell thermostating scheme should be used instead of merely immersing the cell into a liquid bath and circulating the heating/cooling liquid through an external constant temperature liquid circulation bath in order to attain rapid rates of temperature change and control the cell temperature with an uncertainty of ±1 mK which will be better than the ±4 mK uncertainty that was achieved in the present work. The reversal of current for the PRT resistance measurement should be automated for operator convenience.

(7) An integrated program should be developed for: (i) pressure, temperature, weighing balance reading, MSA control box signals, thermopile reading data acquisition (ii) control of the MSA assembly and the two stage cell thermostating scheme (iii) data processing for calculating the experimental density and statistical analysis and (iv) comparison with the predicted density from an EOS such as REFPROP that can be used for pure components as well as mixtures.

Such a program would not only increase the data production rate but would also help in diagnosis of abnormalities.

(8) Two changes are needed to improve the alignment of the MSA parts. The MSA often went out of control during a measurement when the MSA parts touched the cell internal walls because of the small clearances between them. This was possibly aided by the high altitude location of the MSD in the building during the present work and the swaying of the building. Relocating the MSD to a lower altitude will reduce the frequency at which the MSA goes out of control. A fine pitch screw adjustment is needed in both directions in the plane of the balance base plate for nudging the aluminum frame so that the electromagnet suspension tube can be centered along the axis of the thermostatization tube. This would help the horizontal alignment of the MSA parts in a repeatable manner instead of the trial and error approach followed during the present work.

(9) The compact single-sinker MSD built especially for measuring high densities does not measure very low densities with the same accuracy. During the present work, densities of methane and nitrogen at pressures below approximately 6.895 MPa [1,000 psia] were measured with larger uncertainties. Either a Burnett apparatus or a two-sinker MSD should be used for low density measurements with high accuracy at pressures lower than approximately 12.066 MPa [1,750 psia].

NOTATION

a	Calibration constant in the deviation equations of ITS-90 for a PRT
A	Cross sectional area of piston cylinder assembly of dead weight gauge (m^3)
b	Calibration constant in the deviation equations of ITS-90 for a PRT
B	Second virial coefficient (cm^3/mole) or constant in the reference function of ITS-90 for a PRT calibration
C	Third virial coefficient ($cm^6/mole^2$)
D	Constant in the reference function of ITS-90 for a PRT calibration
e	Error in the balance reading introduced because of the presence of a stray magnetic source close to the MSA (mg)
E	Young's modulus (GPa)
I	Current through platinum resistance thermometer (mA) or Intercept of pressure transducer calibration linear fit (MPa)
L	parameter representing linear thermal expansion and contraction
m	Mass of sinker (g)
M	Molar mass (kg/kmole)
n	Number of pairs of thermocouples forming a thermopile
N	Number of components in a natural gas mixture
P	Pressure (MPa) [psia]
R	Resistance of platinum resistance thermometer (ohm) or universal gas constant (8.314 J/mole K)
S	Seebeck coefficient ($\mu V/^oC$) or Slope of pressure transducer calibration linear fit
T	Temperature (K) [^oF, ^oC]
U	Voltage signal from magnetic suspension assembly control box (V)
v	Volume of sinker (cm^3)

V	Voltage drop across platinum resistance thermometer (V) or volume of isochoric apparatus cell (cm^3) or thermoelectric voltage (μV)
W	Ratio of the resistance of a platinum resistance thermometer at a temperature to its resistance at the triple point of water
x	Composition as mole fraction
Z	Compressibility factor ($P/\rho RT$)

Abbreviations

AC	Alternating Current
AGA	American Gas Association
AGA8-DC92	Detailed Characterization method of the American Gas Association
AGA8-GC92	Gross Characterization method of the American Gas Association
AGC-21	Advanced Gas Conversion Technology for the 21st century
AWG	American Wire Gauge
Btu	British thermal units
BOE	Barrels of Oil Equivalent
BWR	Benedict, Webb and Rubin
BWRS	Benedict, Webb, Rubin and Starling
C	Hydrocarbons
CB	Cricondenbar
CP	Critical Point
CT	Cricondentherm
DC	Direct Current
DMM	Digital Multimeter
DOE	Department of Energy
DPDT	Double Pole Double Throw
DPI	Differential Pressure Indicator
DVD	Digital Video Disc

DWG	Dead Weight Gauge
ECS	Extended Corresponding States
EMF	Electromotive force
EOS	Equation of State
FPS	Floating Production System
FPSO	Floating Production Storage Offload
FTE	Force transmission Error
FTS	Fischer-Tropsch synthesis
GoM	Gulf of Mexico
GC	Gas Chromatography
GC-MS	Gas Chromatography – Mass Spectroscopy
GERG	European Group for Gas Research
GTL	Gas to Liquids
HIP	High Pressure Equipment Company
HP	Hand Pump
HY	Hall and Yarborough
IC	Isochore
IGCC	Integrated Gasification Combined Cycle
IPTS-68	International Practical Temperature Scale of 1968
IT	Isotherm
ITS-90	International Temperature Scale of 1990
IUPAC	International Union of Pure and Applied Chemistry
LDC	Local Distribution Company
M78C1	Natural gas mixture with 78 mole percent methane
M88C1	Natural gas mixture with 88 mole percent methane
M91C1	Natural gas mixture with 91 mole percent methane
M94C1	Natural gas mixture with 94 mole percent methane
MBWR	Modified Benedict Webb Rubin
MGERG	Master Version of the equation of state of GERG

MMS	Minerals Management Service
MP	Measurement Point
MSA	Magnetic Suspension Assembly
MSD	Magnetic Suspension Densitometer
MTG	Methanol to Gasoline
NIST	National Institute of Standards and Technology
PID	Proportional Integral Derivative
PR	Peng and Robinson
PRT	Platinum Resistance Thermometer
PT	Patel and Teja
PT02K	13.790 MPa [2,000 psia] range Pressure Transducer
PT06K	41.369 MPa [6,000 psia] range Pressure Transducer
PT30K	206.843 MPa [30,000 psia] range Pressure Transducer
RD&D	Research, Development and Demonstration
RK	Redlich and Kwong
RR	Round Robin
RR-NIST2	Natural gas mixture named ‘NIST2’ measured in the round robin project
SC	Suspension Control
SGERG	Standard version of the equation of state of GERG
SMDS	Shell Middle Distillate Synthesis
SRK	Soave, Redlich and Kwong
SSPD	Sasol Slurry Phase Distillate
SSR	Solid State Relay
T	Tee fitting
Ta	Tantalum
Ti	Titanium
TAMU	Texas A&M University
TCR	Temperature Coefficient of Resistance (ohm / ohm /^{o}C)
TLP	Tension Leg Platform

TPW	Triple Point of Water = 273.16 K [32.018 ^{o}F, 0.01 ^{o}C]
TVD	True Vertical Depth
UK	United Kingdom
US	United States of America
V	Valve
VLE	Vapor Liquid Phase Equilibrium
WD	Water Depth
ZP	Zero Point
ZSM	Zeolite SOCONY (Standard Oil Company of New York) Mobil

Greek letters

α	Temperature distortion coefficient (K^{-1}) or thermal coefficient of expansion (K^{-1})
β	Pressure distortion coefficient (MPa^{-1})
Δ	Difference or deviation
μ	Average
Ω	Ohm, unit of resistance
X	Internal temperature period of pressure transducer quartz crystal (s^{-1})
ρ	Density ($kmole/m^3$)
σ	Standard deviation or deviation at the 68% confidence level
τ	Pressure period of vibration of transducer quartz crystal (s^{-1})
υ	Poisson's ratio

Subscripts

0	Index for constants *B* and *D* in reference functions of ITS-90 for PRT calibration
6+	Hexane and components heavier than hexane such as heptane, octane…

a	Apparent or sensor signal
ag	Control difference
c	Critical condition
d	Disk
i	Component number or index for constants in the reference function of ITS-90 for PRT calibration
m	Electromagnet
o	Reference condition of 23 ^{o}C for cross sectional area of piston cylinder assembly of dead weight gauge or reference condition of 20 ^{o}C and 1 bar pressure for sinker volume
pc	Pseudocritical condition for mixture
pr	Pseudoreduced temperature or pressure for mixture
R	Controller output
s	Initial set-point
sp	Sphere
S	Sinker
So	Sinker at reference condition of 20 ^{o}C and 1 bar pressure
v	Vacuum condition

LITERATURE CITED

Aasberg-Petersen, K, J.H. Bak Hansen, T.S. Christensen, I. Dybkjaer, P. S. Christensen, C.S. Nielsen, S.E.L. Winter Madsen and J.R. Rostrup-Nielsen, "Technologies for Large Scale Gas Conversion," *Applied Catalysis A: General,* **221**, 379 (2001).

Achtermann, H.J., T.K. Bose, H. Rögener and J.M. St-Arnaud, "Precise Determination of the Compressibility Factor of Methane, Nitrogen and Their Mixtures from Refractive Index Measurements," *International Journal of Thermophysics*, **7**(3), 709 (1986).

American Gas Association, "A.G.A. Manual for the Determination of Supercompressibility Factors for Natural Gas, PAR Research Project NX-19," Catalog No. L00340, American Gas Association, Washington, DC (1963).

American Gas Association, "Compressibility and Supercompressibility for Natural Gas and Other Hydrocarbon Gases. A.G.A. Transmission Measurement Committee Report No. 8," K.E. Starling, ed., American Gas Association, Washington, DC (1986).

American Gas Association, "Compressibility Factors of Natural Gas and Other Related Hydrocarbon Gases. A.G.A. Transmission Measurement Committee Report No. 8," Starling K.E. and J.L. Savidge, eds., 2nd ed., Catalog No. XQ9212, American Gas Association, Arlington, VA (Nov. 1992).

Anderson, R.B., *The Fischer-Tropsch Synthesis*, Academic Press, Inc., Orlando, FL, pp 1-8 (1984).

Anonymous, "First Production Modules Delivered to Conoco Pilot Plant," *Remote Gas Strategies*, 5 (Apr. 2002).

Anonymous, "From Natural Gas to Gasoline Source," *Chemical Engineering Progress*, **98**(11), 15 (Nov. 2002).

Anonymous, "Pipeline Construction Scorecard: Projects Planned and Under Construction," *Pipeline & Gas Journal*, **230**(11), 63 (2003).

Atilhan, M., "A New Cubic Equation of State," M.S. Thesis, Texas A&M University, College Station, TX (May 2004).

Ayers, W.B., D.A. McVay, J.L. Jensen, D. Devegowda, J.L. Garduno, H. Morand and R.I. Ramazanova, "Carbon Dioxide Sequestration Potential of Texas Low Rank Coals," Petroleum Engineering Department Seminar Series, Texas A&M University, College Station, TX (Apr. 2004).

Barber, C.R., "The International Practical Temperature Scale of 1968," *Metrologia*, **5**(2), 35 (1969).

Baud, R.D., R.H. Peterson, G.E. Richardson, L.S. French, J. Regg, T. Montgomery, T.S. Williams, C. Doyle and M. Dorner, "Deepwater Gulf of Mexico 2002: America's Expanding Frontier," Minerals Management Service, Gulf of Mexico Outer Continental Shelf Region, US Department of the Interior Publication., OCS Report MMS 2002-021, New Orleans, LA (Apr. 2002).

Beattie, J.A. and O.C. Bridgeman, "A New Equation of State for Fluids," *Proceedings of the American Academy of Arts and Sciences*, **63**, 229 (1928).

Benedict, M., G.B., Webb and L.C. Rubin, "An Empirical Equation for Thermodynamic Properties of Light Hydrocarbons and Their Mixtures. I. Methane, Ethane, Propane and n-Butane," *Journal of Chemical Physics*, **8**, 334 (1940).

Benedict, M., G.B. Webb and L.C Rubin, "An Empirical Equation for Thermodynamic Properties of Light Hydrocarbons and Their Mixtures. II. Mixtures of Methane, Ethane, Propane and n-Butane," *Journal of Chemical Physics*, **10**, 747 (1942).

Benedict, M., G.B. Webb and L.C. Rubin, "Empirical Equation for Thermodynamic Properties of Light Hydrocarbons and Their Mixtures – Constants for Twelve Hydrocarbons," *Chemical Engineering Progress*, **47**(8), 419 (1951a).

Benedict, M., G.B. Webb and L.C. Rubin, "Empirical Equation for Thermodynamic Properties of Light Hydrocarbons and Their Mixtures – Fugacities and Liquid-Vapor Equilibria," *Chemical Engineering Progress*, **47**(9), 449 (1951b).

Black, R.J., L.L. Freeman and J.A. Calderon, "Pioneering Deepwater Gulf Pipeline System Integrates Five Segments," *Oil & Gas Journal*, **101**(19), 58 (2003).

Botros, K.K., "Performance of Five Equations of State for the Prediction of VLE and Densities of Natural Gas Mixtures in the Dense Phase Region," *Chemical Engineering Communications*, **189**(2), 151 (2002).

Bowles, E.B., Personal Communication, Southwest Research Institute, San Antonio, TX (Apr. 2004).

Brachthauser, K., R. Kleinrahm, H.W. Lösch and W. Wagner, "Entwicklung eines neuen Dichtemeβverfahrens und AufBau einer Hochtemperatur-Hochdruck-Dichtemeβanlage," Fortschritt-Berichte VDI Reihe 8 Nr. 371, VDI-Verlag, Dusseldorf, Germany (1993).

British Petroleum, "BP Statistical Review of World Energy 2003," BP Distribution Services, Surrey, UK (Jun. 2003).

Burnett, E.S., "Compressibility Determinations without Volume Measurements," *Journal of Applied Mechanics*, **3**, A-136 (1936).

Burns, G.W., M.G. Scroger, G.F. Strouse, M.C. Croarkin and W.F. Guthrie, "Temperature-Electromotive Force Reference Functions and Tables for the Letter-Designated Thermocouple Types Based on the ITS-90," National Institute of Standards and Technology, US Department of Commerce, Monograph 175, Washington, DC (Apr. 1993).

ChevronTexaco, Press Release, "Chevron and Nigerian National Petroleum Corporation Launch Major Initiative to Put Out Gas Flares and Convert Natural Gas into Clean Fuels: Escravos Gas-to-Liquids Project Set to Take-off," New York, NY (Sep. 8, 2000).

Clouser, G., "Accessing Markets," *Oil and Gas Investor*, Deepwater Investment Supplement, **22**(8), 16 (2002).

ConocoPhillips, Annual Report, Houston, TX, 24 (2003).

Curl, R.F. Jr. and K.S. Pitzer, "Volumetric and Thermodynamic Properties of Fluids – Enthalpy, Free Energy and Entropy," *Industrial and Engineering Chemistry*, **50**(2), 265 (1958).

Curole, M.A., W.D. Grimes, C.B. Wallace, T.R. Judd and R.W. Chin, "Deepwater Gas Processing Challenges," *Proceedings of the 76th Gas Processors' Association Annual Convention*, March 10-12, 1997, Gas Processors Association, Tulsa, OK, pp 212-218 (1997).

DCG Partnership Ltd, *Certificate of Concentration for Serial number: 300-1174*, Pearland, TX (Apr., 2002).

DCG Partnership Ltd, *Certificate of Concentration for Serial number: 300-1164*, Pearland, TX (Apr., 2003).

Der, V. K., "FutureGen: The Energy Plant of the Future, Energy Independence through Carbon Sequestration and Hydrogen," Gasification Technologies Conference, San Francisco, CA (Oct. 2003).

Derman, A. and D. Johnston, "Bonuses Enhance Upstream Fiscal System Analysis," *Oil & Gas Journal*, **97**(6), 51 (1999).

Derman, A.B. and D. Johnston, "Royalty Relief Extension Vital for Continued Deepwater Development," *Oil & Gas Journal*, **98**(19), 24 (2000).

Derman, A.B. and Jacobson, G., "Royalty Relief, Not Industry Windfall Benefits US," *Oil & Gas Journal*, **98**(37), 50 (2000).

Dranchuk, P.M., R.A. Purvis and D.B. Robinson, "Computer Calculation of Natural Gas Compressibility Factors Using the Standing and Katz Correlation," *Institute of Petroleum Technical Series* No. IP 74-008, 1 (1974).

Dranchuk, P.M. and J.H. Abou-Kassem, "Calculation of Z Factors for Natural Gases Using Equations of State," *The Journal of Canadian Petroleum Technology*, **14**(3), 34 (1975).

Duarte-Garza, H.A., "A High Pressure Isochoric Apparatus to Determine Accurate PVT and Phase Equilibria on Fluids: Application to CO_2/N_2," Ph.D. Dissertation, Texas A&M University, College Station, TX (1988).

Duarte-Garza, H.A., J.C. Holste, K.R. Hall, K.N. Marsh and B.E. Gammon, "Isochoric PVT and Phase Equilibrium Measurements for Carbon Dioxide + Nitrogen," *Journal of Chemical and Engineering Data*, **40**, 704 (1995).

Eastman, M.L, "Clean Coal Power Initiative." Office of Fossil Energy, US Department of Energy, Washington, DC (Jul. 2003).

Eisenberg, B., R.A. Fiato, T.G. Kaufmann and R.F. Bauman, "The Evolution of Advanced Gas to Liquids Technology," *CHEMTECH*, **29**(10), 32 (1999).

Elsharkawy, A.M., "Predicting Volumetric and Transport Properties of Sour gases and Gas Condensates Using Equations of State, Corresponding State Models and Empirical Correlations," *Petroleum Science and Technology*, **21**(11&12), 1759 (2003).

Energy Information Administration, "Annual Energy Review 2002," Office of Energy Markets and End Use, US Department of Energy Publication, No. DOE/EIA-0384 (2002), Washington, DC (Oct. 2003).

Energy Information Administration, "Annual Energy Outlook 2004 with Projections to 2025," Office of Integrated Analysis and Forecasting, US Department of Energy Publication, No. DOE/EIA-0383 (2004), Washington, DC (Jan. 2004).

Estela-Uribe, J.F. and J.P.M. Trusler, "Extended Corresponding States Model for Fluids and Fluid Mixtures. I. Shape Factor Model for Pure Fluids," *Fluid Phase Equilibria*, **204**, 15 (2003).

Estela-Uribe, J.F., A. De Mendoza and J.P.M. Trusler, "Extended Corresponding States Model for Fluids and Fluid Mixtures. II. Application to Mixtures and Natural Gas Systems," *Fluid Phase Equilibria*, **216**, 59 (2004).

Estela-Uribe, J.F. and J.P.M. Trusler, Personal Communication, Universidad Javeriana, Cali, Colombia and Imperial College, London, UK (2004).

Estrada-Alexanders, A.F. and Trusler, J.P.M., "Thermodynamic Properties of Gaseous Argon at Temperatures between 110 and 450 K and Densities up to 6.8 mol/dm^3 Determined from the Speed of Sound," *International Journal of Thermophysics*, **17**(6), 1325 (1996).

Eubank, P.T. and W.J. Kerns, "Adsorption and Molecular Association in the Burnett Apparatus," *American Institute of Chemical Engineers Journal*, **19**(4), 711 (1973).

Eubank, P.T. and M.A. Barrufet, "General Conditions of Collinearity at the Phase Boundaries of Fluid Mixtures," *American Institute of Chemical Engineers Journal*, **33**(11), 1882 (1987).

Eubank, P.T., L. Yurttas, L.L. Joffrion, M.R. Patel and W. Warowny, "Experimental Densities and Virial Coefficients for Steam from 348 to 498 K with Correction and Simulation of Adsorption Effects," in *Properties of Water and Steam: Proceedings of the 11th International Conference*, Pichal M. and O. Sifner, eds., Hemisphere Publishing Corporation, New York, NY (1990).

ExxonMobil, Press Release, "Qatar Petroleum and ExxonMobil Sign Letter of Intent for GTL Project," Houston, TX (Jun. 15, 2001).

Feltus, A., *The Unparalleled Potential of the Gulf of Mexico*, The Petroleum Economist Limited, London, UK, pp 45-48 (1998).

Fenghour, A., W.A. Wakeham, D. Ferguson, A.C. Scott and J.T.R. Watson, "Automated Isochoric Apparatus for the Measurement of Density of Fluid Mixtures at Temperatures from 298.15 K to 773.15 K and Pressures up to 40 MPa: Results for Helium and for Nitrogen," *Journal of Chemical Thermodynamics*, **25**, 831 (1993).

Ferguson, B., "Gasification: The Future of Power Generation", Gasification Technologies Conference, San Francisco, CA (Oct. 2002).

Gallagher, J.E., Personal Communication, Savant Measurement Corporation, Kingwood, TX (Jul. 2003).

Gallaher, D.M. and Mahoney, M.J., "Enchilada Platform Anchors Offshore Louisiana Transportation Network," *Oil & Gas Journal*, **95**(43), 45 (1997).

Garcia Fierro, J.L. and A.M. Alvarez Garcia, "Gas Dynamics at Low Pressures in a Vacuum Microbalance," *Vacuum*, **31**, 79 (1981).

General Electric Power Systems, "Power Systems for the 21st Century – H Gas Turbine Combined-Cycles," GE Power Systems Publication, No. GER-3935B, Schenectady, NY (Oct. 2000).

Gilgen, R., R. Kleinrahm and W. Wagner, "Measurement and Correlation of the (Pressure, Density, Temperature) Relation of Argon I. The Homogeneous Gas and Liquid Regions in the Temperature Range from 90 K to 340 K at Pressures up to 12 MPa," *Journal of Chemical Thermodynamics*, **26**, 383 (1994).

Hall, K.R. and P.T. Eubank, "Burnett-Isochoric Coupled Data with Application to Adsorbing Gases," *Physica*, **61**, 346 (1972).

Hall K.R. and L. Yarborough, "A New Equation of State for Z-factor Calculations," *The Oil & Gas Journal*, **71**(25), 82 (1973).

Hall, K.R., Personal Communication, College Station, TX (2000).

Hall, K.R. and Goldman, S., "Acetylene from Natural Gas," Letters to Editor, *Chemical Engineering Progress*, **99**(1), 7 (2003).

Holste, J.C., K.R. Hall, P.T. Eubank, and K.N. Marsh, "High Pressure P-V-T Measurements," *Fluid Phase Equilibria*, **29**, 161 (1986).

Huber, M.L., E.W. Lemmon and R.T. Jacobsen, "Modeling the Thermodynamic Properties of Natural Gas," *Proceedings of the AGA Operations Conference*, May 7-9, 2000, Denver, CO (May 2000).

Hwang, C.A., "PVT Measurements of Carbon Dioxide + Methane Mixtures and an Equation of State Development," Ph.D. Dissertation, Texas A&M University, College Station, TX (1988).

Hwang, C.A., P.P. Simon, H. Hou, K.R. Hall, J.C. Holste and K.N. Marsh, "Burnett and Pycnometric (p, V_m, T) Measurements for Natural Gas Mixtures," *Journal of Chemical Thermodynamics*, **29**, 1455 (1997).

Iglesias-Silva, G.A. and Hall, K.R., "Natural Gas Compression Factors Calculated from Relative Density, Heating Value and Diluent Compositions," *Chemical Engineering Technology*, **19**, 467 (1996).

International Union of Pure and Applied Chemistry, *Experimental Thermodynamics Volume II: Experimental Thermodynamics of Non-reacting Fluids, Chapters 6,7 and 8,* Le Neindre, B. and B. Vodar, eds., Butterworths, London, UK (1975).

International Union of Pure and Applied Chemistry, *Measurement of the Thermodynamic Properties of Single Phases: Experimental Thermodynamics Volume VI*, Chapter 5, Goodwin, A.R.H., K.N. Marsh, and W.A. Wakeham, eds., Elsevier Science B.V., Amsterdam, The Netherlands (2003).

Jacobsen, R.T., Stewart, R.B. and M. Jahangiri, "Thermodynamic Properties of Nitrogen from the Freezing Line to 2000 K at Pressures to 1000 MPa," *Journal of Physical and Chemical Reference Data*, **15**(2), 735 (1986).

Jaeschke, M., S. Audibert, P. van Caneghem, E.E. Humphreys, R. Janssen-van Rosmalen, Q. Pellei, J.P.J. Michels, J.A. Schouten and C.A. Ten Seldam, *High Accuracy Compressibility Factor Calculation for Natural Gases and Similar Mixtures by Use of a Truncated Virial Equation*, Groupe European de Recherches Gazieres Technical Monograph 2 (1988), Reprinted from Fortschritt-Berichte VDI, Reihe 6 No. 231, VDI-Verlag, Dusseldorf, Germany (1989).

Jaeschke, M. and Humphreys, A.E., *The GERG Databank of High Accuracy Compressibility Factor Measurements*, Groupe European de Recherches Gazieres Technical Monograph 4 (1990), Reprinted from Fortschritt-Berichte VDI, Reihe 6 No. 251, VDI-Verlag, Dusseldorf, Germany (1990).

Jager, B., "Developments in Fischer-Tropsch Technology," *Studies in Surface Science and Catalysis*, A. Parmaliana *et al*., eds., Elsevier Science, Amsterdam, The Netherlands, **119**, 25-34 (1998).

Katz, D.L., D. Cornell, J.A. Vary, R. Kobayashi, J.R. Elenbaas, F.H. Poettmann and C.F. Weinaug, *Handbook of Natural Gas Engineering*, McGraw-Hill Book Co. Inc., New York, NY (1959).

Kay, W.B., "Density of Hydrocarbon Gases and Vapors," *Industrial and Engineering Chemistry*, **28**(9), 1014 (1936).

Kleinrahm, R. and W. Wagner, "Development and Construction of a Density Measurement Apparatus for Measurement of Boiling and Dew Densities of Pure Fluids over the Complete Phase Boundary Curve," *Progress Reports of the VDI Journals, Series 3: No. 92*, VDI Verlag, Dusseldorf, Germany (1984).

Kleinrahm, R. and W. Wagner, "Measurement and Correlation of the Equilibrium Liquid and Vapor Densities and the Vapor Pressure along the Coexistence Curve of Methane," *Journal of Chemical Thermodynamics*, **18**, 739 (1986).

Kleinrahm, R., W. Duschek, W. Wagner and M. Jaeschke, "Measurement and Correlation of the (Pressure, Density, Temperature) Relation of Methane in the Temperature Range from 273.15 K to 323.15 K at Pressures up to 8 MPa," *Journal of Chemical Thermodynamics*, **20**, 621 (1988).

Klimeck, J, R. Kleinrahm and W. Wagner, "An Accurate Single-sinker Densimeter and Measurements of the (p, ρ, T) Relation of Argon and Nitrogen in the Temperature Range from (235 to 520) K at Pressures up to 30 MPa," *Journal of Chemical Thermodynamics*, **30**, 1571 (1998).

Klimeck, J., R. Kleinrahm and W. Wagner, "Measurements of the (p, ρ, T) Relation of Methane and Carbon Dioxide in the Temperature Range 240 K to 520 K at Pressures up to 30 MPa using a New Accurate Single-sinker Densimeter," *Journal of Chemical Thermodynamics*, **33**, 251 (2001).

Kunz, O., W. Wagner and M. Jaeschke, "Development of a Reference Equation of State for Natural Gases and Other Multi-component Mixtures Covering the Gas and Liquid Region Including the Vapor-Liquid Phase Equilibrium," *Proceedings of the 15th Symposium on Thermophysical Properties*, June 22-27, 2003, Boulder, CO (2003).

Kuramoto, N., K. Fujii and A. Waseda, "Accurate Density Measurements of Reference Liquids by a Magnetic Suspension Balance," *Metrologia*, **41**, S84 (2004).

Lau, W.R., "A Continuously Weighed Pycnometer Providing Densities for Carbon Dioxide + Ethane Mixtures Between 240 and 350 K at Pressures up to 35 MPa," Ph.D. Dissertation, Texas A&M University, College Station, TX (1986).

Lau, W.R., C.A. Hwang, H.B. Brugge, G.A. Iglesias-Silva, H.A. Duarte-Garza, W.J. Rogers, K.R. Hall and J.C. Holste, "A Continuously Weighed Pycnometer for Measuring Fluid Properties," *Journal of Chemical and Engineering Data,* **42**, 738 (1997).

Lee, B.I and M.G. Kesler, "A Generalized Thermodynamic Correlation Based on Three-parameter Corresponding States," *American Institute of Chemical Engineers Journal*, **21**(3), 510 (1975).

Lemmon, E.W. and R.T. Jacobsen, "A Generalized Model for the Thermodynamic Properties of Mixtures," *International Journal of Thermophysics*, **20**(3), 825 (1999).

Li, Q. and T. Guo, "A Study on the Supercompressibility and Compressibility Factors of Natural Gas Mixtures," *Journal of Petroleum Science and Engineering*, **6**, 235 (1991).

Lomic, *Sonicware® Version 3.1, Build 16, Last Modified 11/26/2001, Speed of Sound Calculation Based on 1994 Version of AGA Report No. 8*, State College, PA (2001a).

Lomic, *PhasePro® Version 2.1, Build 19, Last Modified 06/05/2003, Phase Equilibria Calculations*, State College, PA (2001b).

Lösch, C. and W. Wagner, Personal Communication, Rubotherm Präzisionsmesstechnik GmbH, Bochum, Germany (1998).

Lösch, H.W., "Development and Design of New Magnetic Suspension Balances for Non-Contact Measurements of Vertical Forces," *VDI Progress Reports, Series 3: Process Technology No. 138*, VDI Verlag, Dusseldorf, Germany (1987).

Lösch, C., "Entwicklung und Aufbau von Magnetschwebewaagen zur Messung der Dichte fluider Stoffe," Ph.D. Dissertation, Ruhr University, Bochum, Germany (2005).

Lunsford, J.H., "The Catalytic Conversion of Methane to Higher Hydrocarbons," *Catalysis Today*, **6**(3), 235 (1990).

MacDougall, L.V., "Methanol to Fuels Routes: The Achievements and Remaining Problems," *Catalysis Today,* **8**, 337 (1991).

Magee, J.W., Haynes, W.M. and M.J. Hiza, "Isochoric (p, ρ, T) Measurements for Five Natural Gas Mixtures from T = (225 to 350) K at Pressures to 35 MPa," *Journal of Chemical Thermodynamics*, **29**, 1439 (1997).

Maiden, C.J., "A Project Overview," *CHEMTECH*, **18**(1), 38 (1988).

Mangum, B.W. and Furukawa, G.T., "Guidelines for Realizing the International Temperature Scale of 1990 (ITS-90)," National Institute of Standards and Technology, US Department of Commerce Technical Note 1265, Gaithersburg, MD (Aug. 1990).

Marshall, R., "Gulf Project Advances Deepwater Pipeline Technologies," *Oil & Gas Journal*, **101**(18), 84 (2003).

Massen, C.H., E. Robens, J.A. Poulis and T. Gast, "Disturbances in Weighing – Part I: A Survey of Work Presented at the Preceding VMT Conferences," *Thermochimica Acta*, **82**, 43 (1984).

McLinden, M.O. and N.V. Frederick, "Development of a Dual-Sinker Densimeter for High-accuracy Fluid P-V-T Measurements," *Proceedings of the 11th Symposium on Energy Engineering Sciences*, May 3-5, 1993, Argonne, IL, Appendix A (1993).

McLinden, M.O. and J.C. Holste, Personal Communication, Physical and Chemical Properties Division, National Institute of Standards and Technology, Boulder, CO and Chemical Engineering Department, Texas A&M University (Jun., 2003).

McMurry, J., *Organic Chemistry*, 3rd ed., Brooks/Cole Publishing Company, Belmont, CA, pp 411-423 (1992).

Meisel, S.L., J.P. McCullough, C.H. Lechthaler and P.B. Weisz, "Gasoline from Methanol in One Step," *CHEMTECH*, **6**(2), 86 (1976).

Mettler Toledo, *The New Mettler AT Analytical Balance*, Greifensee, Switzerland (1988).

Mettler Toledo, *Operating Instructions – Bidirectional Data Interface – Mettler AT/MT/UMT Balances*, Greifensee, Switzerland (1990).

Mettler Toledo, *Operating Instructions for Mettler Toledo AT Balances*, Greifensee, Switzerland (1996).

Mettler Toledo, *Balance Calibration Certificate for Model AT261, Serial Number 1117402553*, Columbus, OH (Jun. 2002).

Meyer, H.S., D.A. Dalrymple and K.E. McIntush, "Opportunities for Improvements in Offshore Gas Processing," *Proceedings of the 75th Gas Processors' Association Annual Convention*, March 1996, Gas Processors Association, Tulsa, OK, pp 127-133 (1996).

Miller, R.W., *Flow Measurement Engineering Handbook*, 3rd ed., McGraw-Hill, New York, NY (1996).

Millheim, K., "Alaska Hydrate Project Overview," Petroleum Engineering Department Seminar Series, Texas A&M University, College Station, TX (Feb. 2004).

Minco, *Report of Calibration for Platinum Resistance Thermometer Model S1059-2, Serial Number 204, Report Number 3385*, Friedley, MN (Nov. 2000).

Mollerup, J., "Measurement of the Volumetric Properties of Methane and Ethene at 310 K at Pressures to 70 MPa and of Propene from 270 to 345 K at Pressures to 3 MPa by the Burnett method," *Journal of Chemical Thermodynamics*, **17**, 489 (1985).

Moritis, G., "Hubs, New Technologies Provide Access to More Deepwater Reserves," *Oil & Gas Journal*, **101**(44), 54 (2003).

National Institute of Standards and Technology, *NIST Mixture Property Standard Reference Database 14, Version 9.08B* (formerly called DDMIX), Gaithersburg, MD (1993).

National Institute of Standards and Technology, *Thermodynamic and Transport Properties of Pure Fluids, NIST Standard Reference Database 12, Version 5.0,* US Dept. of Commerce, Boulder, CO (2000).

National Institute of Standards and Technology, *Reference Fluid Thermodynamic and Transport Properties, NIST Standard Reference Database 23, Version 7.1, Beta Version 04/21/04*, Physical and Chemical Properties Division, US Dept. of Commerce, Boulder, CO (2003).

Neubauer, B., B. Tavitian, A. Boutin and P.Ungerer, "Molecular Simulations on Volumetric Properties of Natural Gas," *Fluid Phase Equilibria*, **161**, 45 (1999).

Nowak, P., R. Kleinrahm and W. Wagner, "Measurement and Correlation of the (p, ρ, T) Relation of Nitrogen I. The Homogeneous Gas and Liquid Regions in the Temperature Range from 66 K to 340 K at Pressures up to 12 MPa," *Journal of Chemical Thermodynamics*, **29**, 1137 (1997).

Oppenheimer, E.J, *Natural Gas: The New Energy Leader*, Pen & Podium, Inc., New York, NY (1982).

Parkyns, N.D., C.J. Warburton and J.D. Wilson, "Natural Gas Conversion to Liquid Fuels and Chemicals: Where Does It Stand?" *Catalysis Today*, **18**(4), 385 (1993).

Paroscientific, Inc., *Digiquartz Pressure Instrumentation Product Guide and Certificate of Calibration*, Redmond, WA (Mar. 2001).

Patel, N.C. and A.S. Teja, "A New Cubic Equation of State for Fluids and Fluid Mixtures," *Chemical Engineering Science*, **37**(3)**,** 463 (1982).

Peng, D. and D.B. Robinson, "A New Two-constant Equation of State," *Industrial and Engineering Chemistry Fundamentals*, **15**(1), 59 (1976).

Pieperbeck, N., R. Kleinrahm, W. Wagner and M. Jaeschke, "Results of (Pressure, Density, Temperature) Measurements on Methane and on Nitrogen in the Temperature Range from 273.15 K to 323.15 K at Pressures up to 12 MPa Using a New Apparatus for Accurate Gas Density Measurements," *Journal of Chemical Thermodynamics*, **23**, 175 (1991).

Pitzer, K.S, "The Volumetric and Thermodynamic Properties of Fluids. I. Theoretical Basis and Virial Coefficients," *Journal of the American Chemical Society*, **77**(13), 3427 (1955).

Pitzer, K.S., D.Z. Lippmann, R.F Curl Jr., C.M. Huggins and D.E. Petersen, "The Volumetric and Thermodynamic Properties of Fluids. II. Compressibility Factor, Vapor Pressure and Entropy of Vaporization," *Journal of the American Chemical Society*, **77**(13), 3433 (1955).

Preston-Thomas, H. "The International Temperature Scale of 1990 (ITS-90)," *Metrologia*, **27**, 3 (1990).

Priest, T., "Keys to the Evolution of Offshore Platform," *Proceedings of the 3rd National Congress on Civil Engineering History and Heritage*, October 10-13, 2001, Houston, TX, American Society of Civil Engineers, Reston, VA, pp 263-265 (2001).

Puskas, I., "Natural Gas to Syncrude: Making the Process Payoff," *CHEMTECH*, **25**(12), 43 (1995).

Redlich, O. and J.N.S. Kwong, "On the Thermodynamics of Solutions. V An Equation of State. Fugacities of Gaseous Solutions," *Chemical Review*, **44**, 233 (1949).

Robertson, E.P., "Options for Gas to Liquids Technology in Alaska," Idaho National Engineering and Environmental Laboratory Publication, No. INEEL/EXT-99-01023, Idaho Falls, ID (Dec. 1999).

Robinson, R.L., Jr. and Jacoby, R.H., "Better Compressibility Factors," *Hydrocarbon Processing*, **44**(4), 141 (1965).

Rostrup-Nielsen, J.R., "Production of Synthesis Gas," *Catalysis Today*, **18**, 305 (1993).

Rubotherm GmbH, *Certificate of Calibration of Sinker Number: 27*, Bochum, Germany (Nov. 1998).

Rubotherm GmbH, *Operating Instructions – Densitometer with Magnetic Suspension Balance*, Bochum, Germany (1999).

Rubotherm GmbH, *Certificate of Calibration of Sinker Number: Texas (neu)*, Bochum, Germany (Jan. 2003).

Ruska Instruments Corporation, *User's Manual for Ruska Differential Pressure Indicator*, Houston, TX (1961).

Ruska Instruments Corporation, *Operating Manual for Ruska Dead Weight Gauge*, Houston, TX (1977).

Ruska Instruments Corporation, *Calibration Report 030619V-519 for Deadweight Gauge Piston and Calibration Report 03061923353 for Deadweight Gauge Mass Set*, Houston, TX (2003).

Savidge, J.L., S.W. Beyerlein and E.W. Lemmon, "Technical Reference Document for the 2nd Edition of AGA Report No. 8," *Gas* Research Institute, Topical Report No. GRI-93/0181, Chicago, IL (Mar. 1995).

Schmidt, R. and Wagner, W., "A New Form of the Equation of State for Pure Substances and Its Application to Oxygen," *Fluid Phase Equilibria*, **19**, 175 (1985).

Schouten, J.A., J.P.J. Michels and M. Jaeschke, "Calculation of the Compressibility Factor of Natural Gases Based on the Calorific Value and the Specific Gravity," *International Journal of Thermophysics*, **11**(1), 145 (1990).

Schupp, O.E., *Gas Chromatography, Technique of Organic Chemistry Vol. XIII*, E.S. Perry and A. Weissberger, eds. Interscience Publishers, New York, NY (1968).

Sengers, J.V., R.F. Kayser, C.J. Peters and H.J. White, Jr., eds., *Equations of State for Fluids and Fluid Mixtures. Experimental Thermodynamics, Volume V*, Elsevier, Amsterdam, The Netherlands (2000).

Setzmann, U. and W. Wagner, "A New Equation of State and Tables of Thermodynamic Properties for Methane Covering the Range from the Melting Line to 625 K at Pressures up to 1000 MPa," *Journal of Physical and Chemical Reference Data*, **20**(6), 1061 (1991).

Shell, Press Release, "Qatar Petroleum and Shell Agree to Build the World's Largest Gas to Liquids Plant," Ras Laffan, Qatar (Oct. 20, 2003).

Sie, S.T., M.M.G. Senden and H.M.H. Van Wechem, "Conversion of Natural Gas to Transportation Fuels via the Shell Middle Distillate Synthesis Process," *Catalysis Today*, **8**, 371 (1991).

Sie, S.T., "Process Development and Scale Up: IV Case History of the Development of a Fischer-Tropsch Synthesis Process," *Reviews in Chemical Engineering*, **14**(2), 109 (1998).

Simon, P.P., "*PVT* Measurements for Five Natural Gas Mixtures," M.S. Thesis, Texas A&M University, College Station, TX (1991).

Smith, J.M., H.C. Van Ness and M.M. Abbott, *Introduction to Chemical Engineering Thermodynamics*, 6th ed., McGraw-Hill, New York, NY, pp 283-295 (2001).

Soave, G., "Equilibrium Constants from a Modified Redlich-Kwong Equation of State," *Chemical Engineering Science* **27**, 1197 (1972).

Span, R., E.W. Lemmon, R.T. Jacobsen, W. Wagner and A. Yokozeki, "A Reference Equation of State for the Thermodynamic Properties of Nitrogen for Temperatures from 63.151 to 1000 K and Pressures to 2200 MPa," *Journal of Physical and Chemical Reference Data*, **29**(6), 1361 (2000).

Span, R., *Multiparameter Equations of State: An Accurate Source of Thermodynamic Property Data*, Springer-Verlag, Berlin, Germany (2000).

Span, R., W. Wagner, E.W. Lemmon and R.T. Jacobsen, "Multiparameter Equations of State – Recent Trends and Future Challenges," *Fluid Phase Equilibria*, **183-184**, 1 (2001).

Standing, M.B and D.L. Katz, "Density of Natural Gases," *Transactions of the American Institute of Mining, Metallurgical and Petroleum Engineers*, **146**, 140 (1942).

Starling, K.E., *Fluid Thermodynamic Properties for Light Petroleum Systems*, Gulf Publishing Company, Houston, TX (1973).

Stouffer, C.E., "Densities of Mixtures of Carbon Dioxide and Hydrogen Sulfide from 200 to 450 K to 23 MPa by the Burnett-Isochoric Method," Ph.D. Dissertation, Texas A&M University, College Station, TX (1992).

Stouffer, C.E., S.J. Kellerman, K.R. Hall, J.C. Holste, B.E. Gammon and K.N. Marsh, "Densities of Carbon Dioxide + Hydrogen Sulfide Mixtures from 220 K to 450 K at Pressures up to 25 MPa," *Journal of Chemical and Engineering Data*, **46**, 1309 (2001).

Straty, G.C. and D.E. Diller, "(*p*, *V*, *T*) of Saturated and Compressed Fluid Nitrogen," *Journal of Chemical Thermodynamics*, **12**, 927 (1980).

Syntroleum Corporation, Press Release, "Syntroleum Dedicates Ultra-clean Fuels Plant with Marathon and US DOE: Completes Construction on Plant to Produce Synthetic Diesel from Natural Gas Feedstock for Government Vehicle Fleet Demonstrations," Tulsa, OK (Oct. 3, 2003).

Tampa Electric Company, "The Tampa Electric Gasification Combined Cycle Project," US Department of Energy and Tampa Electric Company Topical Report, No. 6, Tampa, FL (Oct. 1996).

Tampa Electric Company, "Tampa Electric Integrated Gasification Combined Cycle Project: An Update," US Department of Energy and Tampa Electric Company Topical Report, No. 19, Tampa, FL (Jul. 2000).

Taylor, B.N. and C.E. Kuyatt, "Guidelines for Evaluating and Expressing the Uncertainty of NIST Measurement Results," National Institute of Standards and Technology, US Department of Commerce Technical Note 1297, Washington, DC (1994).

Tegeler, C., R. Span and W. Wagner, "A New Equation of State for Argon Covering the Fluid Region for Temperature From the Melting Line to 700 K at Pressures up to 1000 MPa," *Journal of Physical and Chemical Reference Data*, **28**(3), 779 (1999).

Thermodynamic Research Center, *TRC Thermodynamic Tables: Hydrocarbons*, M. Frenkel, ed., Vol. X, National Standard Reference Data Series, National Institute of Standards and Technology. 75-126, US Department of Commerce, Washington, DC (2003a).

Thermodynamic Research Center, *TRC Thermodynamic Tables: Hydrocarbons*, M. Frenkel, ed., Vol. V, National Standard Reference Data Series, National Institute of Standards and Technology. 75-126, US Department of Commerce, Washington, DC (2003b).

Trappeniers, N.J., T. Wassenaar and J.C. Abels, "Isotherms and Thermodynamic Properties of Methane at Temperatures between 0 ^{o} and 150 ^{o}C and at Densities up to 570 Amagat," *Physica*, **98A**, 289 (1979).

Trimm D.L. and M.S. Wainwright, "Steam Reforming and Methanol Synthesis," *Catalysis Today*, **6**(3), 261 (1990).

US DOE, "Hydrogen from Natural Gas and Coal: The Road to a Sustainable Energy Future," Office of Fossil Energy, US Department of Energy Hydrogen Program Plan, Washington, DC (Jun. 2003).

US DOE, "FutureGen: Integrated Hydrogen, Electric Power Production and Carbon Sequestration Research Initiative," Office of Fossil Energy, US Department of Energy Program Plan, Washington, DC (Mar. 2004).

Wagner, W., K. Brachthäuser, R. Kleinrahm and H.W. Lösch, "A New, Accurate Single-sinker Densitometer for Temperatures from 233 to 523 K at Pressures up to 30 MPa," *International Journal of Thermophysics*, **16**(2), 399 (1995).

Wagner, W. and R. Kleinrahm, "Densimeters for Very Accurate Density Measurements of Fluids over Large Ranges of Temperature, Pressure and Density," *Metrologia*, **41**, S24 (2004).

Wang, X. and J.G. Bomba, "Hydrate Problems in Deepwater Flowlines," *Proceedings of the 13th International Conference on Offshore Mechanics and Arctic Engineering*, February 27-March 3, 1994, Houston, TX, American Society of Mechanical Engineers, New York, NY, pp 343-350 (1994).

Warren, T.R., "World Pipeline Construction Looks to Remain Robust to Century's Turn," *Oil & Gas Journal*, **95**(6), 34 (1997).

Watson, J.T.R., "A Report on the Density of Rich Natural Gas Mixtures – A Joint Industrial Project," National Engineering Laboratory, Report No. 110/97, East Kilbride, Glasgow, UK (Feb. 1998).

Yarborough, L. and K.R. Hall, "How to Solve Equation of State for Z-factors," *The Oil & Gas Journal*, **72**(7), 86 (1974).

Younglove, B.A. and Ely J.F., "Thermophysical Properties of Fluids. II. Methane, Ethane, Propane, Isobutane and Normal Butane," *Journal of Physical and Chemical Reference Data*, **16**(4), 577 (1987).

Yurttaş, L., "A New Isochoric Apparatus with Applications to *P-V-T* and Phase Equilibria Studies," Ph.D. Dissertation, Texas A&M University, College Station, TX (1988).

Yurttaş, L., J.C. Holste, K.R. Hall, B.E. Gammon and K.N. Marsh, "Semi-automated Isochoric Apparatus for *P-V-T* and Phase Equilibrium Studies," *Journal of Chemical and Engineering Data*, **39**, 418 (1994).

Zhou, J., Personal Communication, Chemical Engineering Department, Texas A&M University (2002).

APPENDIX A

PREDICTED DENSITIES FOR NATURAL GAS MIXTURES FROM THE HY, AGA8-DC92 AND REFPROP EQUATIONS OF STATE

Table A.1.1. Predicted Density and Compressibility Factor for RR-NIST2 Mixture from HY EOS

Molecular weight		17.59886	kg/kmole		
Specific gravity		0.60999			
T_{pc}		196.745	K		
P_{pc}		4.580	MPa		
T	**P**	**ρ**	**Z**	**T_{pr}**	**P_{pr}**
K	**MPa**	**kmole/m^3**			
270	3.44738	1.711	0.89769	1.372	0.753
	5.17107	2.717	0.84799		1.129
	6.89476	3.834	0.80124		1.505
	8.61845	5.054	0.75966		1.882
	10.34214	6.348	0.72584		2.258
	12.06583	7.657	0.70207		2.634
	13.78952	8.911	0.68946		3.011
	15.51321	10.053	0.68748		3.387
	17.23690	11.059	0.69440		3.763
	18.96059	11.929	0.70812		4.140
	20.68428	12.680	0.72676		4.516
	22.40797	13.330	0.74891		4.892
	24.13166	13.899	0.77353		5.269
	25.85535	14.400	0.79991		5.645
	27.57904	14.848	0.82754		6.021
	29.30273	15.250	0.85608		6.398
	31.02642	15.614	0.88528		6.774
	32.75011	15.947	0.91495		7.150
	34.47380	16.253	0.94497		7.527
290	3.44738	1.553	0.92075	1.474	0.753
	5.17107	2.428	0.88349		1.129
	6.89476	3.369	0.84896		1.505
	8.61845	4.369	0.81832		1.882
	10.34214	5.411	0.79278		2.258
	12.06583	6.471	0.77348		2.634
	13.78952	7.514	0.76119		3.011
	15.51321	8.511	0.75607		3.387
	17.23690	9.437	0.75766		3.763
	18.96059	10.280	0.76506		4.140
	20.68428	11.039	0.77723		4.516
	22.40797	11.719	0.79315		4.892
	24.13166	12.328	0.81198		5.269
	25.85535	12.875	0.83301		5.645
	27.57904	13.368	0.85572		6.021
	29.30273	13.816	0.87972		6.398
	31.02642	14.225	0.90469		6.774
	32.75011	14.600	0.93042		7.150
	34.47380	14.946	0.95672		7.527

Table A.1.1. (Continued)

Molecular weight		17.59886	kg/kmole		
Specific gravity		0.60999			
T_{pc}		196.745	K		
P_{pc}		4.580	MPa		
T	**P**	**ρ**	**Z**	**T_{pr}**	**P_{pr}**
K	**MPa**	**kmole/m^3**			
305	3.44738	1.456	0.93408	1.550	0.753
	5.17107	2.257	0.90366		1.129
	6.89476	3.105	0.87574		1.505
	8.61845	3.994	0.85105		1.882
	10.34214	4.912	0.83038		2.258
	12.06583	5.843	0.81444		2.634
	13.78952	6.766	0.80374		3.011
	15.51321	7.662	0.79850		3.387
	17.23690	8.513	0.79856		3.763
	18.96059	9.307	0.80347		4.140
	20.68428	10.039	0.81259		4.516
	22.40797	10.709	0.82522		4.892
	24.13166	11.321	0.84071		5.269
	25.85535	11.878	0.85850		5.645
	27.57904	12.387	0.87809		6.021
	29.30273	12.853	0.89912		6.398
	31.02642	13.282	0.92128		6.774
	32.75011	13.678	0.94433		7.150
	34.47380	14.044	0.96809		7.527
340	3.44738	1.275	0.95646	1.728	0.753
	5.17107	1.952	0.93706		1.129
	6.89476	2.653	0.91962		1.505
	8.61845	3.371	0.90446		1.882
	10.34214	4.102	0.89189		2.258
	12.06583	4.839	0.88222		2.634
	13.78952	5.571	0.87565		3.011
	15.51321	6.292	0.87230		3.387
	17.23690	6.992	0.87218		3.763
	18.96059	7.665	0.87516		4.140
	20.68428	8.306	0.88103		4.516
	22.40797	8.913	0.88951		4.892
	24.13166	9.483	0.90029		5.269
	25.85535	10.018	0.91306		5.645
	27.57904	10.520	0.92753		6.021
	29.30273	10.989	0.94343		6.398
	31.02642	11.428	0.96053		6.774
	32.75011	11.840	0.97864		7.150
	34.47380	12.226	0.99758		7.527

Table A.1.2. Predicted Density and Compressibility Factor for RR-NIST2 Mixture from AGA8-DC92 EOS

Molecular weight	17.59884	kg/kmole
Specific gravity	0.60875	

T	P	ρ	Z
K	MPa	kmole/m^3	
270	3.44738	1.699	0.90365
	5.17107	2.692	0.85577
	6.89476	3.792	0.80986
	8.61845	4.997	0.76821
	10.34214	6.278	0.73381
	12.06583	7.575	0.70950
	13.78952	8.817	0.69666
	15.51321	9.949	0.69460
	17.23690	10.948	0.70131
	18.96059	11.819	0.71462
	20.68428	12.575	0.73270
	22.40797	13.236	0.75414
	24.13166	13.818	0.77795
	25.85535	14.335	0.80342
	27.57904	14.800	0.83007
	29.30273	15.221	0.85755
	31.02642	15.605	0.88564
	32.75011	15.959	0.91415
	34.47380	16.285	0.94297
290	3.44738	1.544	0.92629
	5.17107	2.407	0.89099
	6.89476	3.333	0.85788
	8.61845	4.316	0.82814
	10.34214	5.341	0.80309
	12.06583	6.383	0.78397
	13.78952	7.412	0.77161
	15.51321	8.397	0.76622
	17.23690	9.316	0.76732
	18.96059	10.159	0.77402
	20.68428	10.924	0.78529
	22.40797	11.614	0.80019
	24.13166	12.236	0.81793
	25.85535	12.798	0.83784
	27.57904	13.309	0.85943
	29.30273	13.774	0.88230
	31.02642	14.200	0.90614
	32.75011	14.593	0.93073
	34.47380	14.957	0.95589

Table A.1.2. (Continued)

Molecular weight	17.59884	kg/kmole
Specific gravity	0.60875	

T	P	ρ	Z
K	MPa	kmole/m^3	
305	3.44738	1.447	0.93933
	5.17107	2.239	0.91090
	6.89476	3.074	0.88459
	8.61845	3.947	0.86115
	10.34214	4.847	0.84139
	12.06583	5.760	0.82603
	13.78952	6.667	0.81558
	15.51321	7.550	0.81028
	17.23690	8.392	0.80997
	18.96059	9.183	0.81422
	20.68428	9.917	0.82245
	22.40797	10.595	0.83402
	24.13166	11.217	0.84833
	25.85535	11.789	0.86487
	27.57904	12.313	0.88321
	29.30273	12.796	0.90299
	31.02642	13.242	0.92393
	32.75011	13.655	0.94578
	34.47380	14.038	0.96836
340	3.44738	1.269	0.96117
	5.17107	1.938	0.94376
	6.89476	2.628	0.92810
	8.61845	3.334	0.91449
	10.34214	4.050	0.90324
	12.06583	4.771	0.89460
	13.78952	5.489	0.88874
	15.51321	6.195	0.88578
	17.23690	6.884	0.88570
	18.96059	7.550	0.88841
	20.68428	8.187	0.89372
	22.40797	8.794	0.90140
	24.13166	9.368	0.91120
	25.85535	9.911	0.92285
	27.57904	10.422	0.93609
	29.30273	10.903	0.95071
	31.02642	11.356	0.96651
	32.75011	11.782	0.98331
	34.47380	12.183	1.00097

Table A.1.3. Predicted Density and Compressibility Factor for RR-NIST2 Mixture from REFPROP EOS

Molecular weight	17.59851	kg/kmole	
Specific gravity	0.60998		
T_{pc}	201.720	K	
P_{pc}	5.351	MPa	

T	**P**	**ρ**	**Z**	**T_{pr}**	**P_{pr}**
K	**MPa**	**kmole/m^3**			
270	3.44738	1.699	0.90413	1.338	0.644
	5.17107	2.690	0.85631		0.966
	6.89476	3.790	0.81029		1.288
	8.61845	4.996	0.76843		1.611
	10.34214	6.279	0.73376		1.933
	12.06583	7.579	0.70917		2.255
	13.78952	8.824	0.69614		2.577
	15.51321	9.957	0.69406		2.899
	17.23690	10.954	0.70092		3.221
	18.96059	11.822	0.71442		3.543
	20.68428	12.576	0.73264		3.865
	22.40797	13.235	0.75417		4.187
	24.13166	13.816	0.77803		4.510
	25.85535	14.333	0.80354		4.832
	27.57904	14.797	0.83022		5.154
	29.30273	15.218	0.85774		5.476
	31.02642	15.601	0.88586		5.798
	32.75011	15.954	0.91441		6.120
	34.47380	16.280	0.94326		6.442
290	3.44738	1.543	0.92669	1.438	0.644
	5.17107	2.406	0.89148		0.966
	6.89476	3.331	0.85836		1.288
	8.61845	4.314	0.82851		1.611
	10.34214	5.340	0.80330		1.933
	12.06583	6.383	0.78400		2.255
	13.78952	7.413	0.77146		2.577
	15.51321	8.400	0.76591		2.899
	17.23690	9.321	0.76692		3.221
	18.96059	10.165	0.77362		3.543
	20.68428	10.928	0.78496		3.865
	22.40797	11.617	0.79996		4.187
	24.13166	12.238	0.81779		4.510
	25.85535	12.799	0.83778		4.832
	27.57904	13.309	0.85941		5.154
	29.30273	13.774	0.88231		5.476
	31.02642	14.200	0.90618		5.798
	32.75011	14.593	0.93078		6.120
	34.47380	14.956	0.95595		6.442

Table A.1.3. (Continued)

Molecular weight		17.59851	kg/kmole		
Specific gravity		0.60998			
T_{pc}		201.720	K		
P_{pc}		5.351	MPa		
T	**P**	**ρ**	**Z**	**T_{pr}**	**P_{pr}**
K	**MPa**	**kmole/m^3**			
305	3.44738	1.447	0.93966	1.512	0.644
	5.17107	2.238	0.91134		0.966
	6.89476	3.072	0.88505		1.288
	8.61845	3.945	0.86155		1.611
	10.34214	4.845	0.84168		1.933
	12.06583	5.759	0.82619		2.255
	13.78952	6.667	0.81561		2.577
	15.51321	7.551	0.81016		2.899
	17.23690	8.394	0.80972		3.221
	18.96059	9.187	0.81388		3.543
	20.68428	9.922	0.82207		3.865
	22.40797	10.599	0.83365		4.187
	24.13166	11.221	0.84802		4.510
	25.85535	11.792	0.86463		4.832
	27.57904	12.316	0.88304		5.154
	29.30273	12.798	0.90289		5.476
	31.02642	13.243	0.92387		5.798
	32.75011	13.655	0.94575		6.120
	34.47380	14.038	0.96836		6.442
340	3.44738	1.268	0.96139	1.686	0.644
	5.17107	1.938	0.94408		0.966
	6.89476	2.627	0.92846		1.288
	8.61845	3.332	0.91486		1.611
	10.34214	4.049	0.90358		1.933
	12.06583	4.770	0.89488		2.255
	13.78952	5.487	0.88896		2.577
	15.51321	6.194	0.88591		2.899
	17.23690	6.884	0.88573		3.221
	18.96059	7.550	0.88832		3.543
	20.68428	8.189	0.89352		3.865
	22.40797	8.797	0.90110		4.187
	24.13166	9.372	0.91082		4.510
	25.85535	9.915	0.92242		4.832
	27.57904	10.427	0.93566		5.154
	29.30273	10.908	0.95029		5.476
	31.02642	11.360	0.96613		5.798
	32.75011	11.786	0.98298		6.120
	34.47380	12.186	1.00069		6.442

Table A.2.1. Predicted Density and Compressibility Factor for M91C1 Mixture from HY EOS

Molecular weight		18.21068	kg/kmole		
Specific gravity		0.63120			
T_{pc}		200.911	K		
P_{pc}		4.568	MPa		
T	**P**	**ρ**	**Z**	**T_{pr}**	**P_{pr}**
K	**MPa**	**kmole/m^3**			
270	3.44738	1.727	0.88942	1.344	0.755
	5.17107	2.759	0.83508		1.132
	6.89476	3.920	0.78371		1.509
	8.61845	5.202	0.73809		1.887
	10.34214	6.567	0.70158		2.264
	12.06583	7.940	0.67702		2.641
	13.78952	9.232	0.66546		3.019
	15.51321	10.381	0.66576		3.396
	17.23690	11.370	0.67542		3.773
	18.96059	12.209	0.69188		4.151
	20.68428	12.924	0.71305		4.528
	22.40797	13.538	0.73744		4.905
	24.13166	14.071	0.76405		5.283
	25.85535	14.540	0.79220		5.660
	27.57904	14.958	0.82144		6.037
	29.30273	15.333	0.85144		6.415
	31.02642	15.672	0.88198		6.792
	32.75011	15.983	0.91291		7.169
	34.47380	16.268	0.94412		7.547
290	3.44738	1.564	0.91423	1.443	0.755
	5.17107	2.455	0.87356		1.132
	6.89476	3.422	0.83574		1.509
	8.61845	4.457	0.80215		1.887
	10.34214	5.540	0.77433		2.264
	12.06583	6.641	0.75367		2.641
	13.78952	7.718	0.74105		3.019
	15.51321	8.737	0.73653		3.396
	17.23690	9.670	0.73940		3.773
	18.96059	10.508	0.74848		4.151
	20.68428	11.253	0.76246		4.528
	22.40797	11.913	0.78020		4.905
	24.13166	12.500	0.80077		5.283
	25.85535	13.024	0.82344		5.660
	27.57904	13.495	0.84768		6.037
	29.30273	13.921	0.87310		6.415
	31.02642	14.309	0.89941		6.792
	32.75011	14.664	0.92639		7.169
	34.47380	14.991	0.95388		7.547

Table A.2.1. (Continued)

Molecular weight		18.21068	kg/kmole		
Specific gravity		0.63120			
T_{pc}		200.911	K		
P_{pc}		4.568	MPa		
T	**P**	**ρ**	**Z**	**T_{pr}**	**P_{pr}**
K	**MPa**	**kmole/m^3**			
305	3.44738	1.464	0.92855	1.518	0.755
	5.17107	2.278	0.89533		1.132
	6.89476	3.145	0.86474		1.509
	8.61845	4.058	0.83766		1.887
	10.34214	5.005	0.81504		2.264
	12.06583	5.965	0.79774		2.641
	13.78952	6.916	0.78638		3.019
	15.51321	7.832	0.78117		3.396
	17.23690	8.695	0.78183		3.773
	18.96059	9.493	0.78776		4.151
	20.68428	10.221	0.79815		4.528
	22.40797	10.881	0.81218		4.905
	24.13166	11.479	0.82911		5.283
	25.85535	12.021	0.84831		5.660
	27.57904	12.513	0.86928		6.037
	29.30273	12.962	0.89162		6.415
	31.02642	13.373	0.91503		6.792
	32.75011	13.751	0.93928		7.169
	34.47380	14.101	0.96418		7.547
340	3.44738	1.280	0.95255	1.692	0.755
	5.17107	1.965	0.93127		1.132
	6.89476	2.675	0.91207		1.509
	8.61845	3.406	0.89531		1.887
	10.34214	4.151	0.88138		2.264
	12.06583	4.903	0.87063		2.641
	13.78952	5.651	0.86331		3.019
	15.51321	6.385	0.85955		3.396
	17.23690	7.096	0.85935		3.773
	18.96059	7.777	0.86255		4.151
	20.68428	8.422	0.86888		4.528
	22.40797	9.029	0.87801		4.905
	24.13166	9.597	0.88957		5.283
	25.85535	10.128	0.90321		5.660
	27.57904	10.622	0.91860		6.037
	29.30273	11.083	0.93544		6.415
	31.02642	11.512	0.95350		6.792
	32.75011	11.914	0.97255		7.169
	34.47380	12.290	0.99243		7.547

Table A.2.2. Predicted Density and Compressibility Factor for M91C1 Mixture from AGA8-DC92 EOS

Molecular weight	18.21067	kg/kmole
Specific gravity	0.63007	

T	P	ρ	Z
K	MPa	kmole/m^3	
270	3.44738	1.721	0.89226
	5.17107	2.749	0.83780
	6.89476	3.912	0.78506
	8.61845	5.208	0.73722
	10.34214	6.594	0.69864
	12.06583	7.983	0.67327
	13.78952	9.276	0.66220
	15.51321	10.416	0.66346
	17.23690	11.393	0.67396
	18.96059	12.224	0.69092
	20.68428	12.936	0.71227
	22.40797	13.552	0.73656
	24.13166	14.091	0.76284
	25.85535	14.570	0.79047
	27.57904	14.999	0.81903
	29.30273	15.388	0.84825
	31.02642	15.743	0.87791
	32.75011	16.069	0.90789
	34.47380	16.370	0.93807
290	3.44738	1.558	0.91760
	5.17107	2.444	0.87765
	6.89476	3.404	0.83993
	8.61845	4.435	0.80598
	10.34214	5.516	0.77759
	12.06583	6.616	0.75641
	13.78952	7.692	0.74350
	15.51321	8.708	0.73887
	17.23690	9.639	0.74163
	18.96059	10.478	0.75045
	20.68428	11.228	0.76403
	22.40797	11.896	0.78123
	24.13166	12.492	0.80116
	25.85535	13.027	0.82313
	27.57904	13.510	0.84662
	29.30273	13.949	0.87123
	31.02642	14.350	0.89669
	32.75011	14.719	0.92277
	34.47380	15.060	0.94933

Table A.2.2. (Continued)

Molecular weight	18.21067	kg/kmole
Specific gravity	0.63007	

T	P	ρ	Z
K	MPa	kmole/m^3	
305	3.44738	1.458	0.93210
	5.17107	2.266	0.89995
	6.89476	3.125	0.87002
	8.61845	4.030	0.84329
	10.34214	4.969	0.82080
	12.06583	5.922	0.80350
	13.78952	6.865	0.79205
	15.51321	7.777	0.78665
	17.23690	8.637	0.78701
	18.96059	9.435	0.79247
	20.68428	10.167	0.80223
	22.40797	10.835	0.81549
	24.13166	11.443	0.83156
	25.85535	11.997	0.84984
	27.57904	12.502	0.86988
	29.30273	12.965	0.89127
	31.02642	13.390	0.91374
	32.75011	13.782	0.93704
	34.47380	14.146	0.96099
340	3.44738	1.275	0.95624
	5.17107	1.953	0.93644
	6.89476	2.655	0.91852
	8.61845	3.377	0.90286
	10.34214	4.111	0.88985
	12.06583	4.851	0.87980
	13.78952	5.588	0.87294
	15.51321	6.312	0.86938
	17.23690	7.016	0.86912
	18.96059	7.692	0.87199
	20.68428	8.336	0.87778
	22.40797	8.945	0.88616
	24.13166	9.518	0.89682
	25.85535	10.057	0.90944
	27.57904	10.561	0.92374
	29.30273	11.034	0.93945
	31.02642	11.476	0.95636
	32.75011	11.891	0.97427
	34.47380	12.280	0.99304

Table A.2.3. Predicted Density and Compressibility Factor for M91C1 Mixture from REFPROP EOS

Molecular weight		18.21044	kg/kmole		
Specific gravity		0.63119			
T_{pc}		208.200	K		
P_{pc}		5.568	MPa		
T	**P**	**ρ**	**Z**	**T_{pr}**	**P_{pr}**
K	**MPa**	**kmole/m^3**			
270	3.44738	1.718	0.89387	1.297	0.619
	5.17107	2.742	0.84005		0.929
	6.89476	3.899	0.78779		1.238
	8.61845	5.186	0.74027		1.548
	10.34214	6.564	0.70180		1.857
	12.06583	7.947	0.67632		2.167
	13.78952	9.235	0.66517		2.477
	15.51321	10.367	0.66656		2.786
	17.23690	11.337	0.67726		3.096
	18.96059	12.163	0.69439		3.405
	20.68428	12.871	0.71583		3.715
	22.40797	13.485	0.74019		4.024
	24.13166	14.024	0.76653		4.334
	25.85535	14.501	0.79422		4.643
	27.57904	14.930	0.82285		4.953
	29.30273	15.318	0.85213		5.263
	31.02642	15.672	0.88186		5.572
	32.75011	15.998	0.91190		5.882
	34.47380	16.300	0.94213		6.191
290	3.44738	1.556	0.91873	1.393	0.619
	5.17107	2.439	0.87923		0.929
	6.89476	3.397	0.84181		1.238
	8.61845	4.424	0.80802		1.548
	10.34214	5.501	0.77968		1.857
	12.06583	6.597	0.75849		2.167
	13.78952	7.671	0.74551		2.477
	15.51321	8.685	0.74083		2.786
	17.23690	9.613	0.74361		3.096
	18.96059	10.449	0.75256		3.405
	20.68428	11.195	0.76630		3.715
	22.40797	11.859	0.78366		4.024
	24.13166	12.452	0.80372		4.334
	25.85535	12.985	0.82579		4.643
	27.57904	13.466	0.84936		4.953
	29.30273	13.904	0.87404		5.263
	31.02642	14.304	0.89956		5.572
	32.75011	14.673	0.92570		5.882
	34.47380	15.013	0.95231		6.191

Table A.2.3. (Continued)

Molecular weight		18.21044	kg/kmole		
Specific gravity		0.63119			
T_{pc}		208.200	K		
P_{pc}		5.568	MPa		
T	**P**	**ρ**	**Z**	**T_{pr}**	**P_{pr}**
K	**MPa**	**kmole/m^3**			
305	3.44738	1.457	0.93296	1.465	0.619
	5.17107	2.263	0.90117		0.929
	6.89476	3.120	0.87147		1.238
	8.61845	4.023	0.84486		1.548
	10.34214	4.959	0.82239		1.857
	12.06583	5.910	0.80507		2.167
	13.78952	6.852	0.79356		2.477
	15.51321	7.762	0.78809		2.786
	17.23690	8.621	0.78840		3.096
	18.96059	9.418	0.79387		3.405
	20.68428	10.149	0.80370		3.715
	22.40797	10.814	0.81709		4.024
	24.13166	11.420	0.83330		4.334
	25.85535	11.971	0.85172		4.643
	27.57904	12.473	0.87188		4.953
	29.30273	12.934	0.89338		5.263
	31.02642	13.358	0.91594		5.572
	32.75011	13.749	0.93931		5.882
	34.47380	14.112	0.96333		6.191
340	3.44738	1.275	0.95671	1.633	0.619
	5.17107	1.952	0.93712		0.929
	6.89476	2.653	0.91933		1.238
	8.61845	3.373	0.90375		1.548
	10.34214	4.107	0.89076		1.857
	12.06583	4.846	0.88069		2.167
	13.78952	5.583	0.87379		2.477
	15.51321	6.306	0.87017		2.786
	17.23690	7.010	0.86983		3.096
	18.96059	7.686	0.87263		3.405
	20.68428	8.330	0.87834		3.715
	22.40797	8.940	0.88668		4.024
	24.13166	9.513	0.89734		4.334
	25.85535	10.051	0.91000		4.643
	27.57904	10.554	0.92436		4.953
	29.30273	11.025	0.94017		5.263
	31.02642	11.466	0.95719		5.572
	32.75011	11.879	0.97522		5.882
	34.47380	12.267	0.99410		6.191

Table A.3.1. Predicted Density and Compressibility Factor for M94C1 Mixture from HY EOS *(Numbers in italics fall in the two-phase region)*

Molecular weight		17.88784	kg/kmole		
Specific gravity		0.62001			
T_{pc}		200.949	K		
P_{pc}		4.577	MPa		
T	**P**	**ρ**	**Z**	**T_{pr}**	**P_{pr}**
K	**MPa**	**kmole/m^3**			
270	*3.44738*	*1.727*	*0.88919*	1.344	*0.753*
	5.17107	*2.760*	*0.83467*		*1.130*
	6.89476	*3.923*	*0.78307*		*1.506*
	8.61845	*5.209*	*0.73719*		*1.883*
	10.34214	*6.579*	*0.70040*		*2.259*
	12.06583	*7.957*	*0.67559*		*2.636*
	13.78952	9.255	0.66383		3.012
	15.51321	10.409	0.66398		3.389
	17.23690	11.401	0.67356		3.766
	18.96059	12.243	0.68996		4.142
	20.68428	12.960	0.71108		4.519
	22.40797	13.575	0.73543		4.895
	24.13166	14.109	0.76200		5.272
	25.85535	14.579	0.79011		5.648
	27.57904	14.997	0.81930		6.025
	29.30273	15.372	0.84926		6.401
	31.02642	15.712	0.87977		6.778
	32.75011	16.022	0.91066		7.155
	34.47380	16.308	0.94182		7.531
290	*3.44738*	*1.564*	*0.91404*	1.443	*0.753*
	5.17107	*2.456*	*0.87323*		*1.130*
	6.89476	*3.424*	*0.83525*		*1.506*
	8.61845	*4.460*	*0.80148*		*1.883*
	10.34214	5.546	0.77346		2.259
	12.06583	6.650	0.75259		2.636
	13.78952	7.732	0.73978		3.012
	15.51321	8.754	0.73510		3.389
	17.23690	9.690	0.73783		3.766
	18.96059	10.531	0.74679		4.142
	20.68428	11.279	0.76069		4.519
	22.40797	11.941	0.77836		4.895
	24.13166	12.530	0.79886		5.272
	25.85535	13.055	0.82148		5.648
	27.57904	13.527	0.84567		6.025
	29.30273	13.954	0.87105		6.401
	31.02642	14.342	0.89731		6.778
	32.75011	14.698	0.92425		7.155
	34.47380	15.025	0.95169		7.531

Table A.3.1. (Continued)

Molecular weight		17.88784	kg/kmole		
Specific gravity		0.62001			
T_{pc}		200.949	K		
P_{pc}		4.577	MPa		
T	**P**	**ρ**	**Z**	**T_{pr}**	**P_{pr}**
K	**MPa**	**kmole/m^3**			
305	*3.44738*	*1.465*	*0.92838*	1.518	*0.753*
	5.17107	2.279	0.89505		1.130
	6.89476	3.146	0.86433		1.506
	8.61845	4.061	0.83709		1.883
	10.34214	5.009	0.81431		2.259
	12.06583	5.972	0.79684		2.636
	13.78952	6.925	0.78531		3.012
	15.51321	7.845	0.77994		3.389
	17.23690	8.710	0.78046		3.766
	18.96059	9.511	0.78626		4.142
	20.68428	10.241	0.79655		4.519
	22.40797	10.904	0.81049		4.895
	24.13166	11.504	0.82734		5.272
	25.85535	12.047	0.84648		5.648
	27.57904	12.540	0.86739		6.025
	29.30273	12.990	0.88968		6.401
	31.02642	13.402	0.91304		6.778
	32.75011	13.781	0.93724		7.155
	34.47380	14.132	0.96209		7.531
340	3.44738	1.281	0.95241	1.692	0.753
	5.17107	1.965	0.93105		1.130
	6.89476	2.675	0.91176		1.506
	8.61845	3.407	0.89490		1.883
	10.34214	4.154	0.88086		2.259
	12.06583	4.907	0.86998		2.636
	13.78952	5.656	0.86254		3.012
	15.51321	6.392	0.85865		3.389
	17.23690	7.105	0.85833		3.766
	18.96059	7.787	0.86141		4.142
	20.68428	8.434	0.86764		4.519
	22.40797	9.043	0.87667		4.895
	24.13166	9.613	0.88814		5.272
	25.85535	10.145	0.90170		5.648
	27.57904	10.640	0.91701		6.025
	29.30273	11.102	0.93379		6.401
	31.02642	11.533	0.95178		6.778
	32.75011	11.936	0.97077		7.155
	34.47380	12.312	0.99059		7.531

Table A.3.2. Predicted Density and Compressibility Factor for M94C1 Mixture from AGA8-DC92 EOS *(Numbers in italics fall in the two-phase region)*

Molecular weight	17.88796	kg/kmole
Specific gravity	0.61891	

T	P	ρ	Z
K	MPa	kmole/m^3	
270	*3.44738*	*1.722*	*0.89181*
	5.17107	*2.751*	*0.83732*
	6.89476	*3.913*	*0.78483*
	8.61845	*5.205*	*0.73762*
	10.34214	*6.581*	*0.70001*
	12.06583	*7.955*	*0.67561*
	13.78952	9.235	0.66512
	15.51321	10.368	0.66651
	17.23690	11.344	0.67686
	18.96059	12.178	0.69356
	20.68428	12.893	0.71462
	22.40797	13.514	0.73863
	24.13166	14.058	0.76467
	25.85535	14.540	0.79209
	27.57904	14.973	0.82047
	29.30273	15.365	0.84953
	31.02642	15.722	0.87906
	32.75011	16.050	0.90892
	34.47380	16.354	0.93901
290	*3.44738*	*1.559*	*0.91714*
	5.17107	*2.445*	*0.87708*
	6.89476	*3.407*	*0.83940*
	8.61845	*4.437*	*0.80564*
	10.34214	5.516	0.77760
	12.06583	6.611	0.75688
	13.78952	7.683	0.74439
	15.51321	8.694	0.74007
	17.23690	9.622	0.74297
	18.96059	10.459	0.75182
	20.68428	11.209	0.76534
	22.40797	11.877	0.78245
	24.13166	12.475	0.80226
	25.85535	13.012	0.82411
	27.57904	13.496	0.84748
	29.30273	13.937	0.87199
	31.02642	14.340	0.89734
	32.75011	14.710	0.92334
	34.47380	15.053	0.94982

Table A.3.2. (Continued)

Molecular weight	17.88796	kg/kmole
Specific gravity	0.61891	

T	P	ρ	Z
K	MPa	kmole/m^3	
305	*3.44738*	*1.459*	*0.93166*
	5.17107	2.267	0.89938
	6.89476	3.127	0.86942
	8.61845	4.033	0.84276
	10.34214	4.971	0.82043
	12.06583	5.922	0.80337
	13.78952	6.864	0.79218
	15.51321	7.773	0.78701
	17.23690	8.631	0.78753
	18.96059	9.428	0.79308
	20.68428	10.159	0.80287
	22.40797	10.827	0.81611
	24.13166	11.436	0.83213
	25.85535	11.990	0.85035
	27.57904	12.496	0.87031
	29.30273	12.959	0.89164
	31.02642	13.385	0.91404
	32.75011	13.779	0.93728
	34.47380	14.143	0.96117
340	3.44738	1.276	0.95587
	5.17107	1.954	0.93594
	6.89476	2.657	0.91792
	8.61845	3.379	0.90221
	10.34214	4.114	0.88919
	12.06583	4.855	0.87918
	13.78952	5.592	0.87238
	15.51321	6.316	0.86889
	17.23690	7.019	0.86869
	18.96059	7.695	0.87162
	20.68428	8.339	0.87744
	22.40797	8.948	0.88584
	24.13166	9.522	0.89651
	25.85535	10.060	0.90912
	27.57904	10.565	0.92340
	29.30273	11.038	0.93909
	31.02642	11.481	0.95597
	32.75011	11.896	0.97386
	34.47380	12.286	0.99260

Table A.3.3. Predicted Density and Compressibility Factor for M94C1 Mixture from REFPROP EOS *(Numbers in italics fall in the two-phase region)*

Molecular weight	17.88421	kg/kmole	
Specific gravity	0.61988		
T_{pc}	206.640	K	
P_{pc}	5.213	MPa	

T	**P**	**ρ**	**Z**	$\mathbf{T_{pr}}$	$\mathbf{P_{pr}}$
K	**MPa**	**kmole/m^3**			
270	*3.44738*	*1.720*	*0.89295*	1.307	*0.661*
	5.17107	*2.747*	*0.83855*		*0.992*
	6.89476	*3.910*	*0.78560*		*1.323*
	8.61845	*5.207*	*0.73732*		*1.653*
	10.34214	*6.599*	*0.69817*		*1.984*
	12.06583	*7.995*	*0.67230*		*2.315*
	13.78952	9.291	0.66115		2.645
	15.51321	10.426	0.66279		2.976
	17.23690	11.395	0.67385		3.307
	18.96059	12.217	0.69133		3.637
	20.68428	12.921	0.71311		3.968
	22.40797	13.530	0.73777		4.299
	24.13166	14.063	0.76437		4.629
	25.85535	14.537	0.79230		4.960
	27.57904	14.961	0.82114		5.291
	29.30273	15.345	0.85060		5.621
	31.02642	15.696	0.88050		5.952
	32.75011	16.019	0.91069		6.283
	34.47380	16.318	0.94107		6.613
290	*3.44738*	*1.558*	*0.91796*	1.403	*0.661*
	5.17107	*2.443*	*0.87801*		*0.992*
	6.89476	*3.404*	*0.84011*		*1.323*
	8.61845	*4.436*	*0.80581*		*1.653*
	10.34214	5.520	0.77700		1.984
	12.06583	6.624	0.75543		2.315
	13.78952	7.705	0.74222		2.645
	15.51321	8.724	0.73747		2.976
	17.23690	9.656	0.74034		3.307
	18.96059	10.492	0.74945		3.637
	20.68428	11.237	0.76339		3.968
	22.40797	11.900	0.78098		4.299
	24.13166	12.490	0.80126		4.629
	25.85535	13.021	0.82354		4.960
	27.57904	13.499	0.84730		5.291
	29.30273	13.934	0.87216		5.621
	31.02642	14.332	0.89785		5.952
	32.75011	14.697	0.92415		6.283
	34.47380	15.035	0.95091		6.613

Table A.3.3. (Continued)

Molecular weight		17.88421	kg/kmole		
Specific gravity		0.61988			
T_{pc}		206.640	K		
P_{pc}		5.213	MPa		
T	**P**	**ρ**	**Z**	**T_{pr}**	**P_{pr}**
K	**MPa**	**kmole/m^3**			
305	*3.44738*	*1.458*	*0.93228*	1.476	*0.661*
	5.17107	2.265	0.90011		0.992
	6.89476	3.125	0.87002		1.323
	8.61845	4.032	0.84301		1.653
	10.34214	4.973	0.82017		1.984
	12.06583	5.929	0.80251		2.315
	13.78952	6.877	0.79077		2.645
	15.51321	7.791	0.78516		2.976
	17.23690	8.654	0.78543		3.307
	18.96059	9.453	0.79094		3.637
	20.68428	10.184	0.80088		3.968
	22.40797	10.850	0.81441		4.299
	24.13166	11.454	0.83078		4.629
	25.85535	12.004	0.84937		4.960
	27.57904	12.505	0.86969		5.291
	29.30273	12.963	0.89135		5.621
	31.02642	13.385	0.91406		5.952
	32.75011	13.774	0.93759		6.283
	34.47380	14.135	0.96174		6.613
340	3.44738	1.275	0.95618	1.645	0.661
	5.17107	1.954	0.93632		0.992
	6.89476	2.656	0.91827		1.323
	8.61845	3.378	0.90243		1.653
	10.34214	4.114	0.88919		1.984
	12.06583	4.856	0.87890		2.315
	13.78952	5.595	0.87180		2.645
	15.51321	6.322	0.86804		2.976
	17.23690	7.028	0.86759		3.307
	18.96059	7.707	0.87032		3.637
	20.68428	8.352	0.87601		3.968
	22.40797	8.963	0.88437		4.299
	24.13166	9.537	0.89506		4.629
	25.85535	10.075	0.90778		4.960
	27.57904	10.579	0.92223		5.291
	29.30273	11.049	0.93812		5.621
	31.02642	11.490	0.95524		5.952
	32.75011	11.902	0.97337		6.283
	34.47380	12.289	0.99235		6.613

Table A.4.1. Predicted Density and Compressibility Factor for M88C1 Mixture from HY EOS *(Numbers in italics fall in the two-phase region)*

Molecular weight	19.15424	kg/kmole	
Specific gravity	0.66390		
T_{pc}	209.472	K	
P_{pc}	4.577	MPa	

T	**P**	**ρ**	**Z**	$\mathbf{T_{pr}}$	$\mathbf{P_{pr}}$
K	**MPa**	**kmole/m^3**			
270	*3.44738*	*1.762*	*0.87175*	1.289	*0.753*
	5.17107	*2.855*	*0.80691*		*1.130*
	6.89476	*4.125*	*0.74474*		*1.506*
	8.61845	*5.567*	*0.68971*		*1.883*
	10.34214	*7.115*	*0.64755*		*2.260*
	12.06583	*8.635*	*0.62256*		*2.636*
	13.78952	9.990	0.61494		3.013
	15.51321	11.125	0.62126		3.389
	17.23690	12.052	0.63719		3.766
	18.96059	12.812	0.65931		4.143
	20.68428	13.446	0.68535		4.519
	22.40797	13.984	0.71391		4.896
	24.13166	14.448	0.74413		5.272
	25.85535	14.855	0.77544		5.649
	27.57904	15.216	0.80749		6.026
	29.30273	15.541	0.84004		6.402
	31.02642	15.835	0.87293		6.779
	32.75011	16.104	0.90604		7.155
	34.47380	16.351	0.93930		7.532
290	*3.44738*	*1.588*	*0.90034*	1.384	*0.753*
	5.17107	*2.517*	*0.85210*		*1.130*
	6.89476	*3.545*	*0.80680*		*1.506*
	8.61845	*4.664*	*0.76648*		*1.883*
	10.34214	*5.848*	*0.73354*		*2.260*
	12.06583	7.048	0.71012		2.636
	13.78952	8.203	0.69729		3.013
	15.51321	9.263	0.69468		3.389
	17.23690	10.203	0.70077		3.766
	18.96059	11.021	0.71363		4.143
	20.68428	11.730	0.73146		4.519
	22.40797	12.346	0.75286		4.896
	24.13166	12.885	0.77682		5.272
	25.85535	13.362	0.80259		5.649
	27.57904	13.788	0.82968		6.026
	29.30273	14.171	0.85772		6.402
	31.02642	14.518	0.88645		6.779
	32.75011	14.835	0.91570		7.155
	34.47380	15.127	0.94531		7.532

Table A.4.1. (Continued)

Molecular weight		19.15424	kg/kmole		
Specific gravity		0.66390			
T_{pc}		209.472	K		
P_{pc}		4.577	MPa		
T	**P**	**ρ**	**Z**	**T_{pr}**	**P_{pr}**
K	**MPa**	**kmole/m^3**			
305	*3.44738*	*1.483*	*0.91676*	1.456	*0.753*
	5.17107	*2.324*	*0.87739*		*1.130*
	6.89476	*3.234*	*0.84081*		*1.506*
	8.61845	*4.205*	*0.80831*		*1.883*
	10.34214	5.221	0.78128		2.260
	12.06583	6.253	0.76103		2.636
	13.78952	7.267	0.74838		3.013
	15.51321	8.229	0.74347		3.389
	17.23690	9.117	0.74569		3.766
	18.96059	9.918	0.75398		4.143
	20.68428	10.634	0.76715		4.519
	22.40797	11.271	0.78410		4.896
	24.13166	11.839	0.80391		5.272
	25.85535	12.347	0.82589		5.649
	27.57904	12.804	0.84948		6.026
	29.30273	13.218	0.87430		6.402
	31.02642	13.596	0.90004		6.779
	32.75011	13.941	0.92649		7.155
	34.47380	14.260	0.95348		7.532
340	3.44738	1.292	0.94420	1.623	0.753
	5.17107	1.991	0.91882		1.130
	6.89476	2.723	0.89571		1.506
	8.61845	3.483	0.87538		1.883
	10.34214	4.263	0.85837		2.260
	12.06583	5.051	0.84516		2.636
	13.78952	5.835	0.83612		3.013
	15.51321	6.601	0.83142		3.389
	17.23690	7.338	0.83103		3.766
	18.96059	8.037	0.83468		4.143
	20.68428	8.691	0.84197		4.519
	22.40797	9.300	0.85244		4.896
	24.13166	9.864	0.86558		5.272
	25.85535	10.384	0.88094		5.649
	27.57904	10.864	0.89813		6.026
	29.30273	11.308	0.91680		6.402
	31.02642	11.719	0.93667		6.779
	32.75011	12.101	0.95752		7.155
	34.47380	12.456	0.97915		7.532

Table A.4.2. Predicted Density and Compressibility Factor for M88C1 Mixture from AGA8-DC92 EOS *(Numbers in italics fall in the two-phase region)*

Molecular weight	19.15424	kg/kmole
Specific gravity	0.66279	

T	P	ρ	Z
K	MPa	kmole/m^3	
270	*3.44738*	*1.761*	*0.87187*
	5.17107	*2.860*	*0.80533*
	6.89476	*4.149*	*0.74024*
	8.61845	*5.625*	*0.68254*
	10.34214	*7.195*	*0.64031*
	12.06583	*8.697*	*0.61802*
	13.78952	10.012	0.61352
	15.51321	11.111	0.62197
	17.23690	12.016	0.63899
	18.96059	12.769	0.66146
	20.68428	13.405	0.68736
	22.40797	13.951	0.71545
	24.13166	14.429	0.74498
	25.85535	14.852	0.77546
	27.57904	15.231	0.80657
	29.30273	15.574	0.83810
	31.02642	15.888	0.86991
	32.75011	16.175	0.90189
	34.47380	16.442	0.93398
290	*3.44738*	*1.585*	*0.90184*
	5.17107	*2.513*	*0.85338*
	6.89476	*3.542*	*0.80730*
	8.61845	*4.666*	*0.76608*
	10.34214	*5.854*	*0.73269*
	12.06583	7.051	0.70967
	13.78952	8.195	0.69789
	15.51321	9.239	0.69636
	17.23690	10.167	0.70312
	18.96059	10.980	0.71617
	20.68428	11.690	0.73382
	22.40797	12.312	0.75479
	24.13166	12.862	0.77813
	25.85535	13.351	0.80317
	27.57904	13.790	0.82942
	29.30273	14.188	0.85655
	31.02642	14.551	0.88431
	32.75011	14.884	0.91254
	34.47380	15.192	0.94110

Table A.4.2. (Continued)

Molecular weight	19.15424	kg/kmole
Specific gravity	0.66279	

T	P	ρ	Z
K	MPa	kmole/m^3	
305	*3.44738*	*1.479*	*0.91887*
	5.17107	*2.318*	*0.87988*
	6.89476	*3.224*	*0.84337*
	8.61845	*4.192*	*0.81081*
	10.34214	5.203	0.78384
	12.06583	6.229	0.76388
	13.78952	7.233	0.75175
	15.51321	8.185	0.74737
	17.23690	9.064	0.74989
	18.96059	9.862	0.75816
	20.68428	10.579	0.77098
	22.40797	11.223	0.78734
	24.13166	11.800	0.80643
	25.85535	12.320	0.82758
	27.57904	12.790	0.85029
	29.30273	13.218	0.87419
	31.02642	13.610	0.89898
	32.75011	13.970	0.92445
	34.47380	14.303	0.95044
340	3.44738	1.288	0.94706
	5.17107	1.982	0.92278
	6.89476	2.708	0.90065
	8.61845	3.460	0.88123
	10.34214	4.229	0.86506
	12.06583	5.006	0.85259
	13.78952	5.778	0.84415
	15.51321	6.534	0.83984
	17.23690	7.262	0.83957
	18.96059	7.955	0.84308
	20.68428	8.608	0.84998
	22.40797	9.219	0.85981
	24.13166	9.788	0.87213
	25.85535	10.317	0.88654
	27.57904	10.807	0.90269
	29.30273	11.263	0.92028
	31.02642	11.687	0.93907
	32.75011	12.082	0.95883
	34.47380	12.451	0.97940

Table A.4.3. Predicted Density and Compressibility Factor for M88C1 Mixture from REFPROP EOS *(Numbers in italics fall in the two-phase region)*

Molecular weight	19.14891	kg/kmole	
Specific gravity	0.66372		
T_{pc}	219.910	K	
P_{pc}	5.890	MPa	

T	**P**	**ρ**	**Z**	$\mathbf{T_{pr}}$	$\mathbf{P_{pr}}$
K	**MPa**	**kmole/m^3**			
270	*3.44738*	*1.758*	*0.87350*	1.228	*0.585*
	5.17107	*2.855*	*0.80697*		*0.878*
	6.89476	*4.145*	*0.74096*		*1.171*
	8.61845	*5.637*	*0.68102*		*1.463*
	10.34214	*7.247*	*0.63571*		*1.756*
	12.06583	*8.790*	*0.61149*		*2.049*
	13.78952	10.117	0.60718		2.341
	15.51321	11.203	0.61683		2.634
	17.23690	12.089	0.63515		2.926
	18.96059	12.821	0.65875		3.219
	20.68428	13.439	0.68560		3.512
	22.40797	13.970	0.71450		3.804
	24.13166	14.434	0.74471		4.097
	25.85535	14.846	0.77577		4.390
	27.57904	15.216	0.80736		4.682
	29.30273	15.552	0.83931		4.975
	31.02642	15.859	0.87146		5.268
	32.75011	16.143	0.90373		5.560
	34.47380	16.406	0.93605		5.853
290	*3.44738*	*1.583*	*0.90308*	1.319	*0.585*
	5.17107	*2.509*	*0.85470*		*0.878*
	6.89476	*3.538*	*0.80816*		*1.171*
	8.61845	*4.667*	*0.76591*		*1.463*
	10.34214	*5.867*	*0.73108*		*1.756*
	12.06583	7.082	0.70657		2.049
	13.78952	8.243	0.69378		2.341
	15.51321	9.298	0.69199		2.634
	17.23690	10.226	0.69909		2.926
	18.96059	11.032	0.71276		3.219
	20.68428	11.734	0.73110		3.512
	22.40797	12.346	0.75271		3.804
	24.13166	12.887	0.77663		4.097
	25.85535	13.367	0.80217		4.390
	27.57904	13.799	0.82888		4.682
	29.30273	14.190	0.85642		4.975
	31.02642	14.547	0.88455		5.268
	32.75011	14.875	0.91311		5.560
	34.47380	15.178	0.94197		5.853

Table A.4.3. (Continued)

Molecular weight		19.14891	kg/kmole		
Specific gravity		0.66372			
T_{pc}		219.910	K		
P_{pc}		5.890	MPa		
T	**P**	**ρ**	**Z**	**T_{pr}**	**P_{pr}**
K	**MPa**	**kmole/m^3**			
305	*3.44738*	*1.478*	*0.91985*	1.387	*0.585*
	5.17107	*2.315*	*0.88095*		*0.878*
	6.89476	*3.221*	*0.84414*		*1.171*
	8.61845	*4.191*	*0.81090*		*1.463*
	10.34214	5.209	0.78298		1.756
	12.06583	6.244	0.76198		2.049
	13.78952	7.260	0.74895		2.341
	15.51321	8.223	0.74397		2.634
	17.23690	9.108	0.74631		2.926
	18.96059	9.907	0.75473		3.219
	20.68428	10.621	0.76793		3.512
	22.40797	11.260	0.78476		3.804
	24.13166	11.831	0.80432		4.097
	25.85535	12.345	0.82592		4.390
	27.57904	12.809	0.84905		4.682
	29.30273	13.231	0.87332		4.975
	31.02642	13.618	0.89846		5.268
	32.75011	13.973	0.92424		5.560
	34.47380	14.302	0.95052		5.853
340	3.44738	1.287	0.94759	1.546	0.585
	5.17107	1.981	0.92339		0.878
	6.89476	2.707	0.90115		1.171
	8.61845	3.459	0.88143		1.463
	10.34214	4.230	0.86482		1.756
	12.06583	5.011	0.85183		2.049
	13.78952	5.787	0.84285		2.341
	15.51321	6.548	0.83805		2.634
	17.23690	7.282	0.83738		2.926
	18.96059	7.979	0.84060		3.219
	20.68428	8.635	0.84734		3.512
	22.40797	9.248	0.85714		3.804
	24.13166	9.817	0.86955		4.097
	25.85535	10.345	0.88414		4.390
	27.57904	10.833	0.90053		4.682
	29.30273	11.287	0.91838		4.975
	31.02642	11.708	0.93744		5.268
	32.75011	12.100	0.95747		5.560
	34.47380	12.465	0.97830		5.853

Table A.5.1. Predicted Density and Compressibility Factor for M78C1 Mixture from HY EOS *(Numbers in italics fall in the two-phase region)*

Molecular weight		21.77743	kg/kmole		
Specific gravity		0.75482			
T_{pc}		225.246	K		
P_{pc}		4.560	MPa		
T	**P**	**ρ**	**Z**	**T_{pr}**	**P_{pr}**
K	**MPa**	**kmole/m^3**			
270	*3.44738*	*1.842*	*0.83403*	1.199	*0.756*
	5.17107	*3.095*	*0.74435*		*1.134*
	6.89476	*4.687*	*0.65535*		*1.512*
	8.61845	*6.624*	*0.57970*		*1.890*
	10.34214	*8.627*	*0.53408*		*2.268*
	12.06583	*10.296*	*0.52208*		*2.646*
	13.78952	11.527	0.53295		3.024
	15.51321	12.432	0.55594		3.402
	17.23690	13.124	0.58512		3.780
	18.96059	13.677	0.61761		4.158
	20.68428	14.135	0.65196		4.536
	22.40797	14.523	0.68739		4.914
	24.13166	14.861	0.72346		5.292
	25.85535	15.159	0.75990		5.670
	27.57904	15.425	0.79656		6.048
	29.30273	15.666	0.83333		6.426
	31.02642	15.886	0.87014		6.804
	32.75011	16.088	0.90693		7.182
	34.47380	16.275	0.94368		7.560
290	*3.44738*	*1.642*	*0.87108*	1.287	*0.756*
	5.17107	*2.661*	*0.80592*		*1.134*
	6.89476	*3.847*	*0.74350*		*1.512*
	8.61845	*5.193*	*0.68840*		*1.890*
	10.34214	*6.636*	*0.64643*		*2.268*
	12.06583	*8.048*	*0.62188*		*2.646*
	13.78952	9.303	0.61481		3.024
	15.51321	10.351	0.62165		3.402
	17.23690	11.206	0.63802		3.780
	18.96059	11.907	0.66049		4.158
	20.68428	12.492	0.68684		4.536
	22.40797	12.987	0.71566		4.914
	24.13166	13.416	0.74611		5.292
	25.85535	13.791	0.77764		5.670
	27.57904	14.125	0.80990		6.048
	29.30273	14.424	0.84264		6.426
	31.02642	14.696	0.87571		6.804
	32.75011	14.944	0.90900		7.182
	34.47380	15.173	0.94243		7.560

Table A.5.1. (Continued)

Molecular weight		21.77743	kg/kmole		
Specific gravity		0.75482			
T_{pc}		225.246	K		
P_{pc}		4.560	MPa		
T	**P**	**ρ**	**Z**	**T_{pr}**	**P_{pr}**
K	**MPa**	**kmole/m^3**			
305	*3.44738*	*1.524*	*0.89209*	1.354	*0.756*
	5.17107	*2.430*	*0.83929*		*1.134*
	6.89476	*3.444*	*0.78948*		*1.512*
	8.61845	*4.561*	*0.74527*		*1.890*
	10.34214	*5.747*	*0.70973*		*2.268*
	12.06583	6.942	0.68552		2.646
	13.78952	8.073	0.67370		3.024
	15.51321	9.087	0.67333		3.402
	17.23690	9.965	0.68219		3.780
	18.96059	10.716	0.69784		4.158
	20.68428	11.357	0.71827		4.536
	22.40797	11.910	0.74202		4.914
	24.13166	12.391	0.76806		5.292
	25.85535	12.815	0.79571		5.670
	27.57904	13.192	0.82449		6.048
	29.30273	13.531	0.85409		6.426
	31.02642	13.838	0.88426		6.804
	32.75011	14.119	0.91484		7.182
	34.47380	14.377	0.94572		7.560
340	3.44738	1.316	0.92688	1.509	0.756
	5.17107	2.049	0.89282		1.134
	6.89476	2.832	0.86142		1.512
	8.61845	3.658	0.83363		1.890
	10.34214	4.515	0.81044		2.268
	12.06583	5.385	0.79278		2.646
	13.78952	6.244	0.78129		3.024
	15.51321	7.071	0.77616		3.402
	17.23690	7.848	0.77708		3.780
	18.96059	8.563	0.78338		4.158
	20.68428	9.214	0.79421		4.536
	22.40797	9.803	0.80871		4.914
	24.13166	10.335	0.82611		5.292
	25.85535	10.816	0.84576		5.670
	27.57904	11.252	0.86716		6.048
	29.30273	11.650	0.88992		6.426
	31.02642	12.013	0.91372		6.804
	32.75011	12.348	0.93834		7.182
	34.47380	12.657	0.96359		7.560

Table A.5.2. Predicted Density and Compressibility Factor for M78C1 Mixture from AGA8-DC92 EOS *(Numbers in italics fall in the two-phase region)*

Molecular weight	21.78290	kg/kmole
Specific gravity	0.75472	

T	P	ρ	Z
K	MPa	kmole/m^3	
270	*3.44738*	*1.866*	*0.82291*
	5.17107	*3.190*	*0.72212*
	6.89476	*4.952*	*0.62023*
	8.61845	*7.048*	*0.54472*
	10.34214	*8.983*	*0.51282*
	12.06583	*10.515*	*0.51116*
	13.78952	11.665	0.52657
	15.51321	12.537	0.55122
	17.23690	13.219	0.58083
	18.96059	13.774	0.61317
	20.68428	14.240	0.64706
	22.40797	14.639	0.68185
	24.13166	14.989	0.71715
	25.85535	15.301	0.75273
	27.57904	15.581	0.78845
	29.30273	15.837	0.82420
	31.02642	16.072	0.85993
	32.75011	16.289	0.89559
	34.47380	16.492	0.93116
290	*3.44738*	*1.652*	*0.86536*
	5.17107	*2.697*	*0.79510*
	6.89476	*3.935*	*0.72667*
	8.61845	*5.355*	*0.66745*
	10.34214	*6.847*	*0.62642*
	12.06583	*8.249*	*0.60665*
	13.78952	9.464	0.60430
	15.51321	10.476	0.61417
	17.23690	11.309	0.63211
	18.96059	12.002	0.65520
	20.68428	12.586	0.68156
	22.40797	13.089	0.71003
	24.13166	13.527	0.73988
	25.85535	13.914	0.77066
	27.57904	14.261	0.80204
	29.30273	14.574	0.83384
	31.02642	14.860	0.86590
	32.75011	15.123	0.89813
	34.47380	15.366	0.93044

Table A.5.2. (Continued)

Molecular weight	21.78290	kg/kmole
Specific gravity	0.75472	

T	P	ρ	Z
K	MPa	kmole/m^3	
305	*3.44738*	*1.529*	*0.88884*
	5.17107	*2.448*	*0.83315*
	6.89476	*3.486*	*0.78001*
	8.61845	*4.636*	*0.73310*
	10.34214	*5.853*	*0.69678*
	12.06583	7.059	0.67406
	13.78952	8.179	0.66485
	15.51321	9.175	0.66677
	17.23690	10.039	0.67705
	18.96059	10.783	0.69336
	20.68428	11.425	0.71391
	22.40797	11.983	0.73740
	24.13166	12.473	0.76295
	25.85535	12.907	0.78993
	27.57904	13.296	0.81792
	29.30273	13.648	0.84663
	31.02642	13.969	0.87586
	32.75011	14.263	0.90545
	34.47380	14.535	0.93529
340	3.44738	1.316	0.92685
	5.17107	2.050	0.89234
	6.89476	2.835	0.86045
	8.61845	3.663	0.83232
	10.34214	4.522	0.80911
	12.06583	5.391	0.79178
	13.78952	6.247	0.78087
	15.51321	7.068	0.77637
	17.23690	7.840	0.77777
	18.96059	8.552	0.78426
	20.68428	9.204	0.79493
	22.40797	9.798	0.80897
	24.13166	10.338	0.82571
	25.85535	10.829	0.84456
	27.57904	11.277	0.86509
	29.30273	11.687	0.88692
	31.02642	12.064	0.90979
	32.75011	12.411	0.93345
	34.47380	12.733	0.95774

Table A.5.3. Predicted Density and Compressibility Factor for M78C1 Mixture from REFPROP EOS *(Numbers in italics fall in the two-phase region)*

Molecular weight		21.77849	kg/kmole		
Specific gravity		0.75486			
T_{pc}		242.370	K		
P_{pc}		6.682	MPa		
T	**P**	**ρ**	**Z**	**T_{pr}**	**P_{pr}**
K	**MPa**	**kmole/m^3**			
270	*3.44738*	*1.854*	*0.82839*	1.114	*0.516*
	5.17107	*3.155*	*0.73008*		*0.774*
	6.89476	*4.892*	*0.62786*		*1.032*
	8.61845	*7.058*	*0.54392*		*1.290*
	10.34214	*9.097*	*0.50642*		*1.548*
	12.06583	*10.605*	*0.50683*		*1.806*
	13.78952	11.685	0.52569		2.064
	15.51321	12.494	0.55307		2.322
	17.23690	13.133	0.58464		2.580
	18.96059	13.658	0.61838		2.838
	20.68428	14.104	0.65329		3.096
	22.40797	14.491	0.68884		3.354
	24.13166	14.833	0.72472		3.611
	25.85535	15.139	0.76075		3.869
	27.57904	15.418	0.79680		4.127
	29.30273	15.673	0.83282		4.385
	31.02642	15.909	0.86876		4.643
	32.75011	16.128	0.90457		4.901
	34.47380	16.332	0.94026		5.159
290	*3.44738*	*1.644*	*0.86952*	1.197	*0.516*
	5.17107	*2.679*	*0.80067*		*0.774*
	6.89476	*3.903*	*0.73257*		*1.032*
	8.61845	*5.322*	*0.67164*		*1.290*
	10.34214	*6.838*	*0.62723*		*1.548*
	12.06583	*8.269*	*0.60519*		*1.806*
	13.78952	9.485	0.60295		2.064
	15.51321	10.476	0.61413		2.322
	17.23690	11.284	0.63351		2.580
	18.96059	11.953	0.65787		2.838
	20.68428	12.517	0.68532		3.096
	22.40797	13.003	0.71470		3.354
	24.13166	13.428	0.74531		3.611
	25.85535	13.805	0.77673		3.869
	27.57904	14.144	0.80865		4.127
	29.30273	14.452	0.84089		4.385
	31.02642	14.734	0.87332		4.643
	32.75011	14.994	0.90586		4.901
	34.47380	15.235	0.93844		5.159

Table A.5.3. (Continued)

Molecular weight		21.77849	kg/kmole		
Specific gravity		0.75486			
T_{pc}		242.370	K		
P_{pc}		6.682	MPa		
T	**P**	**ρ**	**Z**	**T_{pr}**	**P_{pr}**
K	**MPa**	**kmole/m^3**			
305	*3.44738*	*1.524*	*0.89218*	1.258	*0.516*
	5.17107	*2.435*	*0.83752*		*0.774*
	6.89476	*3.465*	*0.78465*		*1.032*
	8.61845	*4.611*	*0.73698*		*1.290*
	10.34214	*5.835*	*0.69899*		*1.548*
	12.06583	7.055	0.67445		1.806
	13.78952	8.186	0.66423		2.064
	15.51321	9.182	0.66625		2.322
	17.23690	10.036	0.67730		2.580
	18.96059	10.765	0.69457		2.838
	20.68428	11.391	0.71604		3.096
	22.40797	11.935	0.74037		3.354
	24.13166	12.412	0.76666		3.611
	25.85535	12.836	0.79429		3.869
	27.57904	13.217	0.82285		4.127
	29.30273	13.561	0.85207		4.385
	31.02642	13.876	0.88174		4.643
	32.75011	14.165	0.91171		4.901
	34.47380	14.433	0.94190		5.159
340	3.44738	1.313	0.92887	1.403	0.516
	5.17107	2.044	0.89498		0.774
	6.89476	2.825	0.86330		1.032
	8.61845	3.651	0.83495		1.290
	10.34214	4.510	0.81118		1.548
	12.06583	5.382	0.79311		1.806
	13.78952	6.242	0.78147		2.064
	15.51321	7.068	0.77640		2.322
	17.23690	7.842	0.77750		2.580
	18.96059	8.555	0.78397		2.838
	20.68428	9.205	0.79488		3.096
	22.40797	9.794	0.80934		3.354
	24.13166	10.328	0.82656		3.611
	25.85535	10.812	0.84593		3.869
	27.57904	11.253	0.86696		4.127
	29.30273	11.656	0.88928		4.385
	31.02642	12.027	0.91259		4.643
	32.75011	12.368	0.93667		4.901
	34.47380	12.685	0.96135		5.159

APPENDIX B

DIMENSIONS OF THE MAGNETIC SUSPENSION ASSEMBLY PARTS AND THE MAGNETIC SUSPENSION DENSITOMETER CELL

Table B.1. Dimensions of the MSA Parts and the Cell

Serial No.	Description of dimension	Dimension mm
	Permanent magnet piece	
1	Height between the permanent magnet top surface and the permanent magnet shaft tip	83.9
2	Height of the permanent magnet	12.3
3	Height of the permanent magnet shaft	71.6
4	Diameter of the permanent magnet	11.3
5	Diameter of the hollow shaft connecting the permanent magnet to the bearing cone piece	2.6
	Sinker	
6	Height of the sinker	30.7
7	Outer diameter of the sinker	18.2
8	Inner diameter of the sinker	5.0
	Bearing cone piece	
9	Height between the tip of the bearing cone including the threads and the sensor core tip	49.9
10	Height of the threaded part of the bearing cone piece	4.1
11	Height of the conical part of the bearing cone piece	2.4
12	Height (thickness) of plate below cone on the bearing cone piece	1.6
13	Height of the shaft with bigger diameter on the bearing cone piece	29.0
14	Height of the shaft with smaller diameter on the bearing cone piece (sensor core)	15.4
15	Height of the bearing cone piece that suspends from the cell flange into the tube surrounded by the sensor coil	43.8
16	Diameter of the bearing cone plate	8.6
17	Diameter of the shaft under the bearing cone plate	2.7
18	Diameter of the sensor core on the bearing cone piece	2.4

Table B.1. (Continued)

Serial No.	Description of dimension	Dimension mm
	Permanent magnet and bearing cone piece together	
19	Height between the permanent magnet top surface and the bearing cone plate bottom with the bearing cone and the permanent magnet pieces completely engaged	86.6
20	Height between the permanent magnet top surface and the bearing cone plate bottom with the bearing cone and the permanent magnet pieces completely disengaged	90.8
21	Rubotherm's recommended distance between the permanent magnet top surface and the bearing cone plate bottom	93.3
	Permanent magnet piece, bearing cone piece, cell flange and cell together	
22	Height available for vertical movement of permanent magnet and bearing cone piece assembly	93.5
	Cell flange and the tube surrounded by the sensor coil	
23	Depth of the tubing for the shaft of the bearing cone piece and the sensor core	50.3
24	Height of the stainless steel flange protrusion into the copper beryllium cell measured from the flange face that touches the cell bottom face	9.8
25	Height from the flange face, of the surface upon which the bearing cone plate rests when the MSA control is 'off'	4.1
26	Inner diameter of the well in the protrusion of the stainless steel flange into which the bearing cone plate rests when the MSA control is 'off'	13.3
27	Diameter of the tube surrounded by the sensor coil in which the senor core moves vertically	5.7

Table B.1. (Continued)

Serial No.	Description of dimension	Dimension mm
	Cell from the permanent magnet side	
28	Inner diameter of the cell around the permanent magnet	16.5
29	Estimated inner diameter of the cell around the sinker	20.5
30	Inner diameter of the cell around the stainless steel flange protrusion	18.4
31	Well depth at the center from the copper beryllium cell face	97.6
32	Well depth from the cell face to the step after the sinker (above the sinker when cell is held upright)	47.1
33	Well depth from the cell face to the step before the sinker (below the sinker when cell is held upright)	9.1
34	Height available in the permanent magnet well for sinker movement by buoyancy lift	37.3
	Cell from the electromagnet side	
35	Electromagnet well depth at the center from the cell surface which touches the bottom surface of the thermostating flange	68.7
36	Electromagnet well depth along the circumference from the cell surface which touches the bottom surface of the thermostating flange	67.3
37	Height between the cell top surface that flushes with the thermostating flange top surface and the reference plane for measuring depths of the electromagnet well	10.3
38	Diameter of the electromagnet well	25.6

Table B.1. (Continued)

Serial No.	Description of dimension	Dimension mm
	Cell as a whole unit	
39	Height of the cell from the copper beryllium cell face in contact with the stainless steel flange to the face that flushes with the thermostating flange top surface, measured at the outer circumference	183.4
40	Thickness of the cell wall at the center of the cell	6.7
41	Thickness of the cell wall measured at the circumference of the electromagnet well wall	8.2
	Thermostating flange and electromagnet extension tube	
42	Height of the thermostating flange	10.3
43	Inner diameter of the thermostating tube at the thermostating flange through which the electromagnet suspension tubing passes	10.5
	Electromagnet suspension tube and electromagnet	
44	Height between electromagnet suspension tube end that engages with threads and the bottom end of the suspension tube	Not measured
45	Height of the electromagnet without the shaft extension at its bottom	13.3
46	Height of the electromagnet with the shaft extension at its bottom	15.8
47	Height between the electromagnet bottom surface and the bottom end of the suspension tube	2.5
48	Outer diameter of the electromagnet suspension tube	4.6
49	Diameter of the electromagnet	21.5

APPENDIX C

TEMPERATURE DEPENDENCE OF PRESSURE TRANSDUCER CALIBRATION COEFFICIENTS

Table C.1. Observed Pressure and Internal Temperature Period Ranges between Ambient Temperature and 80 °C under Vacuum and Pressure Conditions for PT02K and PT06K

PT02K				PT06K			
T °C	X µs	P psia	τ µs	T °C	X µs	P psia	τ µs
21.590	5.867956	vacuum	30.178964	22.678	5.866151	vacuum	30.030631
		1758.087	27.115212			5010.901	27.254405
79.914	5.851830	vacuum	30.174341	80.392	5.850123	vacuum	30.031905
		1754.558	27.115400			5008.490	27.254764

Table C.2. Manufacturer's Calibration Coefficients and Equations for PT02K and PT06K

Manufacturer's calibration coefficients				Equations from calibration certificate
	PT02K	PT06K	Unit	
U_o	5.873541	5.872036	µs	**Temperature coefficients:**
Y_1	-3930.171	-3921.533	°C/µs	X = temperature period (µs)
Y_2	-11485.22	-11539.00	°C/µs^2	$U = X - U_o$
Y_3	0	0		Temperature (°C): $T = Y_1U + Y_2U^2 + Y_3U^3$
C_1	-7273.990	-23214.56	psia	**Pressure coefficients:**
C_2	346.9426	564.4182	psia/µs	τ = pressure period (µs)
C_3	18114.01	73606.34	psia/µs^2	$C = C_1 + C_2U + C_3U^2$
D_1	0.050502	0.037428	-	$D = D_1 + D_2U$
D_2	0	0	-	$\tau_o = \tau_1 + \tau_2U + \tau_3U^2 + \tau_4U^3 + \tau_5U^4$
τ_1	30.18612	30.03705	µs	Pressure (psia):
τ_2	1.516436	1.415628	µs/µs	
τ_3	47.20004	59.87418	µs/µs^2	$P = C * \left(1 - \frac{\tau_o^2}{\tau^2}\right) * \left(1 - D * \left(1 - \frac{\tau_o^2}{\tau^2}\right)\right)$
τ_4	81.02094	190.20780	µs/µs^3	
τ_5	0	0	-	

Table C.3.1. Temperature Dependence of Pressure from Observed Pressure and Internal Temperature Periods and Manufacturer's Calibration Coefficients for PT02K

X	T	τ	Pressure	
			P	$P-P_{minimum}$
µs	°C	µs	psia	
5.867956	21.592	30.178964	0.070	2.660
		29.668339	253.105	2.781
		29.157713	520.507	2.909
		28.647088	803.399	3.045
		28.136463	1103.014	3.192
		27.625837	1420.714	3.375
		27.115212	1758.003	3.570
5.865268	31.727	30.178964	-1.063	1.527
		29.668339	251.938	1.614
		29.157713	519.303	1.705
		28.647088	802.156	1.802
		28.136463	1101.730	1.909
		27.625837	1419.386	2.047
		27.115212	1756.628	2.195
5.862581	41.696	30.178964	-1.881	0.710
		29.668339	251.088	0.764
		29.157713	518.420	0.822
		28.647088	801.238	0.884
		28.136463	1100.774	0.953
		27.625837	1418.390	1.051
		27.115212	1755.590	1.156
5.859893	51.500	30.178964	-2.389	0.202
		29.668339	250.552	0.228
		29.157713	517.854	0.256
		28.647088	800.639	0.285
		28.136463	1100.141	0.319
		27.625837	1417.721	0.382
		27.115212	1754.882	0.448
5.857205	61.137	30.178964	**-2.590**	0.000
		29.668339	**250.324**	0.000
		29.157713	**517.598**	0.000
		28.647088	**800.354**	0.000
		28.136463	1099.825	0.004
		27.625837	1417.372	0.033
		27.115212	1754.498	0.065
5.854518	70.609	30.178964	-2.491	0.099
		29.668339	250.399	0.076
		29.157713	517.649	0.051
		28.647088	800.378	0.024
		28.136463	**1099.821**	0.000
		27.625837	**1417.339**	0.000
		27.115212	**1754.433**	0.000
5.851830	79.914	30.178964	-2.095	0.495
		29.668339	250.774	0.450
		29.157713	518.001	0.402
		28.647088	800.706	0.352
		28.136463	1100.124	0.303
		27.625837	1417.615	0.276
		27.115212	1754.682	0.248

Table C.3.2. Temperature Dependence of Pressure from Observed Pressure and Internal Temperature Periods and Manufacturer's Calibration Coefficients for PT06K

X	T	τ	Pressure	
			P	$P-P_{minimum}$
µs	°C	µs	psia	
5.866151	22.679	30.031905	-1.780	3.591
		29.568988	731.609	3.939
		29.106072	1502.125	4.304
		28.643155	2312.343	4.689
		28.180238	3165.065	5.095
		27.717322	4063.349	5.522
		27.254405	5010.536	5.973
5.863480	32.709	30.031905	-4.179	1.191
		29.568988	729.086	1.416
		29.106072	1499.472	1.651
		28.643155	2309.553	1.899
		28.180238	3162.131	2.160
		27.717322	4060.263	2.435
		27.254405	5007.288	2.725
5.860808	42.575	30.031905	-5.365	0.006
		29.568988	727.785	0.114
		29.106072	1498.050	0.229
		28.643155	2308.002	0.349
		28.180238	3160.446	0.475
		27.717322	4058.436	0.608
		27.254405	5005.311	0.748
5.858137	52.276	30.031905	**-5.370**	0.000
		29.568988	**727.671**	0.000
		29.106072	**1497.821**	0.000
		28.643155	**2307.654**	0.000
		28.180238	**3159.971**	0.000
		27.717322	**4057.828**	0.000
		27.254405	**5004.563**	0.000
5.855466	61.813	30.031905	-4.230	1.140
		29.568988	728.708	1.037
		29.106072	1498.750	0.929
		28.643155	2308.469	0.815
		28.180238	3160.667	0.696
		27.717322	4058.398	0.571
		27.254405	5005.001	0.438
5.852794	71.185	30.031905	-1.979	3.391
		29.568988	730.861	3.190
		29.106072	1500.800	2.979
		28.643155	2310.411	2.757
		28.180238	3162.495	2.524
		27.717322	4060.106	2.279
		27.254405	5006.583	2.021
5.850123	80.392	30.031905	1.349	6.719
		29.568988	734.094	6.423
		29.106072	1503.934	6.112
		28.643155	2313.440	5.786
		28.180238	3165.414	5.444
		27.717322	4062.911	5.084
		27.254405	5009.267	4.705

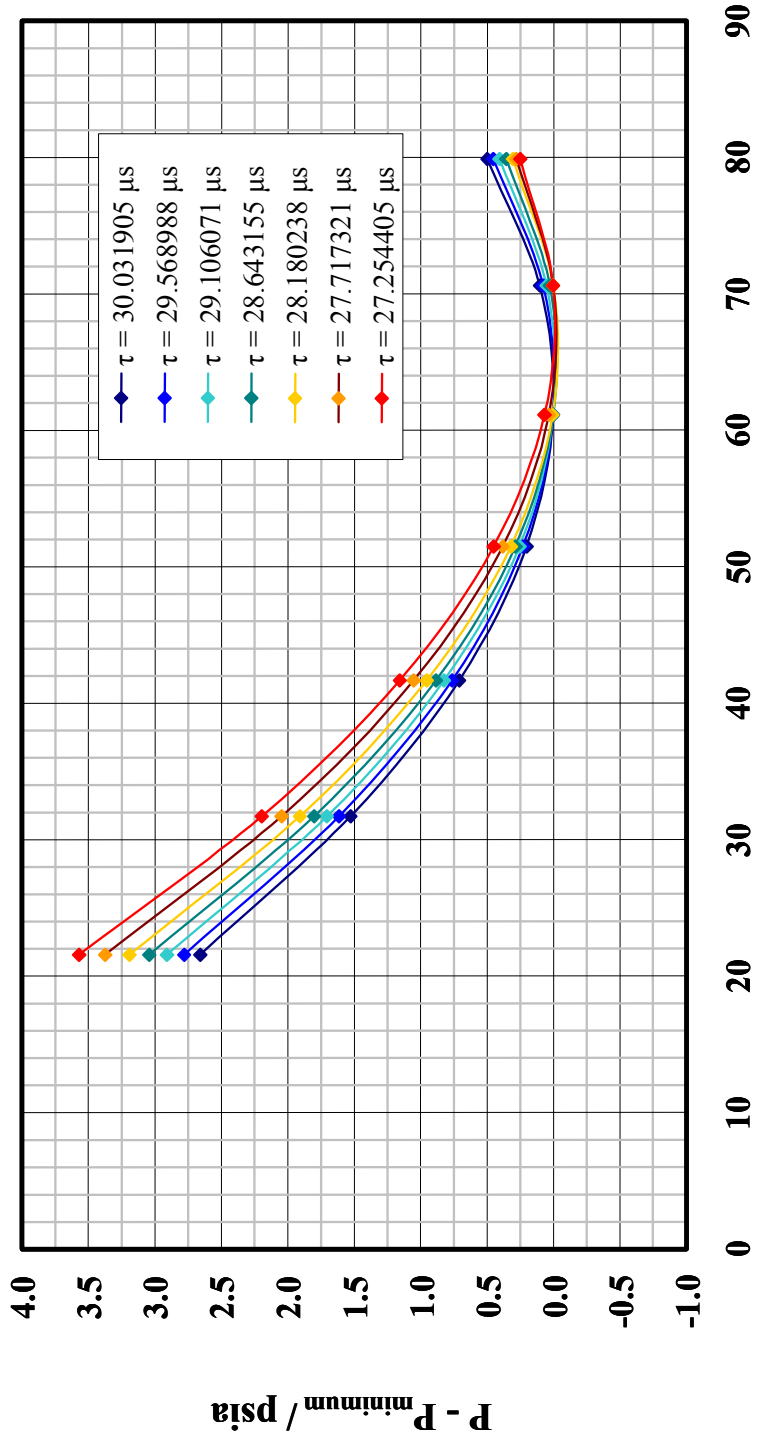

Figure C.1. Choice of Internal Temperature of 66 °C for PT02K Based on Temperature Dependence of Pressure

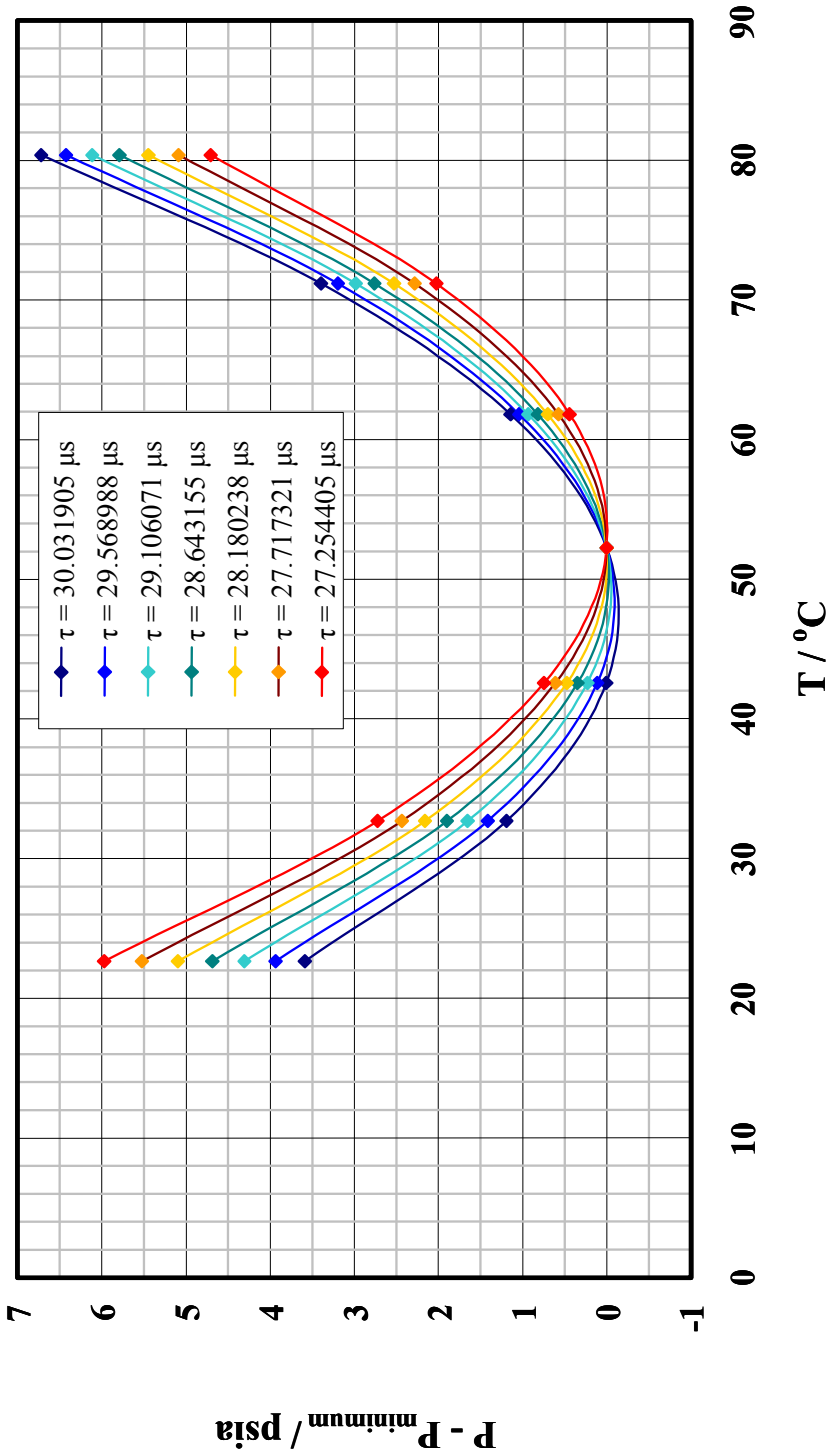

Figure C.2. Choice of Internal Temperature of 52 oC for PT06K Based on Temperature Dependence of Pressure

APPENDIX D

EQUATIONS AND CONSTANTS OF ITS – 90 FOR RESISTANCE TO TEMPERATURE CONVERSION

ITS-90 expresses the temperature in Kelvin in terms of the ratio of the measured resistance of the PRT at the temperature and its resistance at 273.16 K [0.01 ^{o}C] which is the triple point of water as:

$$W(T) = \frac{R(T)}{R(273.16\mathrm{K})} \qquad \text{D.1}$$

The deviation equation given by equation D.2 and reference function given by equation D.3 is used to calculate the temperature, for temperatures below 273.16 K.

$$W_{\mathrm{ref}}(T) = W(T) - a_4[W(T)-1] - b_4[W(T)-1]\ln W(T) \qquad \text{D.2}$$

$$\frac{T}{273.16K} = B_0 + \sum_{1}^{15} B_i \left[\frac{W_{\mathrm{ref}}(T)^{1/6} - 0.65}{0.35}\right]^i \qquad \text{D.3}$$

The deviation equation given by equation D.4 and reference function given by equation D.5 is used to calculate the temperature, for temperatures at and above 273.16 K.

$$W_{\mathrm{ref}}(T) = W(T) - a_8[W(T)-1] - b_8[W(T)-1]^2 \qquad \text{D.4}$$

$$T - 273.15K = D_0 + \sum_{1}^{9} D_i \left[\frac{W_{\mathrm{ref}}(T) - 2.64}{1.64}\right]^i \qquad \text{D.5}$$

The constants a_4, b_4, a_8 and b_8 were determined by Minco by calibrating the PRT at fixed temperature points defined by ITS-90. These constants and values of the constants B_i and D_i are given in Table D.1. The resistance of the PRT at the triple

point of water measured during the original calibration done by Minco on November 16, 2004 was R (273.16K) = 100.4244 Ω.

Table D.1. Constants in Deviation Equations and Reference Functions of ITS-90

a_4	-0.000418264140	B_0	0.183324722
b_4	0.000080228227	B_1	0.240975303
a_8	-0.000568113400	B_2	0.209108771
b_8	0.000260761350	B_3	0.190439972
		B_4	0.142648498
		B_5	0.077993465
D_0	439.932854	B_6	0.012475611
D_1	472.418020	B_7	-0.032267127
D_2	37.6844940	B_8	-0.075291522
D_3	7.472018	B_9	-0.056470670
D_4	2.920828	B_{10}	0.076201285
D_5	0.005184	B_{11}	0.123893204
D_6	-0.963864	B_{12}	-0.029201193
D_7	-0.188732	B_{13}	-0.091173542
D_8	0.191203	B_{14}	0.001317696
D_9	0.049025	B_{15}	0.026025526

APPENDIX E

EFFECT OF CURRENT REVERSAL AND PRT CABLE SHIELD GROUNDING ON MEASURED TEMPERATURE

Table E.1. Effect of Current Reversal on Measured Resistance of PRT

Approximate cell temperature	Test number	R_{PRT}						
		with current reversal		with positive current only		with negative current only		
		Average$^{+/-}$	Standard deviation$^{+/-}$	Average^{+}	Standard deviation^{+}	Average^{-}	Standard deviation^{-}	(Average^{+} - Average^{-})/2
K		Ω	± mΩ	Ω	± mΩ	Ω	± mΩ	± mΩ
340	1	126.923116	0.970	126.923656	0.939	126.922576	0.674	0.540
	2	126.923192	0.850	126.923522	0.604	126.922861	0.959	0.331
	3	126.922308	0.937	126.922732	0.870	126.921883	0.834	0.424
305	1	113.374088	2.693	113.372483	1.739	113.375922	2.457	1.720
	2	113.386617	2.466	113.385882	2.204	113.387353	6.571	0.735
	3	113.385042	2.659	113.384346	2.101	113.385738	3.072	0.696
294	1	108.698865	3.085	108.701715	1.147	108.696016	0.899	2.850
270	1	99.186161	1.502	99.185354	1.121	99.187025	1.473	0.835
	2	99.190189	1.517	99.189869	1.324	99.190556	1.433	0.343
± 10 mK = ± 3.925 mΩ								

Table E.2. Effect of Current Reversal on Measured Voltage Drop across PRT

Approximate cell temperature	Test number	V_{PRT} with current reversal	V_{PRT} with positive current only	V_{PRT} with negative current only	
		Average$^{+/-}$	Average^{+}	Average^{-}	(Average^{+} - Average^{-})/2
K		mV	mV	mV	± μV
340	1	126.923116	126.923656	126.922576	0.540
	2	126.923192	126.923522	126.922861	0.331
	3	126.922308	126.922732	126.921883	0.424
305	1	113.374088	113.372483	113.375922	1.720
	2	113.386617	113.385882	113.387353	0.735
	3	113.385042	113.384346	113.385738	0.696
294	1	108.698865	108.701715	108.696016	2.850
270	1	99.186161	99.185354	99.187025	0.835
	2	99.190189	99.189869	99.190556	0.343
± 10 mK = ± 3.925 μV					

Table E.3. Effect of Current Reversal on Measured Cell Temperature

T								
Approximate cell temperature	Test number	with current reversal		with positive current only		with negative current only		
		Average$^{+/-}$	Standard deviation$^{+/-}$	Average^{+}	Standard deviation^{+}	Average^{-}	Standard deviation^{-}	(Average^{+} - Average^{-})/2
K		K	mK	K	mK	K	mK	± mK
340	1	340.029	2.472	340.030	2.395	340.027	1.718	1.377
	2	340.029	2.168	340.030	1.539	340.028	2.444	0.843
	3	340.027	2.389	340.028	2.218	340.026	2.127	1.082
305	1	305.668	6.794	305.664	4.386	305.673	6.199	4.338
	2	305.700	6.222	305.698	5.559	305.702	6.571	1.854
	3	305.696	6.709	305.694	5.300	305.698	7.751	1.756
294	1	293.895	7.756	293.902	2.884	293.888	2.260	7.163
270	1	270.069	3.748	270.067	2.796	270.071	3.677	2.085
	2	270.079	3.784	270.078	3.949	270.080	3.575	0.914

APPENDIX F

VIDEO CLIPS OF MAGNETIC SUSPENSION ASSEMBLY OPERATION

Table F.1. Description of Video Clips of MSA Coverage in Digital Video Disc (DVD)

Title number	Clip number	Clock time (hour:minute:second)		Focus on	Description of clip coverage
		From	To		
1	1	0:00:00	0:07:03	Overall MSA: electromagnet, permanent magnet, permanent magnet shaft, sinker and sinker rest	
1	2	0:07:04	0:13:32	Close-up: electromagnet and permanent magnet	- SC switched 'on' ZP position - SC 'on' sinker raised to MP position - SC 'on' sinker lowered to ZP position - SC switced 'off'
1	3	0:13:33	0:18:13	Close-up: permanent magnet shaft, sinker and sinker rest	
1	4	0:18:14	0:24:59	Close-up: electromagnet, permanent magnet, permanent magnet shaft and sinker	
2	5	0:00:00	0:34:34	Close-up: electromagnet suspension tube, electromagnet, permanent magnet and permanent magnet shaft	- begins with SC 'on' ZP position - SC 'on' sinker raised to MP position - balance frame moved horizontally so that electromagnet suspension tube moved to front, back, right and left from central position by half a mm - SC 'on' sinker lowered to ZP position - SC switched 'off'
2	6	0:34:35	0:59:51	Close-up: permanent magnet shaft, sinker and sinker rest	- SC switched 'on' ZP position - SC 'on' sinker raised to MP position - balance frame moved horizontally so that electromagnet suspension tube moved to front, back, right and left from central position by half a mm - SC 'on' sinker lowered to ZP position - SC switced 'off'
2	7	0:59:52	1:21:12	Close-up: permanent magnet, permanent magnet shaft, sinker and sinker rest	- SC switched 'on' ZP position - SC 'on' sinker raised to MP position - SC 'on' sinker lowered to ZP position - SC switced 'off' - repeated thrice to check if MSA parts align with multiple cycles

APPENDIX G

PROCEDURE FOR PURE COMPONENT ISOTHERM MEASUREMENT

(1) Switch ‘on’ the trace heaters on the tubing and the old and new manifold heating bulb banks and allow their temperatures to equilibrate to values at which they would be maintained during density measurement of gas mixtures. Although heating the tubing and the manifold is not necessary for pure component density measurements, they are heated and maintained at temperatures above the CT of the gas mixture whose density is to be measured to simulate conditions during natural gas density measurements. An equilibration period of several hours may be needed depending upon the ambient temperature.

(2) Switch the aluminum block heaters and controllers for PT02K and PT06K ‘on’ so that they are maintained at 339.15 K [150.8 ^{o}F, 66 ^{o}C] and 325.15 K [125.6 ^{o}F, 52 ^{o}C] respectively. Once these temperatures are attained, the aluminum block heaters and controllers are left ‘on’ even after completing measurements.

(3) Adjust the regulator valve on the nitrogen cylinder for a pressure of approximately 40 psia so that nitrogen is constantly bled into the PRT isolation tube.

(4) Start the Paroscientific ‘digiquartz assistant’ data acquisition programs for PT02K and PT06K for pressure readings with a frequency of 1 reading per minute or higher over a period of 24 hours.

(5) Ensure that the Keithley DMM is in the ‘rear’ measurement mode so that the PRT resistance measurements are made from the scanner card. Start the LabVIEW data acquisition program for the PRT resistance with the same frequency of data acquisition as used for pressure measurements.

(6) Ensure that the manual/PC switch on the weight changing device control box is switched to the PC position, the SC switch on the MSA control box is ‘off’ and the ZP/MP switch on the MSA control box is switched to the ZP position. Start the Messpro program for the MSA control and weighing balance reading data acquisition. Choose the following options on the configuration tab of Messpro: ‘automatic’ for scaling, ‘yes’ for forerun, ‘yes’ for calibration before measurement, ‘1’ for number of segments, ‘24 hours’ for duration of time based

segment. On the balance tab, choose ‘yes’ for record ZP, ‘10 minutes’ for ZP (min), ‘yes’ for ZP correction, ‘yes’ for draw ZP, ’60 seconds’ for settle time (sec) and a period in seconds equal to the data acquisition frequency used for pressure and PRT resistance measurement for interval time (sec). On the ending requirement tab choose ‘24 hours’ or the period over which the MSA control is desired to be operational. Click ‘start measurement’ to start the MSA control while the cell is at ambient pressure and temperature.

(7) Switch the Keithley DMM for cell axial temperature gradient measurement ‘on’ and in automatic voltage measurement mode.

(8) Start the flow of the heating/cooling liquid between the constant temperature circulation bath and the MSD cell bath after adjusting the set-point temperature to the desired isotherm temperature. Lower the clamp on the aluminum stand so that the liquid level in the cell bath is only about a cm above the top surface of the cell.

(9) Close valves V2, V4, V5, V12, V13 and open valves V9, V10, V11, V6 and V7 on the old manifold. Open valve VSC of the sample cylinder, SC, fill the suction line of the compressor up to the cylinder pressure and then close VSC. The cylinder pressure should be higher than the suction pressure requirement of the compressor. Operate the compressor by opening the valve on the air line driving its piston so that the pressure in the hand pump, HP1 increases. Continue operating the compressor until the pressure in its suction line drops to a pressure slightly above its minimum suction pressure. Open VSC and refill the compressor suction line, close VSC and operate the compressor to increase the pressure in HP1. Draw the piston of HP1 outside its cylinder and charge the pure gas sample into HP1 up to around 10.342 MPa [1,500 psia] always making sure that the compressor suction pressure never drops below its minimum required value and that the compressor is never operated with VSC open which may contaminate the entire cylinder due to back pressure build-up in the suction line. Use the bourdon gauge, GB for crudely knowing the pressure in HP1. Close V10

so that the section of the old manifold between V10 and V5 is filled with gas sample which may be contaminated with pre-existing air in the old manifold tubing.

(10) Close valves VG2K and VG6K and open valves VS2K and VS6K on the new manifold. Close VI1 and open V5 slightly so that the cell pressure gradually increases without disturbing the stability of either the permanent magnet/bearing cone piece in ZP position or the sinker and the permanent magnet/bearing cone piece in MP position. As the pressure in the old manifold section between V10 and V5 decreases, draw the piston of HP1 into its cylinder. If the cell pressure is lower than 10.342 MPa [1,500 psia] and the piston of HP1 is completely drawn into its cylinder, the pressure cannot be increased without more compression. However, operating the compressor directly to increase the cell pressure by keeping both V10 and V5 can cause the MSA parts to destabilize because of the force of the charged gas. Instead, close V5, draw the piston of HP1 completely out of its cylinder, open V10 and charge fresh feed into HP1 by repeating step (9). Close V10 and open V5 slightly and increase the cell pressure to a pressure close to 10.342 MPa [1,500 psia].

(11) Close V5, switch the vacuum pump, VP1 ‘on’, open V14 and then open VI1 to purge the first batch of contaminated gas from the MSD cell. Evacuate the cell until the vacuum thermocouple gauge, GTV1 indicates a reading close to 13.3 Pa [100 mTorr]. Repeat steps (9) and (10) twice to purge the manifold tubing and the MSD cell of the gas sample contaminated with air. While the MSD cell is purged of the earlier contaminated gas it also reaches the desired isotherm temperature.

(12) After the third purge, raise the clamp on the aluminum support to raise the level of the heating/cooling liquid in the cell bath to at least 5 cm above the top surface of the MSD cell, evacuate the cell until GTV1 indicates a vacuum of approximately (1.33 to 2.67) Pa [(10 to 20) mTorr]. Allow a period of at least 8

hours for the final evacuation and thermal equilibration of the cell indicated by stable voltage readings across the thermopile.

(13) Select a period of approximately 30 to 40 minutes immediately following a ZP position balance reading check for measuring the true mass of the sinker in vacuum at the isotherm temperature and manually change the direction of the current through the PRT manually at the frequency of data acquisition.

(14) Stop the MSA control, PRT resistance and PT02K and PT06K pressure data acquisition programs at the end of the 30 to 40 minute period.

(15) Close VI1 and V14 and switch VP1 ‘off’ and restart the pressure, PRT resistance, MSA control and weighing balance data acquisition programs as done previously in steps (4), (5) and (6).

(16) After three purges, the gas in the old manifold section between V10 and V5 is pure gas. Open V5 slightly and increase the pressure in the MSD cell to approximately 3.447 MPa [500 psia]. If needed, draw more pure gas from SC into HP1 as described in step (9) first and then open V5 slightly to reach 3.447 MPa [500 psia] in the cell as indicated by PT02K and PT06K readings. Close V5 and allow the cell temperature and pressure to equilibrate. The cell temperature rises above its previously attained equilibrium value through a few tens of mK immediately following a fresh charge of gas into the cell because of the work of compression.

(17) Keep checking the cell temperature and pressure readings every half an hour. Approximately 2 hours are required for the cell temperature and pressure readings to stabilize. After equilibrium has been reached, select a period of 30 to 40 minutes following a ZP position weighing balance reading check for measuring the apparent mass of the sinker under gas pressure at the isotherm temperature and manually change the direction of the current through the PRT manually at the frequency of data acquisition.

(18) Stop the MSA control, PRT resistance and PT02K and PT06K pressure data acquisition programs at the end of the 30 to 40 minute period. The pressure,

temperature and balance readings at 3.447 MPa [500 psia] and the balance reading in vacuum at the same temperature enable calculation of the experimental density.

(19) Start the data acquisition programs for PT02K, PT06K and the barometer.

(20) Open valves VC1, VC2, VC3, VC4, VC5, VC6 and VC8 and close valves VC7 and VC9 on the DWG/DPI setup for pressure transducer calibrations so that the pressure on the oil and gas sides of the diaphragm is equal to atmospheric pressure. Switch the motor that rotates the DWG piston in its cylinder 'on'. Draw the piston of the oil hand pump to the farthest extent outside its cylinder and fill the oil reservoir cup so that the oil level in it is at the reference plane of the DWG. Adjust the null indicator pointer at zero with the zero adjustment knob of the DPI.

(21) Switch the motor 'off' and load the Ruska DWG with weights that would measure approximately 485 psia and switch it 'on' again. Close VC6 and check if the null indicator pointer moves to the 'high oil pressure' side when the piston of the oil hand pump is drawn into its cylinder.

(22) Open V13 on the old manifold so that the pure gas displaces air from the tubing between V13 and VC1 as well as the high pressure gas chamber of the DPI through VC2. If needed, close V13, increase the pressure in the section of the old manifold between V5 and V10 and HP1 and then reopen V13 to clean the tubing between V13 and VC1 and the gas chamber of the DPI. Caution should be exercised so that the gas side pressure is not much higher than the oil side pressure. If the null indicator pointer goes out of scale on the 'high gas pressure' side, increase the pressure on the oil side of the diaphragm using the oil hand pump.

(23) Close VC2 so that the pressure on the gas side of the diaphragm increases. Increase the oil side pressure so that the null indicator pointer does not go out of scale on the 'high gas pressure' side. Keep increasing the pressure in the gas chamber of the DPI with HP1 on the old manifold while simultaneously

increasing the pressure in the oil chamber with the oil hand pump such that the null indicator pointer is always within the -50 to +50 division scale.

(24) When the pressure is slightly below 3.447 MPa [500 psia], open V5 so that the static pressure measured by PT02K and PT06K on one end is the same as that measured by the DWG/DPI on the other end of the experimental setup. Manipulate HP1 and the oil hand pump to increase or decrease the gas and oil side pressures respectively so that the DWG and the null indicator pointer of the DPI are balanced simultaneously. Make a note of the time, temperature of the DWG piston cylinder assembly, readings from PT02K, PT06K and the barometer when the DPI and DWG are balanced. After a few minutes the balanced states of the DPI and DWG are lost. Balance the DPI and DWG two more times to check for repeatability.

(25) Lower the gas and oil side pressures in turns until the DWG piston rests on its support. Switch the DWG motor ‘off’ and replace the weights measuring approximately 3.343 MPa [485 psia] by those measuring approximately 3.550 MPa [515 psia] and switch the motor ‘on’ again.

(26) Manipulate HP1 and the oil hand pump to balance the DPI and DWG at a pressure close to 3.550 MPa [515 psia]. Make a note of the time, temperature of the DWG piston cylinder assembly, readings from PT02K, PT06K and the barometer when the DPI and DWG are balanced. Balance the DPI and DWG two more times to check for repeatability.

(27) Lower the gas and oil side pressures in turns until the piston rests on its support. Switch the DWG motor ‘off’ and close VC4 so that the gas pressure does not surpass the oil side pressure because of oil leakage from the clearance space between the DWG piston and cylinder when it is not in operation. Close V13 and increase the oil side pressure so that the null indicator pointer is on the extreme end of the scale indicating ‘high oil pressure’.

(28) The absolute pressure readings from PT02K and PT06K on one hand and the DWG pressure and the atmospheric pressure reading from the barometer on the

other hand provide the calibration for PT02K and PT06K at two pressures approximately 15 psia higher and lower than the 500 psia pressure at which the density was measured.

(29) Start the pressure, temperature, MSA control and weighing balance data acquisition programs, open V5 slightly and increase the MSD cell pressure to approximately 6.894 MPa [1,000 psia]. Close V5 and allow a period of approximately two hours for temperature and pressure equilibration and manually change the direction of the current through the PRT at the frequency of data acquisition for a period of 30 to 40 minutes following a ZP position weighing balance reading check. Stop the data acquisition programs for density measurement at approximately 6.894 MPa [1,000 psia].

(30) Start the data acquisition programs for PT02K, PT06K and the barometer. Load the DWG piston with weights meant to measure approximately 6.791 MPa [985 psia], switch the DWG motor 'on' and open VC4.

(31) Open V13 slightly so that the gas side pressure increases in the DPI. Increase the oil and gas pressures in turns so that the null indicator pointer does not go out of scale. If required increase pressure in HP1 by closing V13, opening V1, using the compressor and then closing V10. Open V5 so that PT02K and PT06K measure the same pressure as the DWG. Balance the DWG and DPI at approximately 6.791 MPa [985 psia].

(32) Lower the gas and oil side pressures so that the piston rests on its support, switch the DWG motor 'off', replace the weights meant to measure approximately 6.791 MPa [985 psia] by those meant to measure approximately 6.998 MPa [1,015 psia] and switch the motor 'on'. Balance the DPI and DWG at approximately 6.998 MPa [1,015 psia].

(33) Lower the gas and oil side pressures so that the piston rests on its support, close VC4 and V13 and stop the data acquisition programs. The PT02K and PT06K readings at approximately 6.791 MPa [985 psia] and 6.998 MPa [1,015 psia] and the corresponding DWG pressures along with the barometer readings give the

calibration of the pressure transducers for density measurement at approximately 6.894 MPa [1,000 psia].

(34) Repeat steps (29) through (33) for density measurements at 10.342 MPa [1,500 psia] and 13.789 MPa [2,000 psia] with corresponding calibration points measured at 15 psia above and below these pressure points.

(35) For density measurements at pressure points higher than approximately 13.789 MPa [2,000 psia] up to approximately 34.473 MPa [5,000 psia], close valves VS2K and V15 and open valves VG2K, VI2 and VA on the new manifold so that even if there is a small leakage through VS2K, the pressure between VS2K and VG2K does not build up to a value that exceeds the maximum pressure limit of PT02K of 13.789 MPa [2,000 psia].

(36) After measuring the calibration point at the highest pressure of 34.577 MPa [5,015 psia], close V13 and open VC2 slightly to decrease the gas side pressure of the DPI gradually. The oil side pressure is decreased correspondingly by drawing the piston of the oil hand pump out of its cylinder but always maintaining the oil side pressure higher than the gas side pressure. Upon reaching atmospheric pressure, open VC4 and VC6 and check if the null indicator pointer returns to zero. If it does not return to zero, make a note of the number of divisions that it deviates from the zero position.

(37) Start the pressure, temperature and MSA control and weighing balance data acquisition programs to measure the true mass of the sinker in vacuum at the isotherm temperature again, following the measurements at pressure points.

(38) Switch VP1 ‘on’, open V14 completely but VI1 only slightly while V5 is still closed following density measurement at 34.473 MPa [5,000 psia] and evacuate the cell until GTV1 indicates a vacuum reading close to the one before the pressure points. This evacuation may take as long as 8 to 10 hours and is essential especially if the MSA went out of control during measurements at pressure points and the electromagnet suspension tube had to be gently raised to free the permanent magnet from the electromagnet. A repeatable value for true

mass of the sinker in vacuum means that the raising of the electromagnet did not disturb the horizontal and vertical alignment of the MSA parts. Stop the data acquisition programs.

(39) Open V5 and V10 and evacuate the old manifold between the compressor and V5.

(40) Close V5, VI1 and V14 so that the MSD cell remains evacuated until the next use. Switch VP1 ‘off’. To get ambient air into the cell open VS2K on the new manifold.

(41) Lower the clamp on the aluminum support to lower the level of the heating/cooling liquid in the cell bath to about a cm above the top surface of the MSD cell. Change the set-point temperature on the constant temperature circulation bath to a value close to ambient temperature so that the cell temperature also changes gradually to ambient temperature. Bringing the temperature of the heating/cooling liquid back to ambient temperature is important especially if the isotherm temperature was lower than ambient temperature.

(42) Switch the constant temperature circulation bath and the tubing and manifold heaters ‘off’. Close the regulator valve on the cylinder supplying nitrogen to the PRT isolation tube. Leave the aluminum block heaters and controllers ‘on’ continuously.

VITA

Prashant Vithal Patil was born on June 22, 1971 to Mr. Vithal Gopal Patil and Mrs. Kusum Vithal Patil in Thane city in the state of Maharashtra in India. He is the second among three brothers.

He attended St. John the Baptist High School, Thane and St. Xavier's High School, Nashik for his school education and H.P.T. Arts & R.Y.K. Science College, Nashik for his junior college education. He earned a Bachelor of Chemical Engineering degree from the University of Bombay, Department of Chemical Technology (popularly called U.D.C.T., Bombay in India) in August 1993. He worked as a research assistant at U.D.C.T for a period of a year after his undergraduate education. He came to The University of Tulsa, Tulsa, Oklahoma in August 1994 to pursue a Master of Science degree in chemical engineering which he completed in December 1996. In January 1997, he joined the chemical engineering department at Texas A&M University to pursue a Ph.D. in the area of polymer rheology with Dr. Lynden A. Archer. He requested a long leave of absence from the department between May 1999 and August 2000. While on leave, he worked as an analyst with the Bombay, India office of Andersen Consulting (present day Accenture). He resumed his graduate research work at Texas A&M University in September 2000, albeit in a different area this time, with Dr. Kenneth R. Hall and Dr. James C. Holste. The present dissertation is the result of his research work since September 2000.

He may be reached by E-mail at [pvp9391@yahoo.com] or by contacting Dr. Hall at:

Prashant V. Patil
C/o. Dr. Kenneth R. Hall
Department of Chemical Engineering
255-A Jack E. Brown Engineering Building
Mail Stop 3122, Texas A&M University
College Station, TX 77843-3122